

# Search for a Spin-Dependent Short-Range Force between Nucleons with a ${}^3\text{He}/{}^{129}\text{Xe}$ Clock-Comparison Experiment

## Dissertation

zur Erlangung des Grades  
“Doktor der Naturwissenschaften”

am Fachbereich Physik, Mathematik und Informatik  
der Johannes Gutenberg Universität  
in Mainz



**Kathlyne Tullney**  
geb. in Weilburg

Mainz, November 2013  
D77

1. Berichterstatter: \*)

2. Berichterstatter: \*)

Tag der mündlichen Prüfung: 13. Februar 2014

---

\*) Wurden aus Datenschutzgründen aus der elektronischen Version gelöscht.

Dedicated to my parents.



# Contents

<b>1</b>	<b>Introduction</b>	<b>1</b>
<b>2</b>	<b>Axion Physics</b>	<b>5</b>
2.1	Lagrangian Density of QCD . . . . .	5
2.2	The $U(1)_A$ Problem . . . . .	6
2.3	The Strong $CP$ -Problem . . . . .	8
2.4	Solution to the Strong $CP$ -Problem . . . . .	8
2.5	Properties of Axions . . . . .	9
2.5.1	Couplings of the Axion . . . . .	9
2.6	Axion Models . . . . .	11
2.6.1	Visible Axions . . . . .	11
2.6.2	Invisible Axions . . . . .	12
2.7	Cosmological and Astrophysical Constraints . . . . .	14
2.7.1	Cosmological Constraints . . . . .	14
2.7.2	Astrophysical Considerations . . . . .	15
2.8	Detection of the Axion . . . . .	16
2.8.1	Direct Detection of the Axion . . . . .	17
2.8.2	Indirect Detection of the Axion . . . . .	20
<b>3</b>	<b>Theory of Spin Precession</b>	<b>23</b>
3.1	Spins in a Magnetic Field . . . . .	23
3.2	Polarization and Optical Pumping . . . . .	24
3.2.1	Metastability Exchange Optical Pumping . . . . .	25
3.2.2	Spin Exchange Optical Pumping . . . . .	26
3.3	Spin Precession and Bloch Equations . . . . .	28
3.4	Magnetic Field Produced by Spin Polarized Atoms . . . . .	31
3.5	Relaxation . . . . .	32
3.5.1	Longitudinal Relaxation . . . . .	32
3.5.2	Transverse Relaxation . . . . .	37
<b>4</b>	<b>Experimental Technique and Setup</b>	<b>39</b>
4.1	Experimental Technique . . . . .	39
4.2	Experimental Realization . . . . .	43
4.2.1	Measurement Cells . . . . .	43
4.2.2	Magnetically Shielded Room . . . . .	44
4.2.3	SQUID System and Magnetic Field . . . . .	46
4.2.4	Filling System . . . . .	49
4.2.5	Transport Coil . . . . .	52
4.2.6	BGO Crystal and Suspension Mechanism . . . . .	53
4.2.7	Measurement Procedure . . . . .	53

<b>5</b>	<b><math>^3\text{He}/^{129}\text{Xe}</math> Co-Magnetometer</b>	<b>59</b>
5.1	Estimation of Sensitivity Level . . . . .	59
5.2	Inherent Noise of Magnetometer . . . . .	62
<b>6</b>	<b>Analysis</b>	<b>71</b>
6.1	Piecewise Fitting of Raw Data . . . . .	73
6.2	Phase Determination . . . . .	75
6.3	Weighted Phase Difference and Phase Shifts . . . . .	78
6.3.1	Linear Phase Shifts . . . . .	78
6.3.2	Exponential Phase Shifts . . . . .	83
6.3.3	Other Phase Shifts . . . . .	88
6.4	Phaseresiduals . . . . .	89
6.5	Determination of Transverse Relaxation Times . . . . .	89
6.6	Limit on Spin-Dependent Short-Range Force . . . . .	91
6.7	Discussion of Systematic Uncertainties . . . . .	96
6.8	Bounds on $g_s g_p$ . . . . .	104
<b>7</b>	<b>Conclusion and Outlook</b>	<b>125</b>
<b>A.</b>	<b>Calculation of the Standard Deviation of the Weighted Phase Difference</b>	<b>129</b>
<b>B.</b>	<b>Exact Determination of <math>T_2^*</math></b>	<b>131</b>
B.1	Possible Reason for the Structure in the Amplitude Residuals . . . . .	133
B.2	Method of Exact $T_2^*$ Determination . . . . .	135
<b>C.</b>	<b>Derivation of the Amplitude in Case of a Time Dependent <math>T_2^*</math> time</b>	<b>153</b>
<b>D.</b>	<b>Derivation of Systematic Error <math>\Delta\nu_{\text{sys}}^{T_2^*}</math></b>	<b>155</b>
<b>E.</b>	<b>Derivation of the function <math>f_{\text{BGO}}^\pm(t)</math></b>	<b>159</b>
<b>F.</b>	<b>Calculation of <math>V_\Sigma^c</math></b>	<b>161</b>
<b>G.</b>	<b>Paper</b>	<b>167</b>

# List of Figures

2.1	Primakoff Effect . . . . .	15
2.2	Summary of astrophysical and cosmological bounds . . . . .	21
3.1	Metastability exchange optical pumping of $^3\text{He}$ . . . . .	25
3.2	Scheme of the PTB $^{129}\text{Xe}$ polarizer . . . . .	27
3.3	Free induction decay . . . . .	31
4.1	Scheme of experimental setup. . . . .	40
4.2	Drift of magnetic guiding field $B_0$ during measurement run C68. . . . .	41
4.3	Cylindrical measurement cell. . . . .	44
4.4	BMSR-2 building and shielding . . . . .	45
4.5	Vertical cut view through innermost shield of the BMSR-2. . . . .	47
4.6	Filling station for gas mixture . . . . .	50
4.7	$T_2^*$ time in a $^3\text{He}/^{129}\text{Xe}$ gas mixture as function of the $\text{N}_2$ pressure . . . . .	55
4.8	Transport coil . . . . .	56
4.9	Suspension of BGO crystal. . . . .	57
4.10	Experimental Setup. . . . .	58
5.1	Free spin precession signal of pure polarized $^3\text{He}$ . . . . .	65
5.2	Estimated sensitivity (CRLB) of the $^3\text{He}$ magnetometer in tracing tiny magnetic field fluctuations as a function of the observation time $T$ . . . . .	66
5.3	Estimated measurement sensitivity regarding the frequency $\nu$ of the $^3\text{He}/^{129}\text{Xe}$ co-magnetometer as a function of the observation time $T$ . . . . .	67
5.4	Phase residuals and root mean square (RMS) of measurement C92 (Sept. 2009). . . . .	68
5.5	Allan standard deviation (ASD) of the phase residuals measured in run C92 (Sept. 2009) using nuclear spin precession of co-located $^3\text{He}$ and $^{129}\text{Xe}$ gas. . . . .	69
6.21	Experimental 95% confidence upper limit on $ g_s^N g_p^e $ plotted versus $\lambda$ , the range of the Yukawa-force with $\lambda = \hbar/(m_a c)$ . . . . .	105
6.1	Magnetic flux density spectrum of the $^3\text{He}$ and $^{129}\text{Xe}$ precession signals . . . . .	107
6.2	Gradiometer signals. . . . .	108
6.3	Typical sub-data set of 3.2 s length used for fitting. . . . .	109
6.4	$\chi^2/dof$ distribution of the raw data fits of measurement run C68. . . . .	110
6.5	Illustration of over- and underestimation of the number of periods $n_{\text{He}/\text{Xe}}^i$ . . . . .	111
6.6	Weighted phase difference for measurement run C68 . . . . .	112
6.7	The Earth's rotating coordinate system and direction of the magnetic guiding field inside BMSR-2. . . . .	113
6.8	Illustration of calculation of the center of mass in z-direction. . . . .	114
6.9	Ramsey-Bloch-Siegert shift $\delta\omega_{\text{RBS}}$ . . . . .	115
6.10	Illustration of RBS self-shift. . . . .	116

6.11	Phase residuals of measurement run C68 after subtraction of the fitted function of Eq. 6.16 from $\Delta\Phi_{\text{rem}}(t)$ . . . . .	117
6.12	Decay of the $^3\text{He}$ and $^{129}\text{Xe}$ amplitudes of measurement run C68 for three different gradiometers. . . . .	118
6.13	Amplitude residuals of $^3\text{He}$ and $^{129}\text{Xe}$ of measurement run C68 for three different gradiometers resulting from an exponential fit according to Eq. 6.55. . . . .	119
6.14	Extracted frequency shifts $\Delta\nu_{\text{sp}}$ and $\Delta\nu_{\text{LV}}$ (with correlated $1\sigma$ error). . . . .	120
6.15	Illustration of the change of the magnetic guiding field $\vec{B}_0$ due to the non-zero magnetic susceptibility of the BGO crystal. . . . .	121
6.16	Simulated change of the magnetic guiding field $B_{\text{BGO}} =  \vec{B}_{\text{cal}}  -  \vec{B}_0 $ along the x-direction ( $y=0$ and $z=0$ ) and derivative $\frac{\partial}{\partial x}B_{\text{BGO}}(x)$ for $x > 0$ cm, due to the non-zero magnetic susceptibility of the BGO crystal. . . . .	122
6.17	Simulated change of the magnetic guiding field $B_{\text{BGO}} =  \vec{B}_{\text{cal}}  -  \vec{B}_0 $ along the y-direction ( $x=6.7$ cm and $z=0$ ) and derivative $\frac{\partial}{\partial y}B_{\text{BGO}}(y)$ for $y > 0$ cm, due to the non-zero magnetic susceptibility of the BGO crystal. . . . .	123
6.18	Illustration of the determination of $\Delta T_2^*$ via the difference $\Delta s$ of the slopes of the signal amplitude $A(t)$ at the time $t_0$ . . . . .	124
B.1	Decay of the $^3\text{He}$ and $^{129}\text{Xe}$ amplitudes of measurement run C68 for three different gradiometers. . . . .	140
B.2	Amplitude residuals of $^3\text{He}$ and $^{129}\text{Xe}$ of measurement run C68 for three different gradiometers resulting from an exponential fit according to Eq. B.2. . . . .	141
B.3	Residuals of the amplitudes of $^3\text{He}$ and $^{129}\text{Xe}$ and residuals of the amplitude ratio $\text{Res}(R(t))$ of measurement run C92 (LV 2009). . . . .	142
B.4	Residuals of the amplitude ratio $\text{Res}(R(t))$ for all three gradiometers of measurement run C68 and C65. . . . .	143
B.5	Amplitude residuals of $^3\text{He}$ and $^{129}\text{Xe}$ of measurement run C65 for three different gradiometers resulting from a common exponential fit according to Eq. B.2. . . . .	144
B.6	Amplitude residuals of $^3\text{He}$ and $^{129}\text{Xe}$ of measurement run C68 for three different gradiometers, which result from the fit given by Eq. B.13. . . . .	145
B.7	Illustration of the spline-interpolation. . . . .	146
B.8	Residuals of the amplitude ratio $R(t)$ for all three gradiometers of measurement run C68 determined via a spline-interpolation. . . . .	147
B.9	Residuals of the xenon amplitudes $A_{\text{Xe}}(t)$ for all three gradiometers of measurement run C68. . . . .	148
B.10	Illustration of the determination of the function $f_{\text{res}}(t)$ via spline-interpolation. . . . .	149
B.11	Residuals of the xenon signal amplitudes $A_{\text{Xe}}(t)$ and helium signal amplitudes $A_{\text{He}}(t)$ for all three gradiometers of measurement run C68 determined via a spline-interpolation. . . . .	150
B.12	Amplitude residuals of $^3\text{He}$ and $^{129}\text{Xe}$ of measurement run C68 for three different gradiometers which were determined with a direct fit (Eq. B.24) of the signal amplitudes of helium and xenon. . . . .	151
F.1	Illustration of the arrangement of the BGO crystal and the spin samples. . . . .	163
F.2	Devolution of $\eta(\lambda)$ for our cylindrical measurement cells. . . . .	165



# List of Tables

3.1	Diffusion coefficients for $^3\text{He}$ and $^{129}\text{Xe}$ at a pressure of 1 bar. . . . .	35
4.1	Measured field gradients without and with magnetic guiding field inside BMSR-2. . . . .	48
6.1	Parameters of the 10 main measurements . . . . .	72
6.2	Transverse relaxation times of measurement runs C54-C82. . . . .	91
6.3	Best fit parameters of the fit model according to Eq. 6.59 with correlated $1\sigma$ error of the measurement runs C54-C82. . . . .	93
6.4	Best fit parameters of the fit model according to Eq. 6.70 with correlated $1\sigma$ error of the measurement runs C54-C82. . . . .	95
6.5	Results of $\Delta\nu_{\text{sp}}$ and $\Delta\nu_{\text{LV}}$ with correlated and uncorrelated $1\sigma$ -errors. . . . .	97
6.6	Change of transverse relaxation times of the measurement runs C54-C82. . . . .	100
6.7	Change of the transverse relaxation times of $^3\text{He}$ ( $\Delta T_{2,\text{He}}^*$ ). . . . .	104
B.1	Fit parameters of the temporal development of the total magnetic guiding field $ \vec{B}_{\text{tot}}(t) $ . . . . .	134
B.2	Transverse relaxation times of measurement runs C54-C82. . . . .	139



# Zusammenfassung

Das Standardmodell (SM) der Teilchenphysik beschreibt erfolgreich die Eigenschaften von Teilchen und deren Wechselwirkung miteinander. Allerdings ist das SM nicht vollständig, da es zum Beispiel nur drei der vier fundamentalen Kräfte beinhaltet. Auch die Frage, warum für die starke Wechselwirkung aufgrund seiner nicht trivialen Vakuumstruktur eine Verletzung der  $CP$  Symmetrie<sup>1</sup> erwartet wird ( $\Theta$ -Term), aber experimentell nicht nachweisbar ist, kann im Rahmen des SM nicht erklärt werden. Dieses Problem wird als das *starke CP-Problem* der Quantenchromodynamik bezeichnet und durch die Peccei-Quinn-Weinberg-Wilczek Theorie gelöst. Danach wird ein neues, fast masseloses Boson postuliert, welches man als Axion bezeichnet. Das Axion wechselwirkt nur sehr schwach mit Materie und ist daher auch ein guter Kandidat für die kalte dunkle Materie. Axionen entstehen durch den Primakoff-Effekt, also durch Umwandlung gestreuter Photonen in elektromagnetischen Feldern, z.B. von Atomkernen. Der inverse Primakoff-Effekt, welcher ein Axion wieder in ein Photon umwandelt, kann zum direkten Nachweis von Haloaxionen, solaren Axionen und Labor-Axionen ausgenutzt werden. Kosmologische und astrophysikalische Beobachtungen führten zur Einschränkung der Masse des Axions auf einen Bereich von einigen  $\mu\text{eV}$  bis  $\text{meV}$  (*“axion mass window”*).

Wenn das Axion existiert, dann vermittelt es eine  $CP$  verletzende, kurzreichweitige und spinabhängige Wechselwirkung zwischen einem Fermion und dem Spin eines anderen Fermions. Durch Nachweis dieser Wechselwirkung kann das Axion indirekt nachgewiesen werden. Im Rahmen der vorliegenden Doktorarbeit wurde ein Experiment zur Suche dieser kurzreichweitigen, spinabhängigen Wechselwirkung mit einem ultra-sensitiven Komagnetometer realisiert, welches auf dem Nachweis von frei präzedierenden  $^3\text{He}$  und  $^{129}\text{Xe}$  Kernspins basiert. Das Experiment wurde im magnetisch abgeschirmten Raum BMSR-2 an der Physikalisch-Technische Bundesanstalt Berlin durchgeführt. Die beiden polarisierten Gase befinden sich in einer Glaszelle, welche sich in einem niedrigen Magnetfeld von etwa  $B_0 = 0.35 \mu\text{T}$  mit absoluten Feldgradienten im Bereich von  $\text{pT/cm}$  befindet. Die Spinpräzession von  $^3\text{He}$  und  $^{129}\text{Xe}$  mit den Präzessionsfrequenzen  $\omega_{\text{He}} = \gamma_{\text{He}} \cdot B_0 = 11.4 \text{ Hz}$  und  $\omega_{\text{Xe}} = \gamma_{\text{Xe}} \cdot B_0 = 4.7 \text{ Hz}$  wird mit SQUID Detektoren mit einem niedrigen Rauschen nachgewiesen. Durch Betrachtung der gewichteten Frequenzdifferenz  $\Delta\omega = \omega_{\text{He}} - (\gamma_{\text{He}}/\gamma_{\text{Xe}}) \cdot \omega_{\text{Xe}}$  können Magnetfelddriften beseitigt werden (Zeeman-Term), so dass das Komagnetometer nur noch auf nicht-magnetische Wechselwirkungen empfindlich ist. Aufgrund der erreichten Spinkohärenzzeiten von mehreren Stunden können Frequenzverschiebungen durch nicht-magnetische Wechselwirkungen im Bereich von einigen  $\text{nHz}$  gemessen werden.

Die Grundidee des durchgeführten Experimentes bestand darin, eine unpolarisierte Masse in die Nähe der polarisierten Gase zu bringen und nach einer bestimmten Zeit wieder zu entfernen oder umgekehrt. Falls die kurzreichweitige, spinabhängige Wechselwirkung existiert, dann sollte es, wenn die unpolarisierte Masse in der Nähe des Komagnetometers ist, zu einer Verschiebung der Präzessionsfrequenzen von  $^3\text{He}$  und  $^{129}\text{Xe}$  kommen. Diese Frequenzverschiebung wird sowohl für  $^3\text{He}$  als auch für  $^{129}\text{Xe}$  im wesentlichen durch Kopplung des Axions an den Spin des Valenzneutrons hervorgerufen. Sie ist somit für beide Gase in etwa gleich groß und fällt daher in der gewichteten Frequenzdifferenz nicht raus. Aufgrund der sehr hohen Empfindlichkeit des entwickelten Komagnetometers konnte im Experiment die Obergrenze für diese Frequenzverschiebung zu  $7.1 \text{ nHz}$  bestimmt werden. Mit diesem Wert konnten nun auch innerhalb des *“axion mass window”* Obergrenzen für die skalare-pseudoskalare Kopplung des Axions an den Spin eines gebundenen Neutrons berechnet werden. Für Massen des Axions zwischen  $2 \mu\text{eV}$  und  $500 \mu\text{eV}$  wurden die bisherigen Obergrenzen für Laborexperimente bis zu 4 Größenordnungen verbessert.

---

<sup>1</sup>  $C \hat{=}$  Ladungsumkehr,  $P \hat{=}$  Raumspiegelung



# Abstract

The standard model (SM) of particle physics describes all known particles and their interactions. However, the SM leaves many issues unresolved. For example, it only includes three of the four fundamental forces and does not clarify the question why in the strong interaction  $CP$  symmetry<sup>2</sup> is violated due to its non-trivial vacuum structure is predicted ( $\Theta$ -term), but experimentally unverifiable. The latter one is known as the *strong CP-problem* of quantum chromodynamics (QCD) and is solved by the Peccei-Quinn-Weinberg-Wilczek theory. This theory predicts a new and almost massless boson which is known as the axion. The axion feebly interacts with matter and therefore it is a good candidate for cold dark matter, too. Axions are produced by the Primakoff-effect, i.e. by conversion of photons which are scattered in the electromagnetic field, e.g. of atoms. The inverse Primakoff-effect, which converts axions to photons again, can be used for direct detection of galactic, solar, or laboratory axions. Cosmological and astrophysical observations constrain the mass of the axion from a few  $\mu\text{eV}$  to some  $\text{meV}$  (“*axion mass window*”).

If the axion exists, then it mediates a  $CP$  violating, spin-dependent, short-range interaction between a fermion and the spin of another fermion. By verification of this interaction, the axion can be detected indirectly. In the framework of the present thesis an experiment to search for this spin-dependent short-range interaction was performed in the magnetically shielded room BMSR-2 of the Physikalisch-Technische Bundesanstalt Berlin. An ultra-sensitive low-field co-magnetometer was employed which is based on the detection of free precession of  $^3\text{He}$  and  $^{129}\text{Xe}$  nuclear spins using SQUIDs as low-noise magnetic flux detectors. The two nuclear spin polarized gases are filled into a glass cell which is immersed in a low magnetic field of about  $B_0 = 0.35 \mu\text{T}$  with absolute field gradients in the order of  $\text{pT/cm}$ . The spin precession frequencies of  $^3\text{He}$  and  $^{129}\text{Xe}$  then correspond to  $\omega_{\text{He}} = \gamma_{\text{He}} \cdot B_0 = 11.4 \text{ Hz}$  and  $\omega_{\text{Xe}} = \gamma_{\text{Xe}} \cdot B_0 = 4.7 \text{ Hz}$ . By means of the weighted frequency difference  $\Delta\omega = \omega_{\text{He}} - (\gamma_{\text{He}}/\gamma_{\text{Xe}}) \cdot \omega_{\text{Xe}}$ , magnetic field drifts can be eliminated (Zeeman-term). Thus, the co-magnetometer is only sensitive to non-magnetic interactions. Based on the long spin coherence times of several hours, frequency shifts due to non-magnetic interactions in the order of a few  $\text{nHz}$  can be measured.

The general idea of this experiment was to place an unpolarized matter close to the spin polarized samples, which is then removed to a distant position or vice versa. If the spin-dependent short-range interaction exists, the unpolarized matter causes a shift in the spin precession frequencies of  $^3\text{He}$  and  $^{129}\text{Xe}$  for the unpolarized matter close to the polarized gases. For  $^3\text{He}$  as well as for  $^{129}\text{Xe}$  this frequency shift essentially is stemming from the coupling of the axion to the spin of the valence neutron. Hence it is approximately equal for  $^3\text{He}$  and  $^{129}\text{Xe}$  and therefore does not drop out in the weighted frequency difference. Due to the high sensitivity of the co-magnetometer, the upper limit of this frequency shift could be determined to be  $7.1 \text{ nHz}$ . With this value, an upper limit of the scalar-pseudoscalar coupling of the axion to the spin of a bound neutron could be deduced within the axion mass window. For axion masses between  $2 \mu\text{eV}$  and  $500 \mu\text{eV}$ , the laboratory upper bounds were improved by up to 4 orders of magnitude.

---

<sup>2</sup> $C \hat{=}$  charge conjugation and  $P \hat{=}$  parity



# 1 Introduction

The search of a spin-dependent short-range force, which is mediated by an axion or an axion-like particle, is closely linked to the examination of the discrete symmetries charge  $C$  (interchange of particle and antiparticle), parity  $P$  (space inversion) and time  $T$  (time inversion). The combination of all three symmetries, i.e. the  $CPT$  symmetry, is a fundamental symmetry on which the Standard Model (SM) of particle physics is based on. Each symmetry can be individually broken, whereas strong arguments predict that the  $CPT$  symmetry is a conserved quantity. That means, violation of  $T$  symmetry leads to violation of  $CP$  symmetry. Indeed,  $CP$  violation is included in the SM, e.g. in weak interactions it is a natural consequence, which leads to a complex phase in the CKM matrix<sup>1</sup>.  $CP$  violation in the context of the CKM matrix was investigated in the decay of mesons [1, 2, 3, 4]. In these experiments no deviations from the predictions of the SM were observed.

$CP$  violation also plays an important role in the explanation of the baryon asymmetry, which corresponds to the imbalance of matter over antimatter in the universe. In the Big Bang scenario, matter and antimatter were produced in equal shares. Due to annihilation it is expected that there is no matter and antimatter left at all, resulting in

$$\eta = \frac{\eta_b - \eta_{\bar{b}}}{\eta_\gamma} = 0, \quad (1.1)$$

where  $\eta_b$  and  $\eta_{\bar{b}}$  are the number of baryons and antibaryons respectively and  $\eta_\gamma$  is the number of photons from the annihilation process. However, from today's point of view the whole observable universe is entirely made up of matter. There is no experimental evidence that the observable universe contains any significant concentrations of antimatter. Hence the ratio of visible matter and the observable radiation is unequal to zero, i.e.  $\eta \neq 0$ . Via Planck's law the photon density  $\eta_\gamma$  of the universe can be calculated by considering the cosmic microwave background which results in  $\eta_\gamma \approx 420$  photons per  $\text{cm}^3$ . The visible matter of the universe is given by  $\eta_b \approx 1$  proton per  $\text{cm}^3$ . Thus, the ratio of the visible matter and the observable radiation results in [5]

$$\eta = \frac{\eta_b - \eta_{\bar{b}}}{\eta_\gamma} = \frac{\eta_b}{\eta_\gamma} = (6.1 \pm 0.3) \cdot 10^{-10}. \quad (1.2)$$

A possible explanation of the baryon asymmetry is given by the three Sakharov conditions [6]. These conditions state that matter and antimatter could be produced at different rates after the Big Bang if there was thermal disequilibrium, the baryon number was violated and the  $C$  and  $CP$  symmetries were violated. The baryon asymmetry which results from  $CP$  violating effects of the SM can be calculated to be [7]:

$$\eta = \frac{\eta_b - \eta_{\bar{b}}}{\eta_\gamma} = \frac{\eta_b}{\eta_\gamma} \approx 10^{-18}. \quad (1.3)$$

---

<sup>1</sup>The Cabbibo-Kobayashi-Maskawa (CKM) matrix describes the mixing of quark masses.

This value is 8 orders smaller than the observed one (Eq. 1.2). Hence, the SM does not contain enough  $CP$  violating effects to explain the present imbalance of matter over antimatter in the universe. That means, new sources of  $CP$  violation are needed. A possible source for  $CP$  violation may be the spin-dependent short-range force mediated by the scalar and pseudoscalar coupling of the axion.

In general, our experimental approach to test fundamental symmetries in nature is to use an ultra-sensitive  ${}^3\text{He}/{}^{129}\text{Xe}$  co-magnetometer that is based on clock-comparison, i.e. the comparison of the transition frequencies of two co-located spin systems, which radiate on their Zeeman or hyperfine transitions. In our case co-located nuclear polarized  ${}^3\text{He}$  and  ${}^{129}\text{Xe}$  spin samples are used, which precess in a magnetic guiding field  $\vec{B}$  with the so-called Larmor frequency  $\omega_L = \gamma \cdot |\vec{B}|$ , where  $\gamma$  is the gyromagnetic ratio of the respective spin sample. Non-magnetic spin interactions can be described in general by an additional potential of type

$$V_{\text{PM}} = \vec{a} \cdot \vec{\sigma} \equiv -\vec{\mu}_{\text{PM}} \cdot \vec{B}_{\text{PM}} , \quad (1.4)$$

where  $\vec{a}$  is an anomalous field and  $\vec{\sigma}$  the spin vector. This potential  $V_{\text{PM}}$  describes a pseudo-magnetic interaction and thus can also be written as the scalar product of a pseudomagnetic moment  $\vec{\mu}_{\text{PM}}$  and the corresponding pseudomagnetic field  $\vec{B}_{\text{PM}}$ . Assuming that the anomalous field  $\vec{a}$  does not couple to magnetic moment but directly to the sample spin  $\vec{\sigma}$ , the use of two spin systems allows to distinguish between a normal magnetic field (Zeeman-term) and an anomalous field coupling. This means that, similar to the linear Zeeman-effect the potential  $V_{\text{PM}}$  leads to a shift in the precession frequency given by  $\omega_{\text{PM}} = V_{\text{PM}}/\hbar$ . Violation of fundamental symmetries of nature, which cause a non-magnetic shift  $\omega_{\text{PM}}$  in the precession frequency of polarized spin samples, then can be studied with the  ${}^3\text{He}/{}^{129}\text{Xe}$  co-magnetometer, such as:

- a) Search for spin-dependent short-range interaction induced by light, pseudoscalar bosons ( $CP$  violation) [8]:

$$\omega_{\text{sp}} = V_{\text{sp}}(r)/\hbar = c \cdot \vec{\sigma} \cdot \hat{r}/\hbar . \quad (1.5)$$

- b) Search for Lorentz-violating signatures by monitoring the relative Larmor frequencies or phases of the co-located  ${}^3\text{He}$  and  ${}^{129}\text{Xe}$  spin samples as the laboratory reference frame rotates with respect to distant stars [9]:

$$\omega_{\text{LV}} = V_{\text{LV}}(r)/\hbar = \langle \vec{b} \rangle \hat{e} \cdot \vec{\sigma}/\hbar . \quad (1.6)$$

- c) Search for the electric dipole moment of  ${}^{129}\text{Xe}$  ( $CP$  violation) [10]:

$$\omega_{\text{XeEDM}} = V_{\text{XeEDM}}(r)/\hbar = -|d_{\text{Xe}}| \cdot \vec{\sigma} \cdot \vec{E}/\hbar . \quad (1.7)$$

The observable to trace these obvious tiny frequency shifts  $\omega_{\text{PM}}$  is the weighted frequency



---

difference which is given by

$$\begin{aligned}
\Delta\omega(t) &= \omega_{\text{He}}(t) - \frac{\gamma_{\text{He}}}{\gamma_{\text{Xe}}} \cdot \omega_{\text{Xe}}(t) \\
&= \underbrace{\left(\gamma_{\text{He}} - \frac{\gamma_{\text{He}}}{\gamma_{\text{Xe}}} \gamma_{\text{Xe}}\right)}_{=0} \cdot B(t) + \left(1 - \frac{\gamma_{\text{He}}}{\gamma_{\text{Xe}}}\right) \cdot \omega_{\text{PM}}(t) + \dots \quad (1.8)
\end{aligned}$$

By that measure, any dependence on magnetic field fluctuations and drifts should be eliminated. Within the frame of the nuclear shell model of Th. Schmidt [11], both the spin of the  ${}^3\text{He}$  and the  ${}^{129}\text{Xe}$  nucleus is carried by the valence neutron (bound neutron). Hence, within the Schmidt model all couplings mentioned above (a-c) are roughly the same for  ${}^3\text{He}$  and  ${}^{129}\text{Xe}$ , i.e.  $\omega_{\text{PM}}(t) = \omega_{\text{PM,He}}(t) \approx \omega_{\text{PM,Xe}}(t)$ , so that the pseudomagnetic frequency shift  $\omega_{\text{PM}}(t)$  does not drop out in the weighted frequency difference. That means that the weighted frequency difference  $\Delta\omega(t)$ , or its equivalent, the weighted phase difference  $\Delta\Phi(t) = \Phi_{\text{He}}(t) - \frac{\gamma_{\text{He}}}{\gamma_{\text{Xe}}} \Phi_{\text{Xe}}(t)$ , is the relevant quantity to be further analyzed in order to trace tiny symmetry violations of the type mentioned above (a-c).

In the framework of this thesis the  ${}^3\text{He}/{}^{129}\text{Xe}$  co-magnetometer is used to search for the spin-dependent short-range force (case a) which is mediated by an axion between a fermion and the spin of another fermion. The axion is one of the favourite solution to the strong  $CP$ -problem of quantum chromodynamics (QCD): The non-trivial vacuum structure of strong interaction leads to the so-called  $\Theta$ -term to the QCD Lagrangian, which violates  $CP$  symmetry. However  $CP$  violation in strong interaction has never been observed in nature. In 1977 Peccei and Quinn introduced a new global, chiral symmetry to the QCD Lagrangian. This symmetry is referred to as the Peccei-Quinn-symmetry (PQ-symmetry) which is spontaneously broken at an unknown energy  $f_a$ . Due to non-exact breaking of the PQ-symmetry, a pseudo Nambu-Goldstone boson is expected. This boson has to be a light and electrically neutral pseudoscalar particle, which was named by Wilczek as *axion*. The dynamical field of the axion leads to an additional term to the QCD Lagrangian. At the minimum of this axion field the  $\Theta$ -term is absorbed. Thus, no  $CP$  violation in strong interaction occurs and the strong  $CP$ -problem is solved.

There exist different axion models which differ in the order of the symmetry breaking scale  $f_a$ . In the last decades the *visible* axion models could be precluded by some experiments, i.e. axions which occur at an energy  $f_a$  in the order of the electroweak energy scale ( $\approx 250$  GeV). However, the *invisible* axion models, i.e. axions with a high symmetry breaking scale and a rest mass below 1 eV, are still of high interest. Due to their weak coupling with fundamental particles, these axions are extremely difficult to detect. Hence, beside the WIMP's<sup>2</sup>, the axion can contribute significantly to the cold dark matter<sup>3</sup> of the universe. Based on astrophysical and cosmological considerations it was possible to constrain the

---

<sup>2</sup>WIMP = weakly interacting massive particle

<sup>3</sup>About 4% of the mass of the universe consists of hadronic matter and about 23% consists of dark matter which is non illuminating matter whereby the composition is unknown. The remaining mass of the universe is given by dark energy.

mass of the axion ( $m_a$ ) from a few  $\mu\text{eV}$  to some  $\text{meV}$ . This mass range is also referred to as the *axion mass window*. Several experiments have been searching for this elusive particle in and close to the axion mass window. All experiments that try a direct detection of the axion use the so-called Primakoff effect which allows conversion of axions into photons and vice versa in the presence of strong electromagnetic fields. On the contrary, the axion mediates a  $CP$  violating spin-dependent short-range interaction with range  $\lambda = \hbar/(m_a c)$  between a fermion and the spin of another fermion. This interaction can be described by a pseudoscalar potential and leads to an additional frequency shift in the weighted frequency difference measured with the  $^3\text{He}/^{129}\text{Xe}$  co-magnetometer (see Eq. 1.5). Thus, if this frequency shift can be measured, the axion can be detected indirectly.

The topic of this thesis is the analysis of the data measured in September 2010 at the *Physikalisch-Technische Bundesanstalt* (PTB) in Berlin. Here the precession frequencies of co-located spin polarized  $^3\text{He}$  and  $^{129}\text{Xe}$  with and without an unpolarized mass was measured. If the spin-dependent short-range interaction exists, there should be a constant shift  $\omega_{\text{sp}}^w$  in the weighted frequency difference  $\Delta\omega(t)$  when the unpolarized mass is moved. From this the coupling of pseudoscalar particles, such as the axion, to the sample spins can be determined. In Chap. 2, the theoretical background on axion physics is given as well as methods of direct and indirect detection of the axion are presented. Since in the experiment, which is described in this thesis, free spin precession of polarized  $^3\text{He}$  and  $^{129}\text{Xe}$  is measured, details of the optical pumping process of these noble gases and diverse relaxation mechanisms are given in Chap. 3. In Chap. 4 the measurement principle and the experimental setup are explained. The properties of the  $^3\text{He}/^{129}\text{Xe}$  co-magnetometer, i.e. its sensitivity as well as its inherent noise, are demonstrated in Chap. 5. Finally, in Chap. 6 the data analysis as well as systematic effects are discussed.

## 2 Axion Physics

The axion is a favourite solution of the strong  $CP$ -problem which occurs due to the non-trivial vacuum structure of quantum chromodynamics (QCD). It is a hypothetical neutral pseudoscalar boson, i.e. a particle with spin-0, which feebly couples to ordinary particles like photons and quarks. Therefore it is a good candidate to explain a part of the cold dark matter in the universe.

This chapter summarizes information on the axion, starting with the Lagrangian density of QCD and the  $U(1)_A$  problem. The strong  $CP$ -problem is described in Sec. 2.3. Section 2.4, deals with the solution of Peccei and Quinn to the strong  $CP$ -problem which bears the axion. In section 2.5 the properties of the axion and in Sec. 2.6 the different axion models are outlined. Cosmological and astrophysical constraints, as well as some experimental results, which confine the axion mass to a range from  $\mu\text{eV}$  to  $1\text{eV}$  (axion mass window) are discussed in Sec. 2.7 and 2.8. In Sec. 2.8 beside the direct detection of the axion the indirect detection of the axion via a  $CP$  violating force, which is mediated by the axion between a fermion and the spin of another fermion, is discussed.

### 2.1 Lagrangian Density of QCD

QCD is the theory of the strong interaction. In comparison to quantum electrodynamics (QED), which describes the electromagnetic interaction, QCD is a non-Abelian gauge theory, i.e it is non-commutative. This can be explained as followed: The gauge boson of the electromagnetic interaction, the photon, does not carry electric charge. But the gauge bosons of strong interaction, the gluons, carry color charge. Thus they can interact among themselves. Due to this fact the symmetry group of QCD ( $SU(3)$ ) has a more complicated form than the symmetry group of QED ( $U(1)$ ).

The Lagrangian density of QED is given by

$$\mathcal{L}_{\text{QED}} = \bar{\psi}(\gamma^\mu i D_\mu - m)\psi - \frac{1}{4}F_{\mu\nu}F^{\mu\nu} , \quad (2.1)$$

where  $\psi$  is the wave function of the electric charged particle,  $m$  is the mass of the particle,  $\gamma^\mu$  are the Dirac matrices,  $D_\mu = \partial_\mu - ieA_\mu$  is the covariant derivative and  $F_{\mu\nu}$  are the tensors of the electromagnetic field. The coupling constant is the elementary charge  $e$  and  $A_\mu$  is the covariant four-potential of the electromagnetic field. Thereby the field tensor is specified by

$$F_{\mu\nu} = \partial_\mu A_\nu - \partial_\nu A_\mu . \quad (2.2)$$

For QCD, the Lagrangian density is given by

$$\mathcal{L}_{\text{QCD}} = \sum_f \bar{\psi}_f (i\gamma^\mu D_\mu - m_f) \psi_f - \frac{1}{4} G_{\mu\nu}^b G_b^{\mu\nu}, \quad (2.3)$$

where  $\psi_f$  and  $m_f$  are the wave function and the mass of the quarks respectively.  $f$  indicates the quark flavor,  $\gamma^\mu$  are the Dirac matrices,  $D_\mu = \partial_\mu - igA_\mu$  is the covariant derivative with the coupling constant  $g$  and  $A_\mu = \sum_{a=1}^8 \frac{\lambda_a}{2} A_{\mu a}$  is the covariant four-potential where  $\lambda_a$  are the Gell-Mann matrices. The index  $b$  indicates the color of the gluon and therefore can be  $b = 1, \dots, 8$ .  $G_{\mu\nu}$  are the tensors of the gluon field which are specified by

$$G_{\mu\nu} = \partial_\mu A_\nu - \partial_\nu A_\mu + ig[A_\mu, A_\nu]. \quad (2.4)$$

By comparison of Eq. 2.4 and Eq. 2.2, one can see that there is an additional term in the field tensor of QCD. This term is non-commutative and describes the interaction of the gluons among themselves.

## 2.2 The $U(1)_A$ Problem

In the chiral limit, i.e. in case the mass of the quarks goes to zero ( $m_f \rightarrow 0$ ), the QCD Lagrangian  $\mathcal{L}_{\text{QCD}}$  for  $N$  different quarks given by Eq. 2.3 has a large global symmetry [12]:  $U(N)_V \times U(N)_A$ . Since the masses of the  $u$  quark and the  $d$  quark are small compared to the scale of QCD, i.e.  $m_u, m_d \ll \Lambda_{\text{QCD}}$ , at least for these quarks the chiral limit is valid. Thus, the strong interaction is expected to be approximately invariant under a  $U(2)_V \times U(2)_A$  transformation. Indeed, for  $m_u \neq m_d$ , the vector symmetry  $U(2)_V = SU(2)_V \times U(1)_V$  is approximately an exact symmetry and therefore it is a good symmetry of nature. That means, that under a  $U(1)_V$  transformation the baryon number is conserved and under a  $SU(2)_V$  transformation the isospin is invariant, which leads to nucleon (p, n) and pion multiplets ( $\pi^+, \pi^0, \pi^-$ ) in the spectrum of hadrons. On the contrary the axial symmetry  $U(2)_A = SU(2)_A \times U(1)_A$  is not an exact symmetry. Nonvanishing quark condensates  $\langle \bar{u}u \rangle = \langle \bar{d}d \rangle \neq 0$  lead to a spontaneous breakdown of the  $SU(2)_A$  symmetry. Hence, the  $SU(2)_A$  symmetry is not preserved for the vacuum state of the system. According to the Goldstone theorem, whenever a continuous global symmetry is spontaneously broken, the spectrum will have a massless, spin-0 boson (Nambu-Goldstone boson). If the symmetry is not exact though, the associated particle has a small mass, and is called a ‘‘pseudo Nambu-Goldstone boson’’. Since the  $SU(2)_A$  is not an exact symmetry, the spontaneous symmetry breaking of  $SU(2)_A$  results in three massless pseudoscalar Nambu-Goldstone bosons which correspond to the pion triplet. If strong interaction is invariant under a  $U(1)_A$  transformation, for each particle a mirror particle with opposite parity is expected. However such parity multiplets are not observable in the hadron spectrum. Thus, similar to the  $SU(2)_A$  symmetry it is assumed that the  $U(1)_A$  symmetry is spontaneously broken. Since the  $U(1)_A$  symmetry is not exact, according to the Goldstone theorem a single pseudoscalar Nambu-Goldstone boson  $\eta_1$  is expected, which has to match the quantum numbers  $J^P = 0^-$  and should be a light partner to the pion. By using chiral perturbation theory, the mass of  $\eta_1$  is expected to be  $m(\eta_1) \leq m(\pi)\sqrt{3}$  [13, 14]. Such

a pseudoscalar boson could not be proved so far. The only candidate available is the  $\eta'$  which has the right quantum numbers but is too heavy ( $m_{\eta'} = 957.78$  MeV and  $m_\pi = 135$  MeV [15]). Thus the QCD Lagrangian given by Eq. 2.3 only provides an approximate description of the strong interaction. Steven Weinberg named this problem the  $\eta'$ -mass problem or the  $U(1)_A$  problem. This problem was solved by G.'t Hooft [16, 17]. He showed that the  $U(1)_A$  symmetry has an axial anomaly. That means that the  $U(1)_A$  symmetry is broken at the quantum level but not classically. This results in an additional term  $\mathcal{L}_\theta$  to the Lagrangian, which will be derived in the following: Since QCD is a non-Abelian gauge theory, the QCD vacuum is non-trivial. In fact, it has many degenerate vacua characterized by a topological winding number  $n$ . These vacua  $|n\rangle$  are not invariant under all possible gauge transformations and thus they are not the real vacuum. The real ground state, which is often referred to as the  $\theta$ -vacuum, is the superposition of the various vacua and is gauge invariant

$$|\theta\rangle = \sum e^{-in\theta}|n\rangle \quad (2.5)$$

with  $0 \leq \theta \leq 2\pi$  [18, 19, 20]. The transition from one  $\theta$ -vacuum to another  $\theta'$ -vacuum is classically forbidden, but due to quantum tunneling, this transition has a non-zero amplitude which is given by

$$\langle\theta'|e^{-Ht}|\theta\rangle = \sum \sum e^{i(n'\theta' - n\theta)} \langle n'|e^{-Ht}|n\rangle . \quad (2.6)$$

This causes an additional term  $\mathcal{L}_\theta$  to the Lagrangian, so that the effective Lagrangian of QCD is given by

$$\mathcal{L}_{\text{QCD}}^{\text{eff}} = \mathcal{L}_{\text{QCD}} + \mathcal{L}_\theta \quad (2.7)$$

$$= \mathcal{L}_{\text{QCD}} + \theta \frac{g^2}{32\pi^2} G_{\mu\nu}^b \tilde{G}_b^{\mu\nu} , \quad (2.8)$$

when  $\tilde{G}_b^{\mu\nu}$  is the so-called dual field strength tensor. Including the electroweak interaction, one has to substitute  $\theta$  in Eq. 2.8 by

$$\bar{\theta} = \theta + \theta_{\text{weak}} = \theta + \arg(\det M) . \quad (2.9)$$

Thereby  $M$  denotes the quark mass matrix since quarks acquire their effective masses through the breakdown of the electroweak symmetry. Thus the effective Lagrangian of the Standard Model becomes

$$\begin{aligned} \mathcal{L}_{\text{SM}}^{\text{eff}} &= \mathcal{L}_{\text{SM}} + \mathcal{L}_{\bar{\theta}} \\ &= \mathcal{L}_{\text{SM}} + \bar{\theta} \frac{g^2}{32\pi^2} G_{\mu\nu}^b \tilde{G}_b^{\mu\nu} , \end{aligned} \quad (2.10)$$

In summary, the  $U(1)_A$  symmetry is not a quantum symmetry of QCD but an axial anomaly. Thus, there is no spontaneous breakdown of the  $U(1)_A$  symmetry and hence no pseudo Nambu-Goldstone boson is expected. This means  $\eta'$  does not need to be lighter than it is. However the solution of the  $\eta'$ -mass problem, respectively the  $U(1)_A$  problem, bears a new problem: The new term  $\mathcal{L}_{\bar{\theta}}$  in the Lagrangian of QCD is not invariant under  $CP$  transformation. But since violation of  $CP$  symmetry is not observable in the strong interaction, this problem is called the “strong  $CP$ -problem” which will be explained in the following section.

## 2.3 The Strong $CP$ -Problem

The new term  $\mathcal{L}_{\bar{\theta}}$  in the Lagrangian violates the symmetries parity  $P$  and time reversal  $T$  but conserves charge conjugation  $C$ . Thus,  $\mathcal{L}_{\bar{\theta}}$  violates  $CP$  symmetry. In principle  $CP$  violating effects resulting from the term  $\mathcal{L}_{\bar{\theta}}$  in Eq. 2.10 can be large, unless  $\bar{\theta}$  is very small. Basically there is no obvious reason why the two terms of  $\bar{\theta}$  in Eq. 2.9 should be very small or of opposite sign, such that they cancel.

The new term  $\mathcal{L}_{\bar{\theta}}$  induces a neutron electric dipole moment  $d_n$  (nEDM) [20]. The relation between  $\bar{\theta}$  and  $d_n$  is predicted by the MIT bag model to be [21]

$$d_n = 8.2 \cdot 10^{-16} \cdot \bar{\theta} \text{ ecm} . \quad (2.11)$$

The upper limit of the electric dipole moment of the neutron  $d_n$  could be determined experimentally to [22, 23]

$$|d_n| < 3 \cdot 10^{-26} \text{ ecm (90\% CL)} . \quad (2.12)$$

Hence, the combination of Eq. 2.11 and 2.12 results in  $\bar{\theta} \leq 10^{-10}$ . The smallness of  $\bar{\theta}$  and the non-existence of  $CP$  violation in the strong interaction is referred to as the “*strong CP-problem*”.

## 2.4 Solution to the Strong $CP$ -Problem

The most popular and promising solution of the strong  $CP$ -problem was provided by Peccei and Quinn in 1977 [24, 25]. They introduced a new global, chiral symmetry  $U(1)_{PQ}$ , the so-called Peccei-Quinn symmetry (PQ-Symmetry), which replaces the static  $CP$  violating parameter  $\bar{\theta}$  of Eq. 2.9 with a dynamical  $CP$  conserving field. This  $CP$  conserving field results from the necessary spontaneous breakdown of the  $U(1)_{PQ}$  symmetry and corresponds to a pseudoscalar Nambu-Goldstone boson, which is called axion [26, 27]. The  $CP$  conserving field of the axion can be described by  $a = a(x)$  which gives rise to an additional term  $\mathcal{L}_{\text{axion}}$  to the Lagrangian of the Standard Model

$$\mathcal{L}_{\text{SM}}^{\text{total}} = \mathcal{L}_{\text{SM}} + \mathcal{L}_{\bar{\theta}} + \mathcal{L}_{\text{axion}} \quad (2.13)$$

$$= \mathcal{L}_{\text{SM}} + \bar{\theta} \frac{g^2}{32\pi^2} G_{\mu\nu}^b \tilde{G}_b^{\mu\nu} + \mathcal{L}_{\text{axion}} , \quad (2.14)$$

where the new term is given by

$$\mathcal{L}_{\text{axion}} = \mathcal{L}_{\text{kin}} + \mathcal{L}_{\text{int}} + V_{\text{eff}} . \quad (2.15)$$

$\mathcal{L}_{\text{kin}}$  represents the kinetic energy of the axion which is given by  $\mathcal{L}_{\text{kin}} = \frac{1}{2}(\partial_\mu a)(\partial^\mu a)$ ,  $\mathcal{L}_{\text{int}}$  describes further interactions of the axion and the effective potential of the axion field  $V_{\text{eff}}$ , which describes interactions of the axion with gluons, can be expressed by

$$V_{\text{eff}}(a) = -\zeta \frac{a}{f_a} \frac{g^2}{32\pi^2} G_{\mu\nu}^b \tilde{G}_b^{\mu\nu} . \quad (2.16)$$

Here  $\zeta$  is a parameter that depends on the model,  $g$  is the strong coupling constant and  $f_a$  is the scale of the spontaneous symmetry breaking of the  $U(1)_{\text{PQ}}$ -Symmetry. The vacuum expectation value of the axion field  $\langle a \rangle$  can be calculated by considering the minimum of the effective potential, i.e. [24]

$$\left\langle \frac{\partial V_{\text{eff}}(a)}{\partial a} \right\rangle = -\frac{\zeta}{f_a} \frac{g^2}{32\pi^2} \langle G_{\mu\nu}^b \tilde{G}_b^{\mu\nu} \rangle|_{\langle a \rangle} = 0. \quad (2.17)$$

The vacuum expectation value of the axion field  $\langle a \rangle$  then results in

$$\langle \bar{\theta} | a | \bar{\theta} \rangle = -\bar{\theta} \frac{1}{\zeta} f_a. \quad (2.18)$$

Combination of Eqs. 2.14-2.18 shows that at the minimum the  $\bar{\theta}$ -term is absorbed by the axion field. Thus, no  $CP$  violation in the strong interaction occurs [26, 27] and the *strong CP-problem* is solved theoretically. So, to show that the introduction of the PQ-symmetry is justified, the existence of the axion has to be proven experimentally.

## 2.5 Properties of Axions

In the following the most important properties of the axion are summarized. All properties of the axion are determined by the symmetry breaking scale  $f_a$  of the PQ-symmetry since the mass of the axion and the coupling constants are inversely proportional to it, i.e.

$$g_{ai} \propto \frac{1}{f_a}, \quad (2.19)$$

$$m_a \propto \frac{1}{f_a}, \quad (2.20)$$

where  $i$  indicates the particle the axion couples to.

Axions couple to fundamental bosons and fermions, so that the interaction term  $\mathcal{L}_{\text{int}}$  of Eq. 2.15 can be written as

$$\mathcal{L}_{\text{int}} = \mathcal{L}_{a\gamma} + \mathcal{L}_{af}. \quad (2.21)$$

Here,  $\mathcal{L}_{af}$  describes the interaction of axions with fermions and  $\mathcal{L}_{a\gamma}$  the interaction of axions with photons. According to [28] these terms can be written as

$$\mathcal{L}_{a\gamma} = g_{a\gamma} a \vec{E} \cdot \vec{B}, \quad (2.22)$$

$$\mathcal{L}_{af} = i \frac{g_{aN}}{2m_N} \partial_\mu a (\bar{\psi}_N \gamma^\mu \gamma_5 \psi_N) + i \frac{g_{ae}}{2m_e} \partial_\mu a (\bar{\psi}_e \gamma^\mu \gamma_5 \psi_e), \quad (2.23)$$

where  $N$  indicates the nucleons and  $e$  the electrons.

### 2.5.1 Couplings of the Axion

**Coupling to Gluons:** The axion field couples via a triangle loop to gluons which is a consequence of the axial anomaly of the  $U(1)_A$  symmetry. The Lagrangian describing the axion-gluon coupling is given by

$$\mathcal{L}_{aG} = \frac{\alpha_s}{8\pi f_a} a G_b^{\mu\nu} \tilde{G}_{\mu\nu}^b, \quad (2.24)$$

where  $\alpha_s$  is the strong fine-structure constant. The coupling to gluons implies the coupling to pions so that the axion needs a mass which can be described by [29, 30]

$$m_a = \frac{m_\pi f_\pi}{f_a} \left( \frac{z}{(1+z+w)(1+z)} \right)^{1/2} \simeq 6.0 \text{eV} \frac{10^6 \text{GeV}}{f_a}, \quad (2.25)$$

where  $f_\pi = 93 \text{ MeV}$  and  $m_\pi = 135 \text{ MeV}$  are the decay constant and the mass of the pion, respectively, and the quark mass ratios,  $z$  and  $w$ , are given by [31, 32, 33]

$$z = m_u/m_d \approx 0.553, \quad (2.26)$$

$$w = m_u/m_s \approx 0.029. \quad (2.27)$$

**Coupling to Photons** Since pions decay into photons, the mixing of axions with pions results in coupling of axions to photons. This coupling produces an additional term in the Lagrangian, which can be described by [34]

$$\mathcal{L}_{a\gamma} = \frac{g_{a\gamma}}{4} F_{\mu\nu} \tilde{F}^{\mu\nu} a = -g_{a\gamma} \vec{E} \cdot \vec{B} a. \quad (2.28)$$

$F_{\mu\nu}$  is the electromagnetic field strength tensor,  $\tilde{F}_{\mu\nu}$  its dual,  $a$  is the axion field and  $\vec{E}$  and  $\vec{B}$  describe the electric and the magnetic field, respectively.

However, there exist another contribution to the axion-photon coupling: In some axion models standard fermions carry Peccei Quinn-charges (PQ-charges) in addition to the electric charges. Thus, if the photon carries PQ-charge, the axion couples to the photon via a triangle loop analog to the axion-gluon coupling. The coupling constant of axions to photons  $g_{a\gamma}$  then is given by

$$g_{a\gamma} = \frac{\alpha}{2\pi f_a} \left( \frac{E}{N} - \frac{2}{3} \frac{4+z}{1+z} \right) = \frac{\alpha}{2\pi} \left( \frac{E}{N} - \frac{2}{3} \frac{4+z}{1+z} \right) \frac{1+z}{z^{1/2}} \frac{m_a}{m_\pi f_\pi}, \quad (2.29)$$

with the fine structure constant  $\alpha$  and the quark mass ratios,  $z$  and  $w$ , which are defined in Eq. 2.26 and Eq. 2.27.  $E/N$  is a model dependent parameter which is the ratio of the electromagnetic anomaly  $E$  and the color anomaly  $N$  [35, 36].

**Coupling to Fermions** If fermions, i.e. electrons and quarks, carry PQ-charge, they can couple to axions. The contribution of this interaction to the Lagrangian can be described by a Yukawa potential [28]

$$\mathcal{L}_{af} = \frac{g_{af}}{2m_f} \left( \tilde{\psi}_f \gamma^\mu \gamma_5 \psi_f \right) \partial_\mu a, \quad (2.30)$$

with  $f$  indicating the fermion,  $m_f$  is the mass of the fermion and  $g_{af}$  is the coupling constant of the axion-fermion interaction, which is given by

$$g_{af} = \frac{C_f m_f}{f_a}. \quad (2.31)$$

Thereby  $C_f$  is the effective model dependent PQ-charge. Since in QCD there are no free quarks, only the effective coupling of axions to nucleons can be considered. So, the coupling



of the axion to an electron and to a nucleon is different. That is why in the following the coupling of the axion to a nucleon is considered in more detail.

**Coupling to Nucleons** The effective coupling of axions to nucleons consists of two approximately equal contributions: on the one hand axions couple to light quarks at tree-level and on the other hand the mixing of axions with pions cause axion-nucleon coupling. The axion-nucleon coupling constant is given by [29, 28, 35, 34, 37, 38]

$$g_{aN} = \frac{C_N m_N}{f_a}, \quad (2.32)$$

where  $m_N$  is the mass of the nucleon.  $C_N$  is the effective PQ-charge of the nucleon, which is a combination of the masses of the quarks. For protons and neutrons  $C_N$  is given by

$$C_p = (C_u - \eta)\Delta u + (C_d - \eta z)\Delta d + (C_s - \eta w)\Delta s, \quad (2.33)$$

$$C_n = (C_u - \eta)\Delta d + (C_d - \eta z)\Delta u + (C_d - \eta w)\Delta s. \quad (2.34)$$

Here  $z$  and  $w$  are the quark mass ratios from Eq. 2.27.  $\eta$  is given by  $\eta = 1/(1 + z + w)$  and  $\Delta u$  is the fraction of the spin of the nucleon which is carried by the  $u$  quark (the same holds for the  $d$  and  $s$  quarks).

## 2.6 Axion Models

As already mentioned in Sec. 2.5, the properties of the axion are defined by its mass  $m_a$  and the coupling constant  $g_{ai}$  to other particles  $i$ . Both of them are inversely proportional to the symmetry breaking scale  $f_a$  of the PQ-symmetry (see Eq. 2.19 and Eq. 2.20). So the larger the symmetry breaking scale  $f_a$ , the more weakly the axion couples to other particles and the smaller is the mass of the axion. In the previous considerations the symmetry breaking scale  $f_a$  of the PQ-symmetry was not yet fixed. However, according to its range there are two different axion models which will be explained in the following.

### 2.6.1 Visible Axions

For the original axion, which was proposed by Peccei, Quinn, Weinberg and Wilczek [24, 25, 26, 27], a weak interaction model was adopted. In this model the coupling of axions to leptons and quarks was included. The strength of the interaction of axions with fermions could be calculated by introducing two Higgs-doublets so that the Lagrangian of the Standard Model  $\mathcal{L}_{\text{SM}}$  is invariant under the chiral symmetry. Thereby it was assumed that these Higgs doublets have non-vanishing vacuum expectation values  $\lambda_1$  and  $\lambda_2$ . The symmetry breaking scale then results in

$$f_a = \sqrt{\lambda_1^2 + \lambda_2^2} = \left(\sqrt{2}G_F\right)^{1/2} \equiv f_{\text{weak}} \approx 250 \text{ GeV}, \quad (2.35)$$

where  $G_F$  is the Fermi coupling constant and  $f_{\text{weak}}$  is the electroweak scale. The mass of the axion could be calculated to

$$m_a = N \left( x + \frac{1}{x} \right) \frac{\sqrt{z} f_\pi m_\pi}{z f_a} = 25N \left( x + \frac{1}{x} \right) \text{ keV} , \quad (2.36)$$

where  $N$  is the number of quark generations,  $z$  is given by Eq. 2.26 and  $m_\pi$  and  $f_\pi$  are the mass and the decay constant of the pion, respectively.  $x$  is the ratio of the vacuum expectation values,  $\lambda_1$  and  $\lambda_2$ , which is chosen to be  $x > 1$ . Using all known relations the mass of the axion results in  $m_a \approx 150$  keV. These axions are called *visible axions*. The lifetime of such an axion, which decays in two photons, was calculated in [30] to be  $\tau_{a \rightarrow \gamma\gamma} \approx 0.1$  s.

By combination of astrophysical arguments and the results of several experiments the existence of the visible axion could be excluded: For instance, axions with a mass of about 150 keV would be expected in the Kaon decay

$$K^+ \rightarrow a + \pi^+ . \quad (2.37)$$

In the KEK experiment [39] the upper bound of this branching ratio was determined to be

$$\text{BR}(K^+ \rightarrow \pi^+ + X) \leq 3.8 \cdot 10^{-8} \quad (90\% \text{ CL}) . \quad (2.38)$$

Here  $X$  stays for a particle that was not detected in this process and therefore can be interpreted as a long-lived axion. From this branching ratio upper limits on the symmetry breaking scale  $f_a$  and the mass of the axion  $m_a$  can be calculated to be

$$f_a \gtrsim 10^3 \text{ GeV} \quad (2.39)$$

$$m_a \lesssim 6 \text{ keV} . \quad (2.40)$$

Thus the visible axion could be precluded.

### 2.6.2 Invisible Axions

The main problem of the visible axion is the relation between the symmetry breaking scale of the PQ-symmetry and the electroweak scale, i.e.  $f_a = f_{\text{weak}}$ . However the strong  $CP$ -problem can also be solved by introducing a complex scalar field  $\sigma$  (Higgs field), which carries PQ-charge and has a large expectation value of  $\langle \sigma \rangle = f_a / \sqrt{2} \gg f_{\text{weak}}$ . For  $f_a \gg f_{\text{weak}}$  a light and weak interacting axion is expected, which can have eluded all previous searches so far. This very light axion is called *invisible axion*. The visible and the invisible axions conclude in different couplings of the axion to quarks and leptons. For the invisible axion there exist two different models which will be explained briefly in the following.

#### The KSVZ Model

In the model proposed by Kim, Shifman, Vainshtein and Zakharov [40, 41] (KSVZ) a new heavy quark is introduced which carries PQ-charge. Due to the PQ-charge the heavy quark is able to couple to the scalar field  $\sigma$  and thus it can couple to the axion. In this model usual leptons and quarks do not carry PQ-charge, i.e.  $C_e = C_u = C_d = C_s = 0$ . Since the KSVZ

axion cannot couple to electrons in the tree-level as described in Sec. 2.5.1 it is called the “hadronic” axion. However with one-loop calculations it can be shown that there still is a small contribution to the axion-electron coupling [36].

Although KSVZ axions do not couple to normal quarks, they do couple with nucleons (Eq. 2.32) whereby the effective PQ-charge can be obtained by evaluating Eq. 2.33 and Eq. 2.34

$$\begin{aligned} C_p &= -0.39 , \\ C_n &= -0.04 . \end{aligned} \quad (2.41)$$

The Yukawa coupling of axions to neutrons and protons then are given by

$$g_{ap}^{\text{KSVZ}} = \frac{C_p m_p}{f_a} = -6.01 \cdot 10^{-8} m_a \text{ eV}^{-1} , \quad (2.42)$$

$$g_{an}^{\text{KSVZ}} = \frac{C_n m_n}{f_a} = -0.69 \cdot 10^{-8} m_a \text{ eV}^{-1} . \quad (2.43)$$

The KSVZ model solves the strong  $CP$ -problem but a possible disadvantage might be that there is no distinct physical motivation of the introduction of a heavy quark. In addition, it might be difficult to detect this KSVZ axion since due to the strongly suppressed coupling to photons the KSVZ axion interacts weakly.

### The DFSZ Model

In the model proposed by Dine, Fischler, Srednicki and Zhitnitskii [42, 43] (DFSZ) the quarks and the leptons carry PQ-charge, i.e. they have the same properties as visible axions according to the Peccei-Quinn symmetry. Here the Higgs field  $\sigma$  is replaced by two Higgs fields,  $\Phi_1$  and  $\Phi_2$ , with respective expectation values  $f_1$  and  $f_2$ . With these Higgs field the coupling of the axions to quarks and leptons can be described [44].

For all Grand Unified Theories (GUT) for a given family of quarks and fermions, the ratio  $E/N$  is equal to  $8/3$ . Thus, according to Eq. 2.29 the coupling constant  $g_{a\gamma}$  between axions and photons is given by

$$g_{a\gamma}^{\text{DFSZ}} \approx -0.74 \frac{\alpha}{2\pi f_a} . \quad (2.44)$$

The PQ-charges for the fermions for  $N_f$  number of families are given by

$$\begin{aligned} C_e = C_s = C_d &= \frac{\cos^2 \beta}{N_f} , \\ C_u &= \frac{\sin^2 \beta}{N_f} . \end{aligned} \quad (2.45)$$

Thereby  $x = f_1/f_2$  is the ratio of the vacuum expectation values and  $\beta$  is defined as  $\cos^2 \beta = x^2/(x^2 + 1)$ . With  $N_f = 3$  the PQ-charges of the proton and the neutron given in Eq. 2.33 and Eq. 2.34 emerge to

$$\begin{aligned} C_p &= -0.08 - 0.46 \cos^2 \beta , \\ C_n &= -0.14 + 0.38 \cos^2 \beta . \end{aligned} \quad (2.46)$$

## 2.7 Cosmological and Astrophysical Constraints

The detection of axions is extremely difficult due to its weak coupling with fundamental particles. That is why beside the WIMP's<sup>1</sup>, the axion can contribute significantly to the cold dark matter<sup>2</sup> of the universe. This section gives a short overview of the limitations to the properties of the axion which result from cosmological and astrophysical considerations. Detailed description can be found in [34, 45, 46, 47, 48].

### 2.7.1 Cosmological Constraints

To derive information on the lower limit of the mass of the axion  $m_a$  one has to consider the evolution of the vacuum expectation value of the axion field, i.e.  $\langle a \rangle$ , through the life of the universe [49, 50, 51].

The spontaneous symmetry breaking of the PQ-symmetry happened at a temperature  $T \approx f_a \gg \Lambda_{\text{QCD}}$ , where  $\Lambda_{\text{QCD}}$  is the QCD energy scale. At that time the axion still was massless and the vacuum expectation value of the axion field was not yet fixed and had an arbitrary value, i.e.  $\langle a \rangle = \theta_i$ . When the universe cooled down to  $T \sim \Lambda_{\text{QCD}}$ , the PQ-symmetry was explicitly broken, which led to the mass of the axion and to a dynamic axion field. That means the vacuum expectation value of the axion field went to zero, i.e.  $\langle a \rangle \rightarrow 0$ , whereby this phenomena did not happen instantly but  $\langle a \rangle$  oscillated into its final state. Such coherent oscillations of axions would contribute to the energy density of our universe (vacuum realignment), where the energy density of the oscillations is proportional to the symmetry breaking scale  $f_a$  of the PQ-symmetry. So the axions would be a good candidate for cold dark matter. Estimations of the contribution of cold dark matter to the overall matter in the universe allow to constrict  $f_a$ . The contribution of the axions to the energy density of the universe is given by [52]

$$\Omega_a h^2 = 0.5 \left( \frac{f_a}{10^{12} \text{ GeV}} \right)^{7/6} [\theta_i^2 + \sigma_i^2] \gamma, \quad (2.47)$$

where  $h^2$  is the Hubble constant (in units of  $100 \text{ kms}^{-1} \text{ Mpc}^{-1}$ ),  $\theta_i$  describes the misalignment of  $\langle a \rangle / f_a$ ,  $\sigma_i$  is the average of the strength of the fluctuations and  $\gamma$  is the damping constant. The data of the experiment with the Wilkinson Microwave Anisotropy Probe (WMAP) gives a lower limit on the matter energy density of  $\Omega_m h^2 < 0.12$  [7]. Assuming that the amount of axions is of the same order, i.e. they would dominate the cold dark matter of the universe, and that there are no losses of the energy density due to the axion oscillations, i.e.  $\gamma = 1$ , and  $\theta_i = \pi^2/3$  [53], the symmetry breaking scale  $f_a$ , respectively the mass of the axion  $m_a$ , result in [34]:

$$f_a < 3 \cdot 10^{11} \text{ GeV}^{-1} \quad (2.48)$$

$$m_a > 2 \cdot 10^{-5} \text{ eV} . \quad (2.49)$$

<sup>1</sup>WIMP = weakly interacting massive particle

<sup>2</sup>About 4% of the mass of the universe consists of hadronic matter and about 23% consists of dark matter which is non illuminating matter whereby the composition is unknown. The remaining mass of the universe is given by dark energy.

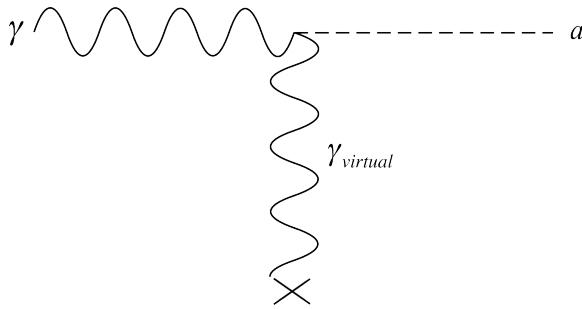


Figure 2.1: The Primakoff Effect describes the conversion of a photon ( $\gamma$ ) in a strong magnetic field ( $\gamma_{\text{virtual}}$ ) to a hypothetical particle such as the axion ( $a$ ).

### 2.7.2 Astrophysical Considerations

The coupling of axions to photons allows the conversion  $a \leftrightarrow \gamma$  in external electric or magnetic fields. This phenomena is called the “Primakoff effect” (Fig. 2.1). So, in principle it is possible that axions are produced in stellar plasma and are emitted by stars. This means that axions modify the energy loss rate of stars and therefore have influence on the lifetime of stars: Due to the emission of axions, stars should have a higher amount of fuel in their core to compensate the energy loss. The increased amount of fuel causes a faster burning of the star so that its lifetime is shortend [54].

A restricted limit on the coupling constant  $g_{a\gamma}$  of axions to photons (DFSZ axions) can be deduced by estimation of the energy loss due to emission of axions in stars of globular clusters. A globular cluster is a star system that is bounded by gravitational force. All stars of this system were produced at the same time so that they just differ in their masses (with masses smaller than the mass of the sun). In the stars of the horizontal branch (HB) helium atoms fusion to carbonate and oxygen. In this process the core ( $\approx 0.5$  mass of the sun) evaporates energy. Emission of axions then would lead to a higher consumption of helium and therefore to a shorter lifetime of the HB stars. The lifetime of the HB stars can be calculated by comparing the number of HB stars to the number of the stars of the Red Giant Branch (RGB) which are brighter than the HB stars. From this the axion to photon coupling can be estimated to be [54]

$$g_{a\gamma}^{\text{DFSZ}} \lesssim 1 \cdot 10^{-10} \text{ GeV}^{-1}, \quad (2.50)$$

and the mass of the axion to

$$m_a^{\text{DFSZ}} \lesssim 0.3 \left( \frac{E}{N} - 1.93 \pm 0.08 \right). \quad (2.51)$$

The RGB stars have a degenerate helium core and the helium discharges explosively when a critical combination of density and temperature is reached. The bremsstrahlung of this process

$$e^- + (A, Z) \rightarrow e^- + (A, Z) + a \quad (2.52)$$

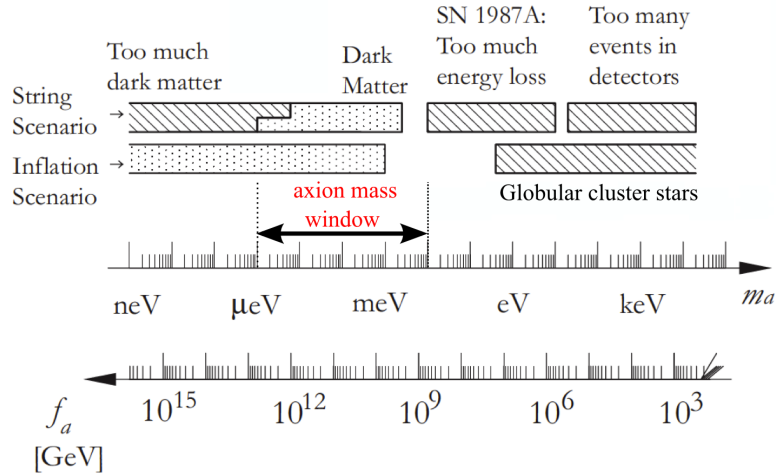


Figure 2.2: Summary of astrophysical and cosmological regions that can be excluded for the axion mass  $m_a$ , respectively for the symmetry breaking scale  $f_a$  of the PQ-symmetry. The SN 1987A limit applies for the axions of the KSVZ model, but approximately also covers the axions of the DFSZ model. The bars with open ends show a rough estimate, for instance the one for the globular cluster stars that is given for the DFSZ model. The regions with the dots indicate the regions where the axion can be the dark matter and the regions with the stripes indicate the sensitivity of the search experiments for galactic and solar dark matter axions. This graph was taken from [55].

decelerates the accumulation of helium due to the cooling by the axions. Observations restrict the axion to electron coupling to (DFSZ axions) [56]

$$g_{ae}^{\text{DFSZ}} \lesssim 2.5 \cdot 10^{13} \text{ GeV}^{-1}. \quad (2.53)$$

The strongest constraints for axions, which are produced by nucleon-nucleon-axion bremsstrahlung

$$N + N \rightarrow N + N + a, \quad (2.54)$$

are made by the observation of the Supernova SN 1987A [57]. The energy loss of this Supernova due to the axion emission would result in a shorter duration of the observed neutrino burst. The measurements of Kamiokande II and the Irvine-Michigan-Brookhaven (IBM) detectors exclude a range for the coupling of axions to nucleons, which is given by [55]

$$3 \cdot 10^{-10} \text{ GeV}^{-1} \lesssim g_{aN}^{\text{KSVZ}} \lesssim 3 \cdot 10^{-7} \text{ GeV}^{-1}. \quad (2.55)$$

This corresponds to a range for the mass of

$$0.01 \text{ eV} \lesssim m_a^{\text{KSVZ}} \lesssim 10 \text{ eV}, \quad (2.56)$$

which can be precluded. Another mass range can be excluded, if heavy hadronic axions could induce nuclear excitations which deexcite by emitting  $\gamma$ -rays. This should increase the

number of counts in the neutrino Cerenkov detectors [58, 59]. Due to this measurements the mass range

$$20 \text{ eV} \lesssim m_a^{\text{KSVZ}} \lesssim 20 \text{ keV} \quad (2.57)$$

can be excluded.

Considering the precluded mass ranges of all astrophysical and cosmological constraints, the mass of the axion is restricted to a range from  $\mu\text{eV}$  to  $\text{meV}$ , which is also referred as the “*axion mass window*”. In Fig. 2.2 all bounds and the axion mass window are shown. Since some of the astrophysical and cosmological considerations are based on rather uncertain models and assumptions, still there exist searches for the axion in regions that were already precluded.

## 2.8 Detection of the Axion

Since the axion is a good candidate for cold dark matter, researchers are highly interested to prove the existence of the axion. In the last century many experimental methods were developed for the search of the axion. Here it is necessary to distinguish between two different types of detection: the *direct* and the *indirect detection* of the axion. Experiments, in which galactic, solar or laboratory origin axions are tried to be detected directly, are based on the Primakoff effect, i.e. the conversion of a photon via an external static magnetic field to an axion (Fig. 2.1). On the other hand, there are several experiments which try to detect the axion indirectly due to the  $CP$  violating interaction it mediates between a fermion and a spin of another fermion. Such interaction can be described by a Yukawa type potential, which, for instance, produces a frequency shift in the Larmor frequency of precessing spins. In the following briefly some of those experiments with their constraints on the mass of the axion are explained.

### 2.8.1 Direct Detection of the Axion

- **Galactic Axions**

- *Microwave Cavity Experiments:*

These experiments are looking for galactic halo axions by using electromagnetic cavities. Here it is assumed that galactic halo axions are converted into photons in the strong static magnetic field of the cavity [60]. The converted photons are monochromatic with a relative width of  $10^{-6}$ . The frequency of the cavity is adjustable so that galactic axions with different masses can be detected. At the very beginning, experiments at the Rochester-BNL-Fermilab [61, 62] and the university of Florida [63], which used cavities with a sensitive volume of about 1 litre, were able to preclude masses of the axion in the range of

$$4.5 \mu\text{eV} < m_a < 16.3 \mu\text{eV}. \quad (2.58)$$

Experiments of second generation used cavities with higher sensitive volume of about 200 litre and higher magnetic fields. For example, the ADMX<sup>3</sup> experiment could exclude the mass range [64, 65]

$$1.9 \mu\text{eV} < m_a < 3.3 \mu\text{eV}. \quad (2.59)$$

This experiment is continuously data taking and it is planned to improve its sensitivity by using a new technology based on Superconducting Quantum Interference Device (dc SQUID) [66]. The CARRACK2<sup>4</sup> experiment uses a Rydberg atom single-quantum detector that covers a large scale for the mass of the axion [67, 68]. This large scale-detector is searching for axions in the region

$$2 \mu\text{eV} < m_a < 30 \mu\text{eV}. \quad (2.60)$$

– *Optical and Radio Telescope Searches:*

Optical searches for thermal axions, which were produced in the early universe, by looking for a monochromatic photon decay line in galaxy cluster, cover the so called “multi-eV” mass range which goes from 3 eV to 8 eV. The Kitt Peak national Observatory (KPNO) studied three cluster (Abell 1413, 2218 and 2256) [69, 70] but could not find a signal. Thus the range

$$3 \text{ eV} < m_a < 8 \text{ eV} \quad (2.61)$$

could be excluded.

In experiments, which use a radio telescope, it is assumed that, if axions had been present in dwarf galaxies, they would decay into photons. These photons would be detected as narrow lines in radio telescope power spectra. With the radio telescope of the Haystack Observatory the mass range

$$298 \mu\text{eV} < m_a < 363 \mu\text{eV} \quad (2.62)$$

could be precluded [71].

• **Laboratory Axions**

– *“Light Shinning through a Wall” Experiments:*

Since axions couple to photons it is assumed that they are produced by radiating a light beam (usually laser) through a transverse magnetic field, i.e. the photons of the laser beam interact with the virtual photons of the magnetic field so that a pseudoscalar axion is produced. If the laser beam is blocked behind the magnetic field by a “wall”, only the axions go through the wall since they are weak interacting particles. Behind the wall there is a second transverse magnetic field in which the

---

<sup>3</sup>Axion Dark Matter eXperiment

<sup>4</sup>Cosmic Axion Research using Rydberg Atoms in a resonant Cavity in Koyoto



axions are reconverted to photons [72]. These regenerated photons can be detected with a photomultiplier. With this kind of experiment an upper limit of

$$g_{a\gamma} < 6.7 \cdot 10^{-7} \text{ GeV}^{-1} \quad (2.63)$$

for the axion-photon coupling constant could be determined [73, 74]. This leads to an upper limit of

$$m_a < 10^{-3} \text{ eV} \quad (2.64)$$

for the mass of the axion.

– *Polarization Experiments:*

With the experiment described before another limit on the axion mass and the coupling of axions to photons can be estimated by assuming that the produced axions change the polarization state of the photons of the laser beam. There are two observable effects [75]:

*Dichroism:* By radiating the laser beam through the transverse magnetic field, the produced axions reduce the component of the electric field parallel to the magnetic field, i.e.  $\vec{E}_{\parallel}$ , which results in a rotation of the polarization vector. This effect is called dichroism.

*Vacuum Birefringence:* In the second transverse magnetic field behind the wall the axions are reconverted into photons. The initially linearly polarized photon beam will become elliptically polarized since the axions will mix again with  $\vec{E}_{\parallel}$ . Such experiments restrict the axion to photon coupling to [76]

$$g_{a\gamma} < 3.6 \cdot 10^{-7} \text{ GeV}^{-1} \quad (2.65)$$

in a mass range of

$$m_a < 5 \cdot 10^{-4} \text{ eV}. \quad (2.66)$$

• **Solar Axions**

The search for axions that were produced in the plasma of stars give answers to many open questions, for instance, the cooling of stars can be explained. The closest and best known star that can be used for observation is the sun. In the last years two different kind of helioscopes have been built which search for solar axions. Both of them are based on the inverse Primakoff effect.

a.) Axions which pass a crystal can interact with the electric field of atomic nuclei. For an axion to photo conversion the Bragg condition has to be fulfilled [77]. That is why Germanium crystal detectors are used. The experiments COSME [78] and SOLAX [79] could determine an upper limit for the coupling constant of  $g_{a\gamma} < 2.7 \cdot 10^{-9} \text{ GeV}^{-1}$  (SOLAX) and  $g_{a\gamma} < 2.8 \cdot 10^{-9} \text{ GeV}^{-1}$  (COSME) in a mass range of  $m_a \leq 1 \text{ keV}$ . The DAMA [80] experiment is using NaI(Tl) crystals and result in a limit of  $g_{a\gamma} < 1.7 \cdot 10^{-9} \text{ GeV}^{-1}$  [DAMA].

b.) In a helioscope solar axions, which propagate to Earth, can be converted to photons by passing a transverse magnetic field. These photons can be detected by  $x$ -ray

detectors. The first kind of this helioscope could obtain an upper limit for the axion to photon coupling constant of [81]

$$g_{a\gamma} < 3.6 \cdot 10^{-9} \text{ GeV}^{-1} \quad (m_a < 0.03 \text{ eV}) \quad (2.67)$$

as well as [82]

$$g_{a\gamma} < 7.7 \cdot 10^{-9} \text{ GeV}^{-1} \quad (0.03 \text{ eV} < m_a < 0.11 \text{ eV}). \quad (2.68)$$

A more sensitive experiment is using the Tokyo helioscope [83] which gives an upper limit of

$$g_{a\gamma} < 6.0 \cdot 10^{-10} \text{ GeV}^{-1} \quad (m_a < 0.03 \text{ eV}). \quad (2.69)$$

The CAST experiment at CERN that is also based on a helioscope could improve the upper limit of the axion to photon coupling to

$$g_{a\gamma} < 1.16 \cdot 10^{-10} \text{ GeV}^{-1} \quad (2.70)$$

in a range  $m_a \leq 0.02 \text{ eV}$  [84].

## 2.8.2 Indirect Detection of the Axion

The experiments, which were explained before, are based on the Primakoff effect, and therefore are searching for a coupling of the axion to a photon. But as already mentioned in chapter 2.5.1, the coupling of axions to fermions is also possible.

In [8] a  $P$ - and  $T$ -violating macroscopic force was proposed which is mediated between unpolarized fermions  $f$  and polarized fermions  $f_\sigma$  by exchanging an axion or axion-like particle (ALP). This force can be parameterized by a Yukawa-type potential with a monopole-dipole coupling [8]

$$V_{\text{sp}}(\vec{r}) = \frac{\hbar^2 g_s^f g_p^{f\sigma}}{8\pi m_{f_\sigma}} (\vec{\sigma} \cdot \hat{r}) \left( \frac{1}{\lambda r} + \frac{1}{r^2} \right) e^{-r/\lambda}. \quad (2.71)$$

Here  $\lambda$  is the range of the Yukawa-force with  $\lambda = \hbar/(m_a c)$ ,  $m_a$  is the mass of the axion or axion-like particle,  $m_{f_\sigma}$  is the mass of the polarized fermion,  $\hat{r}$  is the unit distance vector from the polarized to the unpolarized fermion,  $\hbar$  is the reduced Planck constant, and  $g_s^f$  and  $g_p^{f\sigma}$  are dimensionless scalar and pseudoscalar coupling constants. The search for this spin-dependent short-range interaction between either nucleons or a nucleon and an electron is realized by many experiments which use different techniques, such as sensitive torsion pendula [85, 86], clock comparison between two different polarized spin samples [87, 88, 89], measurements of the spin precession signal of pure spin polarized  $^3\text{He}$  [90] and measurements of the neutron flux between a scatterer and a mirror where the neutrons are bound in quantum states of the gravitational field [91]. The detection of such a spin-dependent short-range interaction is an indirect detection of the axion.

In this work, we present a clock comparison experiment to search for the spin-dependent short-range interaction between bound nucleons and polarized bound neutrons (with  $g_s^f = g_s^N$

and  $g_p^{f\sigma} = g_p^n$ ). Therefore an ultra-sensitive low-field magnetometer is used which is based on the detection of free precession of co-located  $^3\text{He}$  and  $^{129}\text{Xe}$  nuclear spins using SQUIDs as low-noise magnetic flux detectors ( $^3\text{He}/^{129}\text{Xe}$  co-magnetometer). An unpolarized mass sample which is close to the spin samples and moved far away from it or vice versa, may cause a shift  $\omega_{\text{sp}}^w$  in the weighted difference of the precession frequencies of  $^3\text{He}$  and  $^{129}\text{Xe}$  (Eq. 1.8). This frequency shift  $\omega_{\text{sp}}^w$  was measured to determine the coupling of pseudoscalar particles to the spin of the bound neutron ( $g_s^N g_p^n$ ). Our result will be presented in Chap. 6.8 together with the results that were provided by other experiments, which measure the coupling between (bound) nucleons and (bound) neutrons.



## 3 Theory of Spin Precession

Since our experiment is based on precessing nuclear spins in a homogenous magnetic field this chapter deals with the theory of spin precession.

### 3.1 Spins in a Magnetic Field

An atom with a nuclear spin  $\vec{I}$  is associated with a magnetic moment

$$\vec{\mu} = \gamma \cdot \hbar \cdot \vec{I} = g \cdot \mu_N \cdot \vec{I} , \quad (3.1)$$

where  $\gamma = \frac{g\mu_N}{\hbar}$  is the gyromagnetic ratio with the nuclear g-factor  $g$ ,  $\mu_N = \frac{e\hbar}{2m_p} = 5.05078324(13) \cdot 10^{-27} \frac{J}{T}$  is the nuclear magneton and  $\hbar = 1.054571628(53) \cdot 10^{-34}$  Js is the reduced Planck constant. The absolute value of the nuclear spin is given by  $|\vec{I}| = \sqrt{I(I+1)}\hbar$  with the nuclear spin quantum number  $I$  which can take integral or half-integral values. If the spin quantization axis is given by the x-axis, the x-component of the magnetic moment is defined as

$$\mu_x = \gamma \cdot \hbar \cdot m_I , \quad (3.2)$$

where  $m_I = -I, -I+1, \dots, I-1, I$  is the projection of the nuclear spin on the x-axis.

An applied magnetic field  $\vec{B} = B_0 \cdot \hat{e}_x$  interacts with the magnetic moment which leads to a splitting in the energy levels, the so-called Zeeman effect:

$$E_{\text{Zeeman}} = -\vec{\mu} \cdot \vec{B} = -\mu_x \cdot B_0 = -\gamma \cdot \hbar \cdot m_I \cdot B_0 . \quad (3.3)$$

In our experiment the noble gases  $^3\text{He}$  and  $^{129}\text{Xe}$  are used. Both have an electron spin of  $J = 0$  and a nuclear spin of  $I = \frac{1}{2}$ . The projection of the nuclear spin  $m_I$  then can have values  $+\frac{1}{2}$  (“spin-up”) and  $-\frac{1}{2}$  (“spin-down”), i.e. the x-component of the nuclear spin is directed parallel or antiparallel to the applied magnetic field. The g-factors<sup>1</sup> of helium and xenon are given by [92]

$$g_{\text{He}} = -4.254995436(50) , \quad (3.4)$$

$$g_{\text{Xe}} = -1.544978008(100) \quad (3.5)$$

and the gyromagnetic ratios are given by [92]

$$\gamma_{\text{He}} = -20.37894730(56) \cdot 10^7 \frac{1}{\text{Ts}} , \quad (3.6)$$

$$\gamma_{\text{Xe}} = -7.39954378(50) \cdot 10^7 \frac{1}{\text{Ts}} . \quad (3.7)$$

<sup>1</sup>The g-factor and the gyromagnetic ratio of xenon were recalculated with the value of the magnetic moment of the proton  $\mu_p$  [92].

Since the g-factors of both,  $^3\text{He}$  and  $^{129}\text{Xe}$ , are negative, the state with  $m_I = -\frac{1}{2}$  is energetically more favorable. The energy difference  $\Delta E$  of the two Zeeman levels, spin-up and spin-down, is given by

$$\Delta E = g \cdot \mu_N \cdot B_0 = \hbar \cdot \gamma \cdot B_0 . \quad (3.8)$$

The corresponding transition frequency, the so-called Larmor frequency  $\omega_L$ , is defined as

$$\omega_L = \gamma \cdot B_0 . \quad (3.9)$$

## 3.2 Polarization and Optical Pumping

In general polarization is defined as an unequal population of different Zeeman levels

$$P := \frac{1}{F} \frac{\sum_{m_F} m_F \cdot N(m_F)}{\sum_{m_F} N(m_F)} , \quad (3.10)$$

where  $F = I + J$  is the total atomic angular momentum and  $N(m_F)$  the population number of the Zeeman level with the magnetic quantum number  $m_F$ . Since for  $^3\text{He}$  and  $^{129}\text{Xe}$  the total atomic angular momentum is equal to the nuclear spin, i.e.  $F = I = 1/2$ , in the following only nuclear spins are considered.

In thermal equilibrium, for a two-level system with spin-up and spin-down state, such as  $^3\text{He}$  and  $^{129}\text{Xe}$ , the population numbers are distributed according to the Boltzmann statistics. This means that for a given temperature  $T$  in a magnetic field  $B_0$ , the fraction of population numbers is given by

$$\frac{N_-}{N_+} = \exp\left(-\frac{E_+ - E_-}{kT}\right) = \exp\left(-\frac{\Delta E}{kT}\right) . \quad (3.11)$$

Here  $\Delta E$  is the energy difference of the two Zeeman levels (Eq. 3.8),  $k$  the Boltzmann constant and  $N_{+(-)}$  the population numbers of the spin-up and the spin-down state respectively. The nuclear spin polarization then is given by

$$P(I = \frac{1}{2}) = \frac{N_+ - N_-}{N_+ + N_-} . \quad (3.12)$$

At a magnetic field of about 1 T and a temperature of about 300 K, the so-called thermal or Boltzmann polarization  $P_B$  for  $^3\text{He}$  and  $^{129}\text{Xe}$  is in the order of  $10^{-6}$ . Much higher degrees of polarization, the so-called *hyperpolarization*, can be achieved by using the technique of optical pumping, where momentum is transferred to the atom from a resonant light source (usually a laser). In our working group  $^3\text{He}$  is polarized by *metastability exchange optical pumping* (MEOP), where polarization degrees up to 90% can be reached. On the contrary,  $^{129}\text{Xe}$  is polarized by *spin exchange optical pumping* (SEOP). In this method first  $^{87}\text{Rb}$  atoms are polarized by MEOP which then transfer their momentum to the  $^{129}\text{Xe}$  atoms via spin exchange collisions. In the following sections both methods will be explained briefly. More detailed descriptions can be found in [93], [94] and [95].

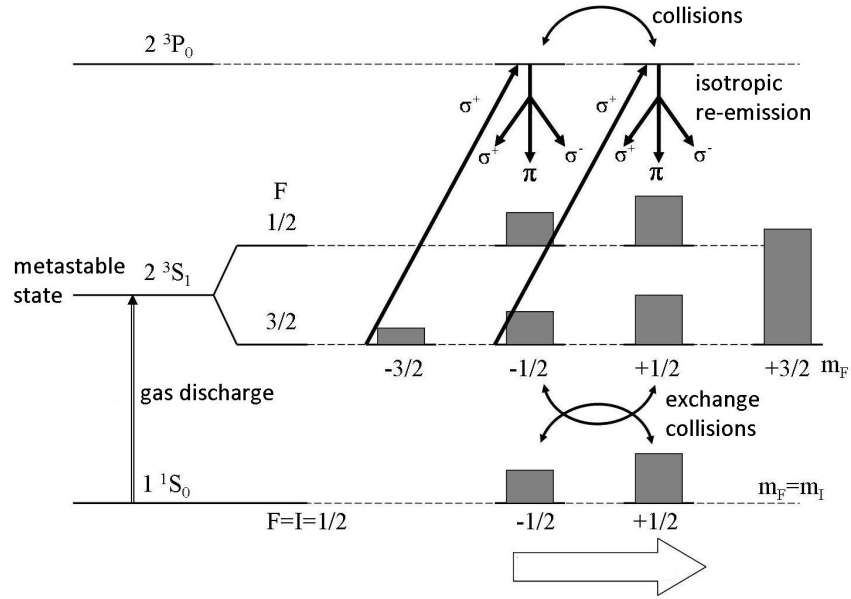


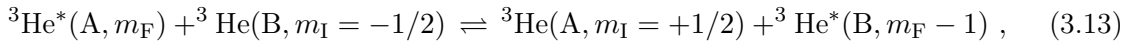
Figure 3.1: Metastability exchange optical pumping (MEOP) of  $^3\text{He}$ : The ground state  $1^1S_0$  is excited by a gas discharge into the metastable  $2^3S_1$  state. From this metastable state the atoms are pumped to the  $2^3P_0$  state by means of resonant  $\sigma^+$  light. Collisional mixing leads to isotropic reemission into the metastable state  $2^3S_1$ . The population numbers of this state are redistributed towards increasing  $m_F$  due to repeated absorption and isotropic reemission. The electronic polarization then is transferred to the nucleus via the hyperfine interaction. Due to exchange collisions between polarized metastable and unpolarized ground state atoms, atoms with nuclear spin polarization in the ground state arise. This graph was taken from [96].

### 3.2.1 Metastability Exchange Optical Pumping

In Mainz several polarizers for  $^3\text{He}$  were developed. All of them use the method of metastability exchange optical pumping (MEOP). Therefore a quantity of  $^3\text{He}$  with a low gas pressure of about 1 mbar is placed in a weak and homogenous magnetic field of roughly 10 G. A weak gas discharge excites the atoms from the ground state  $1^1S_0$  into the  $2^3S_1$  state. Due to angular momentum conservation and the forbidden transition between triplet and singlet system, this state is metastable. Its lifetime is limited to 1 ms due to collisions of the  $^3\text{He}$  atoms with the wall of the pumping cell. Atoms in the metastable state  $2^3S_1$  are pumped into the  $2^3P_{0,1,2}$  states by resonant laser light. Between these levels exist 9 hyperfine structure lines that are named C1 to C9 in the order of increasing energies [97]. For optical pumping the lines C8 and C9, which correspond to transitions from the  $2^3S_1$  into the  $2^3P_0$  state, are the preferred transitions. In the following, the pumping process on the C9 line will be explained (see Fig. 3.1).

The homogenous magnetic field leads to a splitting of the hyperfine levels into the Zeeman

sub-levels with quantum number  $m_F$ . If the pumping light is right-circularly polarized ( $\sigma^+$  light) with  $\lambda = 1083.03\text{nm}$ , only transitions with  $\Delta m_F = +1$  are induced. During the lifetime of the  $2^3P_0$  state of  $\tau \approx 10^{-7}$  s [98] collisions lead to radiationless transitions into the other  $2^3P$  levels. This process is called *collisional mixing*. Since the  $2^3P$  levels are almost equally occupied, deexcitation happens almost isotropically into the Zeeman levels of the  $2^3S_1$  state. By repeated absorption and spontaneous reemission the population numbers are redistributed towards increasing quantum number  $m_F$ , which leads to a polarization of the electronic spin of the  $2^3S_1$  state. Due to the hyperfine interaction between the electronic spin and the nuclear spin, the nuclear spin is also polarized. The characteristic time constant of this interaction is  $\tau_{\text{HF}} \approx 2.23 \cdot 10^{-10}$  s [99], which is much shorter than the lifetime of the  $2^3S_1$  state. For the time being, the nuclear polarized atom is still in the metastable state  $2^3S_1$ . However, due to its long lifetime the nuclear polarized atom collides with unpolarized atoms in the ground state  $1^1S_0$ . Some of these collisions lead to an exchange of the excitation energy between the colliding atoms, while the nuclear spins stay unchanged. These collisions can be described by



where A and B define the nuclei of the atoms and  ${}^3\text{He}^*$  is the excited atom. As a result of the pumping process there are more atoms in the states with higher  $m_F$ , i.e.  $N(m_F) > N(m_F - 1)$ . Hence the reaction predominantly happens from the left to the right side and the ground state atoms go from  $m_F = -1/2$  to  $m_F = +1/2$ , i.e. the polarization according to Eq. 3.12 is positive.

### 3.2.2 Spin Exchange Optical Pumping

To polarize  ${}^{129}\text{Xe}$  the method of spin exchange optical pumping (SEOP) is used. In this method first the electron shell of an alkali atom is polarized via MEOP. Then the polarization is transferred from the atomic shell of the alkali atom to the  ${}^{129}\text{Xe}$  nucleus. This transfer can happen either during binary collisions or during the lifetime of a weak bounded van der Waals molecule. In both cases the relevant interaction is the nuclear–electron spin–exchange interaction which couples the nuclear spin  $\vec{I}$  of the  ${}^{129}\text{Xe}$  atom to the electron spin  $\vec{S}$  of the alkali atom

$$V_{\text{IS}} = \alpha \vec{I} \cdot \vec{S} . \quad (3.14)$$

Here  $\alpha$  is a coupling constant that depends on the internuclear separation between the alkali and the  ${}^{129}\text{Xe}$  atom.

As we will see later on, the wall relaxation time  $T_{1,\text{wall}}$  of  ${}^{129}\text{Xe}$  is much smaller than for  ${}^3\text{He}$ , so that  ${}^{129}\text{Xe}$  has to be polarized next to the experiment. That is why the  ${}^{129}\text{Xe}$  polarizer of the PTB in Berlin [95] was used for our experiment. In the following the method of spin exchange optical pumping (SEOP) will be explained using the example of the PTB polarizer. A scheme of this polarizer is shown in Fig 3.2. The gas mixture, that is filled into



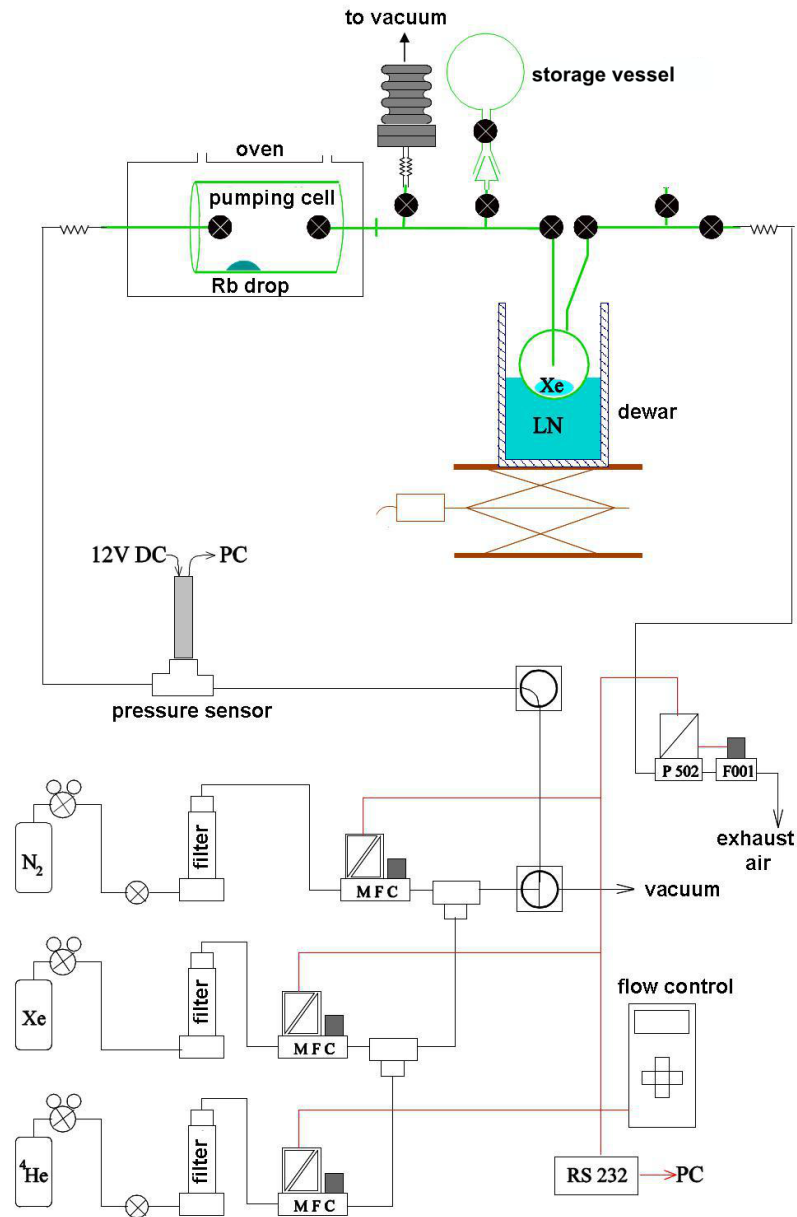


Figure 3.2: Scheme of the PTB  $^{129}\text{Xe}$  polarizer: The gases  $\text{N}_2$ ,  $^{129}\text{Xe}$  and  $^4\text{He}$  are directed through filters to mass flow controllers (MFC) that provide the desired mixing ratios. Then the gas mixture is flowing through the pumping cell, which contains a droplet of Rb metal and is heated to about  $150^\circ\text{C}$ . Two circularly polarized laser beams that are on resonance with the  $D_1$  transition of Rb hit the pumping cell from both sides (not shown in the figure) to optically pump the Rb atoms. Via spin exchange collisions the polarization of the electron spins of the Rb atoms is transferred to the nuclear spins of the  $^{129}\text{Xe}$  atoms. Then the gas mixture flows through a second cell which is placed in a liquid-nitrogen (LN) dewar. Here the polarized  $^{129}\text{Xe}$  atoms are frozen out and thus separated from the buffer gases ( $\text{N}_2$  and  $^4\text{He}$ ). After thawing of the nuclear spin polarized  $^{129}\text{Xe}$  it can be filled into the storage vessel. This figure was taken from the dissertation of W. Kilian [95].

the polarizer, first is cleaned from oxygen and water through filters<sup>2</sup>. It typically contains 100 mbar of isotopically enriched xenon (91.2 %  $^{129}\text{Xe}$ ), 200 mbar of  $\text{N}_2$  and 4.7 bar of  $^4\text{He}$  (the latter ones are used as buffer gases). The polarizer works in a continuous-flow-mode, i.e. the gases are pumped through the system continuously, controlled by digital mass flow controllers (MFC). After mixing, the gases flow through the pumping cell, where the spin exchange optical pumping takes place. The pumping cell is a cylindrical Duran glass cell of volume  $V = 30 \text{ cm}^3$ , that contains a droplet of Rb metal. The cell is heated to about  $150^\circ\text{C}$  to reach a sufficiently Rb vapor pressure such that the Rb can be regarded as optically thick. For optical pumping of Rb two high-power semiconductor lasers (FAB-systems, **Fibre-Array-Packaged**) are needed. By combination of a beam splitter cube and a  $\lambda/4$ -plate the laser light is circularly polarized, so that the  $D_1$  transition ( $\lambda = 794.8 \text{ nm}$ ) of Rb is excited. To reduce the depolarization of Rb due to Rb-Xe collisions a low xenon pressure is needed. On the contrary, a higher total pressure is needed to achieve a pressure broadening of the Rb absorption line, so that it fits better to the spectral linewidth of the laser. That is why  $^4\text{He}$  is used as buffer gas. Additionally, nitrogen ( $\text{N}_2$ ) is used as quenching gas: The excited Rb atoms deexcite by radiating unpolarized fluorescence light, which work to decrease the degree of polarization of the electron spins of the Rb atoms. By adding  $\text{N}_2$  this effect is suppressed since due to collisions with the  $\text{N}_2$  molecules the excited Rb atoms can deexcite non-radiatively. But this advantage has to be weighted against the fact that  $\text{N}_2$  breaks up the Rb-Xe van der Waals molecules and therefore is slowing down the spin transfer. After optical pumping of  $^{129}\text{Xe}$ , the gas mixture flows through a second cell, which is placed in a liquid-nitrogen dewar so that the heavier  $^{129}\text{Xe}$  atoms are frozen out while the other gases are released into the ambient air. Then the nuclear spin polarized  $^{129}\text{Xe}$  can be thawed and filled into the storage vessel. To achieve a pressure of about 1 bar in the storage vessel ( $V \approx 270 \text{ ml}$ ), the flowing gas mixture approximately has to freeze out one hour. After the thawing procedure, in which about half of the polarization is lost, polarizations up to  $(15 \pm 2)\%$  can be achieved.

### 3.3 Spin Precession and Bloch Equations

Each atom of a nuclear spin polarized gas is characterized by a nuclear magnetic moment  $\vec{\mu} = \gamma \cdot \hbar \cdot \vec{I}$ , which follows the rules of quantum mechanics. If the motion of  $\vec{\mu}$  in a magnetic field  $\vec{B}$  is considered, the Schroedinger equation of the Hamiltonian  $H = -\vec{\mu} \cdot \vec{B}$  has to be solved. In [100] it was shown that the equations of motion for a nuclear magnetic moment  $\vec{\mu}$  and a classical magnetic moment  $\vec{m}_{\text{class}}$  are equal. These equations are called the *Bloch equations* which are given by

$$\frac{d}{dt} \vec{m}^*(t) = \gamma \vec{m}^*(t) \times \vec{B}(t) . \quad (3.15)$$

Here  $\gamma$  is the gyromagnetic ratio and  $\vec{m}^*$  stands either for the classical magnetic moment  $\vec{m}_{\text{class}}$  or for the expectation value  $\langle \vec{\mu} \rangle$  of the nuclear magnetic moment. If we assume that

---

<sup>2</sup>OxiSorb from the company MESSER

the single spins of a nuclear spin polarized gas do not interact with each other, Eq. 3.15 even is valid for the expectation value of the total nuclear magnetic moment of the spin polarized gas, which is given by

$$\vec{m} = \sum \langle \vec{\mu} \rangle . \quad (3.16)$$

The absolute value of the total nuclear magnetic moment is given by

$$m = N P \mu = N P \gamma I \hbar , \quad (3.17)$$

with the number of atoms  $N = \frac{pV}{kT}$  (with pressure  $p$ , volume  $V$ , temperature  $T$  and Boltzmann constant  $k$ ), the degree of polarization  $P$ , the gyromagnetic ratio  $\gamma$ , the nuclear spin  $I$  and the reduced Planck constant  $\hbar$ . In addition the nuclear spin polarized gas can be described by a macroscopic quantity, the so-called magnetization  $\vec{M}$ , which is defined as the resulting magnetic moment  $\vec{m}$  per unit volume  $V$ :

$$\vec{M} = \frac{1}{V} \vec{m} = \frac{1}{V} \sum \langle \vec{\mu} \rangle . \quad (3.18)$$

With reference to a homogenous magnetic guiding field  $\vec{B}_0$ , the magnetic moment  $\vec{m}$  can be split in two components: the longitudinal component  $\vec{m}_{||}$ , which is parallel to the direction of the magnetic guiding field  $\vec{B}_0$ , and the transversal component  $\vec{m}_{\perp}$ , that is perpendicular to  $\vec{B}_0$ . If the homogenous magnetic guiding field is constant in time and pointing in x-direction<sup>3</sup>, i.e.  $\vec{B}_0 = B_0 \cdot \hat{e}_x$ , the magnetic moment is also aligned in x-direction, i.e.  $\vec{m} = m \cdot \hat{e}_x$ . By applying an additional alternating magnetic field (RF pulse)

$$\vec{B}_1(t) = B_1(\hat{e}_y \cos \omega_r t + \hat{e}_z \sin \omega_r t) , \quad (3.19)$$

which rotates in the plane perpendicular to the static, homogenous magnetic guiding field  $\vec{B}_0$  with angular frequency  $\omega_r$ , for a duration of  $t_{\text{irr}}$ , the magnetic moment  $\vec{m}$  can be tilted by an angle  $\alpha$ . But tilting of the magnetic moment only takes place if the RF pulse is resonant, i.e.  $\omega_r = \omega_L$ , where  $\omega_L = |\gamma \cdot B_0|$  is the so-called Larmor frequency. After irradiation of a resonant RF pulse the magnetic moment  $\vec{m}$  then is given by

$$\vec{m} = \begin{pmatrix} m \cos \alpha \\ m \sin \alpha \cos \varphi \\ m \sin \alpha \sin \varphi \end{pmatrix} . \quad (3.20)$$

Here  $\varphi$  is an arbitrary angle in the yz-plane and  $\alpha$  is the tilting angle, which is given by

$$\alpha = \gamma B_1 t_{\text{irr}} . \quad (3.21)$$

For our experiment at the PTB in Berlin another method was used to reach tilting of the magnetic moment: A homogenous magnetic field was aligned in y-direction, i.e.  $\vec{B}_1 = B_1 \cdot \hat{e}_y$ .

<sup>3</sup>In our experiment the coordinate system of the magnetically shielded room as shown in Fig. 4.5 was used.

The magnetic guiding field was pointing in x-direction. So, to be consistent with the coordinate system of the magnetically shielded room in the following the x-direction is used as the direction of the magnetic guiding field, i.e.  $\vec{B}_0 = B_0 \cdot \hat{e}_x$ .

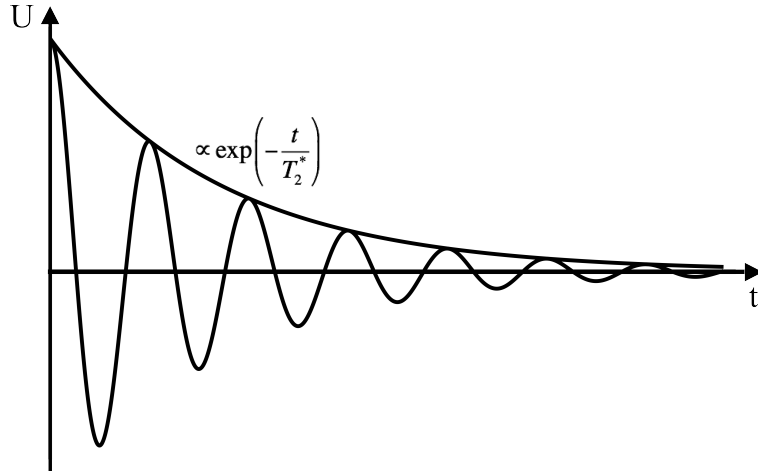


Figure 3.3: Schematic *Free induction decay* (FID) signal, which is induced in a pickup coil pair by the transversal component  $\vec{m}_\perp$  of the magnetic moment that precesses freely around a magnetic guiding field  $\vec{B}_0$ . The envelope of the signal decreases exponentially with the characteristic decay time  $T_2^*$  (see Sec. 3.5).

During a period of  $t_{\text{switch}}$  the magnetic field  $\vec{B}_1$  was switched off while another homogenous field  $\vec{B}_0 = -B_0 \cdot \hat{e}_x$ , that is perpendicular to  $\vec{B}_1$ , was switched on. Thereby the magnitude of both fields is equal, i.e.  $B_0 = B_1$ . If the switching operation happens too slowly (adiabatic field change), i.e.

$$t_{\text{switch}} \gg \frac{2\pi}{\omega_L}, \quad (3.22)$$

the magnetic moment  $\vec{m}$  follows the actual field direction and hence is aligned along the new field axis given by  $\vec{B}_0$ . But if the switching operation happens fairly fast (non-adiabatic field change), i.e.

$$t_{\text{switch}} \ll \frac{2\pi}{\omega_L}, \quad (3.23)$$

the magnetic moment cannot follow the new field axis given by  $\vec{B}_0$  and hence is tilted by an angle  $\alpha = 90^\circ$  relative to  $\vec{B}_0$ . The advantage of this method is that the same flip angle is guaranteed at all times.

In general, tilting of the magnetic moment  $\vec{m}$  relative to the magnetic guiding field  $\vec{B}_0$  is called *spin flip*. Regardless of which method is used for a spin flip, after tilting the magnetic moment  $\vec{m}$  starts to precess freely around the axis of the magnetic guiding field  $\vec{B}_0$  with the angular velocity  $\omega_L = |\gamma \cdot B_0|$ . This rotation is called *Larmor precession* or *spin precession* and the corresponding frequency is the Larmor frequency. For an atom with a nuclear spin of  $I = 1/2$  the precession energy  $\Delta E = \hbar \omega_L$  corresponds to the energy difference between the two Zeeman levels according to Eq. 3.8.

Due to different relaxation processes that are described in Sec. 3.5, the transverse component of the magnetic moment  $\vec{m}_\perp$  decays with a characteristic time constant  $T_2^*$ , while its longitudinal component  $\vec{m}_\parallel$  tends to reach its thermal equilibrium value  $m_{\text{th}}$  with a characteristic

time constant  $T_1$ . Thus, the Bloch equations (Eq. 3.15) have to be extended by relaxation terms

$$\frac{d}{dt}m_x = \gamma(\vec{m} \times \vec{B})_x + \frac{m_{\text{th}} - m_x}{T_1}, \quad (3.24)$$

$$\frac{d}{dt}m_y = \gamma(\vec{m} \times \vec{B})_y - \frac{m_y}{T_2^*}, \quad (3.25)$$

$$\frac{d}{dt}m_z = \gamma(\vec{m} \times \vec{B})_z - \frac{m_z}{T_2^*}. \quad (3.26)$$

In case of hyperpolarized gases with  $m_{\text{th}} \ll m_x$ , the thermal equilibrium value  $m_{\text{th}}$  can be neglected, i.e.  $m_{\text{th}} \approx 0$ .

The spin precession signal can be detected with a so-called pickup coil pair with its axis perpendicular to the  $\vec{B}_0$  axis. Then the precessing transversal component of the magnetic moment induces a periodically varying current in the pickup coil pair. The detected signal is referred to as *Free-Induction-Decay* (FID) and is shown in Fig. 3.3. In our experiment instead of pickup coils SQUID detectors were used (see Sec. 4.2.3).

### 3.4 Magnetic Field Produced by Spin Polarized Atoms

For a nuclear spin polarized gas the total magnetic moment  $\vec{m}$  is aligned parallel to the magnetic guiding field  $\vec{B}_0$ . If the gas is filled into a spherical glass cell, an ideal magnetic dipole field is produced outside the sphere which is given by [101]

$$\vec{B}(\vec{r}) = \frac{\mu_0}{4\pi} \frac{3\hat{r}(\hat{r} \cdot \vec{m}) - \vec{m}}{r^3}. \quad (3.27)$$

If the magnetic guiding field  $\vec{B}_0$  is directed in x-direction, the x-component of the magnetic dipole field is given by

$$B_x(r) = \frac{\mu_0}{4\pi} \frac{m(3\cos^2\Theta - 1)}{r^3} \quad \text{for } r > R_C. \quad (3.28)$$

Here it is assumed that the magnetic moment  $\vec{m}$  of the polarized gas is concentrated in the center of the spherical glass cell and  $r$  describes the distance of  $\vec{m}$  to a measurement point outside the sphere.  $R_C$  is the radius of the cell,  $\mu_0$  the vacuum permeability and  $m = NP\gamma I\hbar$  (Eq. 3.17) the magnitude of the magnetic moment of the nuclear spin polarized gas, such as  $^3\text{He}$  or  $^{129}\text{Xe}$ .  $\Theta$  is the angle between the x-axis and the connection line of the center of the glass cell and the measurement point. Considering a point on the x-axis, i.e.  $\Theta = 0$ , and using the ideal gas law, one can write the above equation as

$$B_x(r) = \frac{pV}{kT} \frac{2\mu_0 P \gamma I \hbar}{4\pi r^3}, \quad (3.29)$$

where  $p$  is the pressure in the cell,  $V$  the volume of the cell,  $k$  the Boltzmann constant,  $T$  the temperature,  $P$  the degree of polarization,  $\gamma$  the gyromagnetic ratio and  $I = \frac{1}{2}$  the nuclear spin of the gas atoms. So, the magnetic field produced by a nuclear spin polarized gas, which is filled into a spherical glass cell, decreases with the distance  $r$  according to  $\frac{1}{r^3}$  and is proportional to the polarization  $P$ .

## 3.5 Relaxation

By means of optical pumping high degrees of polarization  $P$  can be achieved. However, nature strives for thermal equilibrium, so that the polarization is destructed by different effects. That means the polarization  $P$ , respectively the magnetic moment  $\vec{m}$ , is not constant in time, but decays exponentially until the Boltzmann polarization  $P_B$  is reached. This process is called relaxation. Here it is necessary to distinguish between the relaxation of the longitudinal component of the magnetic moment, which is parallel to the magnetic guiding field, and the transverse component of the magnetic moment, which is perpendicular to the magnetic guiding field. The decay of the longitudinal component is similar to the decay of the the polarization  $P$ , which can be described by

$$P(t) = (P_0 - P_B) \cdot e^{-t/T_1} + P_B . \quad (3.30)$$

In case of hyperpolarized gases ( $P_0 \gg P_B$ ) the Boltzmann polarization can be neglected. Equation 3.30 then simplifies to

$$P(t) \approx P_0 \cdot e^{-t/T_1} . \quad (3.31)$$

$T_1$  is the characteristic decay time and is called *longitudinal relaxation time* which will be discussed in the following section. Section 3.5.2 will deal with the decay of the transverse component of the magnetic moment, which decays with a characteristic time constant that is called *transverse relaxation time*  $T_2^*$ .

### 3.5.1 Longitudinal Relaxation

Different mechanisms destruct the longitudinal component of the magnetic moment  $\vec{m}$ . The ones that are relevant for our experiment are the gradient relaxation ( $T_{1,\text{grad}}$ ), as well as the relaxation due to collisions of the polarized atoms with the wall of the gas container ( $T_{1,\text{wall}}$ ) and the binary or van der Waals collisions of the atoms with each other ( $T_{1,\text{bin}}$  and  $T_{1,\text{vdW}}$ ). The total longitudinal relaxation rate then is given by

$$\frac{1}{T_1} = \frac{1}{T_{1,\text{grad}}} + \frac{1}{T_{1,\text{wall}}} + \frac{1}{T_{1,\text{bin}}} + \frac{1}{T_{1,\text{vdW}}} . \quad (3.32)$$

The individual effects will be explained in the following.

#### Wall Relaxation

The polarized gases are filled into cells that are made of glass which may contain small para- or ferromagnetic impurities. During collisions of the polarized noble gas atoms with the wall of the glass cell the dipolar coupling as well as the Fermi-contact interaction with those impurities can lead to spin relaxation. In those collisions the atoms can be adsorbed at the wall or they can diffuse into the glass matrix. The latter one can be strongly suppressed by

using quasi impermeable aluminosilicate glass, such as the GE-180 glass<sup>4</sup>, that was used for our measurement cells.

The wall relaxation rate  $1/T_{1,\text{wall}}$  is proportional to the surface-to-volume ratio of the cell

$$\frac{1}{T_{1,\text{wall}}} = \frac{1}{\eta} \cdot \frac{S}{V}, \quad (3.33)$$

where  $\eta$  is the relaxation coefficient of the wall of the glass cell. Even if the same type of glass is used for all measurement cells, the value of  $\eta$  may vary more than a factor of 10 from one cell to another. Equation 3.33 shows that the smaller the surface-to-volume ratio, the smaller is the wall relaxation rate  $1/T_{1,\text{wall}}$ . For spherical glass cells the wall relaxation rate is given by  $1/T_{1,\text{wall}} \propto 1/R$ . Thus, the use of big spherical glass cells with radius  $R$  can reduce wall relaxation. But the radius  $R$  cannot be arbitrary since the gradient relaxation rate  $1/T_{1,\text{grad}}$ , which will be explained in the next section, is limited by the radius  $R$ , i.e.  $1/T_{1,\text{grad}} \propto R^4$  (Eq. 3.39). So, the choice of the radius  $R$  has to compromise wall and gradient relaxation rate. Optimal conditions for both are given for a spherical cell with a radius of  $R = 3$  cm.

However, due to geometric reasons cylindrical cells were used in our experiment (see Sec. 4.2.1). The diameter  $\varnothing_L$  and length  $L$  of those cells were chosen to be  $L/2 = \varnothing_L/2 = R$  such that the cylindrical cell approximately has the same shape as a spherical cell with radius  $R = 3$  cm. That is why in the following section the cylindrical cells can be approximated by spherical cells. For our experiment in total 4 cylindrical cells with identical measurements were produced, but only two of them had satisfying wall relaxation times for  $^3\text{He}$  with  $T_{1,\text{wall}} > 100$  h. The measurement of the wall relaxation times for  $^{129}\text{Xe}$  were not possible, but in some tests it was discovered that long wall relaxation times measured with  $^3\text{He}$  result in long wall relaxation times of  $^{129}\text{Xe}$  as well.

A detailed description of the wall relaxation of hyperpolarized  $^3\text{He}$  in spherical glass cells can be found in [102], [103] and [104].

### Gradient Relaxation

To maintain the polarization of noble gases a homogeneous magnetic guiding field  $\vec{B}_0$  is needed. In reality this field is not ideally homogeneous, but has some finite field gradients. Then in the rest frame of a polarized noble gas atom, which diffuses through the glass cell, field gradients generate a temporally fluctuating magnetic field. This can cause spin flips if the Fourier spectrum contains frequency components near the Larmor frequency  $\omega_L = |\gamma \cdot B_0|$ . According to [105] for a magnetic guiding field that is aligned in x-direction<sup>5</sup> the longitudinal relaxation rate due to transverse field gradients,  $\vec{\nabla} B_{1,y} = (\frac{\partial B_{1,y}}{\partial x}, \frac{\partial B_{1,y}}{\partial y}, \frac{\partial B_{1,y}}{\partial z})$

<sup>4</sup>GE-180 is produced by ‘‘General Electric’’ and mainly consists of  $\text{SiO}_2$  (60%),  $\text{BaO}$  (18%),  $\text{Al}_2\text{O}_3$  (14%) and  $\text{CaO}$  (7%).

<sup>5</sup>As customary, in [105] it is assumed that the magnetic guiding field is pointing in z-direction. In our experiment the coordinate system of the magnetically shielded room as shown in Fig. 4.5 was used. So, to be consistent with the coordinate system of the magnetically shielded room in the following the x-direction is used as the direction of the magnetic guiding field, i.e.  $\vec{B}_0 = B_0 \cdot \hat{e}_x$ .

Diff. coeff.	Value ( $\frac{\text{cm}^2}{\text{s}}$ )	Ref.	Temperature (K)
$D_{\text{He}}$	$\approx 1.880$	[106]	293
$D_{\text{He in Xe}}$	$\approx 0.600$	[107]	300
$D_{\text{He in N}_2}$	$\approx 0.770$	[107]	300
$D_{\text{Xe}}$	$\approx 0.580$	[108]	300
$D_{\text{Xe in He}}$	$\approx 0.790$	[108]	300
$D_{\text{Xe in N}_2}$	$\approx 0.210$	[108]	353

 Table 3.1: Diffusion coefficients for  $^3\text{He}$  and  $^{129}\text{Xe}$  at a pressure of 1 bar.

and  $\vec{\nabla}B_{1,z} = (\frac{\partial B_{1,z}}{\partial x}, \frac{\partial B_{1,z}}{\partial y}, \frac{\partial B_{1,z}}{\partial z})$ , is given by

$$\frac{1}{T_{1,\text{grad}}} = 2D \frac{|\vec{\nabla}B_{1,y}|^2 + |\vec{\nabla}B_{1,z}|^2}{B_0^2} \times \sum_n \frac{1}{(x_{1n}^2 - 2)(1 + D^2 x_{1n}^4 (\gamma B_0)^{-2} R^{-4})}. \quad (3.34)$$

This equation was derived for a spherical volume. As already mentioned in the former section, our cylindrical measurement cells can be approximated by spherical cells so that Eq. 3.34 is valid for our cylindrical measurement cells, too.  $D$  is the diffusion coefficient,  $\gamma$  the gyromagnetic ratio,  $R$  the radius of the cell and  $x_{1n}$  ( $n = 1, 2, 3, \dots$ ) are the zeros of the derivative of the spherical Bessel function ( $\frac{d}{dx}j_1(x_{1n}) = 0$ ).  $\vec{B}_0 = B_0 \cdot \hat{e}_x$  is the average homogenous field in x-direction and  $\vec{B}_1(\vec{r})$  describes the deviation of the local field from the average homogeneous field  $\vec{B}_0$ . The mean value of  $\vec{B}_1(\vec{r})$  is assumed to be zero.

In our experiment we use a gas mixture of  $^3\text{He}$ ,  $^{129}\text{Xe}$  and  $\text{N}_2$ . Nitrogen is used as buffer gas to suppress the van der Waals relaxation, which will be described in the next section. The diffusion coefficients for  $^3\text{He}$  and  $^{129}\text{Xe}$  in this gas mixture are given by [106]:

$$\frac{1}{D_{\text{He}}^{\text{GM}}} = \left( \frac{p_{\text{He}}}{D_{\text{He}}} + \frac{p_{\text{Xe}}}{D_{\text{He in Xe}}} + \frac{p_{\text{N}_2}}{D_{\text{He in N}_2}} \right) \frac{1}{p_0} \frac{T_0^{3/2}}{T^{3/2}}, \quad (3.35)$$

$$(3.36)$$

$$\frac{1}{D_{\text{Xe}}^{\text{GM}}} = \left( \frac{p_{\text{Xe}}}{D_{\text{Xe}}} + \frac{p_{\text{He}}}{D_{\text{Xe in He}}} + \frac{p_{\text{N}_2}}{D_{\text{Xe in N}_2}} \right) \frac{1}{p_0} \frac{T_0^{3/2}}{T^{3/2}}. \quad (3.37)$$

Here  $p_{\text{He}}$ ,  $p_{\text{Xe}}$  and  $p_{\text{N}_2}$  are the partial pressures of  $^3\text{He}$ ,  $^{129}\text{Xe}$  and  $\text{N}_2$ , which are given in units of bar.  $D_{\text{He/Xe}}$  are the respective diffusion coefficients of pure  $^3\text{He}$  and  $^{129}\text{Xe}$  gas at standard condition ( $p_0 = 1.013$  bar,  $T_0 = 273.15$  K), and  $D_{\text{X in Y}}$  is the diffusion coefficient of species X in species Y (with  $p_X \rightarrow 0$ ). The different coefficients are listed in Tab. 3.1. Here it should be noted that the coefficients are given for gas pressures of 1 bar.

The expression of the gradient relaxation rate in a spherical cell of radius  $R$  ( $\approx$  cylindrical cell with  $L/2 = \varnothing_L/2 = R$ ) given in Eq. 3.34 can be simplified by introducing the *diffusion time*  $\tau_d = R^2/D$  and the characteristic *precession time*  $\tau_p = 1/\omega_L$ . The ratio of both is given



by

$$\frac{\tau_d}{\tau_p} = \frac{R^2 \omega_L}{D} \propto p B_0 . \quad (3.38)$$

For low pressures and low magnetic fields the precession time is long compared to the diffusion time, i.e.  $\tau_d/\tau_p \ll 1$ . This region is called the *low pressure regime* or the *regime of motional narrowing* for which the gradient relaxation rate given in Eq. 3.34 simplifies to

$$\frac{1}{T_{1,\text{grad}}} \approx \frac{8 R^4}{175 D} \gamma^2 (|\vec{\nabla} B_{1,y}|^2 + |\vec{\nabla} B_{1,z}|^2) . \quad (3.39)$$

On the contrary for high pressures and high magnetic fields the precession time is short compared to the diffusion time, i.e.  $\tau_d/\tau_p \gg 1$ . In this so-called *high pressure regime* the gradient relaxation rate given in Eq. 3.34 can be approximated by

$$\frac{1}{T_{1,\text{grad}}} \approx D \frac{|\vec{\nabla} B_{1,y}|^2 + |\vec{\nabla} B_{1,z}|^2}{B_0^2} . \quad (3.40)$$

So, the longitudinal gradient relaxation rate in the *low pressure regime* is proportional to the pressure  $p$  (with  $D \propto \frac{1}{p}$ ) and to the absolute field gradients whereas in the *high pressure regime* it is inversely proportional to the pressure  $p$  and proportional to the relative field gradients.

For a given relative field gradient the absolute field gradient decreases with decreasing magnetic field  $B_0$ . Thus, in the low pressure regime (motional narrowing regime) longer gradient relaxation times can be achieved than in the high pressure regime. That is why in our experiment we worked in the low pressure regime. Consequently Eq. 3.39 describes the correct gradient relaxation rate. Optimal gradient relaxation times can be achieved for a magnetic guiding field in the order of  $\mu\text{T}$ , field gradients in the order of  $\text{pT}/\text{cm}$  and low pressures in the order of  $\text{mbar}$ .

### Binary and Van der Waals Relaxation

In  $^3\text{He}$ - $^3\text{He}$  or  $^{129}\text{Xe}$ - $^{129}\text{Xe}$  collisions short-duration molecules can be formed. The nuclear spins of the atoms that form those molecules couple due to magnetic dipole–dipole interaction. Such molecules have additional rotational and vibrational degrees of freedom. Nuclear spin polarization then is lost due to coupling of the nuclear spin to the rotational angular momentum, which transfers part of the nuclear spin polarization to orbital angular momentum. This relaxation mechanism is proportional to the pressure of the gas. According to [109] the relaxation time due to binary collisions at pressure  $p$  and temperature  $T$  for  $^3\text{He}$  is given by

$$T_{1,\text{bin}}^{\text{He}} \approx (754 \text{ h}) \frac{p_0}{p_{\text{He}}} \frac{T}{T_0} , \quad (3.41)$$

whereas for  $^{129}\text{Xe}$  it is given by [110]

$$T_{1,\text{bin}}^{\text{Xe}} \approx (56 \text{ h}) \frac{p_0}{p_{\text{Xe}}} \frac{T}{T_0} . \quad (3.42)$$

Here  $p_0$  and  $T_0$  are the standard pressure and temperature ( $p_0 = 1.013$  bar,  $T_0 = 273.15$  K) and the partial pressures of  $^3\text{He}$  and  $^{129}\text{Xe}$  are given in units of bar. For the motional narrowing regime, i.e. at low pressures in the order of mbar, the binary relaxation time can be calculated for room temperature ( $T \approx 293.15$  K). Since  $T_{1,\text{bin}}^{\text{He,Xe}} > 7000$  h, the binary relaxation time can be neglected in our experiments.

For heavy polar atoms, such as the  $^{129}\text{Xe}$  atoms, additionally van der Waals molecules can be formed. The lifetime of such molecules is larger than the lifetime of the molecules that are formed in binary  $^{129}\text{Xe}$ - $^{129}\text{Xe}$  collisions. Hence, the loss of nuclear spin polarization in van der Waals molecules is more likely. In [111] the van der Waals relaxation rate for  $^{129}\text{Xe}$  was measured. For pure  $^{129}\text{Xe}$  the maximum relaxation time is given by

$$T_{1,\text{vdW}}^{\text{Xe}} = 4.1 \text{ h} . \quad (3.43)$$

By adding buffer gases the van der Waals molecules can be broken open by the buffer gas molecules, so that the van der Waals relaxation time is increased and given by [111]

$$T_{1,\text{vdW}}^{\text{Xe in B}} = T_{1,\text{vdW}}^{\text{Xe}} (1 + r[\text{B}]/[\text{Xe}]), \quad (3.44)$$

where  $r$  is the breakup rate coefficient and  $[\text{B}]/[\text{Xe}]$  is the ratio of the partial pressures of the buffer gas B and  $^{129}\text{Xe}$ . Equation 3.44 shows that in the limit  $[\text{B}]/[\text{Xe}] \rightarrow \infty$ , van der Waals relaxation can be neglected. In order to suppress the van der Waals relaxation, in our experiment  $\text{N}_2$  was used as buffergas. For  $\text{N}_2$ , the breakup rate coefficient was measured to be  $r = 1.05(8)$ . Typically, we used pressure ratios of  $[\text{N}_2]/[\text{Xe}] \approx 4 : 1$ . Further increase of the buffergas pressure causes considerable losses due to the gradient relaxation rate which scales with the total pressure  $p_{\text{tot}}$  of the gas mixture (see Eq. 3.39). A discussion about the optimum  $^3\text{He}$ ,  $^{129}\text{Xe}$  and  $\text{N}_2$  pressures is given in Sec. 4.2.4.

In addition another relaxation mechanism due to collisions of the polarized noble gas atoms can be considered: Oxygen molecules ( $\text{O}_2$ ) have a molecular spin of  $J = 1$  and thus a magnetic moment which causes strong spin relaxation due to the dipole-dipole interaction in a collision between a polarized noble gas atom and a  $\text{O}_2$  molecule. The relaxation due to  $\text{O}_2$  molecules for  $^3\text{He}$  at temperature  $T = 299$  K was measured to be [112]

$$T_1^{\text{O}_2}(^3\text{He}) = \frac{\text{bar}}{p_{\text{O}_2}} 2.5 \text{ s} \quad (3.45)$$

and for  $^{129}\text{Xe}$  at temperature  $T = 300$  K [113] to

$$T_1^{\text{O}_2}(^{129}\text{Xe}) = \frac{\text{bar}}{p_{\text{O}_2}} 2.1 \text{ s} , \quad (3.46)$$

where  $p_{\text{O}_2}$  is the partial pressure of  $\text{O}_2$  in units of bar. Equation 3.45 and 3.46 show that the relaxation time  $T_1^{\text{O}_2}$  increases for decreasing partial pressure of  $\text{O}_2$ . So, to suppress this relaxation mechanism the partial pressure of  $\text{O}_2$  has to be smaller than  $10^{-3}$  mbar to achieve  $T_1^{\text{O}_2} > 580$  h. This means that the measurement cells as well as the device to mix the gases (filling system) have to be evacuated thoroughly before the gases  $^3\text{He}$ ,  $^{129}\text{Xe}$  and  $\text{N}_2$  are filled in. The relaxation due to oxygen then can be neglected compared to the other relaxation mechanisms.

### 3.5.2 Transverse Relaxation

If the transverse component of the magnetic moment is precessing around the magnetic guiding field (Sec. 3.3) the amplitude of the precession signal decays exponentially with a characteristic time constant, the so-called effective transverse relaxation time  $T_2^*$ . The effective transverse relaxation rate is given by

$$\frac{1}{T_2^*} = \frac{1}{T_{1,\text{wall}}} + \frac{1}{T_{1,\text{vdW}}} + \frac{1}{T_{2,\text{grad}}}, \quad (3.47)$$

where  $T_{1,\text{wall}}$  and  $T_{1,\text{vdW}}$  are the longitudinal relaxation times, which were discussed in the previous section.  $1/T_{2,\text{grad}}$  is the total transverse gradient relaxation rate which can be split in two terms

$$\frac{1}{T_{2,\text{grad}}} = \frac{1}{T_{1,\text{grad}}} + \frac{1}{T'_{2,\text{grad}}}, \quad (3.48)$$

where  $T_{1,\text{grad}}$  is the longitudinal gradient relaxation time discussed in the previous section, which is given by Eq. 3.39.  $T'_{2,\text{grad}}$  describes the relaxation of the transverse component of the magnetic moment due to the loss of phase coherence of the single magnetic moments. This dephasing can be caused by collisions of the atoms with each other and with the wall of the measurement cell and by field gradients of the magnetic guiding field. Due to field gradients the single polarized noble gas atoms see different magnetic fields and thus precess with different Larmor frequencies  $\omega_L = |\gamma \cdot B|$ . That means that some atoms precess faster than others which causes dephasing of the single magnetic moments. According to [105] the total transverse gradient relaxation rate  $1/T_{2,\text{grad}}$  for spherical sample cells ( $\approx$  cylindrical sample cells) in a field  $\vec{B}_0$  that is oriented in x-direction can be expressed by

$$\begin{aligned} \frac{1}{T_{2,\text{grad}}} = & \frac{8R^4\gamma^2|\vec{\nabla}B_{1,x}|^2}{175D} + D \frac{|\vec{\nabla}B_{1,y}|^2 + |\vec{\nabla}B_{1,z}|^2}{B_0^2} \\ & \times \sum_n \frac{1}{(x_{1n}^2 - 2)(1 + D^2x_{1n}^4(\gamma B_0)^{-2}R^{-4})}. \end{aligned} \quad (3.49)$$

Here  $D$  is again the diffusion coefficient according to Eq. 3.35 and Eq. 3.37,  $\vec{B}_0 = B_0 \cdot \hat{e}_x$  is the average homogeneous field in x-direction,  $\vec{B}_1(\vec{r})$  the deviation of the local field from  $\vec{B}_0$ ,  $\gamma$  the gyromagnetic ratio,  $R$  the radius of the cell and  $x_{1n}$  ( $n = 1, 2, 3, \dots$ ) are the zeros of the derivative of the spherical Bessel function ( $\frac{d}{dx}j_1(x_{1n}) = 0$ ).

For the low pressure regime the total transverse gradient relaxation rate simplifies to

$$\frac{1}{T_{2,\text{grad}}} \approx \frac{4R^4\gamma^2}{175D} \cdot \left( |\vec{\nabla}B_{1,y}|^2 + |\vec{\nabla}B_{1,z}|^2 + 2|\vec{\nabla}B_{1,x}|^2 \right). \quad (3.50)$$

Thus, the total transverse relaxation rate is proportional to  $p$  (with  $D \propto \frac{1}{p}$ ) and it depends on the square of the absolute field gradients.



## 4 Experimental Technique and Setup

### 4.1 Experimental Technique

As already mentioned in Chap. 2 the axion or axion-like particles mediate a  $P$ - and  $T$ -violating macroscopic force between unpolarized fermions  $f$  and polarized fermions  $f_\sigma$  which can be described by a Yukawa-type potential  $V_{\text{sp}}(\vec{r})$  given by Eq. 2.71. This potential effectively acts near the surface of a massive unpolarized sample as a pseudo-magnetic field and gives rise to a shift  $\Delta\nu_{\text{sp}} = 2 \cdot V_\Sigma/h$ , e.g. in the precession frequency of nuclear spin polarized gases, such as  $^3\text{He}$  and  $^{129}\text{Xe}$ . The potential  $V_\Sigma$  is obtained by integration of the spin-dependent short-range potential  $V_{\text{sp}}(\vec{r})$  over the volume of the massive unpolarized sample averaged over the volume of the polarized spin sample (see App. F). According to the Schmidt model [11] the nuclear spin of the  $^3\text{He}$  and  $^{129}\text{Xe}$  atoms is carried by a neutron only. Thus both polarized nuclei can be regarded as an effective probe of a spin polarized bound neutron. The mass of the polarized fermion in Eq. 2.71 then corresponds to the mass of a bound neutron, i.e.  $m_{f_\sigma} = m_n$ . In [89], refined theoretical calculations of the neutron spin contribution to the nuclear angular momentum in  $^3\text{He}$  and  $^{129}\text{Xe}$  nuclei are discussed and result in approximately 87% for  $^3\text{He}$  and 75% for  $^{129}\text{Xe}$  (refined nuclear shell model). The mass of the polarized fermion in Eq. 2.71 then is slightly different for  $^3\text{He}$  and  $^{129}\text{Xe}$ :  $m_{f_\sigma}(^3\text{He}) = 0.87 \cdot m_n$  and  $m_{f_\sigma}(^{129}\text{Xe}) = 0.75 \cdot m_n$ .

For a start, the determination of the frequency shift  $\Delta\nu_{\text{sp}}$  due to the spin-dependent short-range interaction, will be illustrated by considering only polarized  $^3\text{He}$ . Cylindrically shaped spin and unpolarized matter samples are used with a finite gap  $\Delta x$  between them. The axes of the cylinders were aligned along the direction of the magnetic guiding field  $\vec{B}_0 = -B_0 \cdot \hat{e}_x$  (Fig. 4.1). The unpolarized matter sample can be moved along the axis of the magnetic field  $\vec{B}_0$  ( $x$ -axis) from “close” position ( $\Delta x_c = 2.2 \text{ mm}$ )<sup>1</sup> to “distant” position ( $\Delta x_d = 170 \text{ mm}$ ) and vice versa. By inducing a spin flip, the polarized nuclear spins of  $^3\text{He}$  start to precess around the direction of the magnetic guiding field  $\vec{B}_0$  with the Larmor precession frequency  $\omega_L = |\gamma_{\text{He}} \cdot B_0|$ . If the unpolarized matter sample is in close position the precession frequency of the polarized  $^3\text{He}$  atoms is shifted due to the spin-dependent short-range interaction. The precession frequency of  $^3\text{He}$  then is given by

$$\omega_{\text{He},c} = \gamma_{\text{He}} \cdot B_0 + 2\pi \cdot \Delta\nu_{\text{sp}} . \quad (4.1)$$

After several hours the unpolarized matter sample is moved to distant position, where the

<sup>1</sup>In “close” position the gap  $\Delta x$  between the polarized  $^3\text{He}$  atoms and the unpolarized matter sample is given by the thickness of the glass of the spin sample cell only.

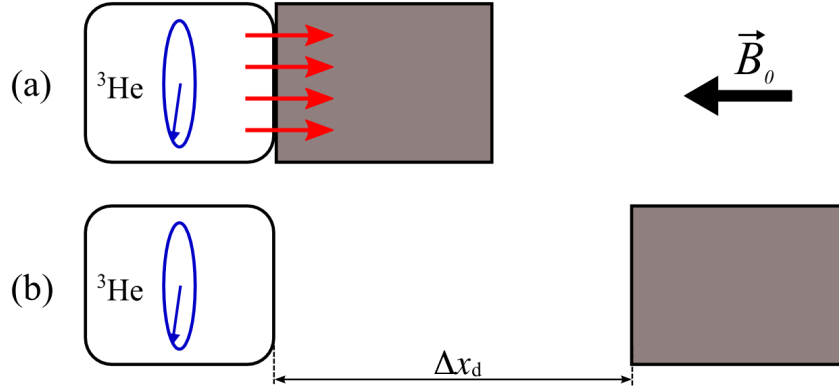


Figure 4.1: Scheme of experimental setup to determine tiny frequency shifts  $\Delta\nu_{\text{sp}}$  due to the spin-dependent short-range interaction. (a) The cylindrically shaped unpolarized mass (gray square) is placed in close position, i.e.  $\Delta x_c = 2.2\text{mm}$ , to the cylindrical spin sample cell. The cylinder axes are aligned along the direction of the magnetic guiding field  $\vec{B}_0$  (x-axis). The force  $\vec{F}_{\text{sp}} = -\vec{\nabla}V_{\text{sp}}(\vec{r})$ , which is caused by the spin-dependent short-range interaction between the polarized bound neutrons of the  $^3\text{He}$  atoms and the nucleons of the unpolarized sample, is indicated by the red arrows. (b) The cylindrically shaped unpolarized mass (gray square) is placed in distant position, i.e.  $\Delta x_d = 170\text{mm}$ , so that the spin-dependent short-range interaction can be considered to be negligible small.

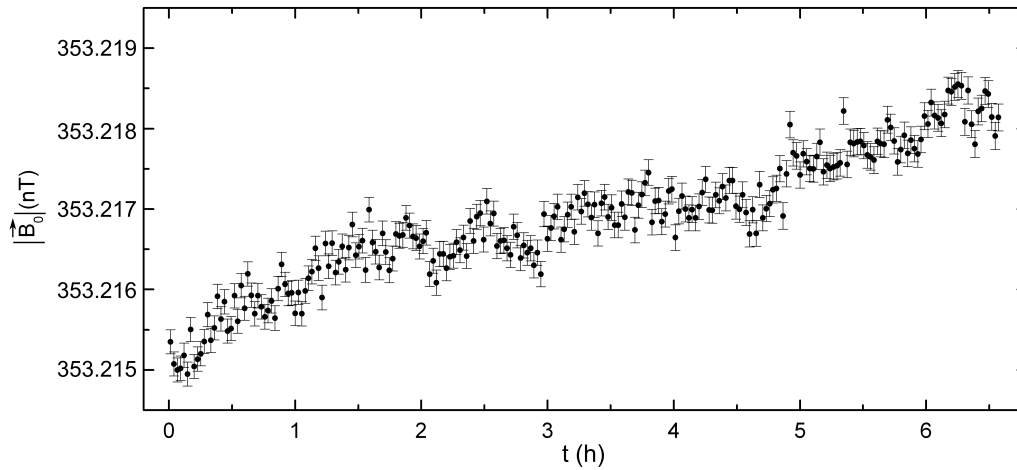


Figure 4.2: Drift of magnetic guiding field  $|\vec{B}_0|$  during measurement run C68. A linear drift of about  $1\text{pT/h}$  is visible that corresponds to a linear drift in frequency of about  $10^{-5}\text{Hz/h}$ .

additional frequency shift  $\Delta\nu_{\text{sp}}$  disappears. Then the spin precession frequency of  $^3\text{He}$  is given by

$$\omega_{\text{He,d}} = \gamma_{\text{He}} \cdot B_0. \quad (4.2)$$

Provided that the magnetic guiding field  $\vec{B}_0$  is constant in time, the frequency shift  $\Delta\nu_{\text{sp}}$  due to the spin-dependent short-range interaction can be calculated by the difference of the two measured spin precession frequencies of  $^3\text{He}$

$$\Delta\nu_{\text{sp}} = \frac{1}{2\pi} (\omega_{\text{He,c}} - \omega_{\text{He,d}}) = \frac{2V_{\Sigma,\text{He}}}{h}. \quad (4.3)$$

But as shown in Fig. 4.2 the magnetic guiding field shows a linear drift of about 1 pT/h which corresponds to a linear drift in frequency of about  $10^{-5}$  Hz/h. To get rid of these magnetic field drifts we use the  $^3\text{He}/^{129}\text{Xe}$  co-magnetometer, i.e. the cylindrical cell is filled with polarized  $^3\text{He}$  and polarized  $^{129}\text{Xe}$ . Then the influence of the magnetic guiding field  $\vec{B}_0$  (Zeeman-term with  $\omega_{\text{L},i} = |\gamma_i \cdot B_0|$  ( $i = \text{He}, \text{Xe}$ )) and its temporal fluctuations drop out in the weighted difference of the measured spin precession frequencies

$$\Delta\omega(t) = \omega_{\text{He}}(t) - \frac{\gamma_{\text{He}}}{\gamma_{\text{Xe}}} \cdot \omega_{\text{Xe}}(t). \quad (4.4)$$

So, the weighted frequency difference  $\Delta\omega(t)$  or its equivalent, the weighted phase difference  $\Delta\Phi(t) = \Phi_{\text{He}}(t) - \frac{\gamma_{\text{He}}}{\gamma_{\text{Xe}}} \cdot \Phi_{\text{Xe}}(t)$ , is sensitive to the pseudomagnetic frequency shift  $\Delta\nu_{\text{sp}}$  due to the spin-dependent short-range interaction. The frequency shift  $\Delta\nu_{\text{sp}}$  then can be extracted from respective frequency measurements in close and distant position by

$$\begin{aligned} \Delta\nu_{\text{sp}}^w &= \frac{1}{2\pi} \left( \omega_{\text{He,c}} - \omega_{\text{He,d}} - \frac{\gamma_{\text{He}}}{\gamma_{\text{Xe}}} (\omega_{\text{Xe,c}} - \omega_{\text{Xe,d}}) \right) \\ &= \frac{2V_{\Sigma}}{h} \cdot \left( 1 - \frac{\gamma_{\text{He}}}{\gamma_{\text{Xe}}} \right) \\ &= \Delta\nu_{\text{sp}} \cdot \left( 1 - \frac{\gamma_{\text{He}}}{\gamma_{\text{Xe}}} \right), \end{aligned} \quad (4.5)$$

where  $V_{\Sigma,\text{He}} = V_{\Sigma,\text{Xe}} = V_{\Sigma,\text{n}} \equiv V_{\Sigma}$  according to the Schmidt model [11]. If the refined nuclear shell model [89] is considered, Eq. 4.5 changes over to

$$\begin{aligned} \Delta\nu_{\text{sp}}^{w*} &= \frac{1}{2\pi} \left( \omega_{\text{He,c}} - \omega_{\text{He,d}} - \frac{\gamma_{\text{He}}}{\gamma_{\text{Xe}}} (\omega_{\text{Xe,c}} - \omega_{\text{Xe,d}}) \right) \\ &= \frac{2}{h} \cdot \left( V_{\Sigma,\text{He}} - \frac{\gamma_{\text{He}}}{\gamma_{\text{Xe}}} V_{\Sigma,\text{Xe}} \right) \\ &= \frac{2}{h} \cdot \left( \frac{1}{0.87} V_{\Sigma} - \frac{\gamma_{\text{He}}}{\gamma_{\text{Xe}}} \frac{1}{0.75} V_{\Sigma} \right) \\ &= \frac{2V_{\Sigma}}{h} \cdot \left( \frac{1}{0.87} V_{\Sigma} - \frac{\gamma_{\text{He}}}{\gamma_{\text{Xe}}} \frac{1}{0.75} V_{\Sigma} \right) \\ &= \Delta\nu_{\text{sp}} \cdot \left( \frac{1}{0.87} V_{\Sigma} - \frac{\gamma_{\text{He}}}{\gamma_{\text{Xe}}} \frac{1}{0.75} V_{\Sigma} \right). \end{aligned} \quad (4.6)$$

Since  $\gamma_{\text{He}}/\gamma_{\text{Xe}} = 2.75408159(20)$  [114, 115], the two nuclear shell models differ by a factor of 1.4, i.e.  $\Delta\nu_{\text{sp}}^{w*} = 1.4 \cdot \Delta\nu_{\text{sp}}^w$ .

For the determination of  $\Delta\nu_{\text{sp}}$ , a high sensitivity  $\sigma_\nu$  regarding the spin precession frequency of the polarized gas is needed. As will be described in Chap. 5, this can be achieved by spin precession signals with a high signal-to-noise ratio (SNR) and a long transverse relaxation time  $T_2^*$ :  $\sigma_\nu \propto 1/(\text{SNR} \cdot (T_2^*)^{3/2})$  (Eq. 5.3). In the motional narrowing regime, long  $T_2^*$  times can be achieved for a low magnetic guiding field  $|\vec{B}_0|$  with low absolute field gradients (Eq. 3.47 and Eq. 3.50). For absolute field gradients in the order of pT/cm,  $T_2^*$  times of several hours can be achieved. On the contrary, a high SNR, which is given by  $\text{SNR} = \bar{A}/N_\alpha$ , can be obtained for a high signal amplitude  $\bar{A}$  and a low signal noise  $N_\alpha$ . For signal amplitudes of about 10 pT, a SNR larger than 1000 : 1 can be realized with a signal noise in the order of fT/ $\sqrt{\text{Hz}}$ . To meet both conditions, i.e. field gradients in the order of pT/cm and a signal noise in the order of fT/ $\sqrt{\text{Hz}}$ , the experiments with the  $^3\text{He}/^{129}\text{Xe}$  co-magnetometer have to be performed in a magnetic shielding. The individual components of the experimental setup have to be optimized to obtain best possible sensitivity  $\sigma_\nu$ , which will be explained in detail in the following sections.

## 4.2 Experimental Realization

### 4.2.1 Measurement Cells

The preparation of the measurement cells is of high importance in order to get long  $T_1$  and therewith long  $T_2^*$  relaxation times (see Eq. 3.47). For our measurement cells we used GE-180 glass that in previous experiments showed the lowest wall relaxation rates [102, 103, 104]. The cells are cylindrical and have a length of  $L = 6$  cm and a diameter of  $\varnothing_L = 6$  cm (see Fig. 4.3). Both end planes of the cells were polished with diamond abrasive paper to keep the distance  $\Delta x$  between the polarized gas and the unpolarized matter sample small. After polishing the thickness  $d$  of the glass was measured with an ultra sonic distance sensor. The maximum value was  $d = 2.2$  mm. To get rid of ferromagnetic contaminations, the cells were cleaned with a two percent solution of Mucasol<sup>2</sup> and afterwards with distilled water. Then a stopcock was glued to the stem of the cell (see Fig. 4.3) so that the cell as a whole could be connected to a vacuum pumping station until the vacuum pressure reached less than  $10^{-7}$  mbar. After the cleaning and pumping process the cells were demagnetized. For this purpose, the cells were put into a strong oscillating magnetic field ( $\nu \approx 3$  Hz) with initial strength of about 0.2 T. The field amplitude was decreased linearly to zero which took about 20 minutes. This procedure demagnetizes possible ferromagnetic particles (e.g. magnetite particles of  $\mu\text{m}$  sizes) sitting on the inner surfaces of the glass cells which are in direct contact with the hyperpolarized noble gases [116].

Finally, the  $T_1$  relaxation times of the cells were measured. The measurements of the  $T_1$  times were made with polarized  $^3\text{He}$  only, since at that time the  $^{129}\text{Xe}$  polarizer was not yet ready at Mainz. Later it was figured out that long  $T_1$  times measured with  $^3\text{He}$  result in long  $T_1$  times of  $^{129}\text{Xe}$  as well. For the measurement of the  $T_1$  times we used an existing NMR setup [117]. The cells were filled with about 200 mbar of polarized  $^3\text{He}$  and kept in a magnetic

---

<sup>2</sup>Mucasol is a cleaning agent of the company Merz that contains surfactants and phosphates.



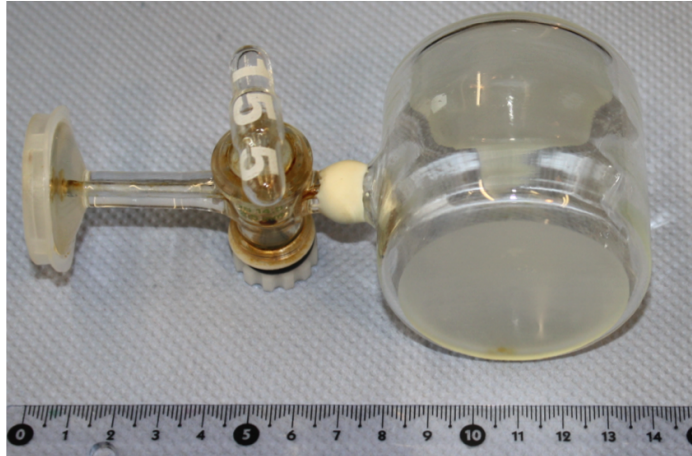


Figure 4.3: Cylindrical measurement cell made out of GE-180 glass.

guiding field of about 8 G. Every 15 minutes the spins were flipped by a small angle ( $\alpha < 3^\circ$ ) and the respective FID signal of the transverse magnetization was recorded. The amplitude of the FID signal, which is proportional to the polarization, was determined via a Fast Fourier Transform. By plotting the recorded data points one gets an amplitude-time diagram that shows exponential decay of the sample magnetization with the characteristic time constant  $T_1$ . By fitting an exponential function to the data, the  $T_1$  time could be determined. One measurement typically took some days, depending on the  $T_1$  time. If the measured relaxation times were too low, the cells were cleaned and demagnetized again, which then in some cases, led to a significant improvement of  $T_1$ . In total 4 cylindrical cells were measured that gave  $T_1$  times for  $^3\text{He}$  between 47 and 110 hours.

#### 4.2.2 Magnetically Shielded Room

The experiments with the  $^3\text{He}/^{129}\text{Xe}$  co-magnetometer were performed at the Physikalisch-Technische Bundesanstalt (PTB) in the *Berlin magnetically shielded room* (BMSR-2, [118]). In Fig. 4.4 a horizontal sectional view of the BMSR-2 is shown. It consists of a highly conductive eddy current cage made out of 10 mm aluminium. In the center of this cage there is a cubic room, the so-called measuring cabin, with an inner edge length of 2.9 m. This room is shielded by 7 layers of  $\mu$ -metal<sup>3</sup>. Additionally there are some coils between the  $\mu$ -metal shield and the aluminium cage with which Earth's field can be compensated. The passive shielding factor of this system exceeds  $10^8$  above 6 Hz. With additional active shielding the shielding factor is more than  $7 \cdot 10^6$  down to 0.01 Hz. The complete system sits in a building with 15 m cubic outer dimension and a two-story outbuilding with rooms for data acquisition and measurement preparation.

A sophisticated demagnetization procedure in BMSR-2 preserves a low residual magnetic field of  $|\vec{B}_{\text{res}}| < 1$  nT in the center of the innermost shield (0, 0, 0) and field gradients around the center of the measurement cell (0, 0, -6.6 cm) below 3.1 pT/cm. This residual

<sup>3</sup> $\mu$ -metal is a nickel-iron alloy with very high magnetic permeability.

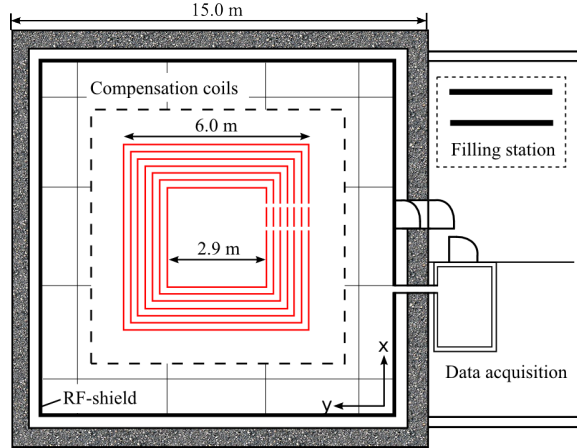


Figure 4.4: Horizontal cut view through building, shielded room and outbuilding where the data acquisition chamber and the filling station for the hyperpolarized gases is placed. The highly conductive eddy current cage (RF-shield) made out of 10 mm aluminium is indicated by the black solid square. The compensation coils are indicated by the black dashed square and the 7 layers of  $\mu$ -metal of the shielded room are colored in red.

field  $\vec{B}_{\text{res}}$  is superimposed by a magnetic guiding field  $\vec{B}_0 = B_0 \cdot \hat{e}_x$ , which serves as the quantization axis of the nuclear spins. The magnitude  $B_0$  of this magnetic guiding field has to compromise a good SNR as well as a long transverse relaxation time  $T_2^*$  to get a high sensitivity regarding the spin precession frequency: According to Eq. 3.47 and Eq. 3.50, the transverse relaxation time  $T_2^*$  depends on the square of the absolute field gradients. Hence, the smaller the magnetic guiding field, the smaller the absolute field gradients and thus a long  $T_2^*$  time can be achieved. On the contrary, the SNR depends on the white system noise of the BMSR-2, which is remarkable low and about  $3 \text{ fT}/\sqrt{\text{Hz}}$ . In the low-frequency region, i.e. for spin precession frequencies  $\nu = \omega/2\pi = \gamma B_0/2\pi < 10 \text{ Hz}$ , the signal noise is elevated, whereby the  $1/f$  limit is at 2 Hz [119] (see Fig. 6.1). That means, if the frequency  $\nu$ , respectively the magnetic guiding field  $B_0$ , decrease, the signal noise increases and hence the SNR is reduced. Thus, to meet a long transverse relaxation time  $T_2^*$  as well as a high SNR, optimum conditions for the magnitude of the magnetic guiding field are given for a magnetic field of about  $1 \mu\text{T}$  ( $\nu_{\text{He},\text{Xe}} \approx 10 \text{ Hz}$ ).

### 4.2.3 SQUID System and Magnetic Field

For the detection of the spin precession signals a SQUID<sup>4</sup> vector magnetometer system was used (Fig. 4.5). The SQUID sensors measure the change of a magnetic field perpendicular to their flat pickup loop and have an unknown DC offset in their output signal. The SQUID

<sup>4</sup>A SQUID (Superconducting Quantum Interference Device) is a highly-sensitive magnetic flux detector based on superconducting loops containing Josephson junctions. A more detailed description of these particular SQUIDs can be found in [96].

vector magnetometer system consists of 304 SQUIDs which are housed in a liquid-helium dewar that is permanently attached to the ceiling of the BMSR-2. The dewar has a flat bottom and an inner diameter of 250 mm. The SQUIDs are divided up into 19 identical modules and arranged in such a way that x-, y- and z-components of the magnetic field can be measured.

Inside the shielded room two square coil pairs ( $B_x$ - and  $B_y$ -coil) of edge length 180 cm and 175 cm respectively and distance 97 cm and 94 cm respectively, were mounted perpendicular to each other (see Fig. 4.5). Each coil pair (with 20 windings per coil) provides a homogeneous magnetic field of around  $0.35 \mu\text{T}$  at a current of 17.5 mA, which was provided by a low noise current source<sup>5</sup>. The use of two coil pairs was chosen in order to manipulate the sample spins. For example, a “ $\pi/2$ -pulse” of the magnetic moment of a nuclear spin polarized gas can be realized by non-adiabatic change of the magnetic field, i.e.  $\Omega_{\text{rot}}/\omega_{\text{L}} \gg 1$  (see Chap. 3.3). This way, nuclear spin precession in the  $yz$ -plane (changing from  $\vec{B}_y$  to  $\vec{B}_x$ ) could be monitored.

To achieve a good homogeneity of the magnetic guiding field a simulation of the magnetic field was done by C. Gemmel [96]. For this simulation, only the inner  $\mu$ -metal layer of the shielded room was considered. The center of the spin sample cell was positioned at (0, 0, -6.6 cm), where the coordinate origin (0, 0, 0) corresponds to the center of the shielding. For symmetry reasons it would have been better to center the cell in the  $z$ -direction, but this was not possible in the experiment due to the dimensions of the dewar which was already shifted up to its highest position. The tensor components  $\partial B_{x,y,z}/\partial(x,y,z)$  of the gradients of the simulated magnetic field ( $B_{\text{sim}} \approx 0.35 \mu\text{T}$ ) were calculated within a cubic volume of  $(10 \times 10 \times 10) \text{ cm}^3$  around the center of the spin sample cell. Here the  $z$ -position of the center of the  $B_x$ -coils was varied to find best field homogeneity. For the position (0, 0, -2 cm) of the center of the  $B_x$ -coils all components  $\partial B_{x,y,z}/\partial(x,y,z)$  of the gradients of the simulated magnetic field were below 4 pT/cm.

The measurement of the tensor components of the gradients  $\partial B_{x,y,z}/\partial(x,y,z)$  with and without the magnetic guiding field in the vicinity of the spin sample cell were operated by means of the SQUID magnetometer system. Thus, at least three SQUIDs with orthogonal pickup loops are needed to evaluate the nine tensor components of the magnetic field gradient. The SQUID magnetometer system and thus the dewar as a whole had to be moved to preset positions forming a grid in 3D-space around the sample position. The gradient was calculated from the measured relative field difference of every single SQUID. The main uncertainty in the determination of the gradient components is the incorrect alignment of the dewar and the fact that in presence of a magnetic guiding field ( $|\vec{B}_x| \neq 0$ ) this misalignment has a strong influence mainly on the extraction of the transverse components of the field gradient. Furthermore, former measurements showed that the dewar can be slightly magnetized and thus produces additional magnetic field gradients. Since the SQUID magnetometer system is moved together with the dewar, these gradients are not included in the measurements of the tensor components of the field gradient. Hence, before the measuring period started

<sup>5</sup>The current source was produced by “Magnicon” as part of the “SEL-1 SQUID Electronics”.

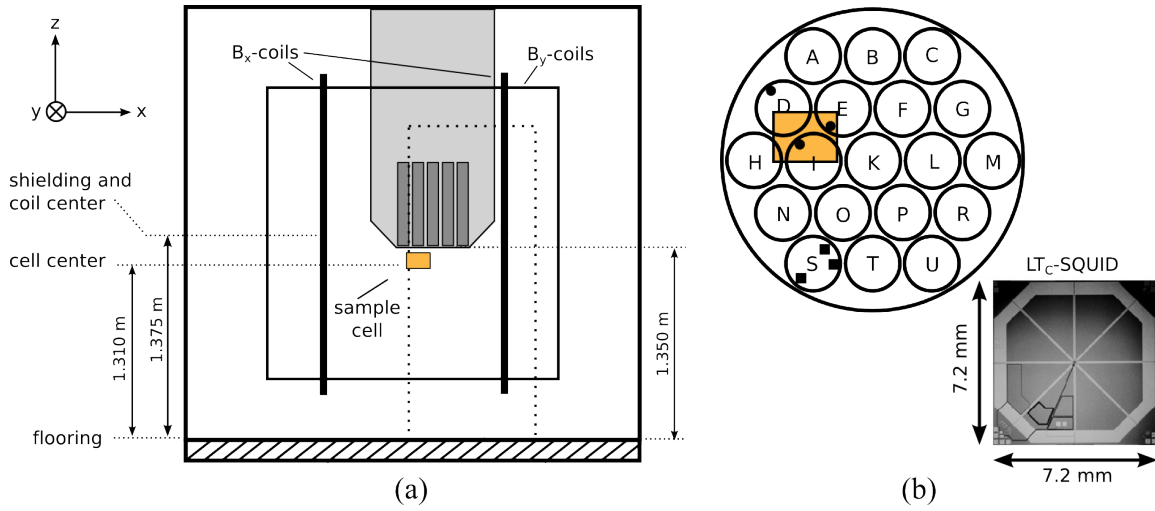


Figure 4.5: (a) Vertical cut view through innermost shield of the BMSR-2 seen from the door opening. The outer rectangle shows the inner shielding layer. The striped area on the bottom shows the flooring, which enables walking within the shielded room without damaging the  $\mu$ -metal. The smaller black squares and the two thick black lines indicate the  $B_x$ - and  $B_y$ -coil pairs. The pneumatically driven sliding doors are indicated by dashed lines. The light gray area is the dewar and the dark gray bars indicate the individual modules housing the low- $T_c$  DC-SQUID magnetometers in different orientations and positions. The cylindrical spin sample cell ( $D = 60$  mm,  $\odot_D = 58$  mm) is denoted by the orange square. Its center has an average distance of  $\bar{z} = 66$  mm to the sensors. The fixation of the spin sample cell is not shown. (b) Horizontal cut view through the dewar. The 304 SQUID sensors are divided up into 19 identical modules (A-U). The lower plane SQUIDs in module D, E, and I marked as (●) are used to detect the free  $^3\text{He}/^{129}\text{Xe}$  spin precession. SQUIDs in module S marked as (■) are used for the gradiometric sensor arrangements. The photograph in the right corner shows a low- $T_c$  DC-SQUID magnetometer which is operated inside the BMSR-2 (photograph taken from [119]). The relative position of the spin sample cell in  $xy$ -plane projection again is indicated by an orange square.

Measured field gradients without magnetic guiding field								
$\frac{\partial B_{1,x}}{\partial x}$	$\frac{\partial B_{1,x}}{\partial y}$	$\frac{\partial B_{1,x}}{\partial z}$	$\frac{\partial B_{1,y}}{\partial x}$	$\frac{\partial B_{1,y}}{\partial y}$	$\frac{\partial B_{1,y}}{\partial z}$	$\frac{\partial B_{1,z}}{\partial x}$	$\frac{\partial B_{1,z}}{\partial y}$	$\frac{\partial B_{1,z}}{\partial z}$
$-0.6 \frac{\text{pT}}{\text{cm}}$	$-2.5 \frac{\text{pT}}{\text{cm}}$	$-1.2 \frac{\text{pT}}{\text{cm}}$	$-1.5 \frac{\text{pT}}{\text{cm}}$	$-2.6 \frac{\text{pT}}{\text{cm}}$	$0.6 \frac{\text{pT}}{\text{cm}}$	$-1.2 \frac{\text{pT}}{\text{cm}}$	$0.3 \frac{\text{pT}}{\text{cm}}$	$2.2 \frac{\text{pT}}{\text{cm}}$
$ \vec{\nabla} B_{1,x}  = (2.8 \pm 1.0) \frac{\text{pT}}{\text{cm}}$			$ \vec{\nabla} B_{1,y}  = (3.1 \pm 1.6) \frac{\text{pT}}{\text{cm}}$			$ \vec{\nabla} B_{1,z}  = (2.5 \pm 1.7) \frac{\text{pT}}{\text{cm}}$		
Measured field gradients with magnetic guiding field								
$\frac{\partial B_{1,x}}{\partial x}$	$\frac{\partial B_{1,x}}{\partial y}$	$\frac{\partial B_{1,x}}{\partial z}$	$\frac{\partial B_{1,y}}{\partial x}$	$\frac{\partial B_{1,y}}{\partial y}$	$\frac{\partial B_{1,y}}{\partial z}$	$\frac{\partial B_{1,z}}{\partial x}$	$\frac{\partial B_{1,z}}{\partial y}$	$\frac{\partial B_{1,z}}{\partial z}$
$-0.5 \frac{\text{pT}}{\text{cm}}$	$-0.8 \frac{\text{pT}}{\text{cm}}$	$-8.0 \frac{\text{pT}}{\text{cm}}$	$-7.3 \frac{\text{pT}}{\text{cm}}$	$-10.3 \frac{\text{pT}}{\text{cm}}$	$16.8 \frac{\text{pT}}{\text{cm}}$	$27.0 \frac{\text{pT}}{\text{cm}}$	$2.5 \frac{\text{pT}}{\text{cm}}$	$2.5 \frac{\text{pT}}{\text{cm}}$
$ \vec{\nabla} B_{1,x}  = (8.1 \pm 3.8) \frac{\text{pT}}{\text{cm}}$			$ \vec{\nabla} B_{1,y}  = (21.0 \pm 33.2) \frac{\text{pT}}{\text{cm}}$			$ \vec{\nabla} B_{1,z}  = (27.2 \pm 2.9) \frac{\text{pT}}{\text{cm}}$		

Table 4.1: Measured field gradients with and without the magnetic guiding field ( $|\vec{B}_x| = 0.35 \mu\text{T}$ ) inside BMSR-2. The errors of the measured values are not known.

several positions in the xy-plane were tested on  $T_2^*$ . The position with highest  $T_2^*$  was chosen as measurement position. In addition, to minimize the gradients of the residual field the shielded room as a whole was degaussed before the measuring period started.

The measured absolute values of the gradient components with and without magnetic guiding field  $B_0 = 0.35 \mu\text{T}$  are summarized in Tab. 4.1. The measured gradients with magnetic guiding field are much higher than the simulated ones. This can have different reasons:

- An incorrect alignment and spacing of the coils can lead to additional field gradients.
- Deviations of the wire windings of the  $B_x$ -coils from the exact quadratic course, for example as a result of deflection of the coil frame, can cause additional field gradients.
- In z-direction the field gradients are bigger than in x- and y-direction. This may be related with the special suspension of the dewar which might produce additional field gradients in z-direction.
- Experience of former measurements showed that the real magnetic field gradients do not correspond to the simulated ones. That is why for symmetry reasons the center of the  $B_x$ -coils was placed in the center of the shielding (0, 0, 0). So, the center of the  $B_x$ -coils in the simulation and in the experimental setup is shifted by 2 cm and thus the simulated and real field gradients may differ.
- The field gradients measured by the SQUID magnetometer system can be split in two fractions: the field gradients of the residual field of the BMSR-2 and the field gradients of the magnetic guiding field  $B_0 = 0.35 \mu\text{T}$ . Since the simulated field gradients do not include the gradients of the residual field, simulated and measured field gradients may differ.

#### 4.2.4 Filling System

The measurement cells have to be filled with nuclear spin polarized  $^3\text{He}$  and  $^{129}\text{Xe}$ , where the pressures  $p_{\text{He,Xe}}$  have to compromise a good SNR as well as a long transverse relaxation time  $T_2^*$  to obtain a high sensitivity regarding the spin precession frequency: According to Eq. 3.47 and Eq. 3.50, the transverse relaxation time  $T_2^*$  is indirect proportional to the pressure  $p$  of the polarized gas. Consequently, the pressure  $p$  should be as low as possible to achieve a long  $T_2^*$  time. On the contrary, the SNR is proportional to the pressure  $p$  ( $\text{SNR} = \bar{A}/N_\alpha \propto p$  (Eq. 3.29)). That means, if the pressure  $p$  decreases, the signal amplitude decreases and hence the SNR is reduced. Thus, to meet a long transverse relaxation time  $T_2^*$  as well as a high SNR, optimum conditions are given for pressures of the polarized gases,  $^3\text{He}$  and  $^{129}\text{Xe}$ , in the order of mbar. Additionally  $\text{N}_2$ , with  $p_{\text{N}_2} \gg p_{\text{Xe}}$ , was needed as buffer gas to suppress the van-der-Waals relaxation of  $^{129}\text{Xe}$  (see Chap. 3.5). An in situ polarization of the gases was not possible. Hence, as a first step  $^3\text{He}$  and  $^{129}\text{Xe}$  have to be polarized separately and then they are mixed together with  $\text{N}_2$  in a specially designed filling station (Fig. 4.4 and Fig. 4.6). The  $^3\text{He}$  gas was polarized at the Mainz polarizer. From there it was transported to the PTB in Berlin in low-relaxation storage vessels. Due to the long wall relaxation times  $T_{1,\text{stor}}$  of typically 200 hours and the use of magnetized transportation boxes, which provided a homogeneous field during transport [120], the loss of polarization from Mainz to the PTB was small. After arrival the storage vessel was transferred to the homogenous magnetic field of the filling station. The polarized  $^3\text{He}$  was delivered at pressures of about 2 bar in a volume of about  $1200 \text{ cm}^3$  and could be used over a period of about three days. The  $^{129}\text{Xe}$  gas was polarized at the PTB polarizer, since short transfer distances were needed due to the shorter total longitudinal relaxation time  $T_1$  of the  $^{129}\text{Xe}$  gas compared to the  $^3\text{He}$  gas. Hence, the polarized  $^{129}\text{Xe}$  could be used only for one measurement run and had to be polarized directly before each measurement run. The transport coil, which will be explained in the next section, was used to bring the  $^{129}\text{Xe}$  storage vessel to the experiment. The polarized  $^{129}\text{Xe}$  was delivered at pressures of about 1 bar in a volume of about  $270 \text{ cm}^3$ .

The filling of the gases  $^3\text{He}$ ,  $^{129}\text{Xe}$  and  $\text{N}_2$  into the measurement cell was done within the filling station which is shown in Fig. 4.6: By means of a pair of Helmholtz coils with a diameter of 140 cm and a field strength of  $B_0 \approx 8.5 \text{ G}$  at 5 A a homogenous magnetic field was produced to maintain the polarization of  $^3\text{He}$  and  $^{129}\text{Xe}$ . The relative field gradient components  $\frac{dB_0/dx}{B_0} = \frac{dB_0/dy}{B_0}$  and  $\frac{dB_0/dz}{B_0}$  have been measured to be  $\approx 10^{-4} \frac{1}{\text{cm}}$  [117]. With these values and the typical storage vessel pressures of  $p_{\text{stor}}^{\text{He}} \approx 2 \text{ bar}$  and  $p_{\text{stor}}^{\text{Xe}} \approx 1 \text{ bar}$  the gradient relaxation times  $T_{1,\text{grad}}$  for  $^3\text{He}$  and  $^{129}\text{Xe}$  can be calculated by using Eq. 3.34. This results in  $T_{1,\text{grad}}^{\text{He}} = 5609 \text{ h}$  and  $T_{1,\text{grad}}^{\text{Xe}} = 80120 \text{ h}$ . Hence the gradient relaxation of the gases within the filling station can be neglected. The mixing of the gases was realized with a specially designed filling system which was made out of glass. It was described in detail in [121] and is shown in Fig. 4.6. The measurement cell is connected by flange F1 to the filling system and the three storage vessels respectively filled with polarized  $^3\text{He}$ , polarized  $^{129}\text{Xe}$  and  $\text{N}_2$  are connected by the flanges F2-F4 to the filling system. Flange F5 on the upper right side in Fig. 4.6 is connected to a vacuum pumping system. For evacuation of

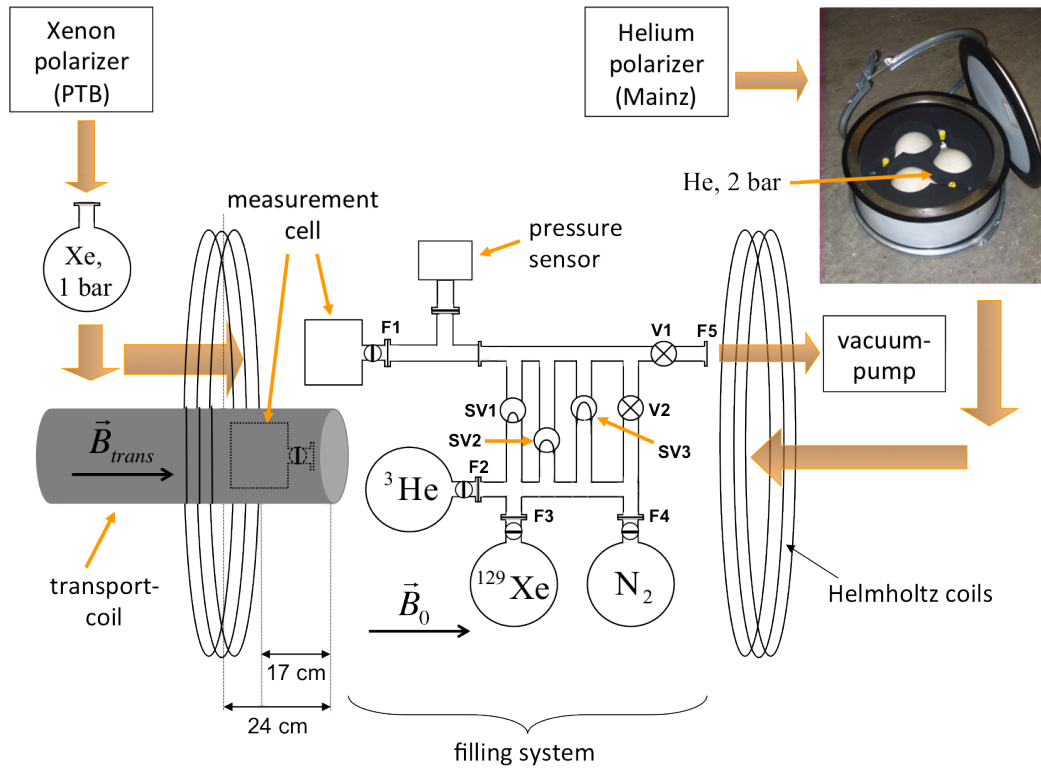


Figure 4.6: Scheme of the gas filling station (not true to scale):  $^3\text{He}$  is polarized in Mainz and then filled into a storage vessel that is transported with magnetized transport boxes to the PTB in Berlin.  $^{129}\text{Xe}$  is polarized at the PTB polarizer and filled into a storage vessel that is carried with the transport coil to the experiment. Both storage vessels have to be placed in the filling station. The filling system made out of glass has three sluce valves in the middle (SV1, SV2 and SV3) with which different gas quantities can be filled into the measurement cell. Additionally  $\text{N}_2$  is used as buffer gas to suppress van der Waals relaxation. The whole filling system sits in a homogeneous magnetic guiding field  $\vec{B}_0$  that is produced by two Helmholtz coils.

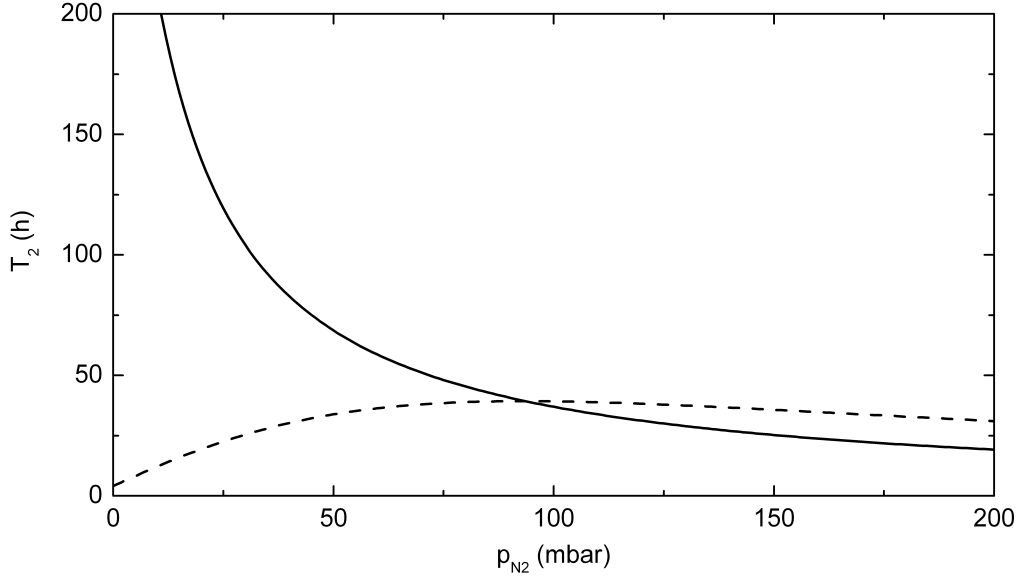


Figure 4.7: Calculated transverse spin relaxation times  $T_2 = \left( \frac{1}{T_{2,\text{grad}}} + \frac{1}{T_{1,\text{vdW}}} \right)^{-1}$  for  $^3\text{He}$  and  $^{129}\text{Xe}$  due to diffusion in magnetic field gradients and due to van der Waals relaxation as a function of the buffer gas pressure  $p_{\text{N}_2}$  in a gas mixture of  $^3\text{He}$ ,  $^{129}\text{Xe}$  and  $\text{N}_2$ . Here the measured field gradients given in Tab. 4.1 and the pressures  $p_{\text{He}} = 2.5$  mbar (solid line) and  $p_{\text{Xe}} = 5.0$  mbar (dashed line) were used.

the whole gas manipulation system, the valves V1 and V2 have to be opened. During the filling process these valves are closed. The valves in the middle (SV1-SV3) serve to fill small amounts of gas from the storage vessel to the measurement cell. These valves are also called sluice valves since they work similar to a sluice, i.e. gas from the storage vessel is absorbed in the small volume of the sluice ( $V_{\text{SV}} < 1 \text{ cm}^3$ ) and after rotation of the valve by  $180^\circ$ , the gas in the volume of the sluice is expanded into the measurement cell. For example, for filling of 5 mbar  $^{129}\text{Xe}$  from the storage vessel ( $p_{\text{Xe}} \approx 1$  bar) to the measurement cell, valve SV2 has to be turned five times. The volume of the sluice differs from valve to valve so that the desired gas quantity of either  $^3\text{He}$ ,  $^{129}\text{Xe}$  or  $\text{N}_2$  can be filled into the measurement cell. With the pressure sensor the total pressure in the measurement cell can be determined.

In the experiments with the  $^3\text{He}/^{129}\text{Xe}$  co-magnetometer the measurement sensitivity is derived from the weighted frequency difference (Eq. 4.4). Consequently an optimum of the pressures of  $^3\text{He}$  as well as for  $^{129}\text{Xe}$  and  $\text{N}_2$  is needed.  $^{129}\text{Xe}$  has the drawback to have a smaller polarization plus a smaller gyromagnetic ratio ( $\gamma_{\text{He}}/\gamma_{\text{Xe}} \approx 2.75$ ) than  $^3\text{He}$ . Hence, the signal of  $^{129}\text{Xe}$  is smaller compared to the  $^3\text{He}$  signal. So, to obtain comparable signals the pressure of  $^{129}\text{Xe}$  has to be higher than the pressure of  $^3\text{He}$ . If the buffer gas  $\text{N}_2$  is included, the total pressure of the gas mixture increases. For the measured field gradients given in Tab. 4.1 optimal conditions are given for pressures of  $p_{\text{He}} = 2.5$  mbar and  $p_{\text{Xe}} = 5.0$  mbar. In Fig. 4.7 the resulting theoretical dependence of  $T_2$  with  $\frac{1}{T_2} = \frac{1}{T_{2,\text{grad}}} + \frac{1}{T_{1,\text{vdW}}}$  is plotted as



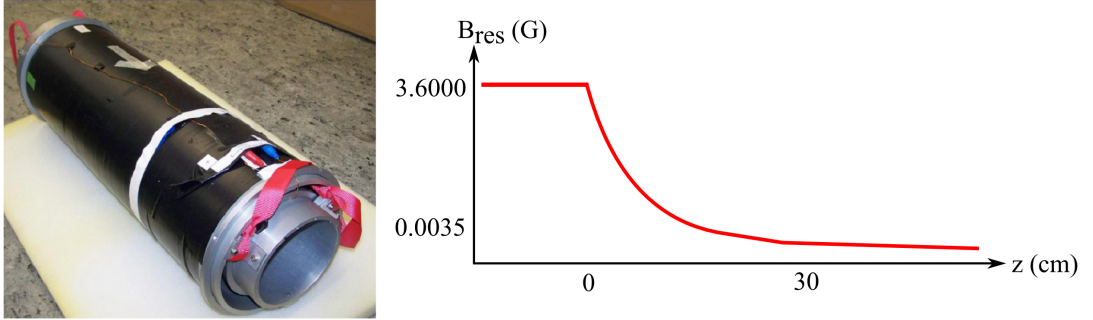


Figure 4.8: Transport coil for the transfer of polarized gas from the filling station into the  $\mu$ -metal shielded room (BMSR-2). *left*: Photograph of the double solenoid transport coil without switch. *right*: Measured development of the magnetic field  $B_{\text{res}}$  along the axis of the two solenoids. Thereby  $z = 0$  cm corresponds to the fringe of the solenoids.

a function of the  $\text{N}_2$  buffer gas pressure in a gas mixture at fixed  $^3\text{He}$  and  $^{129}\text{Xe}$  pressures. For  $^3\text{He}$ , the formation of van der Waals molecules can be neglected, i.e.  $1/T_{1,\text{vdW}}^{\text{He}} = 0$ . Then  $T_{2,\text{He}}$  of helium is equal to the gradient relaxation time  $T_{2,\text{grad}}^{\text{He}}$  which decreases with increasing  $\text{N}_2$  pressure. In case of  $^{129}\text{Xe}$ , for small  $\text{N}_2$  pressures the van der Waals relaxation and for high  $\text{N}_2$  pressures the gradient relaxation is dominant. Hence,  $T_{2,\text{Xe}}$  features a maximum for  $\text{N}_2$  pressures between 80 and 110 mbar.

According to the previous considerations, for the long-term measurements with the  $^3\text{He}/^{129}\text{Xe}$  co-magnetometer pressures of about 2.5 mbar for  $^3\text{He}$ , 5.0 mbar for  $^{129}\text{Xe}$  and about 25 mbar for  $\text{N}_2$  were used. If the relaxation due to binary collisions  $T_{1,\text{bin}}$  and the wall relaxation  $T_{1,\text{wall}}$  (see Chap. 3.5) are included, the transverse relaxation time for  $^3\text{He}$  and  $^{129}\text{Xe}$  for cylindrical cells then can be estimated to be  $T_{2,\text{He}}^* \approx 54$  h and  $T_{2,\text{Xe}}^* \approx 6$  h respectively. For the wall relaxation  $T_{1,\text{wall}}$ , the measured values of 100 h for helium and 8 h for xenon<sup>6</sup> were used.

#### 4.2.5 Transport Coil

For transport of the measurement cell from the filling system to the shielded room as well as for the transport of the  $^{129}\text{Xe}$  storage vessel from the polarizer lab of the PTB to the filling system, a specially designed transport coil was used (see Fig. 4.8). It consists of two nested solenoids of lengths  $L = 60$  cm. The magnetic moments of the inner (i) and the outer (o) solenoid have the same absolute values, i.e.  $M_o = n_o I_o A_o = n_i I_i A_i = -M_i$ . Thereby  $n$  is the

<sup>6</sup>The wall relaxation time  $T_{1,\text{wall}}$  of the cylindrical measurement cells could not be measured for  $^{129}\text{Xe}$ . Hence, for estimation of the transverse relaxation time  $T_2^*$  the wall relaxation time of spherical measurement cells with a diameter of 6 cm was used. The wall relaxation time of the spherical cells was measured to be  $T_{1,\text{wall}} = 8$  h. These spherical cells were used in some former measurements to search for a sidereal modulation in the weighted frequency difference of  $^3\text{He}$  and  $^{129}\text{Xe}$ , which violates Lorentz symmetry [122].

number of windings,  $I$  is the current and  $A$  the cross-sectional area of the coils. With the chosen values  $n_o = n_i/2$ ,  $I_o = -I_i$  and  $A_o = 2 A_i$ , the resulting homogenous field inside the coil has a field strength of  $B_{res} = B_i + B_o = \mu_0 (n_i/2) I_i/L$ . The voltage is provided by two 6 V batteries connected in series, leading to a homogenous magnetic field of about 3 G along the coil axis. The axial stray field at the fringe of the transport coil drops proportional to  $1/z^5$ . Thus, the fringe field reaches the 350 nT level already at a distance of about 30 cm from the solenoid (Fig. 4.8). This avoids magnetization of the inner  $\mu$ -metal walls while entering the shielded room so that the field gradients do not change too much from one measurement run to another.

The transport coil has a specially designed switch for turning on and off, which slowly ramp down, respectively, up the current in the coil, so that the field change happens adiabatically according to Eq. 3.22. Hence the spins follow the direction of the magnetic field, so that spin flips during the switching process are avoided. The up- and down-ramping of the current happens with the same time constant of about 7 s. As magnetic field zero crossings may also cause spin flips, it is very important that the transport coil is inserted into the coils of the filling station, respectively into the coils inside the shielded room, in such a way that the magnetic field lines always point into the same direction.

At the ends of the transport coil high field inhomogeneities and thus high field gradients occur. To prevent polarization losses due to this additional field gradients, it is preferable to put the measurement cell filled with the gas mixture of polarized  $^3\text{He}$ ,  $^{129}\text{Xe}$  and  $\text{N}_2$  into or out of the transport coil when the magnetic field of the coils is switched off. For the transfer of the measurement cell from the filling station into the transport coil, the transport coil is held into the Helmholtz coils of the filling station, where both coils overlap in a region of about 24 cm. Thus, the magnetic guiding field for the polarized gases is provided by the Helmholtz coils of the filling station. Then the measurement cell is placed into the transport coil about 17 cm away from the edge of the Helmholtz coils, thus in a region where the field of the Helmholtz coils is still quite homogeneous. Following, the magnetic field of the transport coil is switched on and after about 10 seconds, when the magnetic field is ramped up to its maximum, the transport coil is carried into the shielded room, where the  $B_y$ -field ( $\approx 0.35 \mu\text{T}$ ) is switched on (see Fig. 4.5). In the shielded room the transport coil is put onto a wooden support. Then the magnetic field of the transport coil is switched off. After about 10 seconds, when the magnetic field of the transport coil is ramped down, the measurement cell can be taken out. Here the position of the transport coil, respectively of the measurement cell, is in a region where the homogeneity of the  $B_y$ -field is still quite good. That means, after the magnetic field of the transport coil is switched off, the magnetic guiding field for the polarized gases is provided by the  $B_y$ -field.

#### 4.2.6 BGO Crystal and Suspension Mechanism

As unpolarized matter we used a cylindrical BGO crystal ( $\text{Bi}_4\text{Ge}_3\text{O}_{12}$ ) that has a length of 7 cm and a diameter of 6 cm. It is characterized by a density of  $\rho = 7.13 \text{g/cm}^3$  and therefore has a high nucleon number density. It is a non-conductive material that shows low electronic

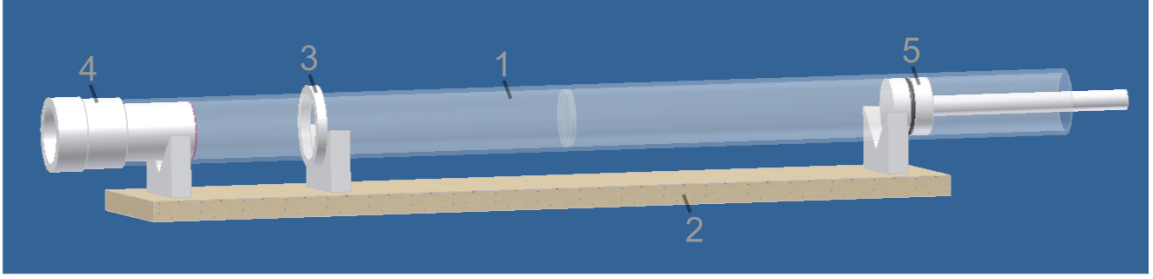


Figure 4.9: Suspension of BGO crystal. (1) Glass tube with glass disc acting as partition wall for the movement in forward direction, i.e. towards close position of the BGO crystal. (2) Wooden plate with V-shaped profiles in which the glass tube can slide forth and back. (3) Tension ring acting as mechanical stopper which prevents that the glass tube slides out of the V-profiles and guarantees a movement of 17 cm which corresponds to the distance of the two front V-profiles. (4) Holder of BGO crystal. (5) Piston with bore along its axis which can be either connected to a vacuum pump (backward movement) or to a compressed air system (forward movement).

noise (Johnson-Nyquist noise) and is said to have an unusual magnetism-related behaviour in weak constant magnetic fields ( $\chi_{\text{mag}} \approx 0$  ppm) as direct and indirect measurements suggest [123, 124, 125]. Thus only a small influence of its residual magnetic susceptibility on the  $^3\text{He}$  and  $^{129}\text{Xe}$  spin precession is expected when the BGO crystal is in close position to the measurement cell. In close position the distance  $\Delta x_c$  between the polarized gases and the front side of the BGO crystal is essentially given by the thickness  $d$  of the glass window of the measurement cell, i.e.  $\Delta x_c = d = 2.2$  mm (see Sec. 4.2.1).

For moving the BGO crystal from close to distant position, or vice versa, a specially designed suspension mechanism was build (Fig. 4.9). It consists of a cylindrical glass tube of 60 cm length which can be moved horizontally along a holder made of V-shaped profiles which are fixed on a massive wooden plate. By means of a tension ring around the glass tube, which works as a stopper, a movement of 17 cm (back and forth) was possible.

The BGO crystal is put in a special holder which is installed at one open end of the glass tube. At the other end of the glass tube a piston with bore along its axis was installed. This piston can be connected via a tube with a vacuum pump or a compressed air system, which are outside of the shielded room. Hence, the forward (compressed air system) and backward (vacuum pump) movement of the BGO crystal to close and distant position can be performed without opening the doors of the BMSR-2. To prevent that the BGO crystal pops out of the glass tube when compressed air is applied for forward motion (close position), the used glass tube had two equal volumes that are separated by a glass disc. The whole construction is placed on a heavy and stable table made out of wood to prevent that mechanical vibrations occur when the BGO crystal is moved.

The spin-dependent short-range potential is given by  $V_{\text{sp}}(\vec{r}) \propto \vec{\sigma} \cdot \vec{r} \propto \vec{B}_0 \cdot \vec{r}$ . Thus, in

order to measure a maximum frequency shift  $\Delta\nu_{\text{sp}}$ , the cylinder axes of the measurement cell and of the BGO crystal have to be aligned along the direction of the magnetic guiding field  $\vec{B}_0$  (x-direction). If the cylinder axes of the measurement cell and of the BGO crystal are aligned perpendicular to the magnetic guiding field, the frequency shift  $\Delta\nu_{\text{sp}}$  due to the spin-dependent short-range interaction would vanish.

### 4.2.7 Measurement Procedure

First of all the cylindrical measurement cell is filled with a gas mixture of polarized  $^3\text{He}$ ,  $^{129}\text{Xe}$  and  $\text{N}_2$  within the filling station. The transfer procedure of the measurement cell from the filling station into the shielded room was already described before. After switching off the magnetic field of the transport coil the measurement cell is taken out and placed in a special holder below the dewar. Then the BGO crystal is positioned close to the cell ( $\Delta x_c = 2.2$  cm) or distant from the cell ( $\Delta x_d = 17$  cm). Afterwards the door of the shielded room is closed. The spin precession of the polarized  $^3\text{He}$  and  $^{129}\text{Xe}$  is actuated by a non-adiabatic change of the magnetic field as described in Chap. 3.3. The spin precession signals were measured by three different SQUID gradiometers (see Fig. 4.5). For each measurement run the BGO crystal was moved after  $t_0 \approx 3$  h from close to distant position (c $\rightarrow$ d) or vice versa (d $\rightarrow$ c).

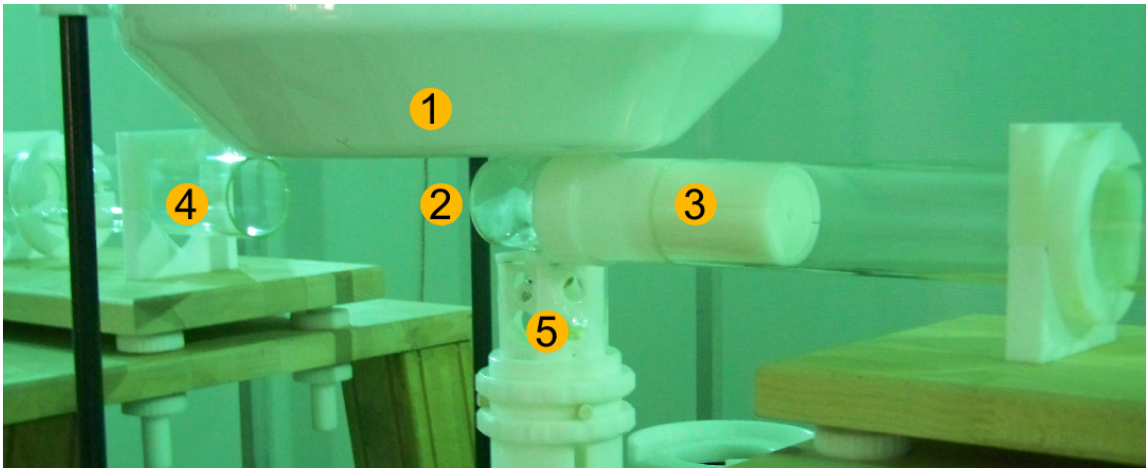
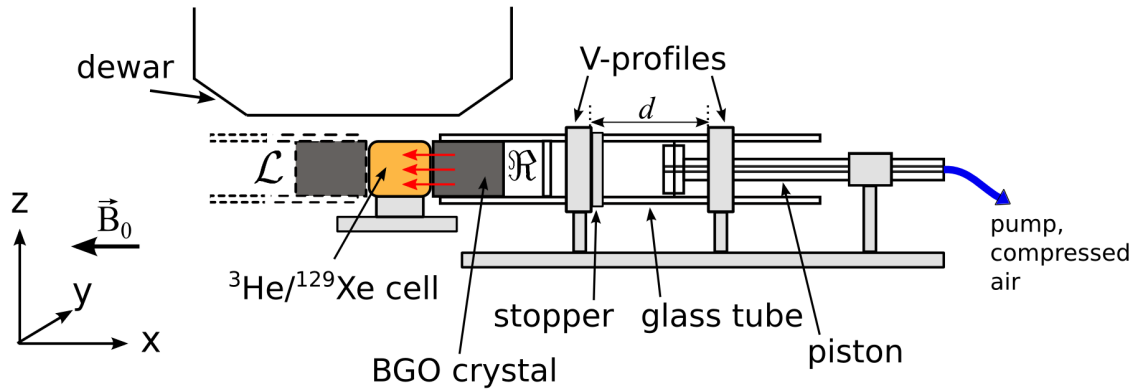


Figure 4.10: Experimental Setup. *Top*: Sketch of experimental setup. The unpolarized mass (cylindrical BGO crystal:  $d = 70$  mm,  $\varnothing_d = 60$  mm) can be moved along the  $x$ -axis ( $\vec{B}_0$ -field axis) to close ( $\Delta x_c = 2.2$  mm) and distant ( $\Delta x_d = d = 170$  mm) position and vice versa. This is accomplished by a piston driven glass tube with the BGO fixed at its cell facing side. The two arrangements right ( $\mathfrak{R}$ ) and left ( $\mathfrak{L}$ ) of the BGO crystal were used. *Bottom*: Real experimental setup. (1) Dewar. (2) Cylindrical measurement cell. (3) Holder and suspension mechanism of the BGO crystal. (4) Suspension mechanism of the BGO crystal in case that the BGO crystal is installed to the left side of the measurement cell. (5) Holder of the measurement cell.



## 5 $^3\text{He}/^{129}\text{Xe}$ Co-Magnetometer

In this chapter our very sensitive low-field co-magnetometer, which is based on the detection of free spin precession of gaseous, nuclear polarized  $^3\text{He}$  and  $^{129}\text{Xe}$  samples with a SQUID as magnetic flux detector, is characterized. In order to provide a more thorough understanding of the advantages of this  $^3\text{He}/^{129}\text{Xe}$  co-magnetometer, first of all a magnetometer based on the spin precession of pure nuclear spin polarized  $^3\text{He}$  is considered.

For the first time in 1969 Cohen-Tannoudji et al. [126] build up a  $^3\text{He}$ -magnetometer based on the detection of spin precession of gaseous, nuclear spin polarized  $^3\text{He}$ . For non-destructive detection of the  $^3\text{He}$  spin precession in a low magnetic guiding field, an optically pumped  $^{87}\text{Rb}$ -magnetometer was used. Here a sensitivity of about  $100 \text{ fT}/\sqrt{\text{Hz}}$  and a transverse relaxation time  $T_{2,\text{He}}^*$  of 140 min were reached. In the meantime a lot of improvements have been made on the parameters which determine the measurement sensitivity of such a free spin precession  $^3\text{He}$ -magnetometer: First of all, by using lasers instead of discharge lamps for optical pumping of  $^3\text{He}$  [127, 128], the sample polarization could be increased from 5%, typically, up to 90% [93]. Secondly, for the signal detection, low- $T_c$  DC-SQUID magnetometers can be used as magnetic flux detectors with a white magnetic noise level of  $\rho_{\text{SQUID}} \approx 2 \text{ fT}/\sqrt{\text{Hz}}$  [129, 119, 130, 131]. Thirdly, the transverse relaxation time  $T_2^*$  could be increased by more than an order of magnitude using low-relaxation glass container for the polarized  $^3\text{He}$  sample, placed in a homogeneous magnetic guiding field of about  $0.35 \mu\text{T}$  inside the magnetically shielded room BMSR-2.

### 5.1 Estimation of Sensitivity Level

The overall sensitivity of atomic magnetometers, such as the  $^3\text{He}$ -SQUID magnetometer, can be estimated using the statistical signal processing theory [132]. Since the magnetic field  $B$  is proportional to the precession frequency  $\omega = 2\pi\nu = |\gamma \cdot B|$ , the sensitivity of the magnetic field measurement can be deduced from the Cramer-Rao lower bound (CRLB), which sets the lower limit on the variance of any frequency estimator. The signal  $S$  from the precessing spins recorded at a sampling rate  $f_s$  with  $f_s/2 \geq \nu$  can be written as

$$\begin{aligned} S[n] &= A \cdot \cos(\pi(\nu/f_s)n + \phi) + w[n] \\ \text{with } n &= 0, 1, \dots, N-1. \end{aligned} \quad (5.1)$$

Here  $\phi$  is the initial phase,  $A$  the signal amplitude and  $w[n]$  the white Gaussian noise. For detection times  $T \ll T_2^*$ , where the exponential damping of the signal amplitude  $A$  does not affect the sensitivity of the magnetometer too much, the average value of the signal amplitude  $\bar{A}$  can be used to determine the signal-to-noise ratio:  $\text{SNR} = \bar{A}/N_\alpha$ . The noise  $N_\alpha$

is defined as the square root of the integrated power spectral density  $\rho_\alpha$  of the corresponding signal fluctuations

$$N_\alpha = \left( \int_0^{f_{\text{BW}}} \rho_\alpha^2 d\nu \right)^{1/2}, \quad (5.2)$$

where  $f_{\text{BW}} = f_s/2$  is the sampling rate limited bandwidth (Nyquist frequency). If the noise is white, i.e.  $\rho_\alpha = \text{const}$ , the noise level is given by  $N_\alpha = \rho_\alpha \sqrt{f_{\text{BW}}}$ . Then according to [132], the lower limit on the sensitivity regarding the frequency can be estimated by the Cramer-Rao lower bound (CRLB)

$$\sigma_\nu \geq \frac{\sqrt{12}}{2\pi \text{SNR} \sqrt{f_{\text{BW}}} T^{3/2}}, \quad (5.3)$$

where  $T$  is the observation time respectively the spin-coherence time of the signal. From this inequation and with the relation  $\omega = 2\pi\nu = \gamma \cdot B$ , the sensitivity  $\delta B$  on the respective magnetic field  $B$  seen by the sample spins can be derived

$$\delta B \geq \frac{\sqrt{12}}{\text{SNR} T^{3/2} \gamma}. \quad (5.4)$$

In summary, Eq. 5.3 and Eq. 5.4 are valid for a sinusoidal spin precession signal with white gaussian distributed noise, constant amplitude and frequency (respectively magnetic field:  $B = 2\pi\nu/\gamma$ ). In the appendix of [133], an improvement to the sensitivity estimate is given that takes the exponential damping of the spin precession signal into account. The sensitivities, given in Eq. 5.3 and Eq. 5.4, then have to be multiplied with a factor  $\sqrt{C(T_2^*, T)}$ .

Examination of Eq. 5.4 suggests the use of magnetometers based on the spin precession of electrons rather than on the spin precession of nuclei due to their three orders of magnitude higher gyromagnetic ratio  $\gamma$ . Indeed, the atomic magnetometer with the best short-term sensitivity is the spin-exchange-relaxation-free (SERF) magnetometer, whose sensitivity surpasses  $\text{fT}/\sqrt{\text{Hz}}$  in practice [134]. However, for long-term magnetic field measurements, the power law  $\delta B \propto T^{3/2}$  can be exploited if the coherent spin-precession can be observed with a long observation time  $T$  respectively with a long transverse relaxation time  $T_2^*$ . Here  $T_2^*$  has to fulfill  $T_2^* \gtrsim T$ . Thus, the total observation time  $T$  is set by the respective  $T_2^*$  time, i.e.  $T_2^* \sim T$ . Usually, the transverse relaxation time  $T_2^*$  of electron spins is short, while nuclei, such as  $^3\text{He}$ , display a much longer  $T_2^*$  time. This may make them competitive or even superior to electron spin magnetometers.

In general, long and short observation times, i.e.  $T_L$  and  $T_S$  respectively, lead to different measurement sensitivities, which will be illustrated in the following: The sensitivity of the measurements with the long and the short observation times are given by  $\sigma_{\nu,L} = V \cdot T_L^{-3/2}$  and  $\sigma_{\nu,S} = V \cdot T_S^{-3/2}$ , respectively (see Eq. 5.3). Here it is assumed that the SNR and the bandwidth  $f_{\text{BW}}$ , and therewith the prefactors  $V$ , for both type of measurements are equal. To obtain comparable sensitivities for both measurements, the total observation time is given by  $T = T_L$ . Thus, the measurement with the short observation time  $T_S$  has to be repeated  $n$  times, i.e.  $T = T_L = n \cdot T_S$ . The sensitivity of an individual measurement  $\sigma_{\nu,S}$  then is



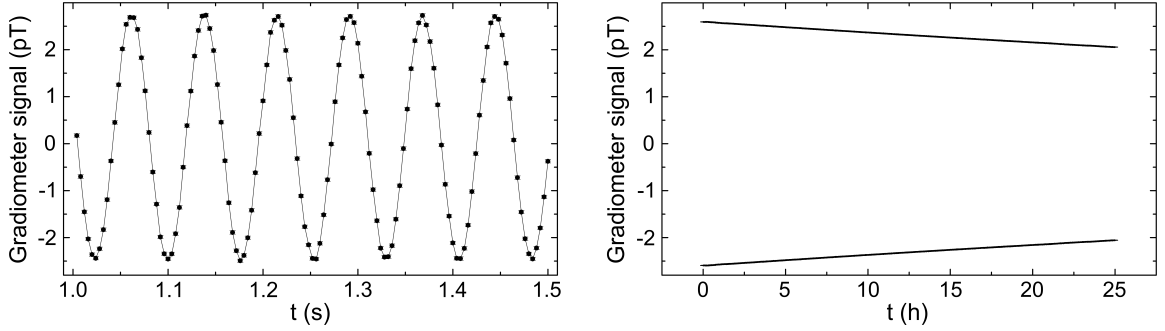


Figure 5.1: Free spin precession signal of pure polarized  $^3\text{He}$ . *left*: Cutout of 0.5 s of the free spin-precession signal of a polarized  $^3\text{He}$  sample cell, recorded by means of a low- $T_c$  SQUID with a sampling rate of  $f_s = 250$  Hz. *right*: Envelope of the decaying signal amplitude. From an exponential fit to the data, a transverse relaxation time of  $T_2^* = (111.0 \pm 0.3)$  h can be deduced.

improved by a statistical factor  $\sqrt{n}$ , i.e.  $\sigma_{\nu,S,n} = \sigma_{\nu,S}/\sqrt{n}$ . Hence, the relation between the measurement sensitivities of the two different measurements then is given by

$$\sigma_{\nu,S,n} = \frac{1}{\sqrt{n}} \frac{V}{T_S^{3/2}} = \sqrt{\frac{T_S}{T_L}} \frac{V}{T_S^{3/2}} = \frac{1}{\sqrt{T_L}} \frac{V}{T_S} = \frac{T_L}{\sqrt{T_S}} \frac{V}{T_L^{3/2}} = \frac{T_L}{\sqrt{T_S}} \sigma_{\nu,L} . \quad (5.5)$$

Considering the relations  $T_L \sim T_{2,L}^*$  and  $T_S \sim T_{2,S}^*$ , the measurement sensitivities differ by a factor of  $T_{2,L}^*/\sqrt{T_{2,S}^*}$ . For example, measurements with a Hg-magnetometer result in a short transverse relaxation time of  $T_{2,S}^* \approx 180$  s [135]. Compared to measurements with a long transverse relaxation time of  $T_{2,L}^* \approx 5$  h the measurements with the Hg-magnetometer have to be repeated 100 times to get comparable sensitivities assuming that the SNR and the bandwidth  $f_{\text{BW}}$  are equal for both type of measurements. The tremendous gain in sensitivity then is given by a factor of  $T_{2,L}^*/\sqrt{T_{2,S}^*} \approx 1300$  for the measurements with the long transverse relaxation time. In summary this means, that a high sensitivity on frequency can be achieved by measurements with a high SNR and a long observation time  $T$ , respectively a long transverse relaxation time  $T_2^*$ .

First, so to say as proof of principle, one has to show that long spin-coherence times  $T$  can be achieved with our  $^3\text{He}$ -SQUID magnetometer. For that, a spherical measurement cell with a radius of 5 cm was filled with polarized  $^3\text{He}$  at a pressure of about 2.7 mbar. This cell was placed directly below a SQUID sensor. The distance  $d$  from the center of the cell to the center of the SQUID was  $d \approx 10.5$  cm. As already mentioned in Sec. 4.2.1, the measurement cell was made from low-relaxation GE-180 glass and the longitudinal relaxation time was measured to be  $T_1 = (176 \pm 11)$  h. After a  $\pi/2$  spin-flip, the  $^3\text{He}$  spins start to precess in the  $yz$ -plane around the direction of the magnetic guiding field  $\vec{B}_0$  ( $x$ -direction). The plot on the left hand side of Fig. 5.1 shows the recorded gradiometer signal over a time interval of 0.5 s at the beginning of the precession cycle (sampling rate  $f_s = 250$  Hz). The signal

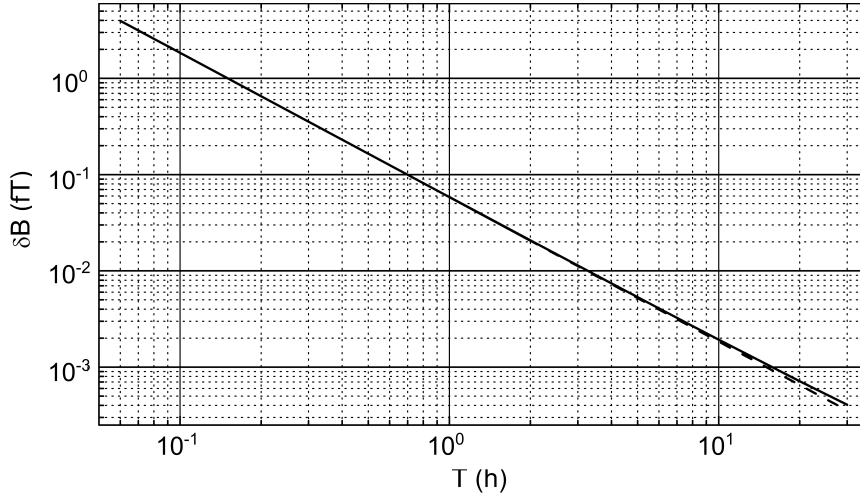


Figure 5.2: Estimated sensitivity (CRLB) of the  $^3\text{He}$  magnetometer in tracing tiny magnetic field fluctuations as a function of the observation time  $T$  with  $T_2^* = 111$  h for the transverse spin relaxation time (solid line). An improvement in sensitivity, for an observation time of one day, is only 18% of an undamped free spin-precession signal ( $T_2^* \rightarrow \infty$ ) (dashed line).

amplitude reaches  $A_{\text{He}} = 2.7 \text{ pT}^{-1}$  and the precession frequency is  $\nu \approx 13$  Hz. In the plot on the right hand side of Fig. 5.1, the exponential decay of the gradiometer signal amplitude (envelope) over a period of about 25 h is shown. From that the transverse relaxation time could be determined by an exponential fit to the amplitude to be  $T_2^* = (111.0 \pm 0.3)$  h. This is the longest spin-coherent relaxation time  $T_2^*$  of a macroscopic spin sample measured so far and it is indeed a world record.

Assuming that the requirements of CRLB are fulfilled, i.e. the  $^3\text{He}$  spin precession signal is characterized by a white gaussian distributed noise and a constant frequency, according to Eq. 5.4 the measurement sensitivity of the magnetic field as a function of the observation time  $T$  can be estimated by

$$\delta B \approx 12591 \text{ fT s}^{3/2} \frac{\sqrt{C(T_2^*, T)}}{T^{3/2}}, \quad (5.6)$$

where the measured value of the signal-to-noise ratio of  $\text{SNR} = 2.7 \text{ pT} : 2.0 \text{ fT} \approx 1350$  at  $t \approx 0$  s in a bandwidth of  $f_{\text{BW}} = 1$  Hz and the gyromagnetic ratio of helium with  $\gamma_{\text{He}} = 20.37894730 \cdot 10^7 \text{ Ts}^{-1}$  [92] were used. Here the effect of exponential damping ( $\sqrt{C(T_2^*, T)}$ ) of the free spin precession signal was taken into account. Figure 5.2 then shows the increase of the estimated measurement sensitivity  $\delta B$  as a function of the observation time  $T$  using  $T_2^* = 111$  h for the transverse spin relaxation time. The level of  $\delta B \approx 3.7$  fT is reached after an integration time of  $T \approx 544$  s and a measurement sensitivity of  $\delta B \approx 5.5 \cdot 10^{-4}$  fT can

<sup>1</sup>Due to low polarization of the  $^3\text{He}$  gas, the amplitude of the  $^3\text{He}$  spin precession signal is about 6 times smaller compared to the measurements of the main experiment to search for a spin-dependent short-range interaction.

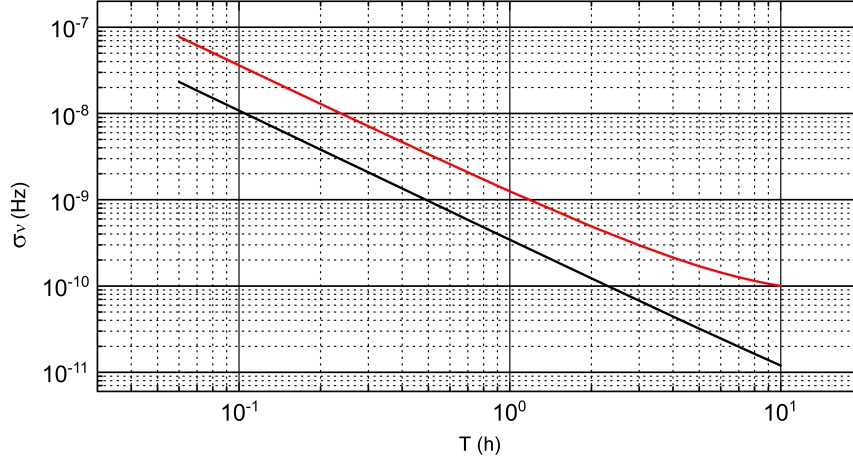


Figure 5.3: Estimated measurement sensitivity regarding the frequency of the  ${}^3\text{He}/{}^{129}\text{Xe}$  co-magnetometer in tracing small frequency shifts as a function of the observation time  $T$  for  ${}^3\text{He}$  (black) and  ${}^{129}\text{Xe}$  (red) with  $\overline{T_{2,\text{He}}^*} = 52.6$  h and  $\overline{T_{2,\text{Xe}}^*} = 4.9$  h.

be reached after one day. To check whether or not the conditions of CRLB are fulfilled, a co-magnetometer, such as the  ${}^3\text{He}/{}^{129}\text{Xe}$  co-magnetometer, is needed. Since the magnetic field dependence drops out in the weighted frequency difference (Eq. 4.4), the statistical behavior of the magnetic noise of the magnetometer and therewith the validity of CRLB can be checked by calculating the Allan standard deviation. These relations will be explained in more detail in the sub-section 5.2.

For the  ${}^3\text{He}/{}^{129}\text{Xe}$  co-magnetometer the sensitivity regarding the spin precession frequency given by Eq. 5.3 is limited by  ${}^{129}\text{Xe}$ . This can be explained by the smaller gyromagnetic ratio ( $\gamma_{\text{He}}/\gamma_{\text{Xe}} \approx 2.75$ ), the smaller polarization (and therefore smaller SNR) and the smaller transverse relaxation time  $T_2^*$  (see Sec. 3.5.1) of  ${}^{129}\text{Xe}$  compared to  ${}^3\text{He}$ . For the measurements to search for a spin-dependent short-range interaction, which are analyzed within this thesis, typical transverse relaxation times of  $\overline{T_{2,\text{He}}^*} = 52.6$  h and  $\overline{T_{2,\text{Xe}}^*} = 4.9$  h and typical values of the signal-to-noise ratio of  $\text{SNR}_{\text{He}} = 15.0 \text{ pT} : 2.0 \text{ fT} \approx 7500$  and  $\text{SNR}_{\text{Xe}} = 4.5 \text{ pT} : 2.0 \text{ fT} \approx 2250$  at  $t \approx 0$  s in a bandwidth of  $f_{\text{BW}} = 1$  Hz were achieved. Assuming that the conditions of CRLB are fulfilled, these values can be used for estimation of the sensitivity regarding the frequency

$$\sigma_{\nu,\text{He}} \approx 73510 \text{ nHz s}^{3/2} \frac{\sqrt{C(T_2^*, T)}}{T^{3/2}}, \quad (5.7)$$

$$\sigma_{\nu,\text{Xe}} \approx 245035 \text{ nHz s}^{3/2} \frac{\sqrt{C(T_2^*, T)}}{T^{3/2}}. \quad (5.8)$$

Here the effect of exponential damping ( $\sqrt{C(T_2^*, T)}$ ) has already been taken into account. In Fig 5.3 the increase of the estimated measurement sensitivity  $\sigma_{\nu}$  for  ${}^3\text{He}$  (black) and  ${}^{129}\text{Xe}$  (red) according to Eq. 5.7 and Eq. 5.8 as a function of the observation time  $T$  are shown. Since

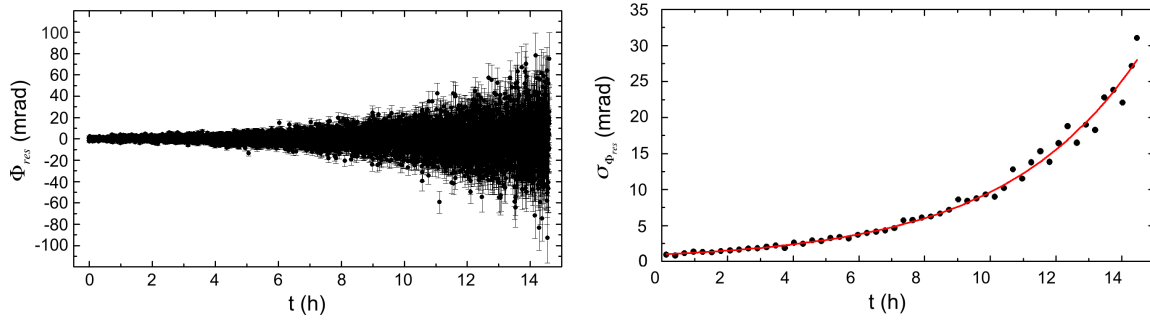


Figure 5.4: Phase residuals and root mean square (RMS). *left*: Phase residuals of measurement C92 (Sept. 2009) of the weighted phase difference  $\Delta\Phi$ . *right*: Root mean square (RMS) of the phase noise of measurement C92 (Sept. 2009) which increases in time with  $H \cdot \exp(t/T_x)$ .

the observation time of the measurements was typically 10 h, theoretically a measurement sensitivity of  $\sigma_\nu \approx 10^{-10}$  Hz can be reached with the  $^3\text{He}/^{129}\text{Xe}$  co-magnetometer.

## 5.2 Inherent Noise of Magnetometer

The Allan standard deviation [136] is the most convenient measure to study temporal characteristics of magnetometers. As in the very high sensitivity range, external field fluctuations are the dominant sources of magnetic noise, deviations from the CRLB power law due to noise sources inherent in the magnetometer itself are difficult to determine. So, to be able to study the remaining noise sources inherent in the magnetometer, the external field fluctuations have to be eliminated by a  $^3\text{He}/^{129}\text{Xe}$  clock comparison experiment.

For demonstration of the determination of the inherent noise of the magnetometer, measurement runs of the measuring period in 2009 were used. These measurements were performed to search for a sidereal modulation in the spin precession frequency of  $^3\text{He}$  and  $^{129}\text{Xe}$  which violate Lorentz symmetry [122]. For these measurements spherical glass cells with a radius of  $R = 3$  cm were used. Since nothing was changed during one measurement run, these measurements are more eligible for the determination of inherent noise sources than the measurements, which are analyzed in this thesis (here during one measurement run a mass sample was moved close or distant to the measurement cell).

First of all, the phases of  $^3\text{He}$  and  $^{129}\text{Xe}$  were determined. Then the accumulated weighted phase difference  $\Delta\Phi(t)$  was calculated (see Chap. 6). After subtraction of the linear phase shift due to Earth's rotation, i.e.  $\Phi_E(t)$ , the remaining phase  $\Phi_{\text{rem}}(t)$  was fitted with the fit function  $\Phi_{\text{fit}}(t)$  of Eq. 6.17. The phase noise then can be determined by composing the difference of the weighted phase difference  $\Delta\Phi(t)$  and the fit function  $\Phi_{\text{fit}}(t)$ . The evolution of the phase noise of measurement C92 (Sept. 2009) is shown in Fig. 5.4 (left). Due to the exponential decrease of the  $^3\text{He}$  and  $^{129}\text{Xe}$  signal amplitudes (in particular the  $^{129}\text{Xe}$  amplitude, which decays with a measured transverse relaxation time of  $T_2^* = 4.40(1)$  h), the

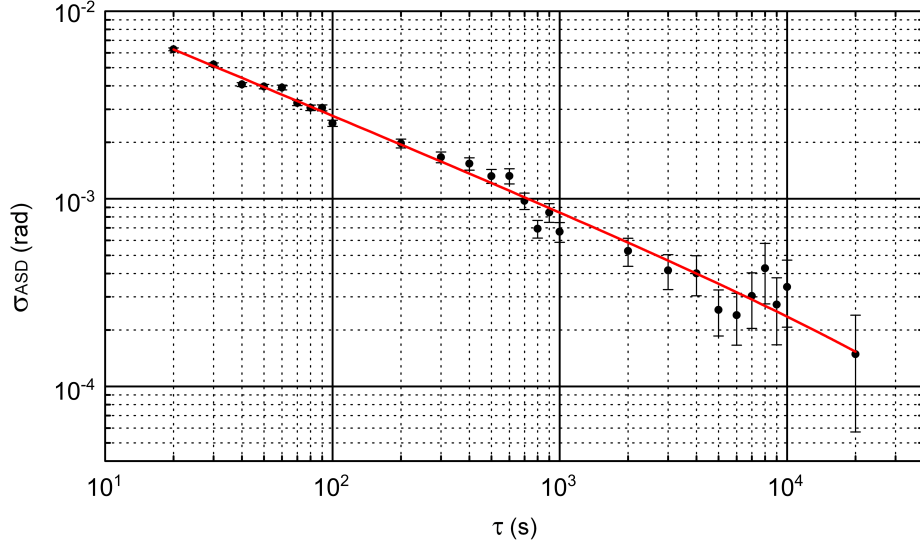


Figure 5.5: Allan standard deviation (ASD) of the phase residuals measured in run C92 (Sept. 2009) using nuclear spin precession of co-located  $^3\text{He}$  and  $^{129}\text{Xe}$  gas. The total observation time was  $T = 52000$  s. For integration times  $\tau$  beyond 4 s and up to 20000 s ( $f_{\text{BW}} = 125$  Hz) the observed fluctuations decrease as  $\propto \tau^{-1/2}$  indicating the presence of white phase noise.

residual phase noise rises in time. By calculating the root mean square (RMS) of the phase residuals for intervals of 1000 s, which is shown in Fig. 5.4 (right), the time evolution of the residual phase noise can be expressed by

$$\sigma_{\Phi_{\text{res}}} [\text{mrad}] = H \cdot e^{t/T_x}. \quad (5.9)$$

The data are best described by  $H = 1.01(40)$  mrad and  $T_x = 4.15(19)$  h. The fact, that we almost exactly observe  $T_x \approx T_{2,\text{Xe}}^*$  (within the  $2\sigma$  error) can be explained by use of Eq. 5.3 and the statistical error propagation law, showing that the phase noise scales like (see App. A)

$$\sigma_{\Phi_{\text{res}}} \propto e^{t/T_{2,\text{Xe}}^*} \left( e^{-2t \left( \frac{1}{T_{2,\text{Xe}}^*} - \frac{1}{T_{2,\text{He}}^*} \right)} + \left( \frac{\gamma_{\text{He}}}{\gamma_{\text{Xe}}} \right)^2 \left( \frac{A_{\text{He}}}{A_{\text{Xe}}} \right)_{t=0}^2 \right). \quad (5.10)$$

Here the ratio of the measured signal amplitudes at  $t = 0$  s is given by  $(A_{\text{He}}/A_{\text{Xe}})_{t=0} = 1.66$ . Since the transverse relaxation time of  $^3\text{He}$  was determined to be  $T_{2,\text{He}}^* = 14.16(1)$  h, the time dependence of Eq. 5.10 is almost entirely determined by its second term, i.e.  $\sigma_{\Phi_{\text{res}}} \propto \exp(t/T_{2,\text{Xe}}^*)$ .

For characterization of the phase noise, the Allan standard deviation (ASD) can be calculated, which depends on the integration time  $\tau$ . This means, that the measurement run of duration  $T$  is separated in  $N$  smaller data sets of length  $\tau$  with  $N \cdot \tau \leq T$ . Then for each data set

( $i = 1, 2, 3, \dots, N - 1$ ) the mean phase noise  $\bar{\Phi}_i(\tau)$  can be determined. The ASD then is given by

$$\sigma_{\text{ASD}}(\tau) = \sqrt{\frac{1}{2} \frac{\sum_{i=1}^{N-1} (\bar{\Phi}_{i+1}(\tau) - \bar{\Phi}_i(\tau))^2}{N-1}}, \quad (5.11)$$

where in the analysis the uncertainty due to the finite number of measurements  $N = T/\tau$  as discussed in [137] was taken into account.

For white noise,  $\sigma_{\text{ASD}}$  coincides with the classical standard deviation. Then a  $\sigma_{\text{ASD}} \propto \tau^{-1/2}$  dependence on the integration time  $\tau$  is expected. Figure 5.5 shows the ASD plot of the residual phase noise for run C92 which indeed decreases as  $\propto \tau^{-1/2}$  and therewith the phase noise of the  $^3\text{He}/^{129}\text{Xe}$  co-magnetometer corresponds to white noise. Hence, the ASD plot shows that the elimination of the magnetic field fluctuations works efficiently, i.e. no noise due to the magnetic field is left. Additionally, the  $\sigma_{\text{ASD}} \propto \tau^{-1/2}$  dependence shows that no noise sources inherent to the  $^3\text{He}/^{129}\text{Xe}$  co-magnetometer exist and thus there is no limitation of the measured sensitivity (CRLB) as shown in Fig. 5.5, at least for integration times up to  $\tau \approx 20000$  s.

## 6 Analysis

For one week in september 2010 we performed altogether 10 measurement runs lasting approximately 10 hours each. For each measurement run the BGO crystal was moved after  $t_0 \approx 3$  h from close to distant position (c→d) or vice versa (d→c). The asymmetric timing takes account for the smaller signal-to-noise ratio (SNR) in the second measurement phase due to the exponential damping of the signal amplitudes. By this measure, comparable statistics were obtained for both positions. Additionally, for systematic checks the BGO crystal was placed to the left side ( $\mathcal{L}$ ) or to the right side ( $\mathcal{R}$ ) of the  ${}^3\text{He}/{}^{129}\text{Xe}$  sample cell (see Fig. 4.10). The parameters (pressures and amplitudes) and the configuration of these measurement runs are listed in Tab. 6.1. With the pressure of the  ${}^3\text{He}$  and  ${}^{129}\text{Xe}$  gas and the initial amplitudes of the  ${}^3\text{He}$  and  ${}^{129}\text{Xe}$  spin precession signals the polarization of  ${}^3\text{He}$  and  ${}^{129}\text{Xe}$  can be estimated by using Eq. 3.29 (cylindrical cell  $\approx$  spherical cell)<sup>1</sup>. For  ${}^3\text{He}$ , we had polarizations between 19% and 46%, for  ${}^{129}\text{Xe}$  between 8% and 11%.

The magnetic flux density spectra<sup>2</sup> (in units  $\text{fT}/\sqrt{\text{Hz}}$ ) of a spin precession signal recorded by a single SQUID detector (sensor Z2E) in the lower plane close to the measurement cell is shown in Fig. 6.1 by the red curve. The two peaks of the  ${}^3\text{He}$  and  ${}^{129}\text{Xe}$  spin precession signals occur at  $\nu_{\text{He}} = \frac{\gamma_{\text{He}}}{2\pi} B_0 \approx 11.4$  Hz and  $\nu_{\text{Xe}} = \frac{\gamma_{\text{Xe}}}{2\pi} B_0 \approx 4.1$  Hz, which correspond to a magnetic guiding field  $B_0$  of about  $0.35 \mu\text{T}$ . Additionally there is a sharp peak at 50 Hz, that corresponds to the supply frequency, and there are some vibrational frequency components. The latter ones occur due to mechanical vibrations of the dewar, i.e. the SQUIDs slightly oscillate within the magnetic guiding field. Due to field gradients the SQUIDs detect changes of the magnetic field which lead to the peaks of the vibrational frequency components. These frequency components partly overlap with the  ${}^3\text{He}$  and  ${}^{129}\text{Xe}$  peaks and thus cause an increased noise around the signal peaks. To avoid additional noise the vibrational frequencies have to be suppressed.

For this purpose there are two possibilities: a.) By supporting the dewar with respect to the walls and the ceiling of the BMSR-2 mechanical vibrations can be reduced. b.) Instead of a single SQUID signal a gradiometer signal can be used, which is the difference of the signals of two SQUIDs, one in the lower plane close to the measurement cell ( $SQ_c$ ) and one in a lower/upper plane far away from the measurement cell ( $SQ_d$ ). The SQUID  $SQ_c$  sees the

<sup>1</sup>For gradiometer Z2E-Z5S the distance between the center of the cell and the SQUID sensors was  $\bar{z} = 5.8\text{cm}$ .

<sup>2</sup>The density spectra were determined as follows: The first  $n = 152 \cdot 2^{14}$  data points of measurement run C68 were used. These amount of data is divided into 152 data sets with  $n_{\text{set}} = 2^{14}$  data points each. Then for each data set the density spectra were determined via a Fast Fourier transform and by using a Blackman-Nutall window [138]. For correct calculation of the Fast Fourier transform,  $n_{\text{set}}$  have to be powers of 2. At the end, an averaging with the Welch method [139] was done over the 152 data sets.

		$T$	$A_{0,\text{He}}$	$A_{0,\text{Xe}}$	$p_{\text{He}}$	$p_{\text{Xe}}$	$p_{\text{N}_2}$	$p_{\text{tot}}$
		(h)	(fT)	(fT)	(mbar)	(mbar)	(mbar)	(mbar)
C54	dc- $\mathfrak{R}$	6.9	15280	5922	2.8	5.2	23.4	31.4
C55	cd- $\mathcal{L}$	10.9	12677	5198	2.7	5.7	28.3	36.7
C60	dc- $\mathcal{L}$	13.6	9469	4241	2.6	5.5	27.6	35.7
C63	dc- $\mathcal{L}$	8.7	17904	4927	2.7	4.9	25.7	33.3
C65	cd- $\mathcal{L}$	8.6	12116	3995	2.7	5.0	25.7	33.4
C67	cd- $\mathfrak{R}$	8.7	13876	4066	2.5	5.0	25.5	33.0
C68	dc- $\mathfrak{R}$	8.8	9186	4945	2.6	4.8	27.2	34.6
C71	cd- $\mathfrak{R}$	8.6	11211	5307	2.5	5.0	27.2	34.7
C80	dc- $\mathcal{L}$	8.7	10990	5642	3.6	5.7	26.6	35.9
C82	cd- $\mathcal{L}$	8.8	9770	4208	3.6	5.3	26.3	35.2

Table 6.1: Parameters of the 10 main measurements: measurement configuration (d = distant, c = close,  $\mathfrak{R}$  = right,  $\mathcal{L}$  = left), observation times  $T$ , initial amplitudes of the precession signals  $A_{0,\text{He}/\text{Xe}}$  (gradiometer sensors Z2E and Z5S) and partial pressures  $p$  of  ${}^3\text{He}$ ,  ${}^{129}\text{Xe}$ ,  $\text{N}_2$  and the total pressure  $p_{\text{tot}}$  in the measurement cell.

spin precession signals and the vibrational frequency components, whereas the SQUID  $SQ_{\text{d}}$  sees a small part of the spin precession signal or no spin precession signal and the same vibrational frequency components as SQUID  $SQ_{\text{c}}$ . Consequently, in the difference of the SQUID signals, i.e.  $SQ_{\text{c}} - SQ_{\text{d}}$ , only the vibrational frequency modes drop out and even a part of the  $1/f$ -noise is reduced. The magnetic flux density spectra of the gradiometer signal (sensors Z2E and Z5S) is shown in Fig. 6.1 by the blue curve. One can see that the vibrational frequencies are quite suppressed and only very small peaks at the main vibrational mode of about 6 Hz and 8 Hz remain. The white system noise for both spectra is given by  $\rho_{\text{system}} \approx 2.4 \text{ fT}/\sqrt{\text{Hz}}$ . The sampling rate used for the detection of the signals was  $f_s = 250 \text{ Hz}$ . Thus  $f_{\text{BW}} = f_s/2 = 125 \text{ Hz}$  is the sampling rate limited bandwidth (Nyquist frequency). But at about 100 Hz the spectra falls down due to internal filters which are used in the SQUID electronics.

The gradiometer signal of measurement run C68 recorded over a time interval of 1 s is shown on the left side of Fig. 6.2. This signal is a superposition of the  ${}^3\text{He}$  and  ${}^{129}\text{Xe}$  spin precession at the Larmor frequencies  $\omega_{\text{He}} \approx 2\pi \cdot 11.4 \text{ Hz}$  and  $\omega_{\text{Xe}} \approx 2\pi \cdot 4.1 \text{ Hz}$ . With our analysis method, which will be explained in detail in the following sections, the signals of both gases can be separated as shown on the right side of Fig. 6.2. The amplitudes at the beginning of measurement run C68 were determined to be  $A_{0,\text{He}} = 9186 \text{ fT}$  and  $A_{0,\text{Xe}} = 4945 \text{ fT}$ . With a white system noise level of about  $2.4 \text{ fT}/\sqrt{\text{Hz}}$  (see Fig. 6.1) the signal-to-noise ratio (SNR) at the beginning of measurement run C68 is given by  $\text{SNR}_{\text{Xe}} \approx \frac{4945 \text{ fT}}{2.4 \text{ fT}} = 2060$  for xenon and  $\text{SNR}_{\text{He}} \approx \frac{9186 \text{ fT}}{2.4 \text{ fT}} = 3828$  for helium in a bandwidth of 1 Hz.



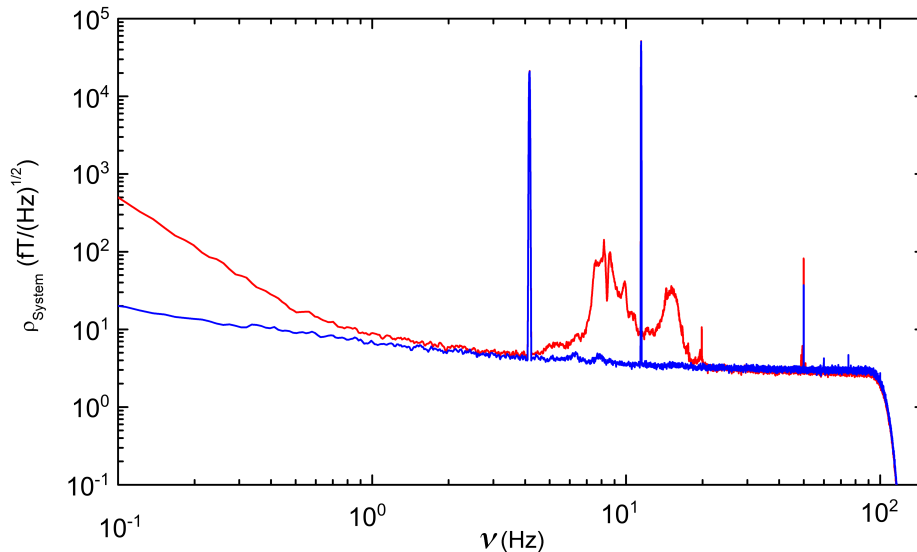


Figure 6.1: Magnetic flux density spectrum of the  $^3\text{He}$  and  $^{129}\text{Xe}$  precession signals of measurement run C68, detected with a single SQUID (sensor Z2E in *red*) and with a gradiometer (sensors Z2E and Z5S in *blue*). In both spectra the lines at about 4.1 Hz and 11.4 Hz correspond to the spin precession frequencies of the co-located  $^{129}\text{Xe}$  and  $^3\text{He}$  spins in a sample cell at a magnetic guiding field of about  $0.35\ \mu\text{T}$ . The line at 50 Hz corresponds to the supply frequency. For frequencies  $\nu > 10\ \text{Hz}$  the white system noise is given by  $\rho_{\text{system}} \approx 2.4\ \text{fT}/\sqrt{\text{Hz}}$ . Due to a sampling rate of  $f_s = 250\ \text{Hz}$ , the cut-off frequency is at 125 Hz. In the spectrum detected with a single SQUID (*red*) disturbances occur due to mechanical vibrations of the dewar respectively of the SQUIDS. By using a gradiometer (*blue*) these disturbances can be suppressed and even the  $1/f$ -noise is reduced.

## 6.1 Piecewise Fitting of Raw Data

For extraction of the time dependence of the  $^3\text{He}$  and  $^{129}\text{Xe}$  amplitudes, phases and frequencies the method of *piecewise fitting of raw data* was used. The piecewise fitting of raw data was done with a *Mathematica* package named “DatFit” which was developed by our collaborator Ulrich Schmidt from University of Heidelberg/GER. The fitting routine is based on the standard Least-Squares method up to  $n$  dimensions, i.e.  $n$  discrete pseudo-dimensions are used to allow the fitting of several data sets simultaneously, while common fit parameters for all data sets and specific fit parameters for each data set can be implemented.

For the piecewise fitting of raw data the gradiometer signals of each run ( $j = 1, \dots, 10$  corresponding to C54, C55, C60, C63, C65, C67, C68, C71, C80, C82) are divided up into  $N_j$  sub-data sets. The length of one sub-data set has to be chosen such that on the one hand the number of data points provide enough statistics for the fit and on the other hand the  $^3\text{He}$  and  $^{129}\text{Xe}$  frequencies can be regarded as constant. To fulfill these conditions sub-

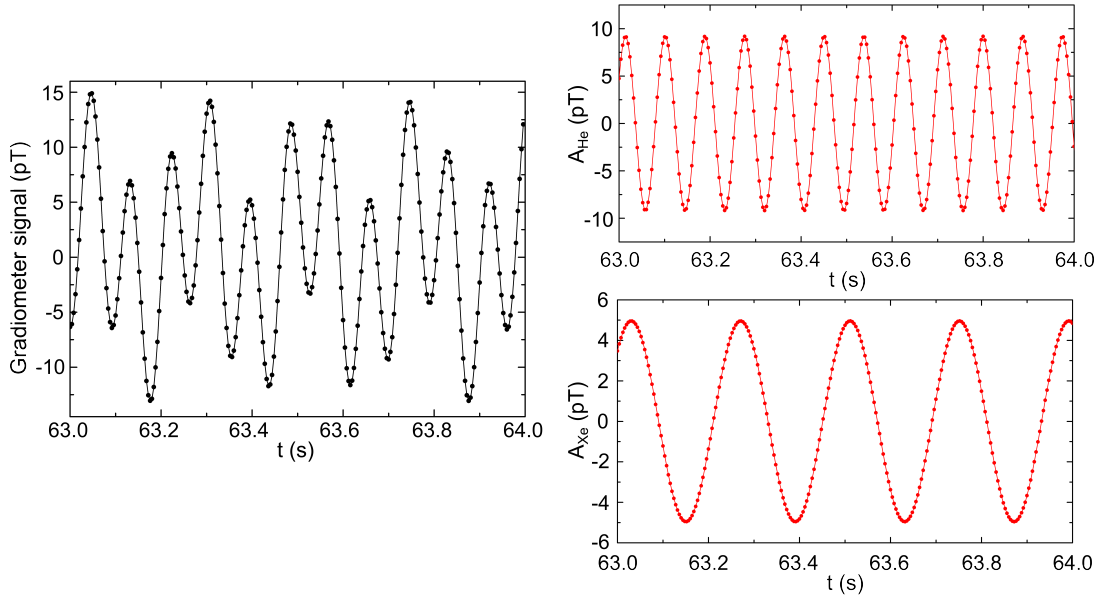


Figure 6.2: Gradiometer signals. *Left*: Cutout of gradiometer signal of measurement run C68. *Right*: Cutout of spin precession signals of  $^3\text{He}$  (above) and  $^{129}\text{Xe}$  (below). In all plots the uncertainty at each data point is  $\pm 27$  fT and therefore the error bars are too small to be visible in the plot.

data sets of 800 data points were used. With a sampling rate of  $f_s = 250$  Hz the sub-data sets have a length of  $\tau = 3.2$  s. The number of obtained sub-data sets laid between  $7760 < N_j < 15300$  corresponding to the observation times  $T_j$  of coherent spin precession in the range of  $6.9 \text{ h} < T_j < 13.6 \text{ h}$ .

For each sub-data set  $i$ , with  $i = 1, \dots, N_j$ , the gradiometer signal can be described by

$$A^i(t) = C_{\text{He}}^i \sin(\omega_{\text{He}}^i t + \varphi_{\text{He}}^i) + C_{\text{Xe}}^i \sin(\omega_{\text{Xe}}^i t + \varphi_{\text{Xe}}^i) + (c_0^i + c_{\text{lin}}^i t) . \quad (6.1)$$

The term  $(c_0^i + c_{\text{lin}}^i t)$  characterizes the gradiometer offset which slightly drifts due to the elevated  $1/f$ -noise at low frequencies ( $< 2$  Hz) [96]. This drift is assumed to be linear within the relatively short sub-data set of length  $\tau = 3.2$  s. The two sine terms describe the spin precession of  $^3\text{He}$  and  $^{129}\text{Xe}$  with the Larmor frequencies  $\omega_{\text{He}}^i = 2\pi\nu_{\text{He}}^i$  and  $\omega_{\text{Xe}}^i = 2\pi\nu_{\text{Xe}}^i$  and the phases  $\varphi_{\text{He}}^i$  and  $\varphi_{\text{Xe}}^i$ . The amplitudes  $C_{\text{He/Xe}}^i$  are linear fit parameters<sup>3</sup>, while the frequencies  $\omega_{\text{He,Xe}}^i$  and the phases  $\varphi_{\text{He/Xe}}^i$  are nonlinear fit parameters, which can lead to problems during the fitting, because nonlinear fit parameters are very sensitive on the initial values used for the fit. That is why it is better to transform the two sine terms via the sine

<sup>3</sup>In statistics, a *linear* fit function is a linear combination of the fit parameters, e.g.  $f(x) = a \cdot x + b \cdot x^2$  is linear in the fit parameters  $a$  and  $b$ . On the contrary, a *nonlinear* fit function is a nonlinear combination of the fit parameters, e.g.  $f(x) = x^a + \cos(x + b)$  is nonlinear in the fitparameters  $a$  and  $b$ .

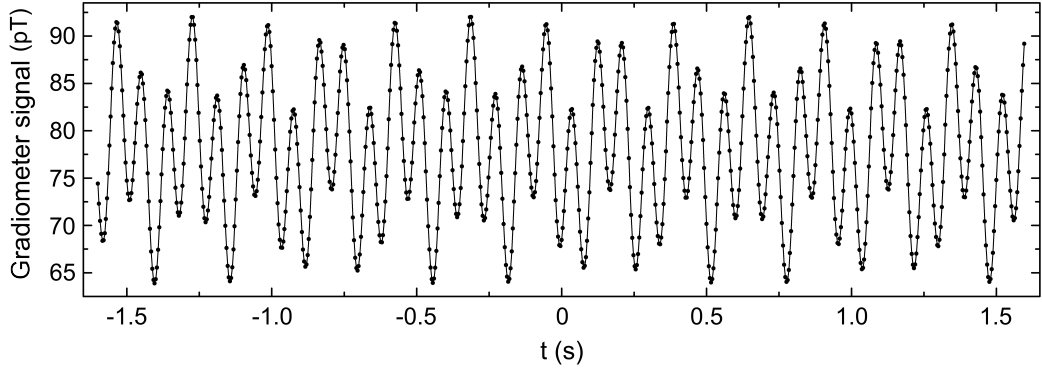


Figure 6.3: Typical sub-data set of 3.2 s length used for fitting. The zero-point of the time lies in the middle of the sub-data set which is done to achieve low correlation between the fit parameters  $c_0^i$  and  $c_{\text{lin}}^i$ . The uncertainty at each data point is  $\pm 27$  fT and therefore the error bars are too small to be visible in the plot.

addition theorem into a sum of sine and cosine terms

$$\begin{aligned} C_{\text{He/Xe}}^i \sin(\omega_{\text{He/Xe}}^i t + \varphi_{\text{He/Xe}}^i) &= C_{\text{He/Xe}}^i \sin(\omega_{\text{He/Xe}}^i t) \cos(\varphi_{\text{He/Xe}}^i) \\ &\quad + C_{\text{He/Xe}}^i \cos(\omega_{\text{He/Xe}}^i t) \sin(\varphi_{\text{He/Xe}}^i) \\ &= a_{\text{s,He/Xe}}^i \sin(\omega_{\text{He/Xe}}^i t) + a_{\text{c,He/Xe}}^i \cos(\omega_{\text{He/Xe}}^i t), \end{aligned} \quad (6.2)$$

where  $a_{\text{s,He/Xe}}^i = C_{\text{He/Xe}}^i \cos(\varphi_{\text{He/Xe}}^i)$  and  $a_{\text{c,He/Xe}}^i = C_{\text{He/Xe}}^i \sin(\varphi_{\text{He/Xe}}^i)$  are termed the *quadrature amplitudes* of the oscillation.

Hence, for each sub-data set a  $\chi^2$  minimization was performed, using the following fit function with a total of 8 fit parameters

$$B_{\text{fit}}^i(t) = a_{\text{c,He}}^i \cos(\omega_{\text{He}}^i t) + a_{\text{s,He}}^i \sin(\omega_{\text{He}}^i t) + a_{\text{c,Xe}}^i \cos(\omega_{\text{Xe}}^i t) + a_{\text{s,Xe}}^i \sin(\omega_{\text{Xe}}^i t) + (c_0^i + c_{\text{lin}}^i t). \quad (6.3)$$

In Fig. 6.3 a typical sub-data set is shown. The time values for each sub-data set are always shifted in such a way that the zero-point lies in the middle of the sub-data set. This is done to get less correlation between the fit parameters  $c_0^i$  and  $c_{\text{lin}}^i$ . The error for each data point corresponds to the typical noise in the sampling rate limited bandwidth  $f_{\text{BW}} = f_s/2 = 125$  Hz. For example, if we consider the magnetic flux density spectrum of measurement run C68 (see Fig. 6.1), the white system noise is approximately  $2.4$  fT/ $\sqrt{\text{Hz}}$  at the  $^3\text{He}$  and  $^{129}\text{Xe}$  frequencies. The total noise then is  $2.4$  fT/ $\sqrt{\text{Hz}} \cdot \sqrt{125 \text{ Hz}} \approx 27$  fT which is assigned as error to each data point.

Since the fit model (Eq. 6.3) is nonlinear in the frequencies  $\omega_{\text{He}}^i$  and  $\omega_{\text{Xe}}^i$ , it is necessary to have good start values for the frequencies. In order to avoid problems with the fitting procedure, the start values of the frequencies are estimated by means of the magnetic flux density spectrum. Then these values of the frequencies are kept fixed so that the fit model given in Eq. 6.3 only contains linear fit parameters. The start values of the other parameters are not critical and the fit converges easily. The best fit parameters of this linear fit are

chosen as start values for a second fit. Now the frequencies are variable parameters as well. This method makes sure that the absolute minimum of  $\chi^2/dof$  is reached with the nonlinear fit. For each sub-data set the second fit provides the 8 best fit parameters for the frequencies  $\omega_{\text{He/Xe}}^i$ , the sine and cosine amplitudes, i.e.  $a_{\text{s,He/Xe}}^i$  and  $a_{\text{c,He/Xe}}^i$ , and the gradiometer drift parameters  $c_0^i$  and  $c_{\text{lin}}^i$ . The fit-routine calculates both the *correlated* and *uncorrelated* error for each parameter, which correspond to the  $1\sigma$  errors, i.e. the interval that contains 68.3% of normally distributed data. The correlated error considers correlations between the fit parameters whereas the uncorrelated error corresponds to the uncertainty of the fit parameter if there would be no correlations. By comparing the correlated and the uncorrelated errors one gets a hint on how strong the fit parameters are correlated: If both errors are roughly equal, one can neglect the correlations. If they differ too much, one has to consider the correlations in the error propagation, i.e. the Gaussian error propagation law cannot be used for the calculation of the errors. For the sub-data sets, which consist of 800 data points each, the correlations between the fit parameters are always small (the correlated and uncorrelated errors differ by less than 10%), so that Gaussian error propagation can be used for determination of the errors of the phases and the amplitudes later on.

Additionally, the fit-routine also calculates two quantities which define the quality of the fit: the reduced  $\chi^2$  value, i.e.  $\chi^2/dof$ , and the probability  $Q$  that this or a higher value for  $\chi^2/dof$  may arise. Here,  $\chi^2/dof$  is the  $\chi^2$  value divided by the degrees of freedom ( $dof$ ). The degrees of freedom for each sub-data set correspond to the difference of the number of data points and the number of fit parameters, i.e.  $dof = 800 - 8 = 792$ . If the raw data fit of Eq. 6.3 results in a  $\chi^2/dof$  value of  $\chi_{\text{meas}}^2/dof$  the probability  $Q$  is given by

$$Q = \int_{\chi_{\text{meas}}^2/dof}^{\infty} \text{PDF}(x; \langle \chi^2/dof \rangle, \sigma) dx, \quad (6.4)$$

where PDF is the probability density function of the  $\chi^2/dof$  distribution.  $\langle \chi^2/dof \rangle$  is the mean value of all  $\chi^2/dof$  values of one measurement run and  $\sigma$  is the standard deviation, which defines the width of the  $\chi^2/dof$  distribution. For each measurement run with up to 15300 sub-data sets, the probability density function (PDF) of the  $\chi^2/dof$  distribution approaches a normal distribution with a maximum at  $\langle \chi^2/dof \rangle \approx 1$ . As example the  $\chi^2/dof$  distribution of measurement run C68 is shown in Fig. 6.4. The hatched area below the PDF curve indicates the probability  $Q$  for a sub-data set which results in a  $\chi^2/dof$  value of  $\chi_{\text{meas}}^2/dof$ . If  $Q$  is smaller than 5%, i.e. for values  $\chi_{\text{meas}}^2/dof$  that are too high, the fit routine automatically re-scales the error of the raw data ( $\pm 27$  fT), and therewith the errors of the best fit parameters, with the factor  $S = \sqrt{\chi^2/dof}$ . That means, if the raw data fit of Eq. 6.3 again is applied to the raw data, where now the errors are re-scaled with the factor  $S$ , the fit results in a  $\chi^2/dof$  value of  $\chi^2/dof = 1$ . This is a standard method often used in error determination, especially when the errors of the primary data are not known or not known accurately (see for example [140], Chap. 15.1). For most of the raw data fits this re-scaling was not needed since the values of  $Q$  were  $> 5\%$ . However there were some sub-data sets with  $\chi^2/dof \geq 2$  (not shown in Fig. 6.4), which result in  $Q < 5\%$ . But for those

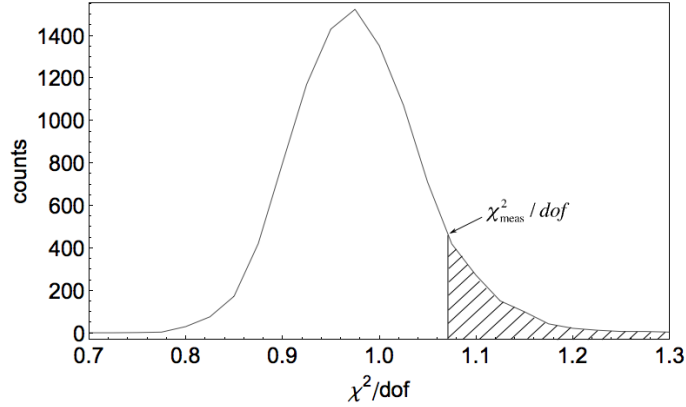


Figure 6.4:  $\chi^2/dof$  distribution of the raw data fits of measurement run C68. The mean value is  $\langle \chi^2/dof \rangle \approx 1$ . The hatched area corresponds to the probability  $Q$  (Eq. 6.4) of a raw data fit with  $\chi^2/dof = \chi_{\text{meas}}^2/dof$ .

sub-data sets a re-scaling of the errors of the raw data did not lead to  $\chi^2/dof = 1$ . This can be explained by jumps in the gradiometer amplitude in the order of 1 pT, which are not visible in the sub-data set of the raw data, but in the residuals of the raw data fits, i.e. by subtracting the fit function given by Eq. 6.3 from the raw data. These sub-data sets as well as sub-data sets with  $\omega_{\text{He/Xe}} > (\overline{\omega_{\text{He/Xe}}} + 3 \cdot \Delta\overline{\omega_{\text{He/Xe}}})$  or  $\omega_{\text{He/Xe}} < (\overline{\omega_{\text{He/Xe}}} - 3 \cdot \Delta\overline{\omega_{\text{He/Xe}}})$  are discarded. Here  $\overline{\omega_{\text{He/Xe}}}$  is the average frequency of helium and xenon of all  $N_j$  sub-data sets of one measurement run and  $\Delta\overline{\omega_{\text{He/Xe}}}$  is the corresponding standard deviation. So, for further analysis only sub-data sets without any disturbances are used. For all 10 measurement runs less than 7% of sub-data sets were discarded.

## 6.2 Phase Determination

For the co-magnetometer the quantity of interest is the time dependence of the phases of  $^3\text{He}$  and  $^{129}\text{Xe}$ . For each sub-data set  $i$  the phase can be determined from the fit parameters,  $a_{\text{s,He/Xe}}^i$  and  $a_{\text{c,He/Xe}}^i$ , of the raw data fit of Eq. 6.3 with the arctangent (atan2) function which is defined as

$$\text{atan2}(y, x) = \begin{cases} \arctan(\frac{y}{x}) & x > 0, \\ \pi + \arctan(\frac{y}{x}) & y \geq 0, x < 0, \\ -\pi + \arctan(\frac{y}{x}) & y < 0, x < 0. \end{cases} \quad (6.5)$$

The atan2 function takes values in the interval from  $-\pi$  to  $\pi$ , where the value of atan2 depends on the quadrant of the x- and y-phase vectors in the unit circle. The phases  $\varphi_{\text{He/Xe}}^i$  of  $^3\text{He}$  and  $^{129}\text{Xe}$  then are given by

$$\varphi_{\text{He/Xe}}^i = \text{atan2} \left( \frac{a_{\text{s,He/Xe}}^i}{a_{\text{c,He/Xe}}^i} \right) + \pi, \quad (6.6)$$

Here the value  $\pi$  was added to avoid phase jumps of  $2\pi$  later on, which can occur when the phases take negative values. Hence, the phases  $\varphi_{\text{He/Xe}}^i$  take values between 0 and  $2\pi$  and correspond to the respective phases of the  $i$ -th sub-data set. For determination of the accumulated phases of  $^3\text{He}$  and  $^{129}\text{Xe}$ , the knowledge of the number of periods  $n_{\text{He/Xe}}^i$  since the beginning of the measurement run is needed. The accumulated phases of  $^3\text{He}$  and  $^{129}\text{Xe}$  of the  $i$ -th sub-data set then are given by

$$\Phi_{\text{He/Xe}}^i(t_i) = n_{\text{He/Xe}}^i \cdot 2\pi + \varphi_{\text{He/Xe}}^i, \quad (6.7)$$

where  $t_i = (i-1) \cdot \tau$  is the time of the  $i$ -th sub-data set and  $\tau$  is the length of each sub-data set. The number of periods  $n_{\text{He/Xe}}^i$  can be determined indirectly, which will be explained in the following: First of all, the phase of the  $i$ -th sub-data set can be estimated by

$$\Phi_{\text{He/Xe}}^{\text{est},i}(t_i) = \Phi_{\text{He/Xe}}^{i-1}(t_i) + \bar{\omega}_{\text{He/Xe}} \cdot \tau. \quad (6.8)$$

$\Phi_{\text{He/Xe}}^{i-1}(t_i)$  is the accumulated phase of the preceding sub-data set, where the phase of the first sub-data set is given by  $\Phi_{\text{He/Xe}}^1(t_1 = 0 \text{ s}) = \varphi_{\text{He/Xe}}^1$ , and  $\bar{\omega}_{\text{He/Xe}}$  is the mean frequency of the corresponding measurement run, which consists of  $N$  sub-data sets, i.e.

$$\bar{\omega}_{\text{He/Xe}} = \frac{1}{N} \sum_{i=1}^N \omega_{\text{He/Xe}}^i. \quad (6.9)$$

The term  $\bar{\omega}_{\text{He/Xe}} \cdot \tau$  in Eq. 6.8 then estimates the accumulated phase between sub-data set  $(i-1)$  and sub-data set  $i$ , if the frequency deviations  $\Delta\omega_{\text{He/Xe}}^i = \omega_{\text{He/Xe}}^i - \bar{\omega}_{\text{He/Xe}}$  of all sub-data sets fulfill  $\Delta\omega_{\text{He/Xe}}^i \cdot \tau \ll 2\pi$ . If the latter condition is not conformed, then the number of periods is not enumerated correctly. Since the maximum frequency deviation  $\Delta\omega_{\text{He/Xe}}^{\text{max}}$  for helium and xenon is smaller than  $3 \cdot 10^{-3}$  Hz for all 10 measurement runs, i.e.  $\Delta\omega_{\text{He/Xe}}^{\text{max}} \cdot \tau \approx 0.01$  rad  $\ll 2\pi$ , it is guaranteed that the number of periods is enumerated correctly. Thus no error of  $2\pi$  in the accumulated phase of Eq. 6.8 occurs.

For sub-data sets with  $\omega_{\text{He/Xe}}^i \neq \bar{\omega}_{\text{He/Xe}}$  the estimated phase  $\Phi_{\text{He/Xe}}^{\text{est},i}(t_i)$  is not correct. Thus a correction phase has to be introduced

$$\begin{aligned} \Delta\Phi_{\text{He/Xe}}^{\text{corr},i} &= \varphi_{\text{He/Xe}}^i - \beta_{\text{He/Xe}}^i \\ &= \varphi_{\text{He/Xe}}^i - \text{mod} \left( \frac{\Phi_{\text{He/Xe}}^{\text{est},i}}{2\pi} \right). \end{aligned} \quad (6.10)$$

In case of  $\omega_{\text{He/Xe}}^i = \bar{\omega}_{\text{He/Xe}}$  the estimated phase  $\Phi_{\text{He/Xe}}^{\text{est},i}$  is correct and thus the correction phase is given by  $\Delta\Phi_{\text{He/Xe}}^{\text{corr},i} = 0$ . The expression  $\beta_{\text{He/Xe}}^i$  contains the modulo operation which gives the remainder of  $\Phi_{\text{He/Xe}}^{\text{est},i}$  of a division by  $2\pi$ , i.e.  $\beta_{\text{He/Xe}}^i < 2\pi$ . The correction phase  $\Delta\Phi_{\text{He/Xe}}^{\text{corr},i}$  can show positive values, if  $\omega_{\text{He/Xe}}^i > \bar{\omega}_{\text{He/Xe}}$ , as well as negative values, if  $\omega_{\text{He/Xe}}^i < \bar{\omega}_{\text{He/Xe}}$ . Including the correction phase, the real accumulated phase  $\Phi_{\text{He/Xe}}^i(t_i)$  of the  $i$ -th sub-data set then is given by

$$\begin{aligned} \Phi_{\text{He/Xe}}^i(t_i) &= \Phi_{\text{He/Xe}}^{\text{est},i} + \Delta\Phi_{\text{He/Xe}}^{\text{corr},i} \\ &= \Phi_{\text{He/Xe}}^{i-1} + \bar{\omega}_{\text{He/Xe}} \cdot \tau + \varphi_{\text{He/Xe}}^i - \text{mod} \left( \frac{\Phi_{\text{He/Xe}}^{i-1} + \bar{\omega}_{\text{He/Xe}} \cdot \tau}{2\pi} \right). \end{aligned} \quad (6.11)$$

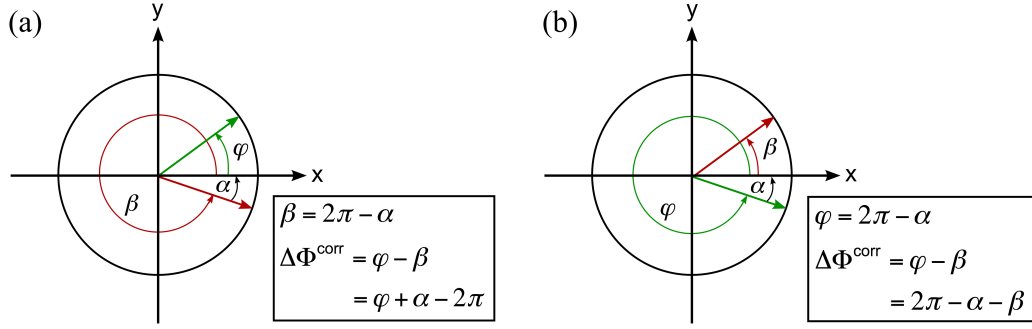


Figure 6.5: Illustration of over- and underestimation of the number of periods  $n_{\text{He/Xe}}^i$ . In both plots the green arrow shows the real phase ( $\varphi$ ) of the  $i$ -th sub-data set and the red arrow shows the modulo of the estimated phase ( $\beta$ ) of the  $i$ -th sub-data set, i.e.  $\beta = \text{mod}(\Phi^{\text{est}}/2\pi)$ . (a) If  $\varphi$  is close to zero and  $\beta$  close to  $2\pi$ , the correction phase should be given by  $\Delta\Phi_{\text{He/Xe}}^{\text{corr},i} = \alpha_{\text{He/Xe}}^i + \varphi_{\text{He/Xe}}^i$ . But Eq. 6.10 results in  $\Delta\Phi_{\text{He/Xe}}^{\text{corr},i} = \alpha_{\text{He/Xe}}^i + \varphi_{\text{He/Xe}}^i - 2\pi$ . Hence the correction phase  $\Delta\Phi^{\text{corr}}$  has an additional term of  $-2\pi$ , i.e. the number of periods is underestimated by one. (b) If  $\varphi$  is close to  $2\pi$  and  $\beta$  close to zero, the correction phase should be given by  $\Delta\Phi_{\text{He/Xe}}^{\text{corr},i} = -\alpha_{\text{He/Xe}}^i - \varphi_{\text{He/Xe}}^i$ . However Eq. 6.10 results in  $\Delta\Phi_{\text{He/Xe}}^{\text{corr},i} = -\alpha_{\text{He/Xe}}^i - \varphi_{\text{He/Xe}}^i + 2\pi$ . Hence the correction phase  $\Delta\Phi^{\text{corr}}$  has an additional term of  $+2\pi$ , i.e. the number of periods is overestimated by one.

Comparing Eq. 6.7 and Eq. 6.11 shows that the number of periods  $n_{\text{He/Xe}}^i$  is given by

$$n_{\text{He/Xe}}^i = \frac{1}{2\pi} \left( \Phi_{\text{He/Xe}}^{i-1} + \bar{\omega}_{\text{He/Xe}} \cdot \tau - \text{mod} \left( \frac{\Phi_{\text{He/Xe}}^{i-1} + \bar{\omega}_{\text{He/Xe}} \cdot \tau}{2\pi} \right) \right). \quad (6.12)$$

But in the determination of the number of periods  $n_{\text{He/Xe}}^i$  an overestimation or an underestimation by one may occur, if the phases  $\varphi_{\text{He/Xe}}^i$  takes values close to 0 or close to  $2\pi$ . For example, if the phase  $\varphi_{\text{He/Xe}}^i$  is close to 0 and the real frequency  $\omega_{\text{He/Xe}}^i$  of the sub-data set  $i$  is bigger than the mean frequency  $\bar{\omega}_{\text{He/Xe}}$ , it may be possible that  $\beta_{\text{He/Xe}}^i$  is close to  $2\pi$ , i.e.  $\beta_{\text{He/Xe}}^i = 2\pi - \alpha_{\text{He/Xe}}^i$ . This relation is illustrated in Fig. 6.5a. Here it is visible with the naked eye, that the correction phase  $\Delta\Phi_{\text{He/Xe}}^{\text{corr},i}$  should be given by  $\Delta\Phi_{\text{He/Xe}}^{\text{corr},i} = \alpha_{\text{He/Xe}}^i + \varphi_{\text{He/Xe}}^i$ . But the calculation of the correction phase  $\Delta\Phi_{\text{He/Xe}}^{\text{corr},i}$  according to Eq. 6.10 results in  $\Delta\Phi_{\text{He/Xe}}^{\text{corr},i} = \alpha_{\text{He/Xe}}^i + \varphi_{\text{He/Xe}}^i - 2\pi$ . Hence, the number of periods  $n_{\text{He/Xe}}^i$  is underestimated by one. On the contrary, if the phase  $\varphi_{\text{He/Xe}}^i$  is close to  $2\pi$ , i.e.  $\varphi_{\text{He/Xe}}^i = 2\pi - \alpha_{\text{He/Xe}}^i$ , and the real frequency  $\omega_{\text{He/Xe}}^i$  of the sub-data set  $i$  is smaller than the mean frequency  $\bar{\omega}_{\text{He/Xe}}$ , then the modulo of the estimated phase  $\beta_{\text{He/Xe}}^i$  may be close to 0. This relation is shown in Fig. 6.5b. Here it is observable, that the correction phase  $\Delta\Phi_{\text{He/Xe}}^{\text{corr},i}$  should be given by  $\Delta\Phi_{\text{He/Xe}}^{\text{corr},i} = -\alpha_{\text{He/Xe}}^i - \varphi_{\text{He/Xe}}^i$ . But the calculation of the correction phase  $\Delta\Phi_{\text{He/Xe}}^{\text{corr},i}$  according to Eq. 6.10 results in  $\Delta\Phi_{\text{He/Xe}}^{\text{corr},i} = -\alpha_{\text{He/Xe}}^i - \varphi_{\text{He/Xe}}^i + 2\pi$ . Hence, the number of periods  $n_{\text{He/Xe}}^i$  is overestimated by one. So, to avoid an overestimation or an

underestimation of the number of periods by one, the correction phase has to be tested with an if statement:

$$\text{If } |\Delta\Phi_{\text{He/Xe}}^{\text{corr},i}| > +\phi_{\text{test}} \Rightarrow \Phi_{\text{He/Xe}}^i(t_i) - 2\pi \quad (6.13)$$

$$\text{If } |\Delta\Phi_{\text{He/Xe}}^{\text{corr},i}| < -\phi_{\text{test}} \Rightarrow \Phi_{\text{He/Xe}}^i(t_i) + 2\pi. \quad (6.14)$$

Since the maximum value of the correction phase for all 10 measurement runs is  $\Delta\Phi_{\text{He/Xe}}^{\text{corr},i} = \Delta\omega_{\text{He/Xe}}^{\text{max}} \cdot \tau \approx 0.01$  rad, the test phase  $\phi_{\text{test}}$  can take any value between 0.01 rad and  $2\pi$ . In our case we choose  $\phi_{\text{test}} = 4$  rad.

Since there is no error in the determination of the number of periods (Eq. 6.12), the error of the accumulated phase  $\Phi_{\text{He/Xe}}^i(t_i)$  given in Eq. 6.7 is only influenced by the phases  $\varphi_{\text{He/Xe}}^i$  and their errors. Thus, according to Eq. 6.6, the error of the accumulated phase  $\Phi_{\text{He/Xe}}^i(t_i)$  depends on the values  $a_{\text{s,He/Xe}}^i$  and  $a_{\text{c,He/Xe}}^i$  and their errors,  $\delta a_{\text{s,He/Xe}}^i$  and  $\delta a_{\text{c,He/Xe}}^i$ , which are determined by the raw data fit of the sub-data sets using Eq. 6.3. These two parameters are not much correlated (the correlated and uncorrelated errors differ by less than 6%), so that the Gaussian error propagation law can be used to determine the errors

$$\delta\Phi_{\text{He/Xe}}^i(t_i) = \frac{\sqrt{\left(a_{\text{c,He/Xe}}^i\right)^2 \cdot \left(\delta a_{\text{s,He/Xe}}^i\right)^2 + \left(a_{\text{s,He/Xe}}^i\right)^2 \cdot \left(\delta a_{\text{c,He/Xe}}^i\right)^2}}{\left(a_{\text{s,He/Xe}}^i\right)^2 + \left(a_{\text{c,He/Xe}}^i\right)^2}, \quad (6.15)$$

where the derivative of the arctangent function,  $\frac{d}{dx}\arctan(x) = \frac{1}{1+x^2}$ , was used.

### 6.3 Weighted Phase Difference and Phase Shifts

With the accumulated phases of  $^3\text{He}$  and  $^{129}\text{Xe}$  (Eq. 6.11) the weighted phase difference  $\Delta\Phi(t_i)$  can be determined

$$\Delta\Phi(t_i) = \Phi_{\text{He}}(t_i) - \frac{\gamma_{\text{He}}}{\gamma_{\text{Xe}}}\Phi_{\text{Xe}}(t_i). \quad (6.16)$$

In the weighted phase difference the Zeeman term, i.e.  $\Phi_{\text{L,He/Xe}}^i(t_i) = \omega_{\text{L,He/Xe}}^i \cdot t_i = \gamma_{\text{He/Xe}} \cdot B_0(t_i) \cdot t_i$ , is eliminated and thus any dependence on fluctuations and drifts of the magnetic guiding field  $\vec{B}_0$ . Hence, the weighted phase difference is expected to be constant in time. However, as shown in Fig. 6.6, where the weighted phase difference  $\Delta\Phi(t_i)$  of measurement C68 is shown (upper curve), the weighted phase difference mainly increases linearly. Thus, there still exist contributions to the weighted phase difference that are not eliminated by the  $^3\text{He}/^{129}\text{Xe}$  co-magnetometer. The time dependence of the weighted phase difference can be best described by

$$\Delta\Phi_{\text{fit}}(t) = \Phi_0 + \Delta\omega_{\text{lin}} \cdot t - \epsilon_{\text{He}} \cdot A_{0,\text{He}} \cdot T_{2,\text{He}}^* \cdot e^{-t/T_{2,\text{He}}^*} + \epsilon_{\text{Xe}} \cdot A_{0,\text{Xe}} \cdot T_{2,\text{Xe}}^* \cdot e^{-t/T_{2,\text{Xe}}^*}. \quad (6.17)$$

Beside a constant phase offset we have a dominant linear term, that arises due to chemical shift and mainly due to Earth's rotation. The latter one can be calculated theoretically (see



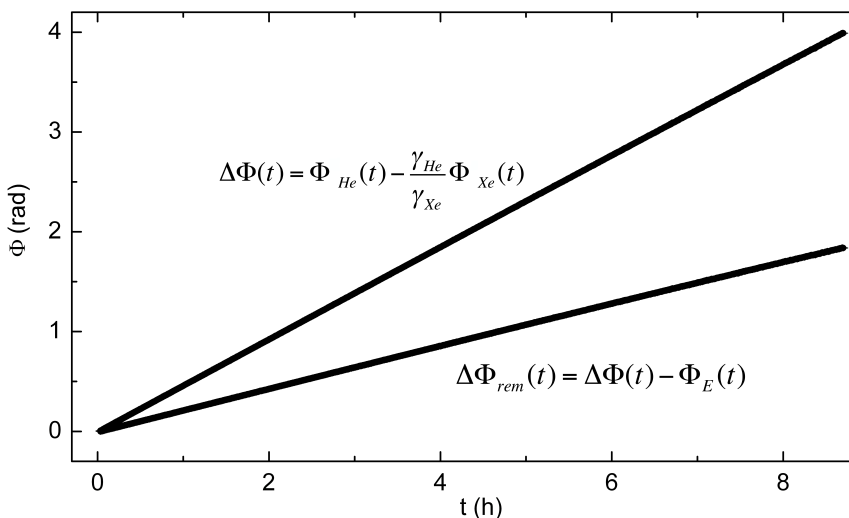


Figure 6.6: Weighted phase difference for measurement run C68 before ( $\Delta\Phi(t)$ ) and after ( $\Delta\Phi_{\text{rem}}(t)$ ) the subtraction of the linear phase shift  $\Phi_E(t)$  due to Earth's rotation (Eq. 6.22). One data point comprises 50 sub-data sets, which corresponds to a time interval of 160 s. The error bars are too small to be visible in the plot.

Sec. 6.3.1) and subtracted from the weighted phase difference  $\Delta\Phi(t)$  to get the remaining phase difference  $\Delta\Phi_{\text{rem}}(t)$  (lower curve in Fig. 6.6). Furthermore, there are two exponential terms, which depend on the transverse relaxation times of helium and xenon and correspond to the Ramsey-Bloch-Siegert self-shifts. All these phase shifts will be explained in detail in the following.

### 6.3.1 Linear Phase Shifts

The linear term of the fit-model given in Eq. 6.17 is the sum of several linear phase shifts that are caused by different effects. The individual linear phase shifts will be explained in the following.

#### Contribution of the Earth's Rotation

The dominant term in the weighted phase difference has a linear time dependence and mainly can be explained by the Earth's rotation ( $\Omega_E = 7.2921150(1) \cdot 10^{-5}$  rad/s [141]), i.e. the rotation of the SQUID detectors ( $\omega_{\text{det}}$ ) with respect to the precessing spins. Since the magnetic moments of  $^3\text{He}$  and  $^{129}\text{Xe}$  as well as the SQUID detectors are rotating in the same sense with respect to the magnetic guiding field<sup>4</sup>, a reduced Larmor precession frequency is

<sup>4</sup>The sense of Earth's rotation is right-handed with respect to the Earth's rotation axis. Since the gyromagnetic ratios  $\gamma$  of both,  $^3\text{He}$  and  $^{129}\text{Xe}$ , are negative (Eq. 3.6 and Eq. 3.7), the total nuclear magnetic moments (Eq. 3.16) are negative as well. According to the Bloch equations given in Eq. 3.15, for a magnetic guiding field  $\vec{B}_0 = -B_0 \cdot \hat{e}_x$  (coordinate system of BMSR-2) the sense of rotation of the total nuclear magnetic moments is right-handed with respect to the field direction and to the Earth's rotation axis. Hence, the Earth and the magnetic moments of  $^3\text{He}$  and  $^{129}\text{Xe}$  rotate in the same sense.

measured in the laboratory system, which is given by  $\omega_{\text{He}/\text{Xe}} = \omega_{\text{L,He}/\text{Xe}} - \omega_{\text{det}}$ . The frequency shift caused by the rotating detector can be calculated by a coordinate transformation from the laboratory system  $(X, Y, Z)$  to the Earth system  $(X', Y', Z')$ . The unit vector in field direction, i.e the axis of precession  $\hat{\omega}_{\text{L}}$ , in the laboratory system is given by (see Fig. 6.7, right side)

$$\hat{\omega}_{\text{L}} = \frac{\vec{\omega}_{\text{L}}}{\omega_{\text{L}}} = \begin{pmatrix} -\cos(-\rho) \\ \sin(-\rho) \\ 0 \end{pmatrix} = \begin{pmatrix} -\cos \rho \\ -\sin \rho \\ 0 \end{pmatrix}. \quad (6.18)$$

Here  $\rho = 28^\circ$  is the angle between the magnetic field direction and the north direction. Since the latitude  $\Theta = 52.5164^\circ$ , where the PTB Berlin is located [142], is known,  $\hat{\omega}_{\text{L}}$  can be transformed into the rotating Earth system  $(X', Y', Z')$ :

$$\hat{\omega}'_{\text{L}} = \begin{pmatrix} \sin \Theta & 0 & \cos \Theta \\ 0 & 0 & 1 \\ -\cos \Theta & 0 & \sin \Theta \end{pmatrix} \cdot \begin{pmatrix} -\cos \rho \\ -\sin \rho \\ 0 \end{pmatrix} = \begin{pmatrix} -\sin \Theta \cos \rho \\ -\sin \rho \\ \cos \Theta \cos \rho \end{pmatrix}. \quad (6.19)$$

By composing the scalar product  $\hat{\Omega}_{\text{E}} \cdot \hat{\omega}'_{\text{L}}$ , the angle  $\chi$  between the Earth's rotation axis and the axis of spin precession can be determined

$$\cos \chi = \hat{\Omega}_{\text{E}} \cdot \hat{\omega}'_{\text{L}} = \begin{pmatrix} 0 \\ 0 \\ 1 \end{pmatrix} \cdot \begin{pmatrix} -\sin \Theta \cos \rho \\ -\sin \rho \\ \cos \Theta \cos \rho \end{pmatrix} = \cos \Theta \cos \rho. \quad (6.20)$$

In our case the angle  $\chi$  results in  $57.33^\circ$ . The frequency shift of the  $^3\text{He}$  and  $^{129}\text{Xe}$  Larmor frequencies caused by the rotating detector can be calculated to be

$$\omega_{\text{det}} = |\Omega_{\text{E}}| \cos \chi. \quad (6.21)$$

The contribution of Earth's rotation to the weighted phase difference then is given by

$$\begin{aligned} \Phi_{\text{E}}(t) &= \Delta\omega_{\text{E}} \cdot t = -\left(1 - \frac{\gamma_{\text{He}}}{\gamma_{\text{Xe}}}\right) \omega_{\text{det}} \cdot t \\ &= 6.87263 \cdot 10^{-5} \frac{\text{rad}}{\text{s}} \cdot t. \end{aligned} \quad (6.22)$$

This linear phase shift  $\Phi_{\text{E}}(t)$  can be subtracted from the weighted phase difference  $\Delta\Phi(t)$ . The temporal dependence of the remaining phase difference  $\Delta\Phi_{\text{rem}}(t) = \Delta\Phi(t) - \Phi_{\text{E}}(t)$  is shown in Fig. 6.6 (lower curve). It is clearly visible that  $\Delta\Phi_{\text{rem}}(t)$  still contains phase shifts. A part of the remaining linear phase shift can be explained due to the uncertainty in determination of the angle  $\rho$  between the magnetic guiding field and the north direction. The uncertainty in the angle  $\rho$  is assumed to be below  $1^\circ$  which leads to a maximum frequency uncertainty of  $\delta(\Delta\omega_{\text{E}}) = 6.3 \cdot 10^{-7} \text{ rad/s}$  and hence to a linear phase shift in the the remaining phase difference  $\Delta\Phi_{\text{rem}}(t)$  of

$$|\delta\Phi_{\text{E}}(t)| \leq 6.3 \cdot 10^{-7} \frac{\text{rad}}{\text{s}} \cdot t. \quad (6.23)$$

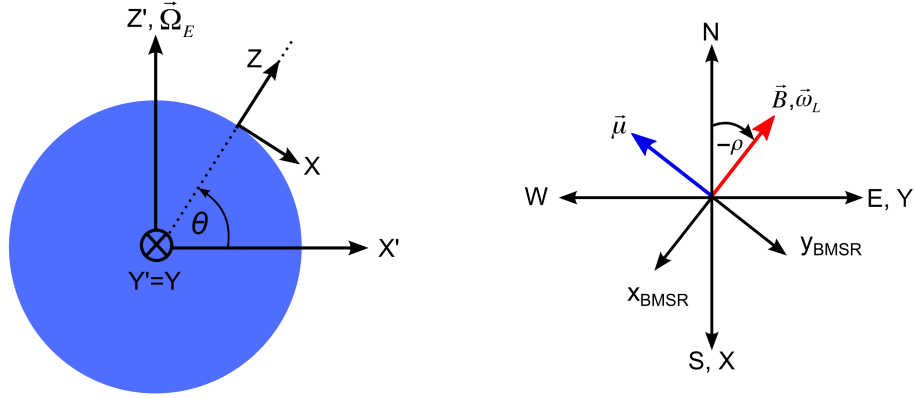


Figure 6.7: The Earth's rotating coordinate system and direction of the magnetic guiding field inside BMSR-2. *Left:* The Earth's rotating coordinate system  $(X', Y', Z')$  is defined such that the  $Z'$ -axis is parallel to the Earth's rotation axis  $(\Omega_E)$ . The laboratory system  $(X, Y, Z)$  is located at Berlin where the angle  $\Theta$  corresponds to the latitude. The  $Y$ - and  $Y'$ -axis of the two different coordinate systems are parallel. *Right:* The  $X$ -axis of the laboratory system points to the southern and the  $Y$ -axis to the eastern direction. The magnetic guiding field inside BMSR-2 points to the north-eastern direction ( $-x$ -direction in the BMSR-2 coordinate system) and the angle between the direction of the magnetic guiding field and the north direction is given by  $\rho = 28^\circ$ .

Here the uncertainties of  $\Omega_E$  and  $\Theta$  were neglected, since they are known with high precision. However the uncertainty  $|\delta\Phi_E(t)|$  does not bother us, since the temporal dependence of the remaining phase difference  $\Delta\Phi_{\text{rem}}(t) = \Delta\Phi(t) - \Phi_E(t)$  still can be described by the fit-model given in Eq. 6.17. Hence the uncertainty of the determination of the linear term due to Earth's rotation is included in the linear term of the remaining phase  $\Delta\Phi_{\text{rem}}(t)$ .

### Gyromagnetic Ratios and Chemical Shift

Another part of the linear shift in the remaining phase  $\Delta\Phi_{\text{rem}}(t)$  can be explained by deviations of the gyromagnetic ratios of  $^3\text{He}$  and  $^{129}\text{Xe}$  from their literature values<sup>5</sup>, which are given by  $\gamma_{\text{He}} = 20.37894730(56) \cdot 10^7 \frac{\text{rad}}{\text{T}\cdot\text{s}}$  and  $\gamma_{\text{Xe}} = 7.39954378(50) \cdot 10^7 \frac{\text{rad}}{\text{T}\cdot\text{s}}$  [92]. These values are valid for the naked nuclei of  $^3\text{He}$  and  $^{129}\text{Xe}$ . The ratio of the gyromagnetic ratios  $\frac{\gamma_{\text{He}}}{\gamma_{\text{Xe}}}$  used in the weighted phase difference (6.16) then becomes

$$\frac{\gamma_{\text{He}}}{\gamma_{\text{Xe}}} = 2.75408159(20) . \quad (6.24)$$

However, within the  $^3\text{He}$  and  $^{129}\text{Xe}$  atoms, the nuclei are shielded by the electrons of the atomic shell against an external field  $\vec{B}_0$  (diamagnetic shielding). Hence, the nuclei see a slightly different external field, which leads to a constant shift in the Larmor frequency,

<sup>5</sup>The gyromagnetic ratio of xenon was recalculated with the value of the magnetic moment of the proton  $\mu_p$  [92].

$\Delta\omega_{L,CS}$ , which is called *chemical shift* (CS). Since for our measurements, a gas mixture of  $^3\text{He}$ ,  $^{129}\text{Xe}$  and  $\text{N}_2$  is filled into a cylindrical measurement cell, the interactions of the noble gas atoms with the wall of the measurement cell [143] as well as the interactions with each other [144] and with the buffer gas  $\text{N}_2$  [145] lead to an increase of the chemical shift. This can be explained by a shift of the electrons of the atomic shell of the  $^3\text{He}$  and  $^{129}\text{Xe}$  atoms due to the collisions of the gas atoms. Thus the diamagnetic shielding against an external field  $\vec{B}_0$  is changed.

Since the pressure  $p$  and the temperature  $T$  can be assumed to be constant during one measurement run, as well as the magnetic guiding field (except for small linear changes (see Fig. 4.2)), the total chemical shift is constant to leading order, which leads to a linear term in the weighted phase difference

$$\Delta\Phi_{CS} = \left( \Delta\omega_{L,He,CS} - \frac{\gamma_{\text{He}}}{\gamma_{\text{Xe}}} \Delta\omega_{L,Xe,CS} \right) \cdot t. \quad (6.25)$$

### Field gradient induced shifts

Cates et al. showed in [146], that for a spin polarized gas in a spherical volume of radius  $R$ , static and oscillating magnetic field gradients produce shifts in the spin precession frequency. The total magnetic guiding field then is given by

$$\vec{B}(\vec{r}, t) = \vec{B}_{\text{stat}}(\vec{r}) + \vec{B}_{\text{osc}}(\vec{r}), \quad (6.26)$$

where the static magnetic field  $\vec{B}_{\text{stat}}(\vec{r})$  is the sum of a static mean field  $\vec{B}_0$ , that is oriented in x-direction, and a static inhomogeneous field  $\vec{B}_1(\vec{r})$ , and the oscillating magnetic field is given by  $\vec{B}_{\text{osc}}(\vec{r}) = \vec{B}'_2(\vec{r}) \cos(\omega t) + \vec{B}''_2(\vec{r}) \sin(\omega t)$ . For the total magnetic field  $\vec{B}(\vec{r}, t)$  the frequency shift was calculated to be

$$\begin{aligned} \Delta\omega_{\text{grad}} &= \omega_{\text{grad,stat}} + \omega_{\text{grad,osc}} \\ &= R^2 \gamma B_0 \sum_n \frac{\gamma^2 (|\vec{\nabla} B_{1,y}|^2 + |\vec{\nabla} B_{1,z}|^2)}{x_{1n}^2 (x_{1n}^2 - 2) (D^2 x_{1n}^4 R^{-4} + \gamma^2 B_0^2)} \\ &\quad + \sum_n \frac{R^2 \gamma^2}{x_{1n}^2 (x_{1n}^2 - 2)} \left( \frac{|\vec{\nabla} B_{2-}|^2 (\omega_0 - \omega)}{D^2 x_{1n}^4 R^{-4} + (\omega_0 - \omega)^2} + \frac{|\vec{\nabla} B_{2+}|^2 (\omega_0 + \omega)}{D^2 x_{1n}^4 R^{-4} + (\omega_0 + \omega)^2} \right), \end{aligned} \quad (6.27)$$

with the gyromagnetic ratio  $\gamma$ , the diffusion constant  $D$  and the mean Larmor frequency  $\omega_0 = \gamma \cdot |\vec{B}_0|$ .  $x_{1n}$  ( $n = 1, 2, 3, \dots$ ) are the zeros of the derivative of the spherical Bessel function ( $\frac{d}{dx} j_1(x_{1n}) = 0$ ) and  $B_{2\pm} = B_{2x} \pm iB_{2y}$ .

The first term  $\Delta\omega_{\text{grad,stat}}$  of Eq. (6.27) describes the frequency shift due to the static, transverse field gradients and the second term  $\Delta\omega_{\text{grad,osc}}$  arises due to the gradients of the oscillating field. Assuming that both type of gradients are constant during the measurement run, the field gradient induced frequency shifts are also constant and yield to a linear shift in the weighted phase difference

$$\Delta\Phi_{\text{grad}} = \left( \Delta\omega_{\text{grad,He}} - \frac{\gamma_{\text{He}}}{\gamma_{\text{Xe}}} \Delta\omega_{\text{grad,Xe}} \right) \cdot t. \quad (6.28)$$

In our experiment cylindrical measurement cells with length  $L$  and diameter  $\odot_L$  were used. As already mentioned before, these cells can be approximated by spherical cells with radius  $R = L/2 = \odot_L/2$ . Hence, the frequency shifts  $\Delta\omega_{\text{grad}}^{\text{He/Xe}}$  of helium and xenon due to field gradients can be described by Eq. 6.27. The frequency shift  $\Delta\omega_{\text{grad,stat}}$  then occurs due to small field gradients of the magnetic guiding field  $\vec{B}_0$ . However the frequency shift  $\Delta\omega_{\text{grad,osc}}$  may occur, too: The total nuclear magnetic moments of the polarized atoms of  $^3\text{He}$  and  $^{129}\text{Xe}$  precess around the direction of the magnetic guiding field  $\vec{B}_0$ . Hence, the precessing  $^3\text{He}$  and  $^{129}\text{Xe}$  atoms produce magnetic fields  $\vec{B}_{\text{spin},G}$  (with  $G = \text{He, Xe}$ ), which precess around the direction of the magnetic guiding field. These magnetic fields are characterized by small field gradients. If the polarized spins see the magnetic field gradients of the oscillating field  $\vec{B}_{\text{spin},G}$  of the own gas species (gradient self-shift) or the one of the other gas species (gradient cross-shift), the spin precession frequency of  $^3\text{He}$  and  $^{129}\text{Xe}$  is shifted by  $\Delta\omega_{\text{grad,osc}}$ .

### Gravitational shift

Due to gravity the difference in the molar masses of  $^3\text{He}$  and  $^{129}\text{Xe}$  ( $M_{3\text{He}} = 3.016 \frac{\text{g}}{\text{mol}}$  and  $M_{129\text{Xe}} = 128.955 \frac{\text{g}}{\text{mol}}$ ) leads to a shift in the center of masses of the  $^3\text{He}$  and the  $^{129}\text{Xe}$  gas, where the center of mass of  $^{129}\text{Xe}$  lies deeper than the one of  $^3\text{He}$ . Due to this spatial shift and due to gradients of the magnetic guiding field, on average  $^3\text{He}$  and  $^{129}\text{Xe}$  do not see the same magnetic field. That means, that in the weighted frequency difference the Zeeman term is not canceled out completely, but a constant frequency shift

$$\Delta\omega_{\text{grav}} = \omega_{\text{He}} - \frac{\gamma_{\text{He}}}{\gamma_{\text{Xe}}} \omega_{\text{Xe}} = \gamma_{\text{He}} \cdot (B_{\text{Xe}} + \Delta B) - \gamma_{\text{He}} \cdot B_{\text{Xe}} = \gamma_{\text{He}} \cdot \Delta B \quad (6.29)$$

remains, which is called *gravitational shift*.

For calculation of the gravitational shift  $\Delta\omega_{\text{grav}}$  the difference  $\Delta z$  of the center of masses of the two gas species has to be calculated: The two gases are filled into a cylindrical measurement cell with diameter  $\odot_L = 6\text{cm}$  and length  $L = 6\text{cm}$ . In the interest of simplification, the center of mass in  $z$ -direction is only calculated for the projection of the cell in the  $zx$ -plane, which corresponds to a circle with radius  $R$  (see Fig. 6.8). The mean value of all possible  $z$ -coordinates can be calculated by

$$\bar{z} = \frac{1}{A} \int z \cdot dA. \quad (6.30)$$

Here  $A = \pi R^2$  is the area of the circle and  $dA = dz \cdot dx$  the element of area. The coordinate  $z$  can take values between  $-R$  and  $R$ , whereas  $x$  can take values between  $-\sqrt{R^2 - z^2}$  and  $\sqrt{R^2 - z^2}$  (see Fig. 6.8). Hence, the expression of  $\bar{z}$  merges into

$$\begin{aligned} \bar{z} &= \frac{1}{\pi R^2} \int_{-R}^R dz z \int_{-\sqrt{R^2 - z^2}}^{\sqrt{R^2 - z^2}} dx \\ &= \frac{2}{\pi R^2} \int_{-R}^R dz z \int_0^{\sqrt{R^2 - z^2}} dx \\ &= \frac{2}{\pi R^2} \int_{-R}^R dz z \sqrt{R^2 - z^2}. \end{aligned} \quad (6.31)$$

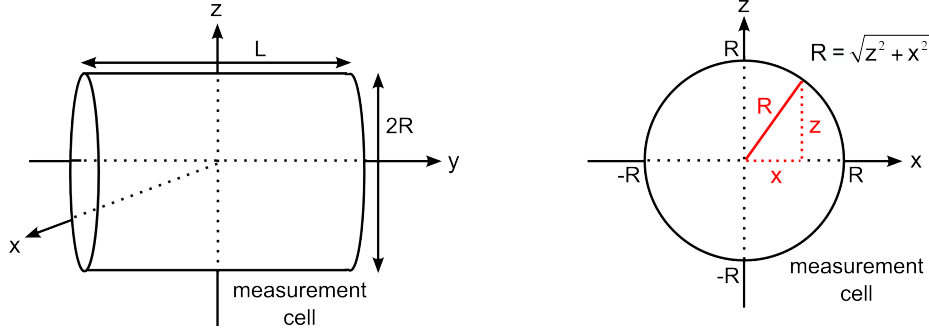


Figure 6.8: Illustration of calculation of the center of mass in  $z$ -direction. *Left*: Cylindrical measurement cell in the coordinate system of the BMSR-2. Due to symmetry reasons, the center of the cell was placed in the point of origin. *Right*: For calculation of the center of mass in  $z$ -direction, only the projection of the cylindrical measurement cell into the  $zx$ -plane is considered. The projection conforms to a circle with radius  $R = \sqrt{x^2 + z^2}$ . Hence, for a given value of the coordinate  $z$ , the coordinate  $x$  can take only values between  $-\sqrt{R^2 - z^2}$  and  $\sqrt{R^2 - z^2}$ .

Using the barometric formula

$$p(z) = p_0 \exp\left(-\frac{Mg_0}{R_G T} z\right), \quad (6.32)$$

which gives the gas pressure  $p(z)$  at height  $z$  for each gas species – where  $p_0$  is the pressure at the bottom of the measurement cell, i.e.  $p_0 = p(z = -R)$ ,  $R_G$  is the molar gas constant ( $R_G = 8.413 \frac{\text{J}}{\text{mol K}}$ ),  $T$  the temperature,  $M$  the molar mass and  $g_0 = 9.81 \frac{\text{m}}{\text{s}^2}$  the gravitational acceleration – the center of mass in  $z$ -direction of each gas species can be calculated by the weighted mean value of all possible  $z$ -coordinates

$$\text{CM} = \frac{\frac{2}{\pi R^2} \int_{-R}^R dz z \sqrt{R^2 - z^2} p(z)}{\frac{2}{\pi R^2} \int_{-R}^R dz \sqrt{R^2 - z^2} p(z)}. \quad (6.33)$$

The difference in the center of masses (CM) for our cylindrical measurement cells then results in

$$\Delta z = \text{CM}_{\text{He}} - \text{CM}_{\text{Xe}} \approx 1.2 \cdot 10^{-7} \text{ m}. \quad (6.34)$$

If a constant field gradient in  $z$ -direction of  $G = \frac{\Delta B}{\Delta z} \approx 27.2 \frac{\text{pT}}{\text{cm}}$  (see Tab. 4.1) is assumed, the field difference amounts to  $\Delta B = G \cdot \Delta z = 0.2 \text{ fT}$ . According to Eq. 6.29, this leads to a linear phase shift of

$$|\Delta \Phi_{\text{grav}}| = \gamma_{\text{He}} \cdot \Delta B \cdot t = 4.1 \cdot 10^{-8} \frac{\text{rad}}{\text{s}} \cdot t. \quad (6.35)$$

This gravitational phase shift is only caused by gradients of the magnetic guiding field. However, in Sec. 6.7 it will be demonstrated that if the BGO crystal produce magnetic field gradients, the movement of the BGO crystal changes the field gradients in the vicinity of the measurement cell. Hence, the movement of the BGO crystal may mimic a pseudoscalar frequency shift or even compensate the effect we are looking for.

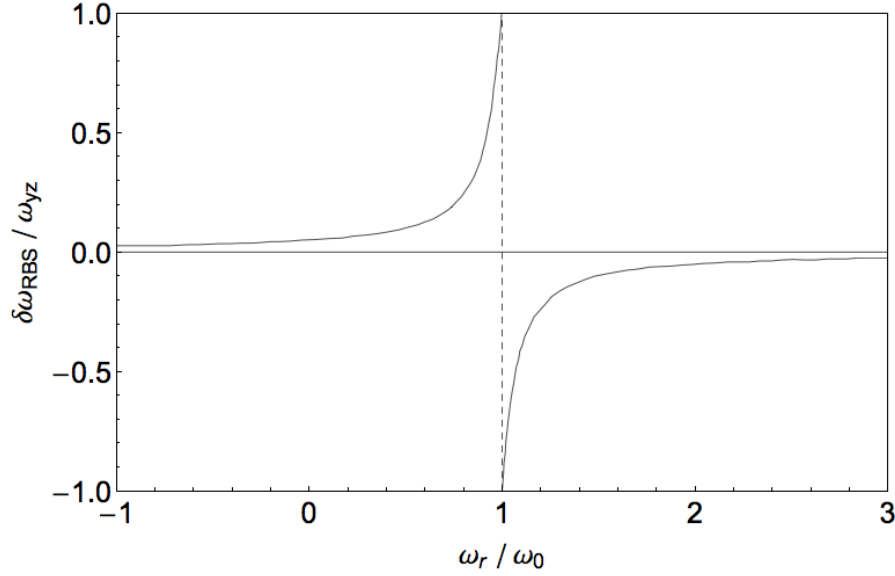


Figure 6.9: Ramsey-Bloch-Siegert shift  $\delta\omega_{\text{RBS}}$ , which is caused by a magnetic field  $\vec{B}_{yz}$  that rotates perpendicular to the magnetic guiding field  $\vec{B}_0 = B_0 \cdot \hat{e}_x$ . In the graph  $\delta\omega_{\text{RBS}}$  is plotted against the angular frequency  $\omega_r$  of the rotating magnetic field  $\vec{B}_{yz}$ . Thereby  $\delta\omega_{\text{RBS}}$  is normalized to the frequency  $\omega_{yz} = \gamma \cdot B_{yz}$  and  $\omega_r$  is normalized to the frequency  $\omega_0 = \gamma \cdot B_0$ . If the rotating magnetic field  $\vec{B}_{yz}$  is on resonance with the magnetic guiding field, i.e.  $\omega_r = \omega_0$ , the RBS-shift  $\delta\omega_{\text{RBS}}$  has peak values of  $\pm\omega_{yz}$  and thus the RBS-shift vanishes.

### 6.3.2 Exponential Phase Shifts

According to Ramsey [147], Bloch and Siegert [148], the spin precession frequency  $\omega_L = \omega_0 = \gamma \cdot B_0$  of a neutral particle in a magnetic guiding field  $\vec{B}_0 = B_0 \cdot \hat{e}_x$  is shifted by irradiating a magnetic field  $\vec{B}_{yz}$  that oscillates at angular velocity  $\omega_r$  in a plane perpendicular to the magnetic guiding field. The Larmor frequency then is given by  $\omega_L = \omega_0 + \delta\omega_{\text{RBS}}$ . The frequency shift  $\delta\omega_{\text{RBS}}$  is called *Ramsey-Bloch-Siegert shift (RBS-shift)* and is defined as

$$\delta\omega_{\text{RBS}} = \begin{cases} +\sqrt{\Delta\omega^2 + \omega_{yz}^2} - \Delta\omega & \text{for } \omega_r/\omega_0 < 1 \\ -\sqrt{\Delta\omega^2 + \omega_{yz}^2} + \Delta\omega & \text{for } \omega_r/\omega_0 > 1 \end{cases} \quad (6.36)$$

where  $\omega_{yz} = \gamma \cdot B_{yz}$  and  $\Delta\omega = |\omega_0 - \omega_r|$ . In Fig. 6.9 the RBS-shift  $\delta\omega_{\text{RBS}}$  is plotted against the angular frequency  $\omega_r$  of the rotating magnetic field  $\vec{B}_{yz}$ . If  $\vec{B}_{yz}$  is on resonance with the magnetic guiding field, i.e.  $\omega_r = \omega_0$ , the RBS-shift  $\delta\omega_{\text{RBS}}$  takes the values  $\pm\omega_{yz}$ . Hence, in case of resonance the RBS-shift  $\delta\omega_{\text{RBS}}$  vanishes. For  $\vec{B}_{yz}$  outside of resonance, i.e.  $|\omega_r/\omega_0| < 1$  or  $|\omega_r/\omega_0| > 1$ , the absolute value of the RBS-shift  $\delta\omega_{\text{RBS}}$  decreases. Depending on the

relative sizes of  $\Delta\omega$  and  $\omega_{yz}$  two different approximations of  $\delta\omega_{\text{RBS}}$  can be derived

$$\begin{aligned}
1. \quad \delta\omega_{\text{RBS}} &= \pm\Delta\omega\sqrt{1 + \left(\frac{\omega_{yz}}{\Delta\omega}\right)^2} \mp \Delta\omega \\
&\approx \pm\Delta\omega\left(1 + \frac{1}{2}\left(\frac{\omega_{yz}}{\Delta\omega}\right)^2\right) \mp \Delta\omega && (\Delta\omega \gg \omega_{yz}) \\
&= \pm\Delta\omega\frac{1}{2}\left(\frac{\omega_{yz}}{\Delta\omega}\right)^2 \\
&= \pm\frac{\gamma^2 B_{yz}^2}{2\Delta\omega} && (6.37)
\end{aligned}$$

$$\begin{aligned}
2. \quad \delta\omega_{\text{RBS}} &= \pm\omega_{yz}\sqrt{1 + \left(\frac{\Delta\omega}{\omega_{yz}}\right)^2} \mp \Delta\omega \\
&\approx \pm\omega_{yz}\left(1 + \frac{1}{2}\left(\frac{\Delta\omega}{\omega_{yz}}\right)^2 - \dots\right) \mp \Delta\omega && (\Delta\omega \ll \omega_{yz}) \\
&\approx \pm\omega_{yz} . && (6.38)
\end{aligned}$$

In our experiment nuclear spin polarized  $^3\text{He}$  and  $^{129}\text{Xe}$  atoms precess with the respective Larmor frequencies  $\omega_{0,\text{He}} \approx 2\pi \cdot 11.4 \text{ Hz}$  and  $\omega_{0,\text{Xe}} \approx 2\pi \cdot 4.1 \text{ Hz}$  in a magnetic guiding field of  $\vec{B}_0 = 0.35 \mu\text{T} \cdot \hat{e}_x$ . The precessing spins produce magnetic fields  $\vec{B}_{\text{spin},G}$  (with  $G = \text{He}, \text{Xe}$ ) which oscillate at an angular frequency  $\omega_{0,G}$  perpendicular to the magnetic guiding field  $\vec{B}_0$ . These magnetic fields are proportional to the magnetization respectively to the amplitude  $A_G(t)$  of the precessing spins. Hence the magnetic fields  $\vec{B}_{\text{spin},G}$  decrease exponentially with the transverse relaxation times  $T_{2,G}^*$ :

$$\begin{aligned}
\vec{B}_{\text{spin},G} &= B_{yz,G}(t) (\hat{e}_z \cos(\omega_{0,G}t) + \hat{e}_y \sin(\omega_{0,G}t)) \\
&= \xi_G \cdot A_{0,G} \cdot e^{-\frac{t}{T_{2,G}^*}} \cdot (\hat{e}_z \cos(\omega_{0,G}t) + \hat{e}_y \sin(\omega_{0,G}t)) . && (6.39)
\end{aligned}$$

$A_{0,G} = A_G(t=0 \text{ s})$  is the initial amplitude of the spin precession signal and  $\xi_G$  is a proportionality factor. Now, the nuclear spin polarized  $^3\text{He}$  and  $^{129}\text{Xe}$  atoms see these oscillating magnetic fields  $\vec{B}_{\text{spin},G}$ , which cause a RBS-shift in their spin precession frequencies, i.e.  $\omega_{L,G} = \omega_{0,G} + \delta\omega_{\text{RBS},G}$ . Here it is necessary to distinguish between the RBS cross-shift and the RBS self-shift, which will be explained in detail in the following.

### RBS cross-shift

In our experiment the spin precession frequency of gas species  $G1$  may be shifted by the oscillating magnetic field  $\vec{B}_{\text{spin},G2}$  produced by the other gas species  $G2$ . This shift is called *RBS cross-shift* with  $\omega_0 = \omega_{0,G1}$ ,  $\omega_r = \omega_{0,G2}$  and  $\omega_{yz} = \omega_{yz,G1} = \gamma_{G1} \cdot B_{yz,G2}$ . The field  $\vec{B}_{\text{spin},G2}$  is off-resonant, i.e.  $\omega_r/\omega_0 = \omega_{0,\text{He}}/\omega_{0,\text{Xe}} = 2.75$  or  $\omega_r/\omega_0 = \omega_{0,\text{Xe}}/\omega_{0,\text{He}} = 1/2.75$ . In both cases the expected RBS cross-shift is small compared to  $\omega_{yz}$  as shown in Fig. 6.9.

For both gas species, the frequency difference  $\Delta\omega$  is given by  $\Delta\omega = |\omega_{0,\text{Xe}} - \omega_{0,\text{He}}| = |\omega_{0,\text{He}} - \omega_{0,\text{Xe}}| \approx 2\pi \cdot 7.3 \text{ Hz}$ . The frequency  $\omega_{yz}$  for  $^3\text{He}$  and  $^{129}\text{Xe}$  can be estimated as follows: The mean values of the initial amplitudes of the  $^3\text{He}$  and  $^{129}\text{Xe}$  spin precession



signals are given by  $\bar{A}_{0,\text{He}} = 12.2$  pT and  $\bar{A}_{0,\text{Xe}} = 4.8$  pT, respectively (see Tab. 6.1). These values were measured at a distance of  $z = 5.8$  cm from the center of the measurement cell. It is assumed, that the amplitude of the oscillating field  $B_{yz,G2}$  approximately is given by the dipole field of  $^3\text{He}$ , respectively of  $^{129}\text{Xe}$ , at a distance of  $z = 3$  cm from the center of the measurement cell. Thus, according to Eq. 3.29 the amplitudes of the oscillating fields can be calculated to be  $B_{yz,\text{He}} \approx \bar{A}_{0,\text{He}} \cdot \left(\frac{5.8 \text{ cm}}{3.0 \text{ cm}}\right)^3 = 128$  pT and  $B_{yz,\text{Xe}} \approx \bar{A}_{0,\text{Xe}} \cdot \left(\frac{5.8 \text{ cm}}{3.0 \text{ cm}}\right)^3 = 53$  pT, respectively. With these values the frequency  $\omega_{yz}$  results in  $\omega_{yz,\text{He}} \approx 2\pi \cdot 108$  mHz for  $^3\text{He}$  and in  $\omega_{yz,\text{Xe}} \approx 2\pi \cdot 9$  mHz for  $^{129}\text{Xe}$ . From this it follows, that  $\Delta\omega \gg \omega_{yz}$ . Thus according to Eq. 6.37 and Eq. 6.39 the RBS cross-shift is given by

$$\delta\omega_{\text{RBS},G1}^{\text{cross}}(t) = \pm \frac{\gamma_{G1}^2 \cdot B_{yz,G2}(t)^2}{2\Delta\omega} = \pm \frac{\gamma_{G1}^2 \cdot \xi_{G2}^2 \cdot A_{0,G2}^2}{2\Delta\omega} \cdot e^{-\frac{2t}{T_{2,G2}^*}}, \quad (6.40)$$

where the negative sign holds for the change of the  $^{129}\text{Xe}$  spin precession frequency and the positive sign for the change of the  $^3\text{He}$  spin precession frequency.

By integration of the RBS cross-shift over time the accumulated phase can be calculated to

$$\begin{aligned} \delta\Phi_{\text{RBS},G1}^{\text{cross}}(t) &= \int_0^t \delta\omega_{\text{RBS},G1}^{\text{cross}}(t') dt' \\ &= \text{const}_{G1} \mp \frac{\gamma_{G1}^2 \cdot \xi_{G2}^2 \cdot A_{0,G2}^2}{2\Delta\omega} \cdot \frac{T_{2,G2}^*}{2} \cdot e^{-\frac{2t}{T_{2,G2}^*}}, \end{aligned} \quad (6.41)$$

where the positive sign corresponds to the phase shift of  $^{129}\text{Xe}$  and the negative sign to the phase shift of  $^3\text{He}$ . The total contribution of the RBS cross-shifts of  $^3\text{He}$  and  $^{129}\text{Xe}$  to the weighted phase difference then is given by

$$\begin{aligned} \Delta\Phi_{\text{RBS}}^{\text{cross}}(t) &= \delta\Phi_{\text{RBS},\text{He}}^{\text{cross}}(t) - \frac{\gamma_{\text{He}}}{\gamma_{\text{Xe}}} \cdot \delta\Phi_{\text{RBS},\text{Xe}}^{\text{cross}}(t) \\ &= -\frac{\gamma_{\text{He}}^2 \cdot \xi_{\text{Xe}}^2 \cdot A_{0,\text{Xe}}^2}{2\Delta\omega} \cdot \frac{T_{2,\text{Xe}}^*}{2} \cdot e^{-\frac{2t}{T_{2,\text{Xe}}^*}} + \text{const}_{\text{He}} \\ &\quad - \frac{\gamma_{\text{Xe}}\gamma_{\text{He}} \cdot \xi_{\text{He}}^2 \cdot A_{0,\text{He}}^2}{2\Delta\omega} \cdot \frac{T_{2,\text{He}}^*}{2} \cdot e^{-\frac{2t}{T_{2,\text{He}}^*}} + \frac{\gamma_{\text{He}}}{\gamma_{\text{Xe}}} \cdot \text{const}_{\text{Xe}}. \end{aligned} \quad (6.42)$$

Hence, in the weighted phase difference the RBS cross-shifts of  $^3\text{He}$  and  $^{129}\text{Xe}$  add with the same sign. Since the RBS cross-shifts are small compared to the other phase shifts, the RBS cross-shifts were not included in the fit model given by Eq. 6.17. If the RBS cross-shifts were implemented to the fit model, the  $\chi^2/dof$  value of the fit of the weighted phase difference would be upgraded nonessential. Hence, it was decided that the RBS cross-shifts are negligible. This has the advantage that in the fit model of the weighted phase difference less fit parameters occur. However, more recent measurements that were performed in march 2012 to search for a Lorentz-violating frequency shift, achieved a higher measurement sensitivity regarding the spin precession frequency due to both a higher signal-to-noise ratio and longer  $T_2^*$  times for  $^3\text{He}$  as well as for  $^{129}\text{Xe}$ . In view of the higher measurement sensitivity of these measurements, the RBS cross-shifts cannot be neglected anymore.

### RBS self-shift

If the magnetic guiding field  $\vec{B}_0$  is absolutely homogeneous, the spin precession frequency of the gas species  $G$  is not influenced by the rotating magnetic field  $\vec{B}_{\text{spin},G}$ , which is produced by the own gas species  $G$ . Here it is of no consequence whether the measurement cell is an ideal sphere or has any other shape. However, if the magnetic guiding field  $\vec{B}_0$  is not absolutely homogeneous but characterized by finite field gradients, the spin precession frequency of the gas species  $G$  is shifted by its own rotating magnetic field  $\vec{B}_{\text{spin},G}$ . This effect will be explained in detail in the following: For a start, the measurement cell is assumed to be an ideal sphere and is placed in a magnetic guiding field  $\vec{B}_0$  with field gradients. If the field gradients are non-linear, the field gradients in a small volume  $V_B$  of the measurement cell may differ from the ones in the remaining volume  $V_A = V_{\text{tot}} - V_B$ , where  $V_{\text{tot}}$  is the total volume of the measurement cell and  $V_A > V_B$  (see Fig. 6.10a). Now if the measurement cell is not an ideal sphere but, for example, has a small stem, similar considerations as for the spherical measurement cell can be applied. That means, that the main part of the measurement cell can be approximated by an ideal sphere with volume  $V_A$ , and the stem as a second small sphere with volume  $V_B$ , where  $V_A > V_B$  (see Fig. 6.10b). In both cases the single spins of gas species  $G$  in volume  $V_A$  and volume  $V_B$  see different magnetic fields and thus precess with different Larmor frequencies, i.e.  $\omega_{0,G,A} = \gamma_G \cdot B_0 \neq \omega_{0,G,B} = \gamma_G \cdot (B_0 - \Delta B)$ , where  $\Delta B$  corresponds to the change of the magnetic guiding field  $\vec{B}_0$  due to field gradients. Furthermore, the spins of the polarized gas in volume  $V_A$  and  $V_B$  produce magnetic fields,  $\vec{B}_{\text{spin},G,A}$  and  $\vec{B}_{\text{spin},G,B}$ , which rotate with respective frequencies,  $\omega_{r,G,A} = \omega_{0,G,A}$  and  $\omega_{r,G,B} = \omega_{0,G,B}$ , around the direction of the magnetic guiding field  $\vec{B}_0$ . Thus, the rotating magnetic field  $\vec{B}_{\text{spin},G,B}$  of volume  $V_B$  leads to a shift  $\delta\omega_{\text{RBS},A}$  in the spin precession frequency of volume  $V_A$  and vice versa. The total frequency shift is called *RBS self-shift* and is given by

$$\delta\omega_{\text{RBS}}^{\text{self}} = \delta\omega_{\text{RBS},A} + \delta\omega_{\text{RBS},B} . \quad (6.43)$$

The frequencies  $\delta\omega_{\text{RBS},A}$  and  $\delta\omega_{\text{RBS},B}$  are defined as (see Eq. 6.36)

$$\delta\omega_{\text{RBS},A} = \pm \sqrt{\Delta\omega^2 + \omega_{yz,G,B}^2} \mp \Delta\omega \quad (6.44)$$

$$\delta\omega_{\text{RBS},B} = \mp \sqrt{\Delta\omega^2 + \omega_{yz,G,A}^2} \pm \Delta\omega , \quad (6.45)$$

with  $\omega_{yz,G,A} = \gamma_G \cdot B_{yz,G,A}$ ,  $\omega_{yz,G,B} = \gamma_G \cdot B_{yz,G,B}$  and  $\Delta\omega = |\omega_{0,G,A} - \omega_{0,G,B}| = \gamma_G \cdot |\Delta B|$ . The upper signs hold for  $\Delta B > 0$ , i.e.  $\omega_{0,G,A}/\omega_{0,G,B} > 1$ , and the lower signs hold for  $\Delta B < 0$ , i.e.  $\omega_{0,G,A}/\omega_{0,G,B} < 1$ .

In our experiment the field gradients are in the order of pT/cm. Thus the change of the magnetic field  $\Delta B$ , respectively the frequency difference  $\Delta\omega$ , are so small, i.e.  $|\omega_{0,G,A}| \approx |\omega_{0,G,B}|$ , that the rotating magnetic fields,  $\vec{B}_{\text{spin},G,A}$  and  $\vec{B}_{\text{spin},G,B}$ , are expected to be close to resonance.

Although the RBS shifts,  $\delta\omega_{\text{RBS},A}$  and  $\delta\omega_{\text{RBS},B}$ , do have opposite sign the sum of both (Eq. 6.43) is not equal to zero. This is because the strength of the rotating magnetic fields

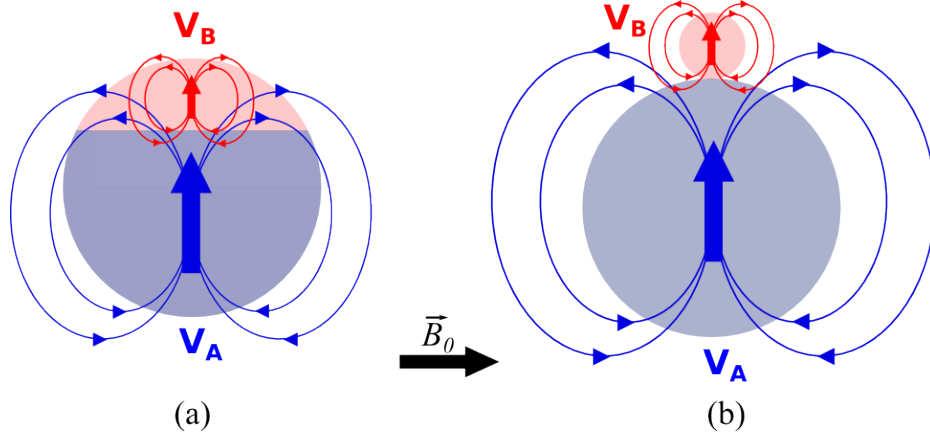


Figure 6.10: Illustration of RBS self-shift. It is assumed that the measurement cell is only filled with one gas species  $G$ . (a) Spherical measurement cell in a magnetic guiding field with non-linear field gradients. (b) Non-spherical measurement cell in a magnetic field with field gradients. In both cases due to field gradients the spins in volume  $V_A$  and  $V_B$  (with  $V_A > V_B$ ) see different magnetic guiding fields and thus precess with different frequencies, i.e.  $\omega_{0,G,A} = \gamma_G \cdot B_0 \neq \omega_{0,G,B} = \gamma_G \cdot (B_0 - \Delta B)$ . Here  $\Delta B$  is the change of the magnetic field due to field gradients. Besides, the spins in volume  $V_A$  and  $V_B$  produce magnetic fields,  $\vec{B}_{\text{spin},G,A}$  and  $\vec{B}_{\text{spin},G,B}$ , which rotate with respective frequencies,  $\omega_{0,G,A}$  and  $\omega_{0,G,B}$ , around the direction of the magnetic guiding field  $\vec{B}_0$ . These fields are indicated by the blue and red arrow. Now the rotating magnetic field  $\vec{B}_{\text{spin},G,B}$  of volume  $V_B$  leads to a shift  $\delta\omega_{\text{RBS},A}$  in the spin precession frequency of volume  $V_A$  and vice versa. Thereby the frequencies,  $\delta\omega_{\text{RBS},A}$  and  $\delta\omega_{\text{RBS},B}$ , do have opposite sign. However, since the amplitudes of the rotating magnetic fields (indicated by different lengths of the blue and red arrow) are not equal, the total RBS self-shift is unequal to zero.

of volume  $V_A$  and  $V_B$  are not equal but given by

$$B_{yz,G,A} = (V_A/V_{\text{tot}}) \cdot B_{yz,G,\text{tot}} , \quad (6.46)$$

$$B_{yz,G,B} = (V_B/V_{\text{tot}}) \cdot B_{yz,G,\text{tot}} , \quad (6.47)$$

where  $B_{yz,G,\text{tot}}$  is the magnetic field produced by the spins of gas species  $G$  in the total volume  $V_{\text{tot}}$  of the measurement cell. Due to the small field gradients in the order of pT/cm, it can be assumed that  $\Delta\omega \ll \omega_{yz}$ . Hence, according to Eq. 6.38 the RBS shifts of volume  $V_A$  and  $V_B$  can be approximated by

$$\delta\omega_{\text{RBS},A} \approx \pm\omega_{yz,G,B}(t) \quad (6.48)$$

$$\delta\omega_{\text{RBS},B} \approx \mp\omega_{yz,G,A}(t) . \quad (6.49)$$

With Eq. 6.39 and Eqs. 6.43-6.49 the RBS self-shift transforms to

$$\begin{aligned}
\delta\omega_{\text{RBS},G}^{\text{self}}(t) &\approx \pm\omega_{yz,G,B}(t) \mp \omega_{yz,G,A}(t) \\
&= \pm\gamma_G \cdot B_{yz,G,B}(t) \mp \gamma_G \cdot B_{yz,G,A}(t) \\
&= \pm\frac{\gamma_G}{V_{\text{tot}}} \cdot \xi_G \cdot (V_B \cdot A_{0,G,B} - V_A \cdot A_{0,G,A}) \cdot e^{-\frac{t}{T_{2,G}^*}} \\
&= \pm\xi_G \cdot A_{0,G} \cdot e^{-\frac{t}{T_{2,G}^*}}, \tag{6.50}
\end{aligned}$$

with  $A_{0,G} = \frac{\gamma_G}{V_{\text{tot}}} \cdot (V_B \cdot A_{0,G,B} - V_A \cdot A_{0,G,A})$ . The negative sign holds for  $\omega_{0,G,A}/\omega_{0,G,B} > 1$  and the positive sign for  $\omega_{0,G,A}/\omega_{0,G,B} < 1$ . Depending on the change of the the magnetic field, i.e.  $\Delta B > 0$  or  $\Delta B < 0$ , the RBS self-shift of one gas species  $G$  can take negative and positive values. By integration of Eq. 6.50 over time the RBS phase shift can be calculated to

$$\begin{aligned}
\delta\Phi_{\text{RBS},G}^{\text{self}}(t) &= \int_0^t \delta\omega_{\text{RBS},G}^{\text{self}}(t') \cdot dt' \\
&= \pm \int_0^t \xi_G \cdot A_{0,G} \cdot e^{-\frac{t'}{T_{2,G}^*}} \cdot dt' \\
&= \pm \text{const}_G \mp \xi_G \cdot A_{0,G} \cdot T_{2,G}^* \cdot e^{-\frac{t}{T_{2,G}^*}} \tag{6.51}
\end{aligned}$$

Hence, the phases caused by the RBS self-shifts decay exponentially with the transverse relaxation time  $T_2^*$ . In the following the constant  $\text{const}_G$  can be neglected, since this value will be included in the constant term of the fit model given by Eq. 6.17. The RBS self-shifts of  $^3\text{He}$  and  $^{129}\text{Xe}$  then lead to a shift in the weighted phase difference, which is given by

$$\begin{aligned}
\Delta\Phi_{\text{RBS}}^{\text{self}}(t) &= \delta\Phi_{\text{RBS,He}}^{\text{self}}(t) - \frac{\gamma_{\text{He}}}{\gamma_{\text{Xe}}} \delta\Phi_{\text{RBS,Xe}}^{\text{self}}(t) \\
&= -\xi_{\text{He}} \cdot A_{0,\text{He}} \cdot T_{2,\text{He}}^* \cdot e^{-t/T_{2,\text{He}}^*} \\
&\quad + \frac{\gamma_{\text{He}}}{\gamma_{\text{Xe}}} \cdot \xi_{\text{Xe}} \cdot A_{0,\text{Xe}} \cdot T_{2,\text{Xe}}^* \cdot e^{-t/T_{2,\text{Xe}}^*} \\
&= -\epsilon_{\text{He}} \cdot A_{0,\text{He}} \cdot T_{2,\text{He}}^* \cdot e^{-t/T_{2,\text{He}}^*} + \epsilon_{\text{Xe}} \cdot A_{0,\text{Xe}} \cdot T_{2,\text{Xe}}^* \cdot e^{-t/T_{2,\text{Xe}}^*}, \tag{6.52}
\end{aligned}$$

with  $\epsilon_{\text{He}} = \xi_{\text{He}}$  and  $\epsilon_{\text{Xe}} = \frac{\gamma_{\text{He}}}{\gamma_{\text{Xe}}} \cdot \xi_{\text{Xe}}$ . Here it was assumed that  $\Delta B > 0$ , i.e.  $\omega_{0,G,A}/\omega_{0,G,B} > 1$ . Hence the upper signs of Eq. 6.51 are valid. But since  $\epsilon_{\text{He}}$  and  $\epsilon_{\text{Xe}}$  are not known, all prefactors in Eq. 6.52 are summarized to  $E_{\text{He(Xe)}} = \epsilon_{\text{He(Xe)}} \cdot A_{0,\text{He(Xe)}} \cdot T_{2,\text{He(Xe)}}^*$ , which then are the fitparameters of the fit model given in Eq. 6.17.  $E_{\text{He(Xe)}}$  can take positive and negative values and thus both cases, i.e.  $\Delta B > 0$  and  $\Delta B < 0$ , are described by the fit model of Eq. 6.52. For the measurements that are discussed in this thesis instead of spherical glass cells, cylindrical glass cells were used. Beside a small stem these cells feature some additional deviations from a spherical measurement cell, so that the effect of the rotating magnetic fields,  $\vec{B}_{\text{spin},G,A}$  and  $\vec{B}_{\text{spin},G,B}$ , will be much stronger as for the spherical cells.

Futhermore it should be noted, that the expression given in Eq. 6.52 is an estimation of the RBS self-shift. Normally, in addition to the field gradients across the measurement cell, the RBS self-shift also depends on the diffusion time  $\tau_D$  of the gases. Taking into account the

effect of diffusion of the gases, the expression of the RBS self-shift in Eq. 6.52 would be much more complicated. Nevertheless, the expression given in Eq. 6.52 is a good approximation of the RBS self-shift.

### 6.3.3 Other Phase Shifts

Beside the effects which were explained in the former sections, there are some other effects that can also shift the phase. But these phase shifts are quite small compared to the ones discussed before. However for the sake of completeness these effects will be explained in the following.

#### Flip angle $\neq 90^\circ$

At the beginning of each measurement run the magnetic field is produced by the  $B_y$ -coils, i.e.  $\vec{B}_1 = B_0 \cdot \hat{e}_y$ . In order to induce a spin flip the  $B_y$ -coils are switched off whereas the  $B_x$ -coils are switched on. The switching operation then leads to a non-adiabatic change of the magnetic guiding field from  $\vec{B}_1 = B_0 \cdot \hat{e}_y$  to  $\vec{B}_0 = B_0 \cdot \hat{e}_x$ . A spin flip of  $90^\circ$  can be realized, if the  $B_x$ - and  $B_y$ -coils are arranged perpendicular to each other. In this case the magnetic fields produced by the polarized gases,  $^3\text{He}$  and  $^{129}\text{Xe}$ , only have an oscillating transversal component. But, if the coils are not arranged perpendicular, then the spins are flipped by an angle  $\alpha < 90^\circ$  relative to the magnetic guiding field  $\vec{B}_0$ . Hence, the magnetic fields of the polarized gases,  $^3\text{He}$  and  $^{129}\text{Xe}$ , have a static longitudinal component in addition to the oscillating transversal component. The longitudinal component of the magnetic field of gas species  $G1$  then leads to a shift in the Larmor frequency of gas species  $G2$  and vice versa:

$$\begin{aligned}
 \omega_{L,G2} &= \gamma_{G2} \cdot B \\
 &= \gamma_{G2} \cdot \sqrt{B_0^2 + (B_{G1} \cdot \cos \alpha)^2} \\
 &\approx \gamma_{G2} \cdot B_0 \left( 1 + \frac{1}{2} \left( \frac{B_{G1} \cdot \cos \alpha}{B_0} \right)^2 \right) \\
 \Rightarrow \Delta\omega_{L,G2} &\approx \frac{1}{2} \cdot \gamma_{G2} \cdot B_0 \left( \frac{B_{G1} \cdot \cos \alpha}{B_0} \right)^2.
 \end{aligned} \tag{6.53}$$

Since the longitudinal magnetic field  $B_{G1}$  decays exponentially with the longitudinal relaxation time  $T_{1,G1}$ , i.e.  $B_{G1} = B_{0,G1} \cdot e^{-t/T_{1,G1}}$ , the frequency shift  $\Delta\omega_{L,G2}$  should decrease exponentially with  $T_{1,G1}/2$ , i.e.  $\Delta\omega_{L,G2} \propto e^{-2t/T_{1,G1}}$ . For example, if the magnetic guiding field is  $B_0 = 0.35 \mu\text{T}$  and  $B_{0,\text{Xe}} \approx 53 \text{ pT}$  and  $\alpha \approx 89^\circ$  then the maximum change in the Larmor frequency of  $^3\text{He}$  is given by  $\Delta\omega_{L,\text{He}} \approx 2 \cdot 10^{-10} \text{ Hz}$ . Since this frequency shift is small and not influenced by the movement of the BGO crystal, it will not cause a similar signature in the weighted phase difference we are looking for. Hence, the frequency shift  $\Delta\omega_{L,G2}$  is negligible.

However the longitudinal components of the magnetic fields of  $^3\text{He}$  and  $^{129}\text{Xe}$  produce additional magnetic field gradients, which may reduce the  $T_2^*$  relaxation times of  $^3\text{He}$  and  $^{129}\text{Xe}$ . These gradients can be roughly estimated: If  $B_{0,\text{Xe}} \cdot \cos(89^\circ) \approx 53 \text{ pT} \cdot 0.02 = 1 \text{ pT}$ , the

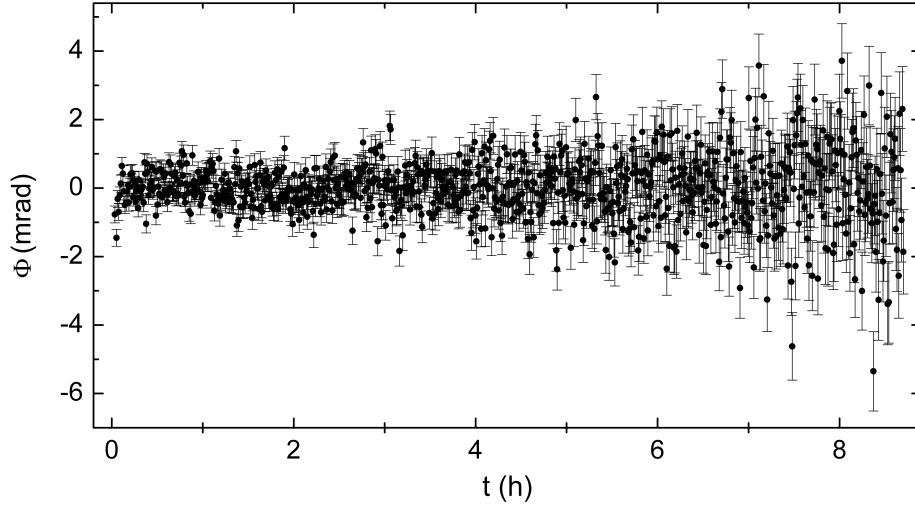


Figure 6.11: Phase residuals of measurement run C68 after subtraction of the fitted function of Eq. 6.16 from  $\Delta\Phi_{\text{rem}}(t)$ . One data point comprises 10 sub-data sets, which corresponds to a time interval of 32 s.

gradients in a cylindrical cell ( $\varnothing_L = L = 6$  cm) produced by the magnetic fields of  $^3\text{He}$  and  $^{129}\text{Xe}$  are smaller than  $1 \text{ pT}/6 \text{ cm} = 0.2 \text{ pT}/\text{cm}$ . These gradients are much smaller than the measured field gradients (see Tab. 4.1) and hence they are negligible.

#### Interaction between precessing spins and SQUID detectors

Since the SQUID sensors are superconducting, dissipation should not happen, i.e. the SQUIDS should not withdraw energy from the precessing spin system. If dissipation occurred, the  $T_2^*$  relaxation time of the precession signal would depend, for example, on the distance  $d$  between the sensor and the measurement cell. However, since this effect is not influenced by the movement of the BGO crystal, it cannot lead to a similar signature in the weighted phase difference we are looking for. Hence, this effect can be neglected.

## 6.4 Phaseresiduals

Assuming that no mass was moved during a measurement run, the temporal dependence of the remaining weighted phase difference  $\Delta\Phi_{\text{rem}}(t)$  can be described by Eq. 6.17. Thereby the  $T_2^*$  times were no fit parameters, but fixed, since they could be determined separately by a fit of the decay of the helium and xenon signal amplitudes (see Sec. 6.5). Hence, the fit model of Eq. 6.17 is a linear function in the fit parameters.

After fitting of the remaining weighted phase difference, the phase residuals can be determined by subtracting the fitted function  $\Delta\Phi_{\text{fit}}(t)$  of Eq. 6.17 from the data  $\Delta\Phi_{\text{rem}}(t)$ . The phase residuals of measurement C68 are shown in Fig. 6.11. The phase noise is statistically distributed, whereby it increases exponentially with the characteristic time constant  $T_{2,\text{Xe}}^*$ , i.e.  $\sigma_{\phi,\text{res}} \propto \exp(t/T_{2,\text{Xe}}^*)$  (see Chap. 5.2). This can be explained by the exponential decay of

the signal amplitudes, mainly that of  $^{129}\text{Xe}$  with the shorter  $T_2^*$  time which was about 5.3 h for measurement run C68.

## 6.5 Determination of Transverse Relaxation Times

Since the transverse relaxation times  $T_2^*$  of  $^3\text{He}$  and  $^{129}\text{Xe}$  are fixed in the fit of the remaining weighted phase difference  $\Delta\Phi_{\text{rem}}(t)$  (see Eq. 6.17), they have to be determined independently. By considering the decay of the signal amplitudes the  $T_2^*$  times of  $^3\text{He}$  and  $^{129}\text{Xe}$  can be calculated: The signal amplitudes of  $^3\text{He}$  and  $^{129}\text{Xe}$  of each sub-data set  $i$  can be evaluated with the fit parameters of the raw data fit given in Eq. 6.3 as

$$A_{\text{He/Xe}}(t_i) = \sqrt{\left(a_{\text{c,He/Xe}}^i\right)^2 + \left(a_{\text{s,He/Xe}}^i\right)^2}, \quad (6.54)$$

where  $t_i = (i-1) \cdot \tau$  is the time of the  $i$ -th sub-data set and  $\tau = 3.2\text{s}$  is the length of each sub-data set. Since the amplitudes,  $a_{\text{c,He/Xe}}^i$  and  $a_{\text{s,He/Xe}}^i$ , of one sub-data set are less correlated, the amplitude errors  $\Delta A_{\text{He/Xe}}(t_i)$  can be determined using the Gaussian error propagation law. Figure 6.12 shows the time developing of the helium (black) and xenon (red) amplitudes of measurement run C68 for three different and independent gradiometers (Z2E-Z5S, Z3D-Z2S, Z3I-Z1S). The amplitudes decay exponentially with the transverse relaxation time  $T_2^*$ , i.e.

$$A_{\text{fit}}(t) = A_0^g \cdot e^{-t/T_2^*}, \quad (6.55)$$

where  $g = 1, 2, 3$  corresponds to the gradiometers Z2E-Z5S, Z3D-Z2S and Z3I-Z1S, respectively. The function  $A_{\text{fit}}(t)$  is used for a common fit of the signal amplitudes. That means, that the data points  $(t_i, A_{\text{He/Xe}}(t_i), \Delta(A_{\text{He/Xe}}(t_i)))$  of all three gradiometers were joined to one big data set. In doing so, an additional dimension was added to each data point so that the data points of the different SQUID gradiometers can be distinguished later on. The data points of the big data set then are given by  $(\{t_i, g\}, A_{\text{He/Xe}}(t_i), \Delta(A_{\text{He/Xe}}(t_i)))$ . The fit function according to Eq. 6.55 then is applied to the big data set, i.e. to the signal amplitudes of all three gradiometers simultaneously. Here the initial amplitudes  $A_0^g$  can be different but the  $T_2^*$  time is equal for all three gradiometers. For measurement run C68, the fit parameters for helium result in  $A_{0,\text{He}}^1 = (9186.37 \pm 0.03)$  fT,  $A_{0,\text{He}}^2 = (4456.42 \pm 0.03)$  fT,  $A_{0,\text{He}}^3 = (6879.08 \pm 0.04)$  fT and  $T_{2,\text{He}}^* = (212019 \pm 9)$  s with  $\chi^2/dof = 1.65$  and the fit parameters for xenon result in  $A_{0,\text{Xe}}^1 = (4945.31 \pm 0.16)$  fT,  $A_{0,\text{Xe}}^2 = (2399.66 \pm 0.13)$  fT,  $A_{0,\text{Xe}}^3 = (3704.47 \pm 0.22)$  fT and  $T_{2,\text{Xe}}^* = (19049 \pm 1)$  s with  $\chi^2/dof = 17.50$ . To check the quality of the fit function, the amplitude residuals  $\text{Res}(A(t_i))$  have to be considered, which are the difference between the real amplitudes  $A_{\text{He/Xe}}(t_i)$  and the fit function  $A_{\text{fit}}(t)$ . In Fig. 6.13 the amplitude residuals of helium and xenon of measurement run C68 for the three different gradiometers are shown. Each data point comprises 50 sub-data sets which corresponds to a time interval of 160 s. Thus the error bar of each data point is smaller by a factor of  $\approx \sqrt{50}$  compared to the error of the amplitude of a single sub-data set. Obviously, the amplitude residuals of helium and xenon do not have the expected statistical distribution around zero, but show a characteristic structure instead, which is more distinct

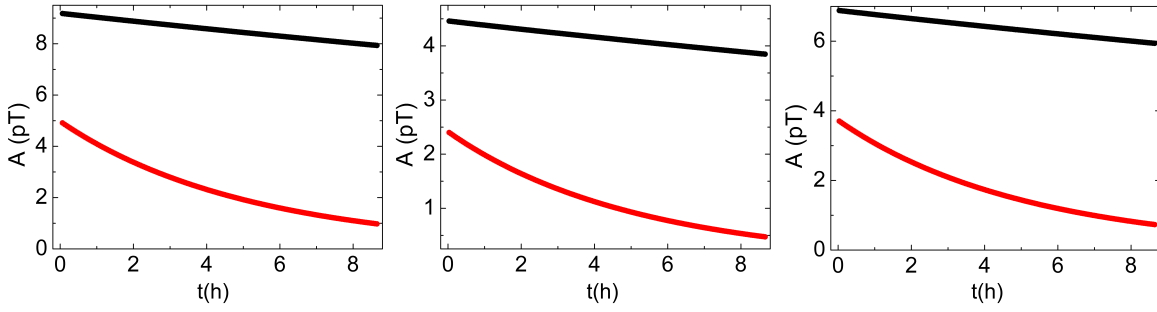


Figure 6.12: Decay of the  $^3\text{He}$  (black) and  $^{129}\text{Xe}$  (red) amplitudes of measurement run C68 for three different gradiometers (left: Z2E-Z5E, middle: Z3D-Z2S, right: Z3I-Z1S). Each data point comprises 50 sub-data sets which corresponds to a time interval of 160 s. Thus the error bar of each data point is smaller by a factor of  $\approx \sqrt{50}$  compared to the error of the amplitude of a single sub-data set. Hence, the error bars are too small to be visible in the plot.

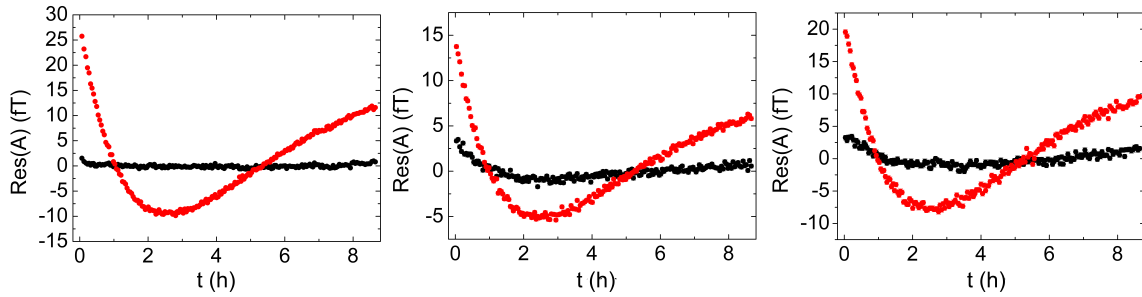


Figure 6.13: Amplitude residuals of  $^3\text{He}$  (black) and  $^{129}\text{Xe}$  (red) of measurement run C68 for three different gradiometers (left: Z2E-Z5E, middle: Z3D-Z2S, right: Z3I-Z1S) resulting from an exponential fit according to Eq. 6.55. Each data point comprises 50 sub-data sets which corresponds to a time interval of 160 s. Thus the error bar of each data point is smaller by a factor of  $\approx \sqrt{50}$  compared to the error of the amplitude of a single sub-data set. Hence, the error bars are too small to be visible in the plot.

for xenon than for helium. This also applies for the other measurement runs (see App. B). The structure in the amplitude residuals shows that there is another effect which causes a non-exponential decay of the signal amplitudes. Thus, we make the following ansatz to describe the real temporal development of the signal amplitudes

$$A(t) = A_0^g \cdot e^{-t/T_2^*} \cdot (1 + g_F(t)). \quad (6.56)$$

For exact determination of the  $T_2^*$  times, the structure in the amplitude residuals has to be parameterized. The whole procedure of the exact  $T_2^*$  determination is summarized in App. B. At the end, the structure in the amplitude residuals, i.e. the function  $g_F(t)$ , was determined via spline-interpolation. Then this function was used to apply the fit function of Eq. 6.56 to



	$T_{2,\text{He}}^*$ (s)	$\delta T_{2,\text{He}}^*$ (s)	$T_{2,\text{Xe}}^*$ (s)	$\delta T_{2,\text{Xe}}^*$ (s)
C54	111443	18	14742.6	0.4
C55	132567	3	14853.2	0.2
C60	176152	11	15395.9	0.3
C63	190472	7	18021.4	0.3
C65	217520	8	18773.9	0.4
C67	209171	9	18657.6	0.4
C68	212055	9	19049.7	0.3
C71	204661	7	18791.6	0.3
C80	229407	19	19165.1	0.4
C82	211347	32	18889.1	0.4

Table 6.2: Transverse relaxation times of  $^3\text{He}$  and  $^{129}\text{Xe}$  of measurement runs C54-C82 which were determined by using a spline-interpolation (Eq. 6.56).

the big data set, i.e. to the signal amplitudes of all three gradiometers simultaneously. The initial amplitudes  $A_0^g$  can be different but the  $T_2^*$  time is equal for all three gradiometers. The resulting transverse relaxation times  $T_2^*$  of helium and xenon of all 10 measurement runs are summarized in Tab. 6.2. The determination of the  $T_2^*$  time of helium for measurement run C60 was more complicated than for the other measurement runs since the structure in the amplitude residuals differed from the characteristic structure which appeared in the amplitude residuals of all other measurement runs.

## 6.6 Limit on Spin-Dependent Short-Range Force

A possible spin-dependent short-range interaction, which is mediated by axions or axion-like particles leads to a constant shift  $\Delta\omega_{\text{sp}}^w = 2\pi\Delta\nu_{\text{sp}} \cdot (1 - \gamma_{\text{He}}/\gamma_{\text{Xe}})$  (see Eq. 4.5) in the weighted frequency difference  $\Delta\omega(t)$  (Eq. 4.4), or to a corresponding linear shift in the weighted phase difference  $\Delta\Phi(t)$ , if the BGO crystal is close to the spin polarized samples. This frequency shift vanishes, if the BGO crystal is moved far away from the spin polarized samples (see Chap. 4).

To extract the frequency shift  $\Delta\nu_{\text{sp}}$  due to the spin-dependent short-range interaction, the weighted phase difference of three different and independent SQUID gradiometers were considered (Z2E-Z5S, Z3D-Z2S, Z3I-Z1S) for each measurement run ( $j = 1, \dots, 10$ ). Since the frequency shift  $\Delta\nu_{\text{sp}}$  is independent of the distance between the SQUID sensors and the polarized spin samples, it should be equal for all three gradiometers. That is why for each measurement run a common fit of the weighted phase difference of all three gradiometers was applied, i.e. similar to the fit of the signal amplitudes, the data points  $(t_i, \Delta\Phi(t_i), \delta(\Delta\Phi)(t_i))$  of all three gradiometers were joined to one big data set. An additional dimension was added to the data points of the big data set, so that the data points of the different SQUID gradiometers can be distinguished later on. The data points of the big data set then are given

by  $(\{t_i, g\}, \Delta\Phi(t_i), \delta(\Delta\Phi)(t_i))$ , where  $g = 1, 2, 3$  again is the number of the corresponding SQUID gradiometer ( $g = 1$  for Z2E-Z5S,  $g = 2$  for Z3D-Z2S,  $g = 3$  for Z3I-Z1S). Including the effect due to the spin-dependent short-range interaction, the fit model of the weighted phase difference given by Eq.6.17 transforms to

$$\begin{aligned}\Delta\Phi_{\text{fit}}(t) &= \Phi_{0,g} + (\Delta\omega_{\text{lin}} + \Delta\omega_{\text{sp}}^w(t)) \cdot t \\ &\quad - \epsilon_{\text{He}} \cdot A_{0,\text{He}} \cdot T_{2,\text{He}}^* \cdot e^{-t/T_{2,\text{He}}^*} + \epsilon_{\text{Xe}} \cdot A_{0,\text{Xe}} \cdot T_{2,\text{Xe}}^* \cdot e^{-t/T_{2,\text{Xe}}^*} \\ &= \Phi_{0,g} + (\Delta\omega_{\text{lin}} + \Delta\omega_{\text{sp}}^w(t)) \cdot t - E_{\text{He}} \cdot e^{-t/T_{2,\text{He}}^*} + E_{\text{Xe}} \cdot e^{-t/T_{2,\text{Xe}}^*}. \quad (6.57)\end{aligned}$$

Here the abbreviation  $E_{\text{He(Xe)}} = \epsilon_{\text{He(Xe)}} \cdot A_{0,\text{He(Xe)}} \cdot T_{2,\text{He(Xe)}}^*$  was used.  $\Phi_{0,g}$  is a constant phase offset which differs from one gradiometer to another. The two exponential terms correspond to the RBS self-shift and

$$\begin{aligned}\Delta\omega_{\text{sp}}^w(t) &= \Delta\omega_{\text{sp}}^w \cdot \Theta(\pm(t - t_0)) \\ &= 2\pi \left(1 - \frac{\gamma_{\text{He}}}{\gamma_{\text{Xe}}}\right) \cdot \Delta\nu_{\text{sp}} \cdot \Theta(\pm(t - t_0))\end{aligned} \quad (6.58)$$

is stemming from the frequency shift  $\Delta\nu_{\text{sp}}$  due to the spin-dependent short-range interaction. Here  $t_0$  is the time when the BGO-crystal was moved and  $\Theta(\pm(t - t_0))$  is the Heaviside step function<sup>6</sup>, which indicates that an additional linear phase shift only occurs, if the BGO crystal is close to the polarized spin samples. So, the  $(\pm)$  in its argument has to be set  $(-)$  for the sequence  $c \rightarrow d$  and  $(+)$  for the reverse one, i.e.  $d \rightarrow c$ . For reduction of the high correlation among the fit parameters of the linear term and the exponential terms, the time scale was shifted for fitting, i.e.  $t \rightarrow t' = t - t_0$ . The fit model of Eq. 6.57 then transforms to

$$\begin{aligned}\Delta\Phi_{\text{fit}}(t') &= (\Phi_{0,g} + \Delta\omega_{\text{lin}} \cdot t_0) + (\Delta\omega_{\text{lin}} + \Delta\omega_{\text{sp}}(t')) \cdot t' \\ &\quad - \epsilon_{\text{He}} \cdot A_{0,\text{He}} \cdot T_{2,\text{He}}^* \cdot e^{-t_0/T_{2,\text{He}}^*} \cdot e^{-t'/T_{2,\text{He}}^*} \\ &\quad + \epsilon_{\text{Xe}} \cdot A_{0,\text{Xe}} \cdot T_{2,\text{Xe}}^* \cdot e^{-t_0/T_{2,\text{Xe}}^*} \cdot e^{-t'/T_{2,\text{Xe}}^*} \\ &= \Phi'_{0,g} + (\Delta\omega_{\text{lin}} + \Delta\omega_{\text{sp}}(t')) \cdot t' - E'_{\text{He}} \cdot e^{-t'/T_{2,\text{He}}^*} + E'_{\text{Xe}} \cdot e^{-t'/T_{2,\text{Xe}}^*}, \quad (6.59)\end{aligned}$$

with

$$E'_{\text{He(Xe)}} = \epsilon_{\text{He(Xe)}} \cdot A_{0,\text{He(Xe)}} \cdot T_{2,\text{He(Xe)}}^* \cdot e^{-t_0/T_{2,\text{He(Xe)}}^*} \quad (6.60)$$

$$\Phi'_{0,g} = \Phi_{0,g} + \Delta\omega_{\text{lin}} \cdot t_0 \quad (6.61)$$

$$\Delta\omega_{\text{sp}}(t') = \Delta\omega_{\text{sp}}(t). \quad (6.62)$$

Since the  $T_2^*$  times of helium and xenon were determined independently by the decay of the signal amplitudes (see Sec. 6.5 and App. B), they were fixed in the fit. Hence the fit is linear in all fit parameters. The  $T_2^*$  times for the measurements C54-C82, that were used for fitting, are summarized in Tab. 6.2. Beside the constant phase offset  $\Phi'_{0,g}$ , all fit parameters for the three different gradiometers are equal, so that for each measurement run seven fit parameters are left. For all 10 measurement runs, a  $\chi^2$  minimization, as described in Sec. 6.1, using the

<sup>6</sup>Heaviside step function:  $\Theta(t) = 1$  for  $t \geq 0$  and  $\Theta(t) = 0$  for  $t < 0$ .

	$\chi^2/dof$		$\Phi'_{0,1}$ (rad)	$\Phi'_{0,2}$ (rad/s)	$\Phi'_{0,3}$ (rad/s)	$\Delta\omega_{\text{lin}}$ (rad/s)	$\Delta\omega_{\text{sp}}$ (rad/s)	$E'_{\text{He}}$ (rad)	$E'_{\text{Xe}}$ (rad)
C54	1.780	value	-5.084	-1.989	-4.452	2.347E-4	1.054E-7	-5.697	-0.151
		$\delta_c$	0.123	0.293	0.218	1.653E-8	9.592E-8	0.217	0.005
C55	1.795	value	-1.984	-1.937	-2.022	-2.304E-4	-1.961E-8	-3.690	0.026
		$\delta_c$	0.087	0.208	0.170	9.800E-7	9.942E-8	0.159	0.004
C60	1.851	value	11.185	11.344	11.955	8.514E-5	-2.170E-7	10.339	0.064
		$\delta_c$	0.015	0.333	0.422	1.379E-6	1.312 E-7	0.306	0.005
C63	1.821	value	27.781	26.484	27.049	6.547E-5	-7.519E-9	25.385	0.251
		$\delta_c$	0.207	0.457	0.531	1.877E-6	8.325E-8	0.402	0.004
C65	1.816	value	21.867	23.582	20.915	6.478E-5	-5.533E-8	20.792	0.231
		$\delta_c$	0.351	0.737	0.867	2.714E-6	1.016E-7	0.657	0.006
C67	1.839	value	20.552	20.993	17.187	6.630E-5	1.902E-7	18.144	0.139
		$\delta_c$	0.300	0.650	0.995	2.814 E-6	1.081E-7	0.654	0.006
C68	1.836	value	13.348	13.728	13.023	7.500E-5	4.382E-6	-12.043	0.063
		$\delta_c$	0.269	0.560	0.645	2.082E-6	7.995E-8	0.496	0.005
C71	1.867	value	8.619	8.682	9.360	-1.141E-4	-3.612E-	7.702	0.260
		$\delta_c$	0.224	0.465	0.562	1.838E-6	7.387E-8	0.421	0.004
C80	1.695	value	16.498	15.331	16.887	6.935E-5	-1.607E7	14.576	-0.131
		$\delta_c$	0.358	0.639	0.905	2.521E-6	8.003e-8	0.645	0.006
C82	1.803	value	16.902	17.600	15.155	4.218E-5	3.032E-7	-15.840	0.292
		$\delta_c$	0.310	0.495	0.731	2.192E-6	8.497E-8	0.517	0.005

Table 6.3: Best fit parameters of the fit model according to Eq. 6.59 with correlated  $1\sigma$  error of the measurement runs C54-C82.

fit model of Eq. 6.59 was performed. The fit parameters are summarized in Tab. 6.3. Due to the long  $T_2^*$  times ( $\overline{T_{2,\text{He}}^*} = 52.6$  h,  $\overline{T_{2,\text{Xe}}^*} = 4.9$  h), the parameters of the linear terms, i.e.  $\Delta\omega_{\text{lin}}$  and  $\Delta\omega_{\text{sp}}$ , and the amplitudes  $E'_{\text{He(Xe)}}$  of the exponential terms are highly correlated. The correlations between these parameters were up to 99.9%. From this it follows that the values of  $\Delta\nu_{\text{sp}}^w$ , which can be calculated out of the fit parameter  $\Delta\omega_{\text{sp}}$  using Eq. 6.58, are not really meaningful. To extract significant values of  $\Delta\nu_{\text{sp}}$ , high correlations between the linear and exponential fit parameters have to be avoided. That is why a Taylor expansion of the two exponential terms around the time  $t_0$  was done, so that Eq. 6.59 merges into a polynomial of 5th order<sup>7</sup>:

$$\Delta\Phi_{\text{fit}}(t') = a_g + b(t') \cdot t' + c \cdot t'^2 + d \cdot t'^3 + e \cdot t'^4 + f \cdot t'^5. \quad (6.63)$$

<sup>7</sup>With increasing order  $n$  of the polynomial expansion the reduced  $\chi^2/dof$  decreases. Since for polynomial expansions with  $n > 5$  the reduced  $\chi^2/dof$  of the fit did not decrease anymore, a polynomial expansion up to the 5th order is sufficient.

The parameters  $a_g, c, d, e$  and  $f$  are given by

$$a_g = \Phi'_{0,g} - E'_{\text{He}} + E'_{\text{Xe}}, \quad (6.64)$$

$$c = -\frac{E'_{\text{He}}}{2(T_{2,\text{He}}^*)^2} + \frac{E'_{\text{Xe}}}{2(T_{2,\text{Xe}}^*)^2}, \quad (6.65)$$

$$d = +\frac{E'_{\text{He}}}{6(T_{2,\text{He}}^*)^3} - \frac{E'_{\text{Xe}}}{6(T_{2,\text{Xe}}^*)^3}, \quad (6.66)$$

$$e = -\frac{E'_{\text{He}}}{24(T_{2,\text{He}}^*)^4} + \frac{E'_{\text{Xe}}}{24(T_{2,\text{Xe}}^*)^4}, \quad (6.67)$$

$$f = +\frac{E'_{\text{He}}}{120(T_{2,\text{He}}^*)^5} - \frac{E'_{\text{Xe}}}{120(T_{2,\text{Xe}}^*)^5}. \quad (6.68)$$

By use of Eq. 6.57 and Eq. 6.58 the linear term  $b(t')$  is given by

$$\begin{aligned} b(t') &= \Delta\omega_{\text{lin}} + \Delta\omega_{\text{sp}}^w(t') + \frac{E'_{\text{He}}}{T_{2,\text{He}}^*} - \frac{E'_{\text{Xe}}}{T_{2,\text{Xe}}^*} \\ &= \Delta\omega_{\text{lin}} + \epsilon_{\text{He}} \cdot A_{0,\text{He}} \cdot e^{-t_0/T_{2,\text{He}}^*} - \epsilon_{\text{Xe}} \cdot A_{0,\text{Xe}} \cdot e^{-t_0/T_{2,\text{Xe}}^*} \\ &\quad + 2\pi \cdot \left(1 - \frac{\gamma_{\text{He}}}{\gamma_{\text{Xe}}}\right) \cdot \Delta\nu_{\text{sp}} \cdot \Theta(\pm(t')). \end{aligned} \quad (6.69)$$

Again the Heaviside step function states, that the linear term  $b(t')$  differs at close ( $b_c$ ) and distant ( $b_d$ ) position of the BGO crystal due to the spin-dependent short-range interaction, whereas the other fit parameters, i.e.  $a_g, c, d, e$  and  $f$ , do not. Instead of using the Heaviside step function in our fit model, two fit functions for close and distant position of the BGO crystal were used for each measurement run, i.e.

$$\Delta\Phi_{\text{fit},c/d}(t') = a_g + b_{c/d} \cdot t' + c \cdot t'^2 + d \cdot t'^3 + e \cdot t'^4 + f \cdot t'^5. \quad (6.70)$$

This fit model is used for a common fit where the fit parameters  $a_g, b_c, b_d, c, d, e$  and  $f$  are free fit parameters. That means for each measurement run the fit according to Eq. 6.70 was applied to the weighted phase difference of all three gradiometers simultaneously. The resulting fit parameters  $a_g, b_c, b_d, c, \dots$  are summarized in Tab. 6.4. By use of Eq. 6.69, the frequency shift  $\Delta\nu_{\text{sp}}$  due to the spin-dependent short-range interaction then can be extracted from

$$\Delta\nu_{\text{sp}} = \frac{b_c - b_d}{2\pi \cdot \left(1 - \frac{\gamma_{\text{He}}}{\gamma_{\text{Xe}}}\right)}. \quad (6.71)$$

For systematic checks, the BGO crystal was positioned to the left side of the measurement cell ( $\mathcal{L}$ ) in the measurement runs C55, C60, C63, C65, C80, C82 and to the right side of the measurement cell ( $\mathcal{R}$ ) in the measurement runs C53, C54, C67, C68. Since the sign of the frequency shift  $\Delta\nu_{\text{sp}} \propto \vec{\sigma} \cdot \hat{r}$  (see Eq. 4.5 and Eq. 2.71) depends on the alignment of the quantization axis of the spins  $\vec{\sigma}$  relative to the unit distance vector  $\hat{r}$ , which points from the polarized to the unpolarized sample, the frequency shift  $\Delta\nu_{\text{sp},\mathcal{L}}$  has opposite sign to the

$\chi^2/\text{dof}$	$a_1$ (rad)	$a_2$ (rad)	$a_3$ (rad)	$b_c$ (rad/s)	$b_d$ (rad/s)	$c$ (rad/s <sup>2</sup> )	$d$ (rad/s <sup>3</sup> )	$e$ (rad/s <sup>4</sup> )	$f$ (rad/s <sup>5</sup> )		
C54	1.821	value	1.70275	-	1.70350	19380E-9	193818E-9	-1110.0E-13	8602.9e-18	-1488.5E-22	-1448.8E-27
		$\delta_c$	0.00007	-	0.00008	54E-9	56E-9	94.4E-13	292.7E-18	593.3E-22	3147.6E-27
		$\delta_{\text{uc}}$	0.00002	-	0.00004	5E-9	4E-9	3.6E-13	32.7E-18	25.7e-22	185.9E-27
C55	1.790	value	1.72929	1.73808	1.73612	2.40074E-9	200670E-9	1678.1E-13	-918.3E-18	-63.6E-22	-124.6E-27
		$\delta_c$	0.00006	0.00005	0.00007	30E-9	33E-9	35.7E-13	112.1E-18	133.8E-22	515.5E-27
		$\delta_{\text{uc}}$	0.00002	0.00005	0.00004	4E-9	3E-9	17.6E-13	8.0E-18	3.2E-22	11.9E-27
C60	1.851	value	1.21777	1.21699	1.22296	139498E-9	139615E-9	-376.3E-13	-2415.6E-18	491.4E-22	-541.9E-27
		$\delta_c$	0.00007	0.00009	0.00010	32E-9	33E-9	31.2E-13	132.7E-18	84.2E-22	150.2E-27
		$\delta_{\text{uc}}$	0.00002	0.00006	0.00007	4E-9	5E-9	1.8E-13	7.0E-18	2.3E-22	7.2E-27
C63	1.821	value	1.96401	1.97092	1.97814	184794E-9	184807E-9	380.9E-13	-6607.5E-18	1024.5E-22	-1209.0E-27
		$\delta_c$	0.00007	0.00008	0.00009	42E-9	44E-9	59.1E-13	134.5E-18	237.4E-22	963.9E-27
		$\delta_{\text{uc}}$	0.00002	0.00005	0.00005	4E-9	3E-9	21.3E-13	15.3E-18	9.3E-22	52.5E-27
C65	1.818	value	1.54598	1.57022	1.56589	147953E-9	148077E-9	1017.0E-13	-5573.61E-18	1057.2E-22	-1245.5E-27
		$\delta_c$	0.00009	0.00010	0.00010	53E-9	52E-9	734.9E-13	160.8E-18	302.2E-22	1213.1E-27
		$\delta_{\text{uc}}$	0.00002	0.00006	0.00006	4E-9	5E-9	257.1E-13	18.1E-18	10.9E-22	61.1E-27
C67	1.814	value	1.60343	1.60156	-	148954E-9	148672E-9	272.7E-13	-3971.1E-18	-306.9E-22	2626.1E-27
		$\delta_c$	0.00008	0.00010	-	54E-9	52E-9	72.4E-13	166.6E-18	285.2E-22	1161.3E-27
		$\delta_{\text{uc}}$	0.00002	0.00005	-	4E-9	5E-9	2.6E-13	18.6E-18	11.4E-22	64.3E-27
C68	1.837	value	1.38352	1.38818	1.38705	128429E-9	128599E-9	-302.4E-13	-1545.9E-18	-610.7E-22	2865.5E-27
		$\delta_c$	0.00007	0.00008	0.00008	41E-9	43E-9	579.6E-13	128.9E-18	234.3E-22	944.1E-27
		$\delta_{\text{uc}}$	0.00002	0.00004	0.00005	4E-9	3E-9	204.3E-13	14.3E-18	8.6E-22	48.4E-27
C71	1.866	value	1.44156	1.44648	1.44543	137888E-9	137924E-9	2753.3E-13	-5987.8E-18	919.4E-22	-1996.7E-27
		$\delta_c$	0.00006	0.00007	0.00008	39E-9	38E-9	53.2E-13	120.8E-18	211.1E-22	855.5E-27
		$\delta_{\text{uc}}$	0.00002	0.00005	0.00005	3E-9	3E-9	1.9E-13	13.4E-18	8.1E-22	45.5E-27
C80	1.714	value	1.51730	1.53758	1.53875	139528E-9	139682E-9	-3161.4E-13	3422.6E-18	-415.3E-22	108.5E-27
		$\delta_c$	0.00007	0.00007	0.00008	41E-9	43E-9	60.6E-13	148.8E-18	266.2E-22	1145.4E-27
		$\delta_{\text{uc}}$	0.00002	0.00004	0.00006	4E-9	3E-9	2.2E-13	16.0E-18	10.1E-22	59.6E-27
C82	1.820	value	1.06022	1.06422	1.05553	101558E-9	101629E-9	2055.3E-13	-6914.7E-18	1855.7E-22	-3384.6E-27
		$\delta_c$	0.00008	0.00008	0.00010	48E-9	46E-9	64.0E-13	146.1E-18	252.6E-22	1025.6E-27
		$\delta_{\text{uc}}$	0.00002	0.00004	0.00006	3E-9	4E-9	22.8E-13	16.8E-18	9.8E-22	55.3E-27

Table 6.4: Best fit parameters of the fit model according to Eq. 6.70 with correlated  $1\sigma$  error of the measurement runs C54-C82.

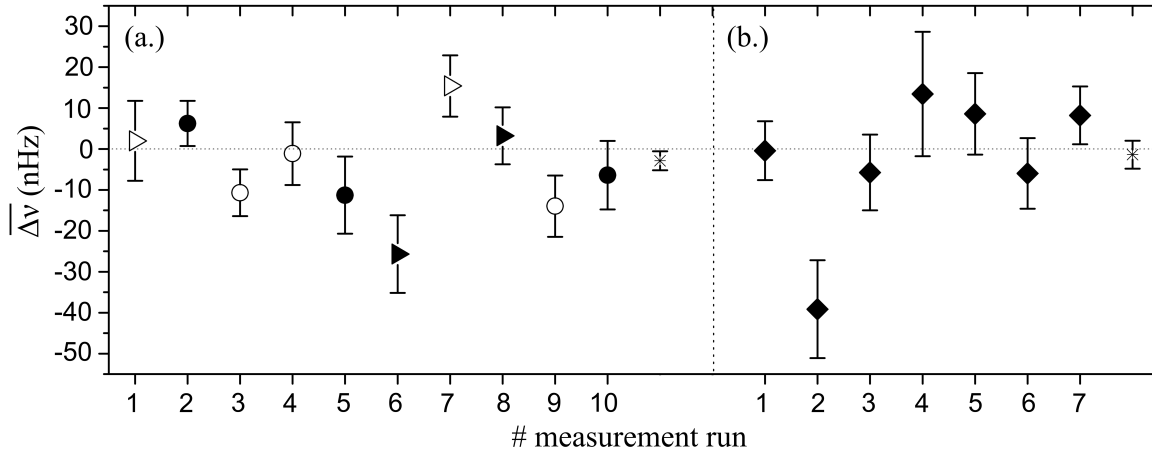


Figure 6.14: (a) Extracted frequency shifts  $\Delta\nu_{\text{sp}}$  (with correlated  $1\sigma$  error) of the 10 measurement runs. The triangles specify the  $\mathfrak{R}$  and the circles the  $\mathcal{L}$  arrangement of the BGO crystal. Full symbols indicate the  $c \rightarrow d$  sequence of the BGO crystal and hollow symbols the opposite case, i.e.  $d \rightarrow c$ . (b) Results of  $\Delta\nu_{\text{LV}}$  (with correlated  $1\sigma$  error) obtained from the LV 2009 data using the same fit model (Eq. 6.70). Since no mass was moved, we expect no shift in the spin precession frequency. The rightmost symbols in both plots (stars) indicate the respective weighted means with their correlated  $1\sigma$  error.

frequency shift  $\Delta\nu_{\text{sp},\mathfrak{R}}$ . For comparison of the frequency shifts of the different measurement runs, the results of all  $\mathcal{L}$  runs are multiplied by  $(-1)$ , whereas the results of the  $\mathfrak{R}$  runs are not modified, i.e.  $\Delta\nu_{\text{sp}} = (-1) \cdot \Delta\nu_{\text{sp},\mathcal{L}}$  and  $\Delta\nu_{\text{sp}} = \Delta\nu_{\text{sp},\mathfrak{R}}$ . In Tab. 6.5 the values  $\Delta\nu_{\text{sp}}$  for the individual measurement runs are summarized and in Fig. 6.14a they are shown together with their correlated  $1\sigma$  errors<sup>8</sup>. In the phase residuals of the gradiometer Z3D-Z2S of measurement run C54 and the gradiometer Z3I-Z1S of measurement run C67 a jump at the time  $t_0$ , at which the BGO crystal was moved, occurred. Consequently, the data of these two gradiometers were skipped in the further analysis. In calculating the weighted mean, we get  $\overline{\Delta\nu_{\text{sp}}} = (-2.9 \pm 2.3 \pm 0.2)$  nHz with  $\chi^2/dof = 2.29$ . The second and the third value correspond to the correlated and uncorrelated  $1\sigma$  error, respectively.

As consistency check, we re-analysed our data of 2009, where we looked for a possible Lorentz-violating sidereal frequency modulation (LV 2009) [96]. That means, that the fit model of Eq. 6.70 was applied to the weighted phase difference of each measurement run of the LV 2009 data (7 measurement runs in total). The time  $t_0$  was chosen to be  $t_0 = 10800$  s. From the fit parameters  $b_c$  and  $b_d$ , the frequency shift  $\Delta\nu_{\text{LV}}$  according to Eq. 6.71 can be calculated. Since no mass was moved during those measurement runs, the frequency shift  $\Delta\nu_{\text{LV}}$  is expected to be zero. In Tab. 6.5 the values  $\Delta\nu_{\text{LV}}$  for the 7 measurement runs are summarized and they are shown together with their correlated  $1\sigma$  errors in Fig. 6.14b. The

<sup>8</sup>The correlated errors are calculated as square root of the diagonal elements of the covariance matrix of the least  $\chi^2$  fit-model of Eq. 6.63 with the proper statistical weights. The uncorrelated errors are about a factor of 15 smaller and not included in the error bars shown in Fig. 6.14.

		$\Delta\nu_{\text{sp}}$	$\delta_{\text{c}}(\Delta\nu_{\text{sp}})$	$\delta_{\text{uc}}(\Delta\nu_{\text{sp}})$	$\chi^2/dof$		$\Delta\nu_{\text{LV}}$	$\delta_{\text{c}}(\Delta\nu_{\text{LV}})$	$\delta_{\text{uc}}(\Delta\nu_{\text{LV}})$	$\chi^2/dof$
		(nHz)	(nHz)	(nHz)			(nHz)	(nHz)	(nHz)	
C54	dc- $\mathfrak{R}$	2.00	9.77	0.59	1.97	C92	-0.41	7.18	0.64	1.71
C55	cd- $\mathcal{L}$	6.25	5.50	0.47	1.82	C94	-39.15	11.96	0.95	2.01
C60	dc- $\mathcal{L}$	-10.68	5.71	0.55	1.79	C95	-5.73	9.25	0.86	2.06
C63	dc- $\mathcal{L}$	-1.12	7.67	0.44	1.85	C99	13.43	15.20	1.07	1.75
C65	cd- $\mathcal{L}$	-11.27	9.42	0.53	1.82	C01	8.59	9.95	0.90	2.21
C67	cd- $\mathfrak{R}$	-25.67	9.48	0.54	1.81	C02	-5.95	8.63	0.85	1.86
C68	dc- $\mathfrak{R}$	15.4	7.50	0.42	1.84	C03	8.22	7.05	0.70	1.50
C71	cd- $\mathfrak{R}$	3.23	6.95	0.39	1.87					
C80	dc- $\mathcal{L}$	-13.96	7.50	0.44	1.71					
C82	cd- $\mathcal{L}$	-6.39	8.37	0.47	1.82					

Table 6.5: Results of  $\Delta\nu_{\text{sp}}$  and  $\Delta\nu_{\text{LV}}$  with correlated ( $\delta_{\text{c}}(\Delta\nu_{\text{sp}})$ ,  $\delta_{\text{c}}(\Delta\nu_{\text{LV}})$ ) and uncorrelated ( $\delta_{\text{uc}}(\Delta\nu_{\text{sp}})$ ,  $\delta_{\text{uc}}(\Delta\nu_{\text{LV}})$ )  $1\sigma$ -errors determined by a  $\chi^2$  minimization using the model given by Eq. 6.70. For the measurement runs C54-C60, the time  $t_0$  of the movement of the BGO crystal was at 8700 s and for the other measurement runs C63-C82 at 10800 s. In the second row, the measurement configuration is listed. For example, dc- $\mathfrak{R}$  means that the BGO crystal was installed to the right side of the measurement cell (see Fig. 4.10) and the BGO crystal was in distant position (d) relative to the measurement cell at the beginning of the measurement run. At the time  $t_0$  the BGO crystal was moved close (c) to the measurement cell. For the LV data of 2009 it was assumed that for each measurement run the measurement configuration was cd- $\mathfrak{R}$ , where the time for the fictitious movement of the BGO crystal was set to  $t_0 = 10800$  s for each measurement run.

weighted mean of the LV 2009 data gives  $\overline{\Delta\nu}_{\text{LV}} = (-1.4 \pm 3.4 \pm 0.3)$  nHz with  $\chi^2/dof = 2.38$ . Again the second and the third value correspond to the correlated and uncorrelated  $1\sigma$  error, respectively.

The  $\chi^2/dof$  values of the weighted mean values,  $\overline{\Delta\nu}_{\text{sp}}$  and  $\overline{\Delta\nu}_{\text{LV}}$ , indicate that the errors of the measured frequency shifts (Tab. 6.5) are somewhat underestimated. In order to take this into account, the errors were multiplied by  $\sqrt{\chi^2/dof}$  in order to obtain a  $\chi^2/dof$  of one, as recommended, e.g. by [149, 150]. Then our results for the measured frequency shifts are given by

$$\overline{\Delta\nu}_{\text{sp}} = (-2.9 \pm 3.5 \pm 0.3) \text{ nHz}, \quad (6.72)$$

$$\overline{\Delta\nu}_{\text{LV}} = (-1.4 \pm 5.2 \pm 0.5) \text{ nHz}. \quad (6.73)$$

These results indicate that i.) we find no evidence for a pseudoscalar spin-dependent short-range interaction mediated by axions or axion-like particles and ii.) as expected, the cross check analysis of our LV 2009 data is also compatible with zero (within the error bars).

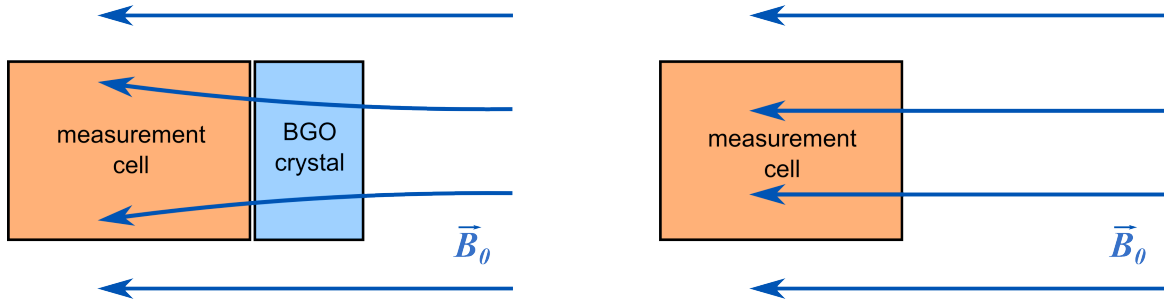


Figure 6.15: Illustration of the change of the magnetic guiding field  $\vec{B}_0$  due to the non-zero magnetic susceptibility of the BGO crystal. In close position (left) the additional field gradients produced by the BGO crystal change the magnetic field across the measurement cell. In distant position (right) these additional field gradients vanish.

## 6.7 Discussion of Systematic Uncertainties

The BGO crystal was used as unpolarized matter sample since it is said to have an unusual magnetism-related behavior in weak constant magnetic fields ( $\chi = 0$  ppm) [123, 124, 125]. But in the high field limit ( $B > 1$  T) the BGO crystal shows a magnetic susceptibility of  $\chi \approx -19 \cdot 10^{-6}$  [124]. For conservative estimation of the systematic errors we used the magnetic susceptibility of the BGO crystal in the high field limit. As illustrated in Fig. 6.15, the magnetic susceptibility of the BGO crystal leads to additional field gradients across the measurement cell if the BGO crystal is at close position. However, these additional field gradients disappear if the BGO crystal is in distant position. Hence, the movement of the BGO crystal can produce correlated effects that may mimic a pseudoscalar frequency shift or even compensate the effect we are looking for. Before these effects can be explained in detail the field gradients that are produced by the BGO crystal have to be estimated: The distribution of the total magnetic field  $|\vec{B}_{\text{cal}}|$  across the measurement cell with the BGO crystal in close position immersed in a homogeneous magnetic guiding field of  $|\vec{B}_0| = 0.35 \mu\text{T}$  pointing in x-direction (see Fig. 4.10) was simulated with *COMSOL Multiphysics*, a finite element analysis software. In Fig. 6.16 (left side) the change of the magnetic guiding field  $B_{\text{BGO}} = |\vec{B}_{\text{cal}}| - |\vec{B}_0|$  along the x-direction ( $y=0$  and  $z=0$ ), i.e. along the cylinder axis of the BGO crystal and the measurement cell, is shown. The center of the BGO crystal is at  $x = 0$  cm, where the change of the magnetic guiding field is maximal. The curve profile of  $B_{\text{BGO}}(x)$  can be described by a Gauss function which is given by

$$B_{\text{BGO}}(x) = 5 \text{ pT} \cdot e^{-x^2/16} . \quad (6.74)$$

Calculating the derivative leads to

$$\frac{\partial}{\partial x} B_{\text{BGO}}(x) = \frac{5}{8} \frac{\text{pT}}{\text{cm}} \cdot x \cdot e^{-x^2/16} . \quad (6.75)$$

In Fig. 6.16 (right side) the derivative  $\frac{\partial}{\partial x} B_{\text{BGO}}(x)$  for  $x > 0$  cm is shown. The mean value of



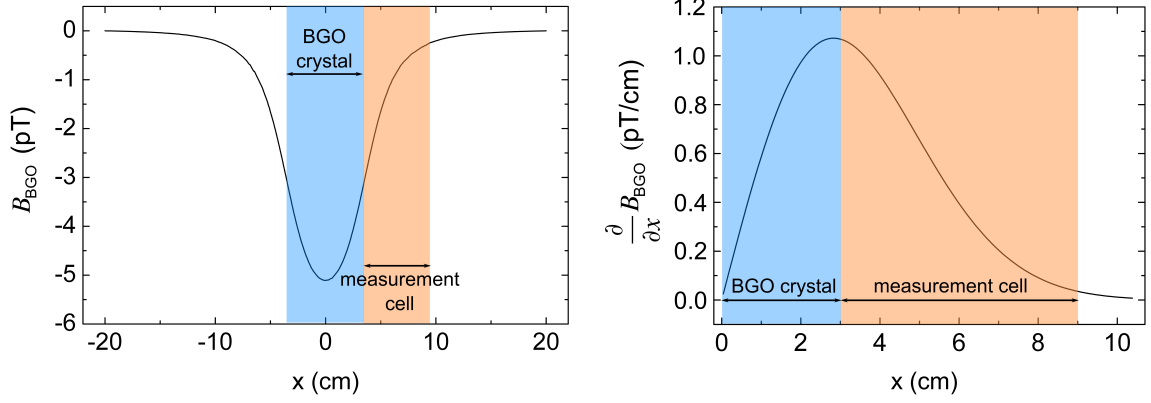


Figure 6.16: *Left*: Simulated change of the magnetic guiding field  $B_{\text{BGO}} = |\vec{B}_{\text{cal}}| - |\vec{B}_0|$  along the  $x$ -direction ( $y=0$  and  $z=0$ ) due to the non-zero magnetic susceptibility of the BGO crystal. *Right*: Derivative  $\frac{\partial}{\partial x} B_{\text{BGO}}(x)$  for  $x > 0$  cm from which the mean value across the measurement cell can be calculated. In both plots the position of the BGO crystal and the position of the measurement cell are indicated by the blue and orange area, respectively.

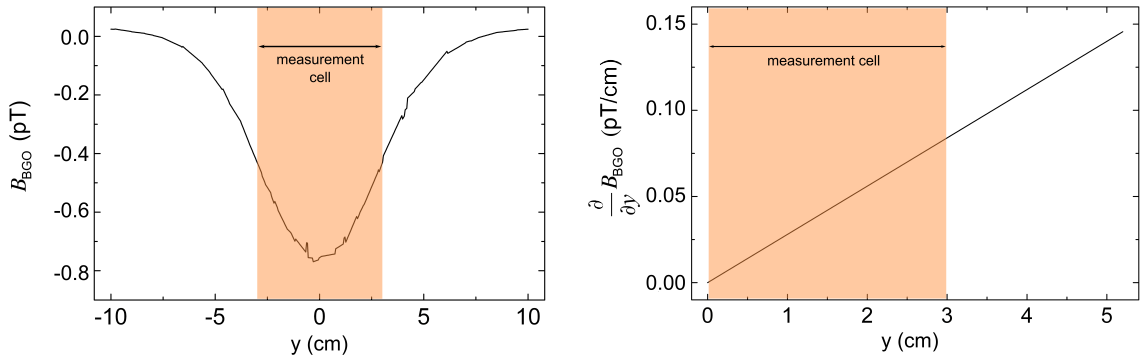


Figure 6.17: *Left*: Simulated change of magnetic guiding field  $B_{\text{BGO}} = |\vec{B}_{\text{cal}}| - |\vec{B}_0|$  along the  $y$ -direction ( $x=6.7$  cm and  $z=0$ ) due to the non-zero magnetic susceptibility of the BGO crystal. *Right*: Derivative  $\frac{\partial}{\partial y} B_{\text{BGO}}(y)$  for  $y > 0$  cm from which the mean value across the measurement cell can be calculated. In both plots the position of the measurement cell is indicated by the orange area.

the derivative across the measurement cell ( $3.7 \text{ cm} \leq x \leq 9.5 \text{ cm}$ ) then can be calculated to

$$\overline{\frac{\partial}{\partial x} B_{\text{BGO}}(x)} \approx 0.47 \frac{\text{pT}}{\text{cm}}. \quad (6.76)$$

For a given  $x$ , the same calculations can be done for the transversal directions, i.e. the  $y$ - and  $z$ -direction ( $y, z : [-3 \text{ cm}, +3 \text{ cm}]$ ). For  $x=6.7 \text{ cm}$  and  $z=0$ , the change of the magnetic guiding field along the  $y$ -direction, i.e.  $B_{\text{BGO}}(y)$ , is shown in Fig. 6.17 (left side).  $B_{\text{BGO}}(y)$  can be described by  $B_{\text{BGO}}(y) \approx a \cdot y^2 + b$  and hence the derivative is given by  $\frac{\partial}{\partial y} B_{\text{BGO}}(y) \approx 2a \cdot y$  (Fig. 6.17 right side). For different  $x$ -positions the derivative results in

$$\frac{\partial}{\partial y} B_{\text{BGO}}(y) = \begin{cases} 0.044 \frac{\text{pT}}{\text{cm}} \cdot y & \text{for } x = 4.2 \text{ cm} , \\ 0.028 \frac{\text{pT}}{\text{cm}} \cdot y & \text{for } x = 6.7 \text{ cm} , \\ 0.007 \frac{\text{pT}}{\text{cm}} \cdot y & \text{for } x = 9.7 \text{ cm} . \end{cases} \quad (6.77)$$

Due to symmetry reasons, the same relations hold for the  $z$ -direction. A rough estimate of the mean value of the transverse field gradients across the measurement cell can be calculated by averaging the transverse field gradients at  $y = 3 \text{ cm}$  for all  $x$ -positions. Hence, the mean values of the transverse field gradients across the measurement cell result in

$$\overline{\frac{\partial}{\partial y} B_{\text{BGO}}(y)}, \overline{\frac{\partial}{\partial z} B_{\text{BGO}}(z)} \leq 0.08 \frac{\text{pT}}{\text{cm}}. \quad (6.78)$$

The transverse as well as the longitudinal field gradients produced by the BGO crystal can cause systematic effects which will be discussed in the following.

### Effect of transverse field gradients

The BGO crystal at close position slightly changes the magnetic field across the volume of the  $^3\text{He}/^{129}\text{Xe}$  sample cell (see Fig. 6.15). This effect drops out to first order due to co-magnetometry. However, to second order, this effect does not drop out: According to the barometric formula the center of masses (CM) of helium and xenon are slightly shifted by  $\Delta s = 1.2 \cdot 10^{-7} \text{ m}$  in the gravitational field of the Earth due to their different molar masses (see *gravitational shift* in Sec. 6.3.1). The vertical field gradient due to the BGO crystal is  $\frac{\partial}{\partial z} B_{\text{BGO}}(z) \leq 0.08 \text{ pT/cm}$ . In accordance with Eq. 6.29 these vertical field gradients lead to a frequency shift of

$$\Delta \nu_{\text{sys}}^{\text{CM}} = \Delta z \cdot \overline{\frac{\partial}{\partial z} B_{\text{BGO}}(z)} \cdot \frac{\gamma_{\text{He}}}{2\pi} \leq 0.03 \text{ nHz}. \quad (6.79)$$

Compared to the measured frequency shift (Eq. 6.72), this systematic effect is negligible.

### Effect of longitudinal field gradients

In our analysis we assumed that the  $T_2^*$  times of  $^3\text{He}$  and  $^{129}\text{Xe}$  are constant over the whole measurement run. But according to Eq. 3.50 the transverse relaxation rate in the motional narrowing regime is proportional to the magnetic field gradients, so that the additional

gradients produced by the BGO crystal lead to different  $T_2^*$  times for the close and distant position of the BGO crystal, i.e.  $T_{2,c}^* \neq T_{2,d}^*$ . Since the RBS self-shift of the weighted phase difference (Eq. 6.52) depends on the  $T_2^*$  times of  $^3\text{He}$  and  $^{129}\text{Xe}$ , a change in the  $T_2^*$  times leads to an additional shift in the weighted phase difference and hence gives rise to a systematic frequency shift which has the same signature as the linear phase shift due to the spin-dependent short-range interaction. The systematic frequency shift is derived in App. D and is given by

$$\left| \Delta\nu_{\text{sys}}^{T_2^*} \right| \leq \left| \frac{\frac{\Delta T_{2,\text{He}}^*}{(T_{2,\text{He}}^*)^2}}{2\pi \cdot \left(1 - \frac{\gamma_{\text{He}}}{\gamma_{\text{Xe}}}\right)} \cdot \left( \frac{E'_{\text{He(Xe)}}}{T_{2,\text{He}}^* + \Delta T_{2,\text{He}}^*} - \frac{1}{2} \cdot \frac{E'_{\text{He(Xe)}}}{T_{2,\text{Xe}}^* + \Delta T_{2,\text{Xe}}^*} \right) \cdot \frac{t_0}{2} \right| \quad (6.80)$$

Again  $t_0$  is the time of the movement of the BGO crystal. Values for the respective phase amplitudes  $E'_{\text{He(Xe)}}$  were extracted from the fit given by Eq. 6.59 and are summarized in Tab. 6.3. For the determination of the systematic error, the change in the  $T_2^*$  times of helium and xenon have to be known, i.e.  $\Delta T_{2,\text{He}}^*$  and  $\Delta T_{2,\text{Xe}}^*$ .

The easiest method to determine  $\Delta T_2^*$  is to measure the  $T_2^*$  times directly, both for the BGO crystal in close and distant position. Therefore a modified fit model for the amplitudes is defined:

$$\begin{aligned} A_{\text{He(Xe),fit}}^g(t) &= A_{0,\text{He(Xe)}}^g \cdot e^{-t/(T_{2,\text{He(Xe)}}^* + \Delta T_{2,\text{He(Xe)}}^*)} \cdot (1 + g_{\text{F}}^{\text{He(Xe)}}(t)) \cdot \Theta(\mp(t - t_0)) \\ &+ A_{0,\text{He(Xe)}}^g \cdot e^{-t/T_{2,\text{He(Xe)}}^*} \cdot (1 + g_{\text{F}}^{\text{He(Xe)}}(t)) \cdot \Theta(\pm(t - t_0)). \end{aligned} \quad (6.81)$$

The function  $g_{\text{F}}^{\text{He(Xe)}}(t)$  is equal for all three gradiometers ( $g=1, 2, 3$ ). It is determined via spline-interpolation as described in App. B.  $\Delta T_2^*$  is defined as  $\Delta T_2^* = T_{2,c}^* - T_{2,d}^*$  and  $T_2^*$  is given by  $T_2^* = T_{2,d}^*$ . The  $(\mp)$  and the  $(\pm)$  in the argument of the Heaviside step function of the first term and the second term, respectively, occur due to the close to distant (cd  $\hat{=}$  +, -) sequence of the BGO crystal and the distant to close (dc  $\hat{=}$  -, +) sequence. The fit model of Eq. 6.81 again is used for a common fit, i.e. it is applied to the signal amplitudes of all three gradiometers simultaneously, where the initial amplitudes  $A_{0,\text{He(Xe)}}^g$  can be different, but  $T_{2,\text{He(Xe)}}^*$  and  $\Delta T_{2,\text{He(Xe)}}^*$  are equal for all three gradiometers. The resulting values of  $\Delta T_2^*$  are summarized in Tab. 6.6. For measurement run C60 the determination of the  $T_2^*$  times was difficult (see Sec. 6.5). Thus, this measurement run will be neglected in the following. For  $\Delta T_{2,\text{He}}^*$  values up to 4500 s and for  $\Delta T_{2,\text{Xe}}^*$  values up to 200 s appear, whereas the values of  $\Delta T_{2,\text{He}}^*$  and  $\Delta T_{2,\text{Xe}}^*$  vary up to one order of magnitude. The function  $g_{\text{F}}^{\text{He(Xe)}}(t)$ , which describes the non-exponential decay of the signal amplitudes, make problems in the determination of  $\Delta T_{2,\text{He(Xe)}}^*$ . Thus the values of  $T_{2,\text{He(Xe)}}^*$  and  $\Delta T_{2,\text{He(Xe)}}^*$  are highly correlated, so that the values summarized in Tab. 6.6 are not significant. Hence, another method is needed to determine or estimate the difference in the  $T_2^*$  times due to the field gradients produced by the BGO crystal: The movement of the BGO crystal at the time  $t_0$  leads to a discontinuity in the amplitude signals at the time  $t_0$ . Via this discontinuity the change in the  $T_2^*$  times can be determined. This new ansatz will be explained in the following.

	$\Delta T_{2,\text{He}}^*$ (s)	$\delta(\Delta T_{2,\text{He}}^*)$ (s)	$\Delta T_{2,\text{Xe}}^*$ (s)	$\delta(\Delta T_{2,\text{Xe}}^*)$ (s)
C54	-2482	114	+4	2
C55	-376	42	+32	2
C60	-53001	1512	-24	2
C63	-4438	78	-147	4
C65	+288	53	+150	3
C67	+3864	58	+181	3
C68	+357	60	-188	4
C71	+624	70	+197	4
C80	-1363	132	-83	3
C82	+2381	222	+182	4

Table 6.6: Change of transverse relaxation times of  $^3\text{He}$  and  $^{129}\text{Xe}$  due to the magnetic field gradients produced by the BGO crystal for the measurement runs C54-C82.  $\Delta T_2^*$  was determined by using the fit model according to Eq. B.24.

#### Determination of $\Delta T_2^*$ :

If there is a change in the  $T_2^*$  times due to additional field gradients produced by the BGO crystal, there should be a discontinuity in the amplitudes at the time  $t_0$  when the BGO crystal was moved, i.e. at the time  $t_0$  a kink in the temporal development of the amplitudes should appear, which is illustrated in Fig. 6.18. Consequently, at the time  $t_0$  two different values of the slope of the signal amplitudes should arise. The difference of the slopes  $\Delta s$  at the time  $t_0$  then contains the change of the  $T_2^*$  times. Assuming that  $\Delta T_2^* \ll T_2^*$ , the dependence of  $\Delta s$  on  $\Delta T_2^*$  can be estimated:

$$\begin{aligned}
& A_d(t) = A_0 \cdot e^{-\frac{t}{T_2^*}}, \quad A_c(t) = A_0 \cdot e^{-\frac{t}{T_2^* + \Delta T_2^*}} \\
\Rightarrow \quad & \frac{d}{dt} A_d(t = t_0) = -\frac{A_0}{T_2^*} \cdot e^{-\frac{t_0}{T_2^*}}, \quad \frac{d}{dt} A_c(t = t_0) \approx -\frac{A_0}{T_2^* + \Delta T_2^*} \cdot e^{-\frac{t_0}{T_2^*}} \\
\Rightarrow \quad & \Delta s = \frac{d}{dt} A_c(t = t_0) - \frac{d}{dt} A_d(t = t_0) \\
& \approx -\frac{A_0}{T_2^* + \Delta T_2^*} \cdot e^{-\frac{t_0}{T_2^*}} + \frac{A_0}{T_2^*} \cdot e^{-\frac{t_0}{T_2^*}} \\
& = A_0 \cdot e^{-\frac{t_0}{T_2^*}} \left( \frac{1}{T_2^*} - \frac{1}{T_2^* + \Delta T_2^*} \right) \\
& \approx \frac{A_0}{T_2^*} \cdot e^{-\frac{t_0}{T_2^*}} \left( 1 - 1 + \frac{\Delta T_2^*}{T_2^*} \right) \\
\Rightarrow \quad & \Delta T_2^* \approx \Delta s \cdot \frac{(T_2^*)^2}{A_0} \cdot e^{t_0/T_2^*}. \tag{6.82}
\end{aligned}$$

Here the relation  $\frac{1}{1+\beta} \approx 1 - \beta$  for  $\beta \ll 1$  was used. Considering the real amplitudes, the change in the slope at the time  $t_0$  has to be small, since a discontinuity is not visible with the naked eye (see Fig. 6.12). But with a new fit model it can be tested if there is a discontinuity at the time  $t_0$ . Since the amplitude ratio is less marked by disturbances (e.g. drift due to

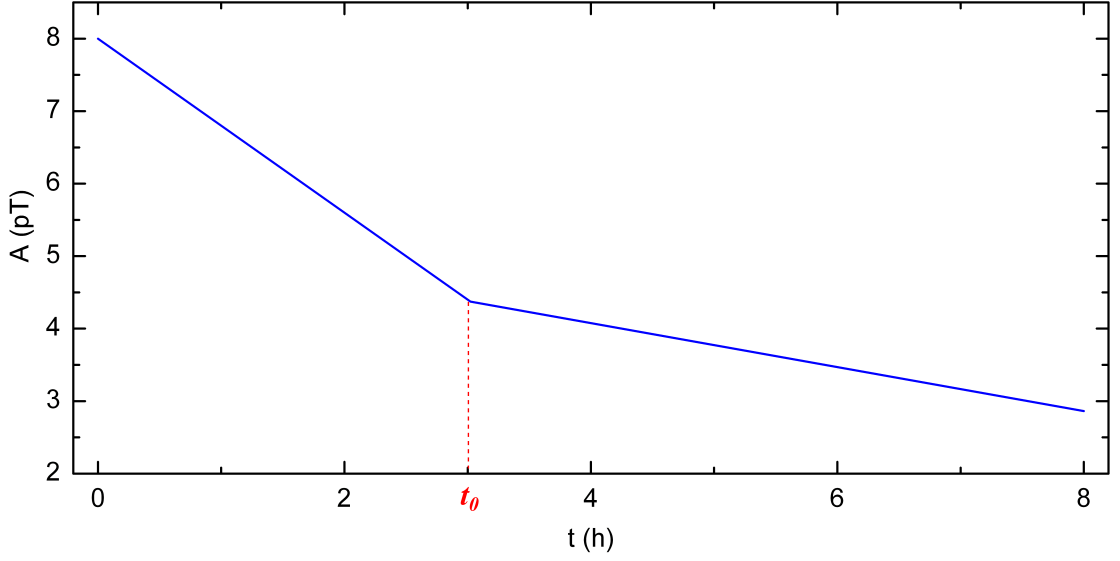


Figure 6.18: Illustration of the determination of  $\Delta T_2^*$  via the difference  $\Delta s$  of the slopes of the signal amplitude  $A(t)$  at the time  $t_0$ .

the movement of the SQUID detectors within the magnetic guiding field (see Chap. B)) compared to the amplitudes of helium and xenon (see Fig. B.2, Fig. B.4 and Fig. B.5), the amplitude ratio is used to define a new fit model. The derivation of the new fit model will be explained in the following: In case that the effective relaxation time  $T_{\text{eff}}$ , which is given by

$$\frac{1}{T_{\text{eff}}} = \frac{1}{T_{2,\text{Xe}}^*} - \frac{1}{T_{2,\text{He}}^*}, \quad (6.83)$$

changes at the time  $t_0$ , due to the field gradients produced by the BGO crystal, the temporal dependence of the amplitude ratio is given by (see App. E)

$$R_{\text{cd/dc}}(t) = \frac{A_{\text{Xe}}(t)}{A_{\text{He}}(t)} = R'_0 \cdot e^{-\frac{(t-t_0)}{T_{\text{eff}}}} (1 + G_{\text{cd/dc}}(t)), \quad (6.84)$$

with  $R'_0 = R_0 \cdot e^{-t_0/T_{\text{eff}}}$ . The function  $G_{\text{cd/dc}}(t)$  can be separated in two parts (see App. E)

$$\begin{aligned} G_{\text{cd/dc}}(t) &= g_{\text{F}}(t) + f_{\text{BGO}}^{\text{cd/dc}}(t) \\ &= g_{\text{F}}(t) + \frac{\Delta T_{\text{eff}}}{T_{\text{eff}}^2} \cdot (t - t_0) \cdot \Theta(\pm(t - t_0)). \end{aligned} \quad (6.85)$$

The first term  $g_{\text{F}}(t)$  corresponds to a continuous function of order  $10^{-3}$  and reflects the deviation from the pure exponential decay essentially caused by magnetic relaxation of the residual field inside the innermost shield after opening and closing the sliding door of the BMSR-2 (see App. B). The Heaviside step function  $\Theta(\pm(t - t_0))$  of the second term  $f_{\text{BGO}}^{\text{cd/dc}}(t)$  indicates a discontinuity at  $t = t_0$ , i.e. a change in the slope of the amplitude ratio due to the change of the  $T_2^*$  times of helium and xenon. The  $(\pm)$  in the argument of the Heaviside

step function has to be set (−) for the sequence c→d and (+) for the reverse one, i.e. d→c. The factor  $\frac{\Delta T_{\text{eff}}}{T_{\text{eff}}^2}$  can be expressed by the  $T_2^*$  times of helium and xenon, i.e.

$$\frac{1}{T_{\text{eff}}} = \frac{1}{T_{2,\text{Xe}}^*} - \frac{1}{T_{2,\text{He}}^*} \Rightarrow \frac{\Delta T_{\text{eff}}}{T_{\text{eff}}^2} = \frac{\Delta T_{2,\text{Xe}}^*}{(T_{2,\text{Xe}}^*)^2} - \frac{\Delta T_{2,\text{He}}^*}{(T_{2,\text{He}}^*)^2}. \quad (6.86)$$

By considering the transverse relaxation rate of the motional narrowing regime (Eq. 3.50), the expression of the  $T_2^*$  times, i.e.  $\Delta T_2^*/(T_2^*)^2$ , can be calculated as follows

$$\frac{1}{T_{2,\text{d}}^*} = \frac{1}{T_1} + \frac{4R^4\gamma^2}{175D} \cdot \underbrace{\left( |\vec{\nabla} B_{1,y}|^2 + |\vec{\nabla} B_{1,z}|^2 + 2|\vec{\nabla} B_{1,x}|^2 \right)}_{\text{Grad}} \quad (6.87)$$

$$\frac{1}{T_{2,\text{c}}^*} = \frac{1}{T_1} + \frac{4R^4\gamma^2}{175D} \cdot \underbrace{\left( |\vec{\nabla} B_{1,y}|^2 + |\vec{\nabla} B_{1,z}|^2 + 2|\vec{\nabla} B_{1,x,\text{BGO}}|^2 \right)}_{\text{Grad}_{\text{BGO}}} \quad (6.88)$$

$$\Rightarrow \frac{1}{T_{2,\text{d}}^*} - \frac{1}{T_{2,\text{c}}^*} \approx \frac{\Delta T_2^*}{(T_2^*)^2} = \frac{4R^4\gamma^2}{175D} \cdot \{ \text{Grad}_{\text{BGO}} - \text{Grad} \}, \quad (6.89)$$

where the squares of the absolute field gradients are given by

$$|\vec{\nabla} B_{1,i}|^2 = \left( \frac{\partial B_{1,i}}{\partial x} \right)^2 + \left( \frac{\partial B_{1,i}}{\partial y} \right)^2 + \left( \frac{\partial B_{1,i}}{\partial z} \right)^2 \quad (6.90)$$

$$|\vec{\nabla} B_{1,x,\text{BGO}}|^2 = \left( \frac{\partial B_{1,x}}{\partial x} \pm \frac{\partial B_{\text{BGO}}}{\partial x} \right)^2 + \left( \frac{\partial B_{1,x}}{\partial y} \right)^2 + \left( \frac{\partial B_{1,x}}{\partial z} \right)^2 \quad (6.91)$$

with  $i = x, y, z$ . The ( $\pm$ ) in Eq. 6.91 indicates that the field gradients produced by the BGO crystal can add or subtract to the field gradients of the magnetic guiding field. According to Eq. 6.89 the expressions  $\Delta T_2^*/(T_2^*)^2$  for the helium and xenon relaxation times then are given by

$$\frac{\Delta T_{2,\text{He}}^*}{(T_{2,\text{He}}^*)^2} = \frac{\gamma_{\text{He}}^2}{D_{\text{He}}^{\text{GM}}} \cdot C \quad \text{and} \quad \frac{\Delta T_{2,\text{Xe}}^*}{(T_{2,\text{Xe}}^*)^2} = \frac{\gamma_{\text{Xe}}^2}{D_{\text{Xe}}^{\text{GM}}} \cdot C. \quad (6.92)$$

The factor  $C$  contains the prefactors which are the same for helium and xenon. The gyromagnetic ratios of helium and xenon are known (Eq. 3.6 and Eq. 3.7). The diffusion coefficients of helium and xenon can be calculated with Eq. 3.35 and Eq. 3.37 by using the partial pressures of the gas mixtures that were used for our measurement runs (see Tab. 6.1). The mean values of the diffusion coefficients then result in  $\overline{D_{\text{He}}^{\text{GM}}} \approx 17.0 \text{ cm}^2/\text{s}$  and  $\overline{D_{\text{Xe}}^{\text{GM}}} \approx 4.7 \text{ cm}^2/\text{s}$ . With these values the ratio of the two terms given in Eq. 6.92 can be calculated to be

$$\frac{\Delta T_{2,\text{He}}^*}{(T_{2,\text{He}}^*)^2} / \frac{\Delta T_{2,\text{Xe}}^*}{(T_{2,\text{Xe}}^*)^2} = \frac{\gamma_{\text{He}}^2}{D_{\text{He}}^{\text{GM}}} / \frac{\gamma_{\text{Xe}}^2}{D_{\text{Xe}}^{\text{GM}}} = \frac{\gamma_{\text{He}}^2}{D_{\text{He}}^{\text{GM}}} \cdot \frac{D_{\text{Xe}}^{\text{GM}}}{\gamma_{\text{Xe}}^2} \approx 2. \quad (6.93)$$

With Eq. 6.86 and Eq. 6.93, the function  $G_{\text{cd/dc}}(t)$  given in Eq. 6.85 then results in

$$G_{\text{cd/dc}}(t) = g_{\text{F}}(t) + \frac{1}{2} \cdot \frac{\Delta T_{2,\text{He}}^*}{(T_{2,\text{He}}^*)^2} \cdot (t - t_0) \cdot \Theta(\pm(t - t_0)). \quad (6.94)$$

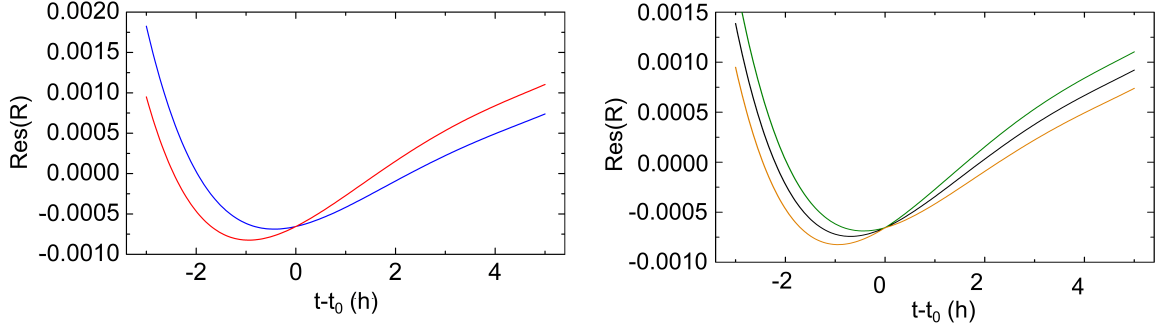


Figure 6.19: Illustration of the determination of the fit model  $F_{cd/dc}(t)$ . *Left*: In case that the BGO crystal is at distant position during the whole measurement run, the temporal dependence of the residuals of the amplitude ratio is given by the blue curve. On the contrary, if the BGO crystal is at close position during the whole measurement run, the temporal dependence of the residuals of the amplitude ratio is given by the red curve. *Right*: For a measurement run where the BGO crystal was moved from c→d at the time  $t_0$ , the expected residuals  $\text{Res}(R_{cd}(t))$  are described by the orange curve, which is composed of the red curve for  $t \leq t_0$  and the blue curve for  $t > t_0$ . On the other hand, for a measurement run where the BGO crystal was moved from d→c, the temporal development of the residuals of the amplitude ratio  $\text{Res}(R_{dc}(t))$  is given by the green curve, which is composed of the blue curve ( $t \leq t_0$ ) and the red curve ( $t > t_0$ ). The average of the green and the orange curve is given by the black curve  $\overline{\text{Res}(R(t))} = (\text{Res}(R_{cd}(t)) + \text{Res}(R_{dc}(t)))/2$ . The function  $\overline{\text{Res}(R(t))}$  can be determined by applying a spline–interpolation simultaneously to the residuals of the two considered measurement runs.

Thus, the temporal development of the amplitude ratio can be expressed by

$$R_{cd/dc}(t) = R'_0 \cdot e^{-\frac{(t-t_0)}{T_{\text{eff}}}} \left( 1 + g_{\text{F}}(t) + \frac{1}{2} \cdot \frac{\Delta T_{2,\text{He}}^*}{(T_{2,\text{He}}^*)^2} \cdot (t - t_0) \cdot \Theta(\pm(t - t_0)) \right). \quad (6.95)$$

With this expression the change in the  $T_2^*$  times can be determined as follows: From a pure exponential fit to the amplitude ratio  $R_{cd/dc}(t)$  (Eq. B.15) the effective relaxation time  $T_{\text{eff}}$  and the residuals  $\text{Res}(R_{cd/dc}(t))$  can be extracted. If the BGO is at distant position during the whole measurement, i.e. no effect on magnetic field gradients with  $\Delta T_{\text{eff}} = 0$ , the expected temporal development of the residuals is given by (see Fig. ?? left side: blue curve)

$$f_{\text{res}}(t) = R'_0 \cdot e^{-\frac{(t-t_0)}{T_{\text{eff}}}} \cdot g_{\text{F}}(t). \quad (6.96)$$

This expression corresponds to the second term of Eq. 6.95. On the contrary, if the BGO crystal is close to the measurement cell during the whole measurement run, the expected temporal development of the residuals is changed by a linear term due to the change of the

$T_2^*$  times of helium and xenon (see Fig. ?? left hand side: red curve)

$$f_{\text{res,BGO}}(t) = R'_0 \cdot e^{-\frac{(t-t_0)}{T_{\text{eff}}}} \cdot \left( g_{\text{F}}(t) + \frac{1}{2} \cdot \frac{\Delta T_{2,\text{He}}^*}{(T_{2,\text{He}}^*)^2} \cdot (t - t_0) \right). \quad (6.97)$$

This expression corresponds to the second and third term of Eq. 6.95 without the Heaviside step function. As shown in Fig. ?? the function  $f_{\text{res,BGO}}(t)$  (red curve) has the same form as the function  $f_{\text{res}}(t)$  (blue curve). However, compared to  $f_{\text{res}}(t)$  the function  $f_{\text{res,BGO}}(t)$  is slightly tilted at the time  $t - t_0 = 0$  h. Looking at two measurement runs with different measurement sequence, i.e.  $c \rightarrow d$  and  $d \rightarrow c$ , the residuals  $\text{Res}(R_{cd/dc}(t))$  are roughly congruent, if the data points of one measurement run are multiplied with a factor  $S$ . In both measurement runs the BGO crystal was either arranged to the right side ( $\mathfrak{R}$ ) or to the left side ( $\mathcal{L}$ ) of the measurement cell. For the measurement run where the BGO crystal was moved from  $c \rightarrow d$  at the time  $t_0$ , the expected temporal dependence of the residuals  $\text{Res}(R_{cd}(t))$  can be described by the orange curve of Fig. ?? (right side), which is composed of the red curve for  $t \leq t_0$  and the blue curve for  $t > t_0$  of Fig. ?? (left side). On the contrary, for the measurement run where the BGO crystal was moved from  $d \rightarrow c$ , the residuals of the amplitude ratio  $\text{Res}(R_{dc}(t))$  are given by the green curve, which is composed of the blue curve for  $t \leq t_0$  and the red curve for  $t > t_0$ . The average of the residuals  $\text{Res}(R_{cd/dc}(t))$  then is given by

$$\overline{\text{Res}(R(t))} = R'_0 \cdot e^{-\frac{(t-t_0)}{T_{\text{eff}}}} \cdot \left( g_{\text{F}}(t) + \frac{1}{2} \cdot \left( \frac{1}{2} \cdot \frac{\Delta T_{2,\text{He}}^*}{(T_{2,\text{He}}^*)^2} \cdot (t - t_0) \right) \right). \quad (6.98)$$

In Fig. ??,  $\overline{\text{Res}(R(t))}$  is indicated by the black curve. By applying a spline-interpolation simultaneously to the residuals  $\text{Res}(R_{cd/dc}(t))$  of the two measurement runs, the function  $\overline{\text{Res}(R(t))}$  can be determined. Then  $\overline{\text{Res}(R(t))}$  can be used to extract  $\Delta T_{2,\text{He}}^*$  by applying the fit function

$$F_{cd/dc}(t) = \overline{\text{Res}(R(t))} \pm \frac{1}{2} \cdot \left( \frac{1}{2} \cdot \frac{\Delta T_{2,\text{He}}^*}{(T_{2,\text{He}}^*)^2} \cdot (t - t_0) \right) \quad (6.99)$$

to the residuals  $\text{Res}(R_{cd/dc}(t))$  for  $t \geq t_0$ . Here the (+) is used for the  $d \rightarrow c$  measurement run and the (-) is used for the  $c \rightarrow d$  measurement run. In total, 6 measurement runs were used for this fitting procedure, which could be combined as follows:

- A: C63 (dc) and C65 (cd)  $\rightarrow \mathcal{L}$
- B: C63 (dc) and C82 (cd)  $\rightarrow \mathcal{L}$
- C: C67 (cd) and C68 (dc)  $\rightarrow \mathfrak{R}$
- D: C68 (dc) and C71 (cd)  $\rightarrow \mathfrak{R}$

The values for  $\Delta T_{2,\text{He}}^*$  are summarized in Tab. 6.7. From these values a possible  $T_2^*$  change of  $|\Delta T_{2,\text{He}}^*| < 170$  s can be inferred. According to Eq. 6.93, for xenon a possible  $T_2^*$  change then is given by  $|\Delta T_{2,\text{Xe}}^*| < 1$  s. Using these upper limits for  $\Delta T_{2,\text{He}(\text{Xe})}^*$ , the systematic error given in Eq. 6.80 can be calculated to  $|\Delta \nu_{\text{sys}}^{T_2^*}| = 0.1$  nHz. Here, for  $T_{2,\text{He}(\text{Xe})}^*$  the mean values



			$\Delta T_{2,\text{He}}^*$ (s)	$\delta(\Delta T_{2,\text{He}}^*)$ (s)
A	C63	dc- $\mathcal{L}$	-52.7	47.3
A	C65	cd- $\mathcal{L}$	-127.5	67.8
B	C63	dc- $\mathcal{L}$	-66.1	47.6
B	C82	cd- $\mathcal{L}$	-115.1	52.6
C	C67	cd- $\mathfrak{R}$	97.5	50.2
C	C68	dc- $\mathfrak{R}$	167.2	64.4
D	C68	dc- $\mathfrak{R}$	59.8	59.9
D	C71	cd- $\mathfrak{R}$	44.5	51.5

Table 6.7: Change of the transverse relaxation times of  $^3\text{He}$  ( $\Delta T_{2,\text{He}}^*$ ) resulting from the fit function given by Eq. 6.99 which is applied to the residuals of the amplitude ratio of two measurement runs with the same position of the BGO crystal relative to the measurement cell, but different measurement configurations.

$\overline{T_{2,\text{He}}^*} = 52.6$  h and  $\overline{T_{2,\text{Xe}}^*} = 4.9$  h were used and for the phase amplitudes  $E'_{\text{He(Xe)}}$  the mean values  $\langle E'_{\text{He}} \rangle \approx 11.5$  and  $\langle E'_{\text{Xe}} \rangle \approx 0.1$  with  $\langle E'_{\text{Xe}} \rangle \ll \langle E'_{\text{He}} \rangle$  (see Tab. 6.3). The final result of the frequency shift  $\Delta\nu_{\text{sp}}$  (Eq. 6.72) due to the spin-dependent short range interaction then is given by

$$\overline{\Delta\nu_{\text{sp}}} = (-2.9 \pm 3.7 \pm 0.4) \text{ nHz} . \quad (6.100)$$

The second and the third value correspond to the correlated and uncorrelated  $1\sigma$  error, respectively.

## 6.8 Bounds on $g_s g_p$

The resulting value of the frequency shift  $\overline{\Delta\nu_{\text{sp}}}$  (Eq. 6.100) is compatible with zero within the error bars and hence there is no evidence for a spin-dependent short-range interaction mediated by axions or axion-like particles. The upper bound of the frequency shift  $\overline{\Delta\nu_{\text{sp}}}$ , which corresponds to the 95% CL, can be calculated by assuming that the probability function of the measured pseudoscalar frequency shift is given by a Gauss function

$$P(x, \mu, \sigma) = \frac{1}{\sigma \cdot \sqrt{2\pi}} \cdot \text{Exp} \left[ \frac{-(x - \mu)^2}{2 \cdot \sigma^2} \right] \quad (6.101)$$

with  $\mu = 0$  nHz and  $\sigma = 3.7$  nHz, which corresponds to the correlated  $1\sigma$  error. The upper bound  $\delta(\overline{\Delta\nu_{\text{sp}}})$  on the pseudoscalar frequency shift then can be determined via the following integral

$$\int_{-\delta(\overline{\Delta\nu_{\text{sp}}})}^{+\delta(\overline{\Delta\nu_{\text{sp}}})} P(x, \mu, \sigma) dx = 0.95 . \quad (6.102)$$

This integral results in  $\delta(\overline{\Delta\nu_{\text{sp}}}) = 7.1$  nHz. With this value exclusion bounds for the product  $|g_s^N g_p^n|$ , which are the coupling constants between the axion and the (bound) nucleon, can be derived. For this purpose the average of the potential  $V_\Sigma^c$  of the spin-dependent short-range

interaction on each polarized atom has to be calculated:  $V_{\Sigma}^c$  can be obtained by integration of  $V_{\text{sp}}(\vec{r})$  from Eq. 2.71 over the volume of the unpolarized matter sample (BGO crystal) and over the volume of the polarized spin samples. Based on the analytical derivation of  $V_{\Sigma,\infty}$  for disc-shaped samples which are infinite in transverse direction ( $yz$ -plane) [151], the following expression for  $V_{\Sigma}^c$  can be derived (see App. F)

$$\begin{aligned} V_{\Sigma}^c &= V_{\Sigma,\infty} \cdot \eta_{\text{fit}}(\lambda) \\ &= 2\pi N\kappa \frac{\lambda^2}{D} \cdot e^{-\Delta x/\lambda} \cdot \left(1 - e^{-D/\lambda}\right) \cdot \left(1 - e^{-d/\lambda}\right) \cdot \eta_{\text{fit}}(\lambda), \end{aligned} \quad (6.103)$$

where  $\Delta x$  represents the distance between the surfaces of the unpolarized and the polarized sample ( $\Delta x_{\text{max}} = 2.2$  mm),  $D$  is the length of the measurement cell,  $d$  is the length of the BGO crystal,  $N$  is the nucleon number density of the BGO crystal and  $\kappa$  is given by  $\kappa = \hbar^2 g_s^N g_p^n / (8\pi \cdot m_{f_\sigma})$ , where  $m_{f_\sigma} = m_n$  is the mass of the bound neutron (Schmidt model [11]).  $\eta_{\text{fit}}(\lambda)$  takes account for the finite size of the cylindrically spin sample in transverse direction ( $yz$ -plane) and can be expressed reasonably well by  $\eta_{\text{fit}}(\lambda) = (1 + 27.8 \cdot \lambda^{1.31}) / (1 + 234 \cdot \lambda^{1.31})$  (see App. F). Using the relation  $|\delta(\overline{\Delta\nu}_{\text{sp}})| \geq 2 \cdot V_{\Sigma}^c/h$  and the expression of  $V_{\Sigma}^c$  given in Eq. 6.103 the exclusion bounds for  $|g_s^N g_p^n|$  can be derived from

$$|g_s^N g_p^n| \leq \frac{1}{\eta_{\text{fit}}(\lambda)} \frac{2\pi D m_{f_\sigma} |\delta(\overline{\Delta\nu}_{\text{sp}})|}{N \hbar \lambda^2} \cdot e^{\Delta x/\lambda} \cdot \left(1 - e^{-D/\lambda}\right)^{-1} \cdot \left(1 - e^{-d/\lambda}\right)^{-1}. \quad (6.104)$$

The upper limit on  $|g_s^N g_p^n|$  is shown in Fig. ?? together with the results of some other measurements which search for scalar-pseudoscalar coupling between nucleons and axions. Till this day these experiments provided the best constraints on axions or axion-like particles. In the experiment of *Youdin et al.* [87], the spin precession frequencies of  $^{199}\text{Hg}$  and Cs magnetometers were measured as a function of the position of two lead masses with respect to an applied magnetic field to determine the bound on  $|g_s^N g_p^n|$  (Fig. ?? (2)). Similar to our experiment, *Bulatowicz et al.* [153] used a magnetically shielded co-magnetometer cell containing spin-polarized  $^{129}\text{Xe}$  and  $^{131}\text{Xe}$ . For the determination of the bound on  $|g_s^N g_p^n|$ , the frequency ratio of the two xenon species were measured by recording their FID (Fig. ?? (3)). In the experiment of *Jenke et al.* [152] gravity resonance spectroscopy of polarized ultracold neutrons was used to determine the bound on  $|g_s^N g_p^n|$  (Fig. ?? (1)). It is impressive how our result improved the bounds on a spin-dependent short-range interaction between polarized (bound) neutrons and unpolarized (bound) nucleons over most of the axion window, tightening existing constraints on axions or axion-like particles heavier than  $20 \mu\text{eV}$  by up to four orders of magnitude. However, it should be mentioned that if the refined nuclear shell model (see Chap. 4.1) is considered, which goes beyond the Schmidt model, the mass of the polarized fermion in Eq. 6.104 is slightly different for  $^3\text{He}$  and  $^{129}\text{Xe}$ :  $m_{f_\sigma}(^3\text{He}) = 0.87 \cdot m_n$  and  $m_{f_\sigma}(^{129}\text{Xe}) = 0.75 \cdot m_n$ . This refined nuclear shell model was used by *Youdin et al.* and increases our upper bounds by a factor of 1.4 (see Chap. 4.1), which will not be visible with the naked eye in Fig. ??.

For the sake of completeness, it should be mentioned that there exist a lot of experiments that search for a spin-dependent short-range force between polarized electrons and unpolarized

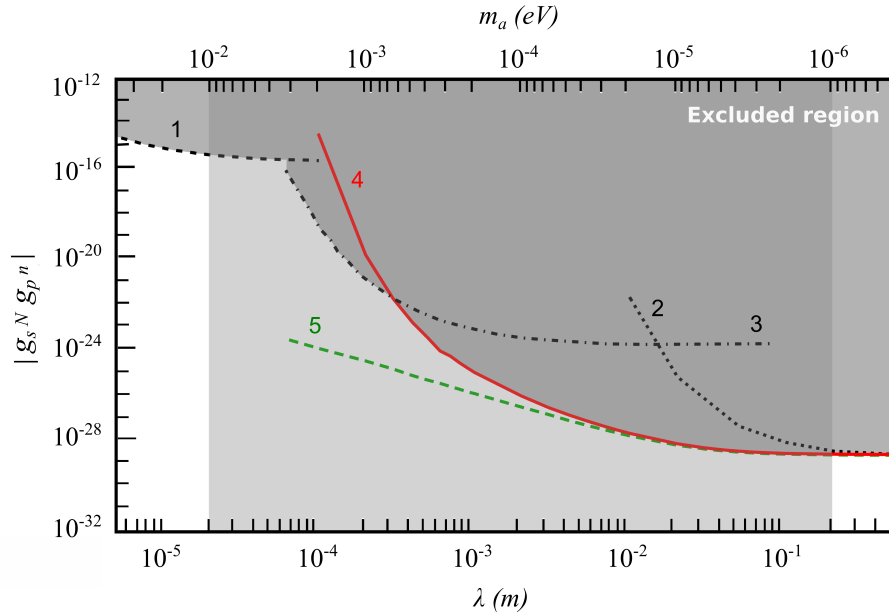


Figure 6.20: Experimental 95% confidence upper limit on  $|g_s^N g_p^n|$  plotted versus  $\lambda$ , the range of the Yukawa-force with  $\lambda = \hbar/(m_a c)$ . The axion window is indicated by the light gray area. The dark gray area indicates the excluded region. (1): result of [152], (2): result of [87], (3): result of [153], (4): this experiment. Curve (5) shows the expected results for our experiment if  $\Delta x \approx 0$  mm, whereby the same data set was used. This curve demonstrates the gain in measurement sensitivity for  $\lambda < 10^{-3}$  m by reducing the gap between the polarized and unpolarized matter sample.

nucleons. The results of the experiments which provide the best constraints on axions or axion-like particles are shown in Fig. 6.21. Since the coupling between electrons and axions and the coupling between nucleons and axions are different (see Chap. 2.5.1), the results are shown in two different plots. In the experiment of *Hoedel et al.* [154] an unshielded, highly non-magnetic torsion pendulum was used, which was suspended by a tungsten fiber between two halves of a stationary split toroidal electromagnet. The bound on  $|g_s^N g_p^e|$  could be determined via the measurement of the magnetic-field-dependent torque of the pendulum, which is generated by the spin-dependent short-range force between the polarized electrons in the electromagnet and the unpolarized silicon atoms in the pendulum (Fig. 6.21 (1)). In the experiment of *Hammond et al.* [85] a spherical superconducting torsion balance was used. Here the bound on  $|g_s^N g_p^e|$  was determined by measuring the oscillation of the torsion balance (Fig. 6.21 (2)). In the experiment of *Ni et al.* [155] the interaction of a rotating copper mass with paramagnetic salt  $\text{TbF}_3$  was measured. A low noise DC-SQUID system was connected to a superconducting pickup loop which was coupled to the salt, i.e. any changes of the magnetization of the salt could be detected. From the change of the magnetization the bound on  $|g_s^N g_p^e|$  was extracted (Fig. 6.21 (3)).

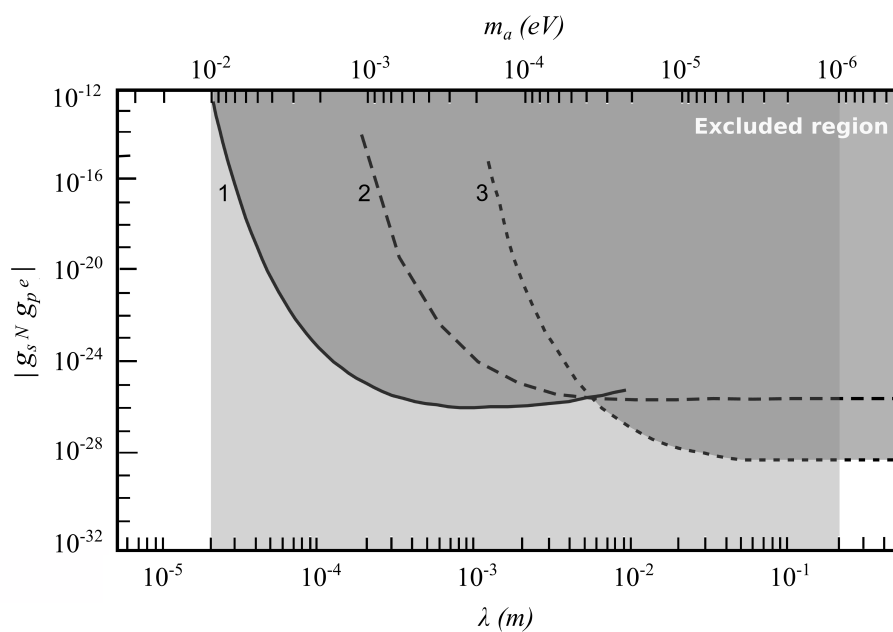


Figure 6.21: Experimental 95% confidence upper limit on  $|g_s^N g_p^e|$  plotted versus  $\lambda$ , the range of the Yukawa-force with  $\lambda = \hbar/(m_a c)$ . The axion window is indicated by the light gray area and the excluded region by the dark gray area. (1): result of [154], (2): result of [85], (3): result of [155].

## 7 Conclusion and Outlook

The axion is a light and weak interacting particle and thus it is difficult to detect. Since it neither absorbs nor emits electromagnetic radiation it is a good candidate for cold dark matter and hence it is a particle of high interest in modern physics. The axion is a spin-0 particle which mediates a spin-dependent short-range force between polarized and unpolarized fermions. This interaction leads to a shift, e.g. in the precession frequency of nuclear spin polarized gases.

In this thesis the ultra-sensitive low-field  $^3\text{He}/^{129}\text{Xe}$  co-magnetometer was used to search for non-magnetic, spin-dependent short-range interaction between polarized bound neutrons and unpolarized bound nucleons. As unpolarized matter sample a BGO crystal was used. The influence of the ambient magnetic field and its temporal fluctuations cancels in the weighted difference of the measured Larmor frequencies of the co-located spin samples. A shift in the weighted frequency difference could be extracted from respective frequency measurements in close and distant position of the BGO crystal relative to the spin samples. Our measurements result in

$$\overline{\Delta\nu_{\text{sp}}} = (-2.9 \pm 3.7) \text{ nHz} , \quad (7.1)$$

where the second value corresponds to the correlated  $1\sigma$  error. This result could be used to calculate an upper bound of  $\delta(\overline{\Delta\nu_{\text{sp}}}) = 7.1 \text{ nHz}$  (95% CL). With this value exclusion bounds for the dimensionless product  $|g_s^N g_p^n|(\lambda)$  of the coupling constants between the nucleons and the axions or axion-like particles could be derived. Within the axion mass window we have substantially improved the bounds, tightening existing constraints on axion-like particles heavier than  $20 \mu\text{eV}$  by up to four orders of magnitude.

For future measurements there are clear strategies on how to improve our experimental sensitivity:

- If the spin/unpolarized sample is moved more frequently between its set positions ( $c \leftrightarrow d$  and/or  $\mathcal{L} \leftrightarrow \mathcal{R}$ ), a different time structure for the linear term in the fit model of Eq. 6.63 occurs such that the correlated error should approach the uncorrelated one. This was demonstrated in [122, 96], already.
- Magnetic susceptibility related artefacts have to be eliminated by taking zero-susceptibility matched unpolarized samples ( $\chi_{\text{mag}} \approx 0 \text{ ppm}$ ) as it is common practice in high resolution NMR spectroscopy [156].
- By reducing the distance  $\Delta x$  between the end faces of the unpolarized sample and the volume of the spin samples to  $\Delta x \approx 0 \text{ mm}$  the sensitivity on  $|g_s^N g_p^n|$  can be improved.

For example, having the same sensitivity of  $\delta(\overline{\Delta\nu_{\text{sp}}}) = 7.1$  nHz (95% CL), the present sensitivity on  $|g_s^N g_p^n|$  will significantly increase for  $\lambda < 10^{-3}$  m (see Fig. ??, green dashed curve (5)). Reduction of the gap  $\Delta x$  can be realized by cutting one of the end faces of the cylindrical measurement cell. The measurement cell then is closed again by gluing the BGO crystal to the open end face. For this special cell-BGO assembly it has to be tested if transverse relaxation times  $T_2^*$  of about 53 h and 5 h for  $^3\text{He}$  and  $^{129}\text{Xe}$  respectively, can be achieved. Since the BGO crystal is fixed to the measurement cell, it is not possible to move the BGO crystal during one measurement run from close to distant position or vice versa. But by rotation of the cell-BGO assembly, it is possible to extract the frequency shift  $\Delta\nu_{\text{sp}} = 2V_{\Sigma}/h \propto \vec{\sigma} \cdot \hat{r}$  due to the spin-dependent short-range interaction. That means, first the precession frequency of  $^3\text{He}$  and  $^{129}\text{Xe}$  has to be recorded for several hours for the  $0^\circ$  position, i.e. the magnetic guiding field  $\vec{B}_0 \propto \vec{\sigma}$  and the unit distance vector  $\hat{r}$ , which points from the polarized sample to the unpolarized sample, are aligned parallel. Then the cell-BGO assembly is rotated by  $180^\circ$  degrees, i.e. the magnetic guiding field  $\vec{B}_0 \propto \vec{\sigma}$  and the unit distance vector  $\hat{r}$  are aligned antiparallel. Since the frequency shift due to the spin-dependent short-range interaction is proportional to  $\vec{\sigma} \cdot \hat{r}$ , the sign of  $\Delta\nu_{\text{sp}}$  will change after rotation of the cell-BGO assembly. Hence,  $\Delta\nu_{\text{sp}}$  can be extracted by composing the difference of the measured weighted spin precession frequencies of the  $0^\circ$  and the  $180^\circ$  orientation:

$$\Delta\omega_{0^\circ} = \underbrace{\omega_{\text{He,L}} - \frac{\gamma_{\text{He}}}{\gamma_{\text{Xe}}}\omega_{\text{Xe,L}}}_0 + \left(1 - \frac{\gamma_{\text{He}}}{\gamma_{\text{Xe}}}\right) 2\pi\Delta\nu_{\text{sp}} \quad (7.2)$$

$$\Delta\omega_{180^\circ} = \underbrace{\omega_{\text{He,L}} - \frac{\gamma_{\text{He}}}{\gamma_{\text{Xe}}}\omega_{\text{Xe,L}}}_0 - \left(1 - \frac{\gamma_{\text{He}}}{\gamma_{\text{Xe}}}\right) 2\pi\Delta\nu_{\text{sp}} \quad (7.3)$$

$$\Rightarrow \Delta\nu_{\text{sp}} = \frac{\Delta\omega_{0^\circ} - \Delta\omega_{180^\circ}}{4\pi\left(1 - \frac{\gamma_{\text{He}}}{\gamma_{\text{Xe}}}\right)}. \quad (7.4)$$

However the extraction of the frequency shift  $\Delta\nu_{\text{sp}}$  will be difficult since the rotation of the cell-BGO assembly can lead to different magnetic field gradients across the measurement cell. For instance, this can be explained by the actual geometry of the spin-sample cell or by the accuracy of the rotation of the cell complex. Furthermore, due to the rotation the position of the BGO crystal within the magnetic guiding field is changed. Hence, the magnetic susceptibility of the BGO crystal has a different impact on the resulting gradients of the magnetic field within the spin sample cell. Different field gradients will lead to different  $T_2^*$  times for the  $0^\circ$  and the  $180^\circ$  positions. As already mentioned in Chap. 6.6 the change in  $T_2^*$  leads to a similar effect as the spin-dependent short-range interaction, i.e. a constant frequency shift which is given by  $\Delta\omega_{T_2^*} = 2\pi\nu_{T_2^*}\Theta(t - t_0)$ , where  $t_0$  is the time when the cell-BGO assembly is rotated. Thus, this frequency shift will not vanish in the difference of the two measured

---

frequencies, i.e.  $\Delta\nu_{\text{sp}}$  given in Eq. 7.4 will transform to

$$\Delta\nu_{\text{sp}} = \frac{\Delta\omega_{0^\circ} - \Delta\omega_{180^\circ} - 2\pi\nu T_2^*}{4\pi \left(1 - \frac{\gamma_{\text{He}}}{\gamma_{\text{Xe}}}\right)}. \quad (7.5)$$

That means, for correct extraction of  $\Delta\nu_{\text{sp}}$  the effect of the change of the  $T_2^*$  times has to be estimated and eliminated.





## A. Calculation of the Standard Deviation of the Weighted Phase Difference

In general, according to the Gaussian error propagation, the error of a quantity  $C = C(A, B)$ , which is a function of the defective quantities  $A$  and  $B$ , is given by

$$\delta C = \sqrt{\left(\frac{\partial C(A, B)}{\partial A} \cdot \delta A\right)^2 + \left(\frac{\partial C(A, B)}{\partial B} \cdot \delta B\right)^2}. \quad (\text{A.1})$$

Thereby  $\delta A$  and  $\delta B$  are the errors of the quantities  $A$  and  $B$  respectively and  $\frac{\partial C}{\partial A}$  and  $\frac{\partial C}{\partial B}$  are the respective partial derivatives of the quantity  $C$  to  $A$  and  $B$ . The error of the weighted phase difference, which is given by

$$\Delta\Phi(t) = \Phi_{\text{He}}(t) - \frac{\gamma_{\text{He}}}{\gamma_{\text{Xe}}} \cdot \Phi_{\text{Xe}}(t), \quad (\text{A.2})$$

then results in

$$\begin{aligned} \delta(\Delta\Phi) &= \sqrt{\left(\frac{\partial(\Delta\Phi)}{\partial\Phi_{\text{He}}} \cdot \delta\Phi_{\text{He}}\right)^2 + \left(\frac{\partial(\Delta\Phi)}{\partial\Phi_{\text{Xe}}} \cdot \delta\Phi_{\text{Xe}}\right)^2} \\ &= \sqrt{\delta\Phi_{\text{He}}^2 + \left(\frac{\gamma_{\text{He}}}{\gamma_{\text{Xe}}} \cdot \delta\Phi_{\text{Xe}}\right)^2}. \end{aligned} \quad (\text{A.3})$$

In [132] the sensitivity regarding the phase was deduced from the Cramer-Rao lower bound (CRLB). The error of the phases of helium and xenon, i.e.  $\delta\Phi_{\text{He}}$  and  $\delta\Phi_{\text{Xe}}$ , then are given by:

$$\delta\phi_{\text{He}} = \sigma_{\phi_{\text{He}}} = \frac{4}{\text{SNR}_{\text{He}} \cdot T}, \quad (\text{A.4})$$

$$\delta\phi_{\text{Xe}} = \sigma_{\phi_{\text{Xe}}} = \frac{4}{\text{SNR}_{\text{Xe}} \cdot T}. \quad (\text{A.5})$$

Since the signals of helium and xenon, i.e.  $A_{\text{He}}(t)$  and  $A_{\text{Xe}}(t)$ , decay exponentially with the transverse relaxation times  $T_{2,\text{He}}^*$  and  $T_{2,\text{Xe}}^*$  respectively, the SNR is given by

$$\text{SNR}_{\text{He}} = \frac{A_{\text{He}}(t)}{N_{\text{He}}(t)} \propto A_{t=0,\text{He}} \cdot e^{-\frac{t}{T_{2,\text{He}}^*}} \quad (\text{A.6})$$

$$\text{SNR}_{\text{Xe}} = \frac{A_{\text{Xe}}(t)}{N_{\text{Xe}}(t)} \propto A_{t=0,\text{Xe}} \cdot e^{-\frac{t}{T_{2,\text{Xe}}^*}}. \quad (\text{A.7})$$

$A_{t=0,\text{He}}$  and  $A_{t=0,\text{Xe}}$  are the initial amplitudes of the helium and the xenon signals, respectively. The noise of helium and xenon, i.e.  $N_{\text{He}}(t)$  and  $N_{\text{Xe}}(t)$ , approximatively is assumed to

be constant. By inserting Eqs. A.4–A.7 in Eq. A.3, the error of the weighted phase difference results in

$$\begin{aligned}\delta(\Delta\phi) &\propto \sqrt{\left(\frac{1}{\text{SNR}_{\text{He}}}\right)^2 + \left(\frac{\gamma_{\text{He}}}{\gamma_{\text{Xe}}} \cdot \frac{1}{\text{SNR}_{\text{Xe}}}\right)^2} \\ &\propto \sqrt{\frac{e^{\frac{2t}{T_{2,\text{He}}^*}}}{(A_{t=0,\text{He}})^2} + \left(\frac{\gamma_{\text{He}}}{\gamma_{\text{Xe}}}\right)^2 \cdot \frac{e^{\frac{2t}{T_{2,\text{Xe}}^*}}}{(A_{t=0,\text{Xe}})^2}}.\end{aligned}\quad (\text{A.8})$$

By extracting the first term of the square root function, the error of the weighted phase difference transforms to

$$\delta(\Delta\phi) \propto \frac{e^{\frac{t}{T_{2,\text{He}}^*}}}{A_{\text{He},t=0}} \cdot \sqrt{1 + \left(\frac{\gamma_{\text{He}}}{\gamma_{\text{Xe}}}\right)^2 \left(\frac{A_{\text{He}}}{A_{\text{Xe}}}\right)_{t=0}^2 \frac{e^{\frac{2t}{T_{2,\text{Xe}}^*}}}{e^{\frac{2t}{T_{2,\text{He}}^*}}}}.\quad (\text{A.9})$$

Extraction of the exponential functions of the second term of the square root function leads to

$$\delta(\Delta\phi) \propto e^{\frac{t}{T_{2,\text{Xe}}^*}} \cdot \sqrt{e^{-2t\left(\frac{1}{T_{2,\text{Xe}}^*} - \frac{1}{T_{2,\text{He}}^*}\right)} + \left(\frac{\gamma_{\text{He}}}{\gamma_{\text{Xe}}}\right)^2 \cdot \left(\frac{A_{\text{He}}}{A_{\text{Xe}}}\right)_{t=0}^2}}.\quad (\text{A.10})$$

## B. Exact Determination of $T_2^*$

The signal amplitudes of  $^3\text{He}$  and  $^{129}\text{Xe}$  of each sub-data set  $i$  can be calculated with the fit parameters of Eq. 6.3 as

$$A_{\text{He/Xe}}(t_i) = \sqrt{\left(a_{\text{c,He/Xe}}^i\right)^2 + \left(a_{\text{s,He/Xe}}^i\right)^2}, \quad (\text{B.1})$$

where  $t_i = (i - 1) \cdot \tau$  is the time of the  $i$ -th sub-data set and  $\tau = 3.2$  s is the length of each sub-data set. Since the amplitudes  $a_{\text{c,He/Xe}}^i$  and  $a_{\text{s,He/Xe}}^i$  of the raw data fit are less correlated, the amplitude errors  $\Delta A_{\text{He/Xe}}(t_i)$  can be determined by the Gaussian error propagation law. Figure B.1 shows the time developing of the helium (black) and xenon (red) amplitudes of measurement run C68 for three different and independent gradiometers (Z2E-Z5S, Z3D-Z2S, Z3I-Z1S). The amplitudes decay exponentially with the transverse relaxation time  $T_2^*$ , i.e.

$$A_{\text{fit}}(t) = A_0^g \cdot e^{-t/T_2^*}, \quad (\text{B.2})$$

where  $g = 1, 2, 3$  corresponds to the gradiometers Z2E-Z5S, Z3D-Z2S and Z3I-Z1S, respectively. The function  $A_{\text{fit}}(t)$  is used for a common fit of the amplitudes, i.e. the data points  $(t_i, A_{\text{He/Xe}}(t_i), \Delta(A_{\text{He/Xe}}(t_i)))$  of all three gradiometers were joined to one big data set. In doing so, an additional dimension was added to each data point so that the data points of the different SQUID gradiometers can be distinguished later on. The data points of the big data set then are given by  $(\{t_i, g\}, A_{\text{He/Xe}}(t_i), \Delta(A_{\text{He/Xe}}(t_i)))$ . The fit function according to Eq. B.2 then is applied to the big data set, i.e. to the signal amplitudes of all three gradiometers simultaneously. Here the initial amplitudes  $A_0^g$  can be different but the  $T_2^*$  time is equal for all three gradiometers. For measurement run C68, the fit parameters for helium result in  $A_{0,\text{He}}^1 = (9186.37 \pm 0.03)$  fT,  $A_{0,\text{He}}^2 = (4456.42 \pm 0.03)$  fT,  $A_{0,\text{He}}^3 = (6879.08 \pm 0.04)$  fT and  $T_{2,\text{He}}^* = (212019 \pm 9)$  s with  $\chi^2/dof = 1.65$  and the fit parameters for xenon result in  $A_{0,\text{Xe}}^1 = (4945.31 \pm 0.16)$  fT,  $A_{0,\text{Xe}}^2 = (2399.66 \pm 0.13)$  fT,  $A_{0,\text{Xe}}^3 = (3704.47 \pm 0.22)$  fT and  $T_{2,\text{Xe}}^* = (19049 \pm 1)$  s with  $\chi^2/dof = 17.50$ . To check the quality of the fit function the amplitude residuals  $\text{Res}(A(t_i))$  have to be considered, which are the difference between the real signal amplitudes  $A(t_i)$  and the fit function  $A_{\text{fit}}(t)$ . In Fig. B.2 the amplitude residuals of helium and xenon of measurement run C68 for the three different gradiometers are shown. Each data point comprises 50 sub-data sets which corresponds to a time interval of 160 s. Thus the error bar of each data point is smaller by a factor of  $\approx \sqrt{50}$  compared to the error of the amplitude of a single sub-data set. It stands out that the amplitude residuals of helium and xenon do not have the expected statistical distribution around zero but show a characteristic structure instead which is more distinct for xenon than for helium. This also applies for the other measurement runs. In the first instance we assumed that this structure occurs

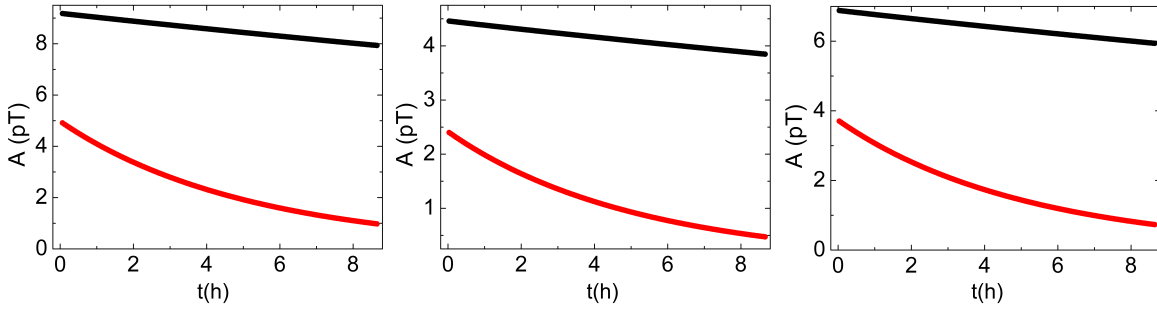


Figure B.1: Decay of the  $^3\text{He}$  (black) and  $^{129}\text{Xe}$  (red) amplitudes of measurement run C68 for three different gradiometers (left: Z2E-Z5E, middle: Z3D-Z2S, right: Z3I-Z1S). Each data point comprises 50 sub-data sets which corresponds to a time interval of 160 s. Thus the error bar of each data point is smaller by a factor of  $\approx \sqrt{50}$  compared to the error of the amplitude of a single sub-data set. Hence, the error bars are too small to be visible in the plot.

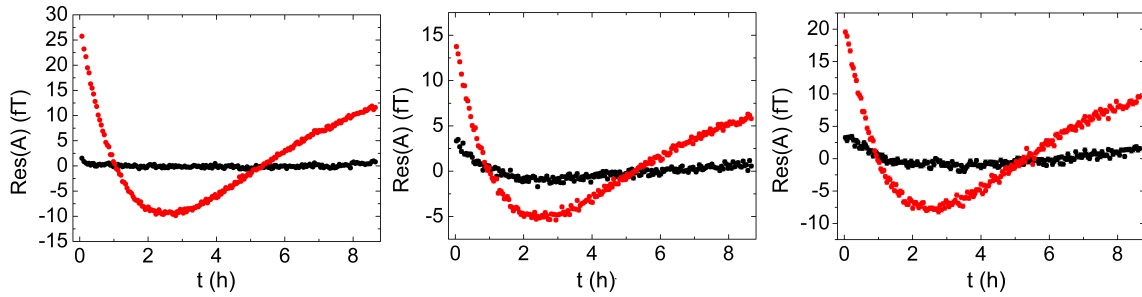


Figure B.2: Amplitude residuals of  $^3\text{He}$  (black) and  $^{129}\text{Xe}$  (red) of measurement run C68 for three different gradiometers (left: Z2E-Z5E, middle: Z3D-Z2S, right: Z3I-Z1S) resulting from a common exponential fit according to Eq. B.2. Each data point comprises 50 sub-data sets which corresponds to a time interval of 160 s. Thus the error bar of each data point is smaller by a factor of  $\approx \sqrt{50}$  compared to the error of the amplitude of a single sub-data set. Hence, the error bars are too small to be visible in the plot.

due to the movement of the BGO crystal. However, consideration of the amplitude residuals of the measurement runs that were performed in 2009 to search for a sidereal modulation in the spin precession frequency, which violates Lorentz symmetry (LV 2009) [96, 122], the same characteristic structure occurs. Since no mass was moved during those measurement runs, the structure in the amplitude residuals cannot be caused by the BGO crystal. As example the amplitude residuals of measurement run C92 (LV 2009) is shown in Fig. B.3 on the left.

Comparing the amplitude residuals of the measurement runs of 2009 and 2010 it emerges that the structure in the amplitude residuals of xenon is similar for all measurement runs

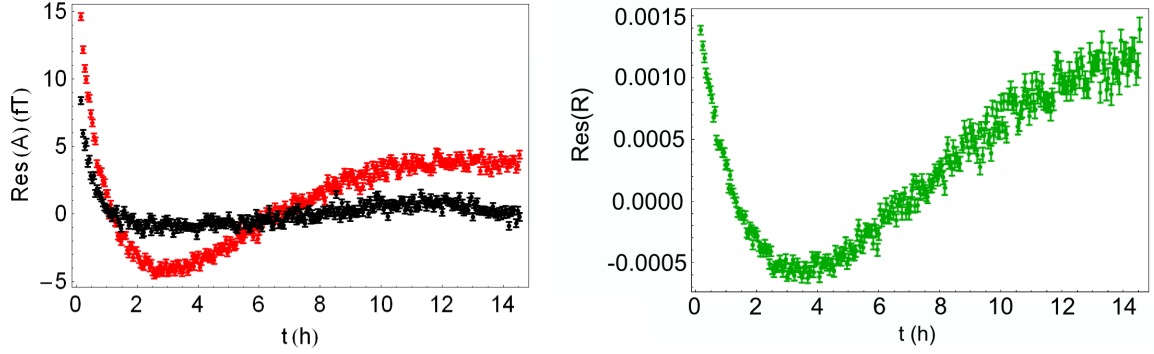


Figure B.3: *Left*: Amplitude residuals of  $^3\text{He}$  (black) and  $^{129}\text{Xe}$  (red) of measurement run C92 (LV 2009) for one gradiometer (Z2E-Z9E) resulting from an exponential fit according to Eq. B.2. *Right*: Residuals of the amplitude ratio  $\text{Res}(R(t))$  of measurement run C92 (LV 2009) for one gradiometer (Z2E-Z9E) resulting from an exponential fit according to Eq. B.5. In both plots each data point comprises 50 sub-data sets which corresponds to a time interval of 160 s. Thus the error bar of each data point is smaller by a factor of  $\approx \sqrt{50}$  compared to the error of the amplitude of a single sub-data set.

with a minimum between 1 and 3 hours.

From the amplitude residuals it is possible to infer that the decay of the signal amplitudes is not purely exponential. Possible reasons can be:

- a) Drift due to the motion of the SQUID detectors within the magnetic guiding field.
- b) Change of the magnetic field gradients in time (see Sec. B.1).

These effects can be parameterized by  $f_a(t)$  and  $f_b(t)$  respectively, so that the temporal development of the helium and xenon signal amplitudes can be described by

$$A_{\text{He/Xe}}(t) = f_a(t) \cdot f_b(t) \cdot A_0 \cdot e^{-t/T_{2,\text{He/Xe}}^*} . \quad (\text{B.3})$$

For a single gradiometer the function  $f_a(t)$ , that describes the drift due to the motion of the SQUID detectors within the magnetic guiding field, should be equal for helium and xenon, i.e.  $f_{a,\text{He}}(t) = f_{a,\text{Xe}}(t)$ . So, by considering the ratio  $R(t)$  of the xenon and helium signal amplitudes this effect should drop out. The temporal development of the ratio  $R(t)$  then can be described by

$$\begin{aligned} R(t) = \frac{A_{\text{Xe}}(t)}{A_{\text{He}}(t)} &= \frac{f_{c,\text{Xe}}(t)}{f_{c,\text{He}}(t)} \cdot \frac{A_{0,\text{Xe}}}{A_{0,\text{He}}} \cdot e^{-\frac{t}{T_{\text{eff}}}} \\ &= f(t) \cdot R_0 \cdot e^{-t/T_{\text{eff}}} , \end{aligned} \quad (\text{B.4})$$

where  $T_{\text{eff}}$  is an effective relaxation time given by  $\frac{1}{T_{\text{eff}}} = \frac{1}{T_{2,\text{Xe}}^*} - \frac{1}{T_{2,\text{He}}^*}$ . By applying only an exponential fit, i.e.

$$R_{\text{fit}}(t) = R_0 \cdot e^{-\frac{t}{T_{\text{eff}}}} , \quad (\text{B.5})$$

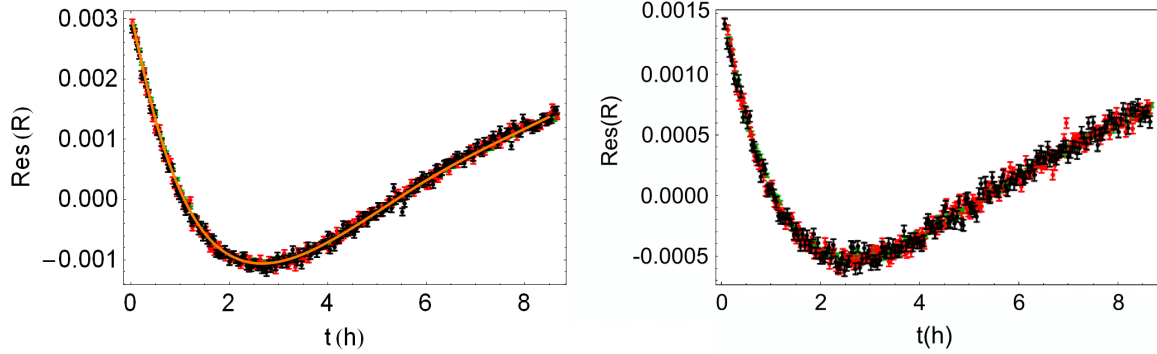


Figure B.4: Residuals of the amplitude ratio  $\text{Res}(R(t_i))$  for all three gradiometers (green: Z2E-Z5S, red: Z3D-Z2S, black: Z3I-Z1S) of measurement run C68 (left) and C65 (right) resulting from a common exponential fit according to Eq. B.5. Each data point comprises 50 sub-data sets which corresponds to a time interval of 160 s. Thus the error bar of each data point is smaller by a factor of  $\approx \sqrt{50}$  compared to the error of the amplitude ratio of a single sub-data set. Hence, the error bars are too small to be visible in the plot. Via spline-interpolation the structure in the residuals can be described by a function  $f_{\text{res}}(t)$  (orange line).

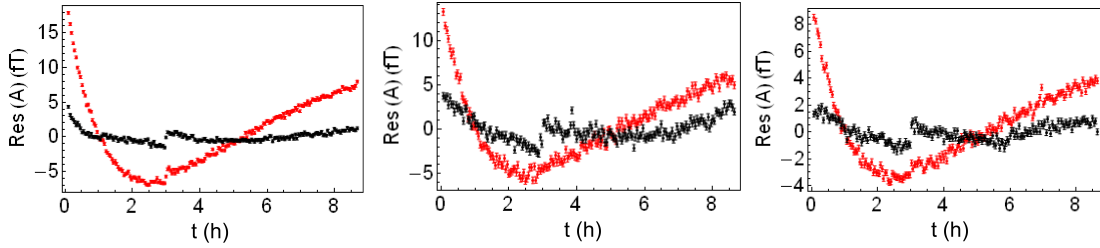


Figure B.5: Amplitude residuals of  $^3\text{He}$  (black) and  $^{129}\text{Xe}$  (red) of measurement run C65 for three different gradiometers (left: Z2E-Z5E, middle: Z3D-Z2S, right: Z3I-Z1S) resulting from a common exponential fit according to Eq. B.2. Each data point comprises 50 sub-data sets which corresponds to a time interval of 160 s. Thus the error bar of each data point is smaller by a factor of  $\approx \sqrt{50}$  compared to the error of the amplitude of a single sub-data set. Hence, the error bars are too small to be visible in the plot. At the time  $t_0$  when the BGO crystal was moved a jump occurs in the residuals.

to the amplitude ratio  $R(t)$  and afterwards calculating the residuals, a structure remains, which is equal for all three gradiometers (see Fig. B.4 left). The same structure remains if the amplitude ratios of the measurement runs of 2009 are considered. As example the residuals of the amplitude ratio of measurement run C92 are shown in Fig. B.3 on the right. For some measurement runs of 2010 a small jump in the amplitude residuals of helium and xenon occurred at the time  $t_0$  when the BGO crystal was moved (see Fig. B.5). For instance, this jump can be caused by a change of the distance between the SQUID gradiometer and the

spin sample due to the movement of the BGO crystal. However, this jump disappears by considering the residuals of the amplitude ratio (see Fig. B.4 right).

## B.1 Possible Reason for the Structure in the Amplitude Residuals

Before each measurement run, the measurement cell has to be filled with a new gas mixture of polarized  $^3\text{He}$ , polarized  $^{129}\text{Xe}$  and  $N_2$  within the filling station. Then the measurement cell is transferred to the measurement setup in the BMSR-2. For this purpose, the doors of the BMSR-2 have to be opened. While the doors are open, the Earth's magnetic field partly enters the shielded room and thus the residual field inside the BMSR-2 is changed. After closing the doors of the BMSR-2 the Earth's magnetic field disappears. Then the innermost  $\mu$ -metal shield causes magnetic relaxation, i.e. the residual field relaxes to its initial state. Hence, at the beginning of each measurement run the magnetic guiding field  $\vec{B}_0$  is superposed by a residual field  $\vec{B}_1$  which decays exponentially with a time constant  $\alpha$ . The amplitude as well as the relaxation time of this residual field  $\vec{B}_1$  strongly depends on the time for which the doors of the BMSR-2 were open. Without loss of generality it is assumed that the magnetic guiding field and the residual field are given by  $\vec{B}_0 = (B_{0,x}, 0, 0)$  and  $\vec{B}_1 = (0, B_{1,y}, B_{1,z}) \cdot e^{-t/\alpha}$ . Then the total vector of the magnetic guiding field seen by the precessing spins is given by

$$\vec{B}_{\text{tot}}(t) = \begin{pmatrix} B_{0,x} \\ B_{1,y} \cdot e^{-t/\alpha} \\ B_{1,z} \cdot e^{-t/\alpha} \end{pmatrix}, \quad (\text{B.6})$$

with an absolute value of

$$|\vec{B}_{\text{tot}}(t)| = \sqrt{B_{0,x}^2 + (B_{1,y} \cdot e^{-t/\alpha})^2 + (B_{1,z} \cdot e^{-t/\alpha})^2}. \quad (\text{B.7})$$

Assuming that  $B_{1,y}, B_{1,z} \ll B_{0,x}$ , the relation  $\sqrt{1+x^2} \approx 1 + \frac{1}{2}x^2$  can be used, so that  $|\vec{B}_{\text{tot}}(t)|$  simplifies to

$$|\vec{B}_{\text{tot}}(t)| = B_{0,x} + B_1 \cdot e^{-t/\beta}, \quad (\text{B.8})$$

with  $\beta = \alpha/2$  and  $B_1 = (B_{1,y} + B_{1,z})^2 / (2B_{0,x}^2)$ .

Additionally, the magnetic guiding field slightly drifts linear in time since the current source slightly drifts linear in time ( $I \propto |\vec{B}_0|$ ). The total temporal development of the magnetic guiding field approximately then can be described by

$$|\vec{B}_{\text{tot}}(t)| \approx B_{0,x} + B_1 \cdot e^{-t/\beta} + B_2 \cdot t. \quad (\text{B.9})$$

The real temporal development of the absolute value of the total magnetic guiding field  $|\vec{B}_{\text{tot}}(t)|$  can be calculated directly from the measured precession frequencies, e.g. of the  $^3\text{He}$  spins, for each sub-data set  $i$ , by using the relation  $\omega_{\text{He/Xe}}(t_i) = \gamma_{\text{He/Xe}} \cdot |\vec{B}_{\text{tot}}(t_i)|$ . In Fig. 4.2  $|\vec{B}_{\text{tot}}(t)|$  of measurement run C68 is shown. Fitting the data  $|\vec{B}_{\text{tot}}(t_i)|$  by using

	$\beta$ (s)	$\Delta\beta$ (s)	$B_{0,x}$ (nT)	$B_1$ (nT)	$B_2$ (nT/s)
C54	8519	296	353.2	$-4.1 \cdot 10^{-3}$	$3.3 \cdot 10^{-7}$
C55	3385	68	353.2	$-4.7 \cdot 10^{-3}$	$3.1 \cdot 10^{-7}$
C60	3098	187	353.2	$-3.1 \cdot 10^{-3}$	$1.8 \cdot 10^{-7}$
C63	4766	78	353.2	$-7.6 \cdot 10^{-3}$	$1.9 \cdot 10^{-7}$
C65	4041	78	353.2	$-8.3 \cdot 10^{-3}$	$1.5 \cdot 10^{-7}$
C67	4023	211	353.2	$-2.6 \cdot 10^{-3}$	$2.0 \cdot 10^{-7}$
C68	4101	129	353.2	$-5.0 \cdot 10^{-3}$	$0.9 \cdot 10^{-7}$
C71	5267	157	353.2	$-5.2 \cdot 10^{-3}$	$2.7 \cdot 10^{-7}$
C80	1955	29	353.2	$-8.2 \cdot 10^{-3}$	$3.6 \cdot 10^{-7}$
C82	164	11	353.2	$-4.9 \cdot 10^{-3}$	$4.7 \cdot 10^{-7}$

Table B.1: Fit parameters of the temporal development of the absolute total magnetic guiding field  $|\vec{B}_{\text{tot}}(t)|$  using Eq. B.9. Since the errors of the fit parameters  $B_{0,x}$ ,  $B_1$  and  $B_2$  are three orders of magnitude smaller than the corresponding values, the errors of these fit parameters are not listed in the table.  $B_2$ , which corresponds to the linear drift of the magnetic field due to the drift of the current source, is much smaller than the exponential drift  $B_1$ . The relaxation time  $\beta$  for the runs C80 and C82 are much shorter than the ones for the other measurement runs. This can be explained by the fact that at the end of the measuring period of 2010 it was noted that the longer the doors of the BMSR-2 were open, the longer is the relaxation of the innermost  $\mu$ -metal shield, i.e. the longer is the relaxation time  $\beta$ .

Eq. B.9 the unknown parameters  $B_{0,x}$ ,  $B_1$ ,  $B_2$  and  $\beta$  can be determined. The fit results for all 10 measurement runs are summarized in Tab. B.1. The linear drift of the magnetic field ( $B_2$ ), due to the drift of the current source, is much smaller than the exponential drift of the magnetic field ( $B_1$ ). At the end of the measuring period of 2010 it was noted that the longer the doors of the BMSR-2 were open, the longer is the relaxation of the innermost  $\mu$ -metal shield, i.e. the longer is the relaxation time  $\beta$ . Thus for the last two measurement runs (C80 and C82) the doors of the BMSR-2 were opened only for a short while.

The temporal change of the total magnetic field can lead to a temporal change in the transverse relaxation time  $T_2^*$  and thus to a temporal change of the signal amplitudes. This relation will be explained in more detail in the following: According to Eq. 3.50 the transverse relaxation rate in the motional narrowing regime is given by

$$\frac{1}{T_2^*} \propto \frac{4R^4\gamma^2}{175D} \cdot \left( |\vec{\nabla} B_{1,y}|^2 + |\vec{\nabla} B_{1,z}|^2 + 2|\vec{\nabla} B_{1,x}|^2 \right). \quad (\text{B.10})$$

The relative gradients of the magnetic field are constant in time. But as shown in Fig. 4.2 the total magnetic guiding field is not constant in time and hence the absolute gradients of the magnetic field slightly changes in time, too. From that it follows, that the transverse



relaxation time depends on time:  $T_2^*(t)$ . Assuming that the expression in brackets of Eq. B.10 is proportional to  $|\vec{B}_{\text{tot}}(t)|^2 = (B_{0,x} + B_1 \cdot e^{-t/\beta} + B_{2,x} \cdot t)^2$  (Eq. B.9) the time dependent transverse relaxation rate then is given by

$$\frac{1}{T_2^*(t)} \propto k \cdot (B_{0,x} + B_1 \cdot e^{-t/\beta} + B_2 \cdot t)^2, \quad (\text{B.11})$$

where  $k$  is a proportionality constant. Since  $B_{0,x} \gg B_1, B_2$  (see Tab. B.1), those terms, which do not contain a factor of  $B_{0,x}$ , are small compared to the other terms and hence they can be neglected. The expression of Eq. B.11 then can be simplified to

$$\frac{1}{T_2^*(t)} \propto \frac{1}{T_2^*} \left( 1 + \frac{2B_1}{B_{0,x}} \cdot e^{-t/\beta} + \frac{2B_2}{B_{0,x}} \cdot t \right). \quad (\text{B.12})$$

Here  $T_2^* = 1/(k \cdot B_{0,x}^2)$  is an effective transverse relaxation time, which is constant in time and reflects the purely exponential decay of the signal amplitudes. For the time dependent transverse relaxation rate  $T_2^*(t)$ , the temporal development of the amplitude of the spin precession signal can be calculated to (see App. C)

$$A_{\text{fit}}(t) = A_0^g \cdot e^{-t/T_2^*} \left( 1 - \frac{m}{T_2^*} \left( \frac{2B_1\beta}{B_{0,x}} (1 - e^{-t/\beta}) + \frac{B_2}{B_{0,x}} \cdot t^2 \right) \right), \quad (\text{B.13})$$

where  $m$  is a proportionality factor and  $g = 1, 2, 3$  again corresponds to the three different gradiometers Z2E-Z5S, Z3D-Z2S and Z3I-Z1S, respectively. This fit function can be used for a common fit of the amplitudes of all three gradiometers simultaneously. Here the amplitudes  $A_0^g$  can differ from one gradiometer to another, while all the other fit parameters are equal for all three gradiometers.

## B.2 Method of Exact $T_2^*$ Determination

The fit function given in Eq. B.13 was applied to the amplitudes  $A_{\text{He/Xe}}(t_i)$  of the three different gradiometers of each measurement run. For measurement run C68 the fit of Eq. B.13 results in

$$\begin{aligned} \chi^2/dof &= 1.58, \quad T_{2,\text{He}}^* = (211548.0 \pm 15.6) \text{ s}, \\ A_{0,\text{He}}^1 &= (9186.17 \pm 0.03) \text{ fT}, \quad A_{0,\text{He}}^2 = (4456.32 \pm 0.03) \text{ fT}, \quad A_{0,\text{He}}^3 = (6878.92 \pm 0.04) \text{ fT}, \\ \chi^2/dof &= 2.02, \quad T_{2,\text{Xe}}^* = (18972.5 \pm 0.4) \text{ s}, \\ A_{0,\text{Xe}}^1 &= (4924.28 \pm 0.07) \text{ fT}, \quad A_{0,\text{Xe}}^2 = (2389.22 \pm 0.05) \text{ fT}, \quad A_{0,\text{Xe}}^3 = (3688.28 \pm 0.08) \text{ fT}. \end{aligned}$$

The amplitude residuals are shown in Fig. B.6. Compared to the amplitude residuals which result from a purely exponential fit (see Fig. B.2), the structure in the residuals could be reduced from about 35 fT to about 6 fT. However the residuals are not statistically distributed and show that the temporal dependence of the signal amplitudes is not described properly by Eq. B.13. From that it follows, that it is not possible to parameterize the temporal dependence of the signal amplitudes completely. However, without knowing the exact physical model which causes the non-exponential decay of the signal amplitudes, the structure in

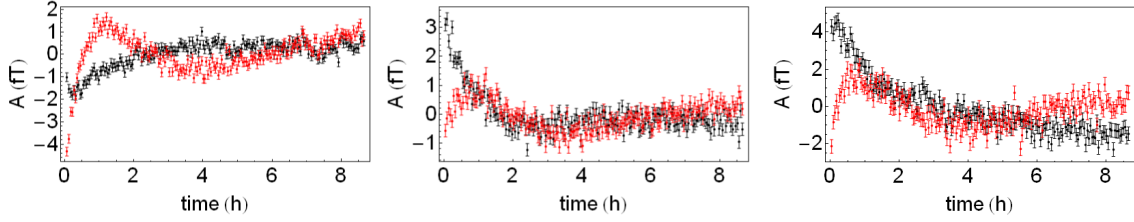


Figure B.6: Amplitude residuals of  $^3\text{He}$  (black) and  $^{129}\text{Xe}$  (red) of measurement run C68 for three different gradiometers (left: Z2E-Z5S, middle: Z3D-Z2S, right: Z3I-Z1S), which result from the fit given by Eq. B.13. Each data point comprises 50 sub-data sets which corresponds to a time interval of 160 s. Thus the error bar of each data point is smaller by a factor of  $\approx \sqrt{50}$  compared to the error of the amplitude ratio of a single sub-data set.

the amplitude residuals can be determined sufficiently by using a spline–interpolation. The principle of the spline–interpolation and the whole procedure to determine the transverse relaxation times  $T_2^*$  will be explained in the following on the example of measurement run C68.

### Spline–Interpolation

In general, the development of a data set of form  $(x, f(x))$ , which consists of  $N$  data points, can be described by a function  $F(x)$ . This function  $F(x)$  can be determined via spline–interpolation (Fig. B.7). For this purpose some points of the data set are selected as so-called *knots*. Taking into account the data points between the knots, the region between two neighboring knots can be interpolated by a polynomial, which is also called *spline*. In our case we used the cubic spline–interpolation, i.e. the region between two knots is interpolated by a polynomial of third order. The resulting function  $F(x)$  is a continuous function which is two times continuously differentiable in each point.

### Residuals of the Amplitude Ratio

First of all the residuals of the amplitude ratio  $R(t) = A_{\text{Xe}}(t)/A_{\text{He}}(t)$  are considered, since the structure in the residuals is equal for all three gradiometers (Fig. B.4). Thus the explanation of the determination of  $T_{\text{eff}}$  via spline–interpolation is simpler than for the determination of the  $T_2^*$  times of helium and xenon as we will see in the following sections. After selecting appropriate knots from the data of the residuals of the amplitude ratio, the spline–interpolation is applied to the residuals of all three gradiometers simultaneously. Then the resulting function  $f_{\text{res}}(t)$  describes the temporal development of the structure in the residuals of all three gradiometers and is related to the real amplitude ratio  $R(t)$  via the following expression

$$f_{\text{res}}(t) = R(t) - R_0 \cdot e^{-t/T_{\text{eff}}} = R_0 \cdot e^{-t/T_{\text{eff}}} \cdot g_{\text{F}}^*(t). \quad (\text{B.14})$$

Here the term  $R_0 \cdot e^{-t/T_{\text{eff}}}$  is the fit function, which was used to determine the residuals of the amplitude ratio, and the function  $g_{\text{F}}^*(t)$  is given by  $g_{\text{F}}^*(t) = f_{\text{res}}(t)/(R_0 \cdot e^{-t/T_{\text{eff}}})$ . For

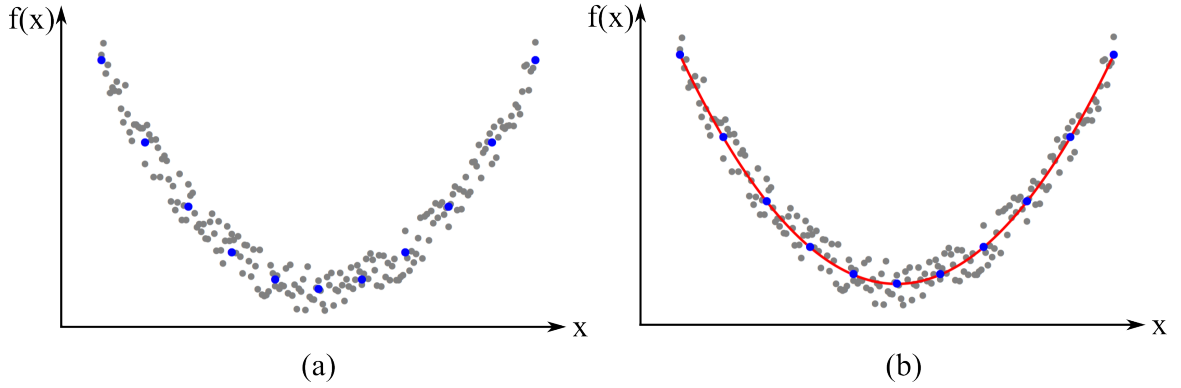


Figure B.7: Illustration of the spline-interpolation. (a) For a given data set of form  $(x, f(x))$ , which consists of  $N$  data points (gray dots), the dependence of  $f(x)$  on  $x$  can be determined by a spline-interpolation. Therefore some appropriate knots (blue dots) have to be selected. (b) By considering the data points between two knots, the region between the knots can be interpolated by piecewise polynoms. The resulting function  $F(x)$ , which is given by the red line, is two times continuously differentiable in each point.

exact determination of the function  $g_F^*(t)$  again a spline-interpolation is used. Therefore some data points of the function  $g_F^*(t) = (R(t)/(R_0 \cdot e^{-t/T_{\text{eff}}}) - 1)$  have to be calculated. These data points are used as knots for the spline-interpolation with which the function  $g_F(t)$  can be determined. This function then can be used to define a new fit function for the amplitude ratio given by

$$R_{\text{fit}}(t) = R_0 \cdot e^{-t/T_{\text{eff}}} \cdot (1 + g_F(t)). \quad (\text{B.15})$$

Since the function  $g_F(t)$  was determined by spline-interpolation, the fit function  $R_{\text{fit}}(t)$  can be used for a common fit to determine  $R_0$  and  $T_{\text{eff}}$ . The fit function  $R_{\text{fit}}(t)$  then is applied to the data points of the amplitude ratio  $R(t)$  of all three gradiometers simultaneously, where  $R_0$ ,  $T_{\text{eff}}$  and the function  $g_F(t)$  are equal for all three gradiometers. The fit parameters for measurement run C68 result in  $R_0 = (0.473181 \pm 0.000004)$  and  $T_{\text{eff}} = (20712.5 \pm 0.4)$  s with  $\chi^2/dof = 1.88$ . Calculating the residuals of the amplitude ratio for the new fit function (Eq. B.15) the structure in the residuals disappear and the data points are statistically distributed (Fig. B.8). This shows that the new fit function describes the temporal dependence of the amplitude ratio quite well.

### Residuals of the Xenon Amplitudes

As shown in Fig. B.9, the structure in the amplitude residuals of the xenon amplitudes of the three different gradiometers look similar but are not congruent with each other. However, a closer look suggests that the structure in the amplitude residuals of all three gradiometers can be described by one function  $f_{\text{res}}(t)$  which is stretched or distorted depending on the gradiometer. To check this, for measurement run C68 the residuals of the xenon amplitude of the gradiometer Z2E-Z5S were chosen as reference. Then some suitable knots were selected

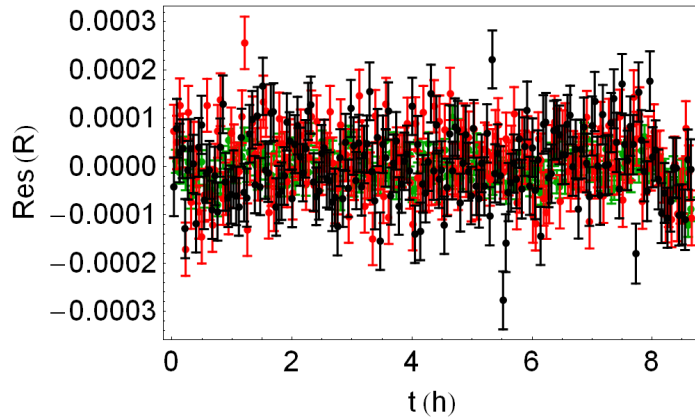


Figure B.8: Residuals of the amplitude ratio  $R(t)$  for all three gradiometers of measurement run C68 (green: Z2E-Z5S, red: Z3D-Z2S, black: Z3I-Z1S) which were determined using the fit function according to Eq. B.15. Each data point comprises 50 sub-data sets which corresponds to a time interval of 160 s. Thus the error bar of each data point is smaller by a factor of  $\approx \sqrt{50}$  compared to the error of the amplitude ratio of a single sub-data set.

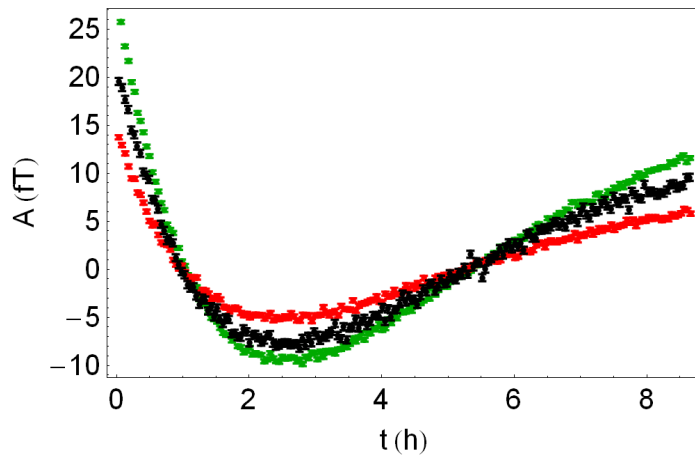


Figure B.9: Residuals of the xenon amplitudes  $A_{Xe}(t_i)$  for all three gradiometers of measurement run C68 (green: Z2E-Z5S, red: Z3D-Z2S, black: Z3I-Z1S). Each data point comprises 50 sub-data sets which corresponds to a time interval of 160 s. Thus the error bar of each data point is smaller by a factor of  $\approx \sqrt{50}$  compared to the error of the amplitude ratio of a single sub-data set. Hence, the error bars are too small to be visible in the plot.

and afterwards a spline-interpolation was applied to the residuals of the xenon amplitude of the gradiometer Z2E-Z5S which results in a function  $f_{\text{res}}(t)$ . By multiplying this function with a factor  $c_g$  ( $g=1$  for gradiometer Z2E-Z5S, i.e.  $c_1 = 1$ ,  $g=2$  for gradiometer Z3D-Z2S and  $g=3$  for gradiometer Z3I-Z1S) it is possible to describe the structure in the xenon amplitude

residuals of the other two gradiometers, too. The factors  $c_2$  and  $c_3$  result in

$$c_2 = 0.507 = \frac{A_{0,\text{Xe}}^2}{A_{0,\text{Xe}}^1}, \quad (\text{B.16})$$

$$c_3 = 0.752 = \frac{A_{0,\text{Xe}}^3}{A_{0,\text{Xe}}^1}. \quad (\text{B.17})$$

This values conform to the ratio of the initial amplitude of the corresponding gradiometer  $A_{0,\text{Xe}}^g$  (with  $g=2,3$ ) to the initial amplitude of the reference gradiometer  $A_{0,\text{Xe}}^1$ . This relation will be explained in the following: As already mentioned before the time dependence of the amplitude is given by (Eq. B.3), i.e.

$$A_{\text{Xe}}^g(t) = f(t) \cdot A_{0,\text{Xe}}^g \cdot e^{-t/T_{2,\text{Xe}}^*}. \quad (\text{B.18})$$

But the fit function, which was used to determine the amplitude residuals, is a pure exponential function, i.e.

$$A_{\text{Xe,fit}}^g(t) = A_{0,\text{Xe}}^g \cdot e^{-t/T_{2,\text{Xe}}^*}. \quad (\text{B.19})$$

For convenience it is assumed that the correct  $T_{2,\text{Xe}}^*$  time for xenon was determined by the fit. The residuals of the xenon amplitudes then are given by

$$\text{Res}(A_{\text{Xe}}^g(t)) = A_{\text{Xe}}^g(t) - A_{\text{Xe,fit}}^g(t) = A_{0,\text{Xe}}^g \cdot e^{-t/T_{2,\text{Xe}}^*} (f(t) - 1). \quad (\text{B.20})$$

$T_{2,\text{Xe}}^*$  and the function  $f(t)$  should be equal for all three gradiometers but the initial amplitude  $A_{0,\text{Xe}}^g$  is different from one gradiometer to another. Hence, the form of the structure in the amplitude residuals depends on the initial amplitude  $A_{0,\text{Xe}}^g$ . Consequently, the structure in the amplitude residuals of all three gradiometers can be described by one function, i.e.

$$\text{Res}(A_{\text{Xe}}^g(t)) = c_g \cdot f_{\text{res}}(t) = A_{0,\text{Xe}}^g \cdot e^{-t/T_{2,\text{Xe}}^*} (f(t) - 1). \quad (\text{B.21})$$

For correct determination of the function  $f_{\text{res}}(t)$ , a spline-interpolation is applied to the amplitude residuals of xenon of all three gradiometers. The knots are selected from the reference gradiometer Z2E-Z5S. Then the resulting function  $f_{\text{res}}(t)$  describes the structure in the amplitude residuals of the reference gradiometer,  $c_2 \cdot f_{\text{res}}(t)$  the amplitude residuals of the gradiometer Z3D-Z2S and  $c_3 \cdot f_{\text{res}}(t)$  the amplitude residuals of the gradiometer Z3I-Z1S (Fig. B.10). Here the factors  $c_g$  were no fit parameters, but calculated from the initial amplitudes which were determined with the exponential fit according to Eq. B.2. Then the function  $f_{\text{res}}(t)$  can be used to determine the functions  $g_{\text{F},g}^{\text{Xe}}(t)$  (similar to the amplitude ratio):

$$\begin{aligned} g_{\text{F},1}^{\text{Xe}}(t) &= c_1 \cdot f_{\text{res}}(t) / \left( A_{0,\text{Xe}}^1 \cdot e^{-t/T_{2,\text{Xe}}^*} \right), \\ g_{\text{F},2}^{\text{Xe}}(t) &= c_2 \cdot f_{\text{res}}(t) / \left( A_{0,\text{Xe}}^2 \cdot e^{-t/T_{2,\text{Xe}}^*} \right), \\ g_{\text{F},3}^{\text{Xe}}(t) &= c_3 \cdot f_{\text{res}}(t) / \left( A_{0,\text{Xe}}^3 \cdot e^{-t/T_{2,\text{Xe}}^*} \right). \end{aligned}$$

With Eq. B.16 and Eq. B.17 it follows that

$$g_{\text{F}}^{\text{Xe}}(t) = g_{\text{F},1}^{\text{Xe}}(t) = g_{\text{F},2}^{\text{Xe}}(t) = g_{\text{F},3}^{\text{Xe}}(t) = f_{\text{res}}(t) / \left( A_{0,\text{Xe}}^1 \cdot e^{-t/T_{2,\text{Xe}}^*} \right). \quad (\text{B.22})$$

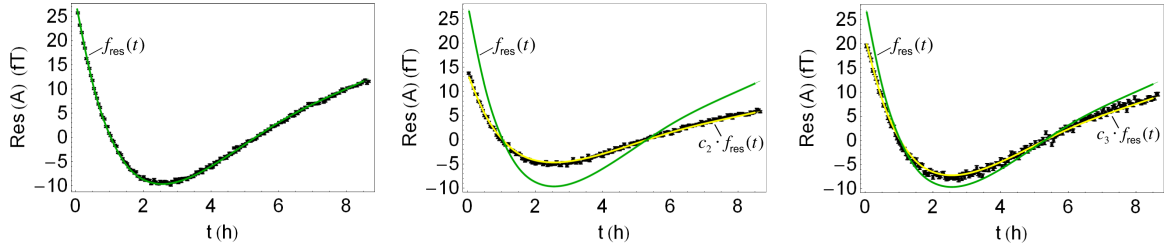


Figure B.10: Illustration of the determination of the function  $f_{\text{res}}(t)$  via spline-interpolation. The residuals of the xenon amplitudes  $A_{\text{Xe}}(t)$  for all three gradiometers of measurement run C68 are shown (left: Z2E-Z5S, middle: Z3D-Z2S, right: Z3I-Z1S). The residuals of gradiometer Z2E-Z5S are used as reference, i.e. the knots for the spline-interpolation are selected from the data of the amplitude residuals of gradiometer Z2E-Z5S. The spline-interpolation is applied to the residuals of all three gradiometers simultaneously so that the function  $f_{\text{res}}(t)$  (green curve in all plots) describes the structure in the residuals of the reference gradiometer,  $c_2 \cdot f_{\text{res}}(t)$  (yellow curve in the middle plot) the residuals of the gradiometer Z3D-Z2S and  $c_3 \cdot f_{\text{res}}(t)$  (yellow curve in the right plot) the residuals of the gradiometer Z3I-Z1S.

Since the function  $g_{\text{F}}^{\text{Xe}}(t)$  is equal for all three gradiometers, Eq. B.21 transforms to

$$\text{Res}(A_{\text{Xe}}^{\text{g}}(t)) = c_{\text{g}} \cdot f_{\text{res}}(t) = A_{0,\text{Xe}}^{\text{g}} \cdot e^{-t/T_{2,\text{Xe}}^*} (f(t) - 1) = A_{0,\text{Xe}}^{\text{g}} \cdot e^{-t/T_{2,\text{Xe}}^*} \cdot g_{\text{F}}^{\text{Xe}}(t). \quad (\text{B.23})$$

With the function  $f_{\text{res}}(t)$  some knots of the function  $g_{\text{F}}^{\text{Xe}}(t)$  can be calculated and afterwards a spline-interpolation can be applied. With the resulting function  $g_{\text{F}}^{\text{Xe}}(t)$  a new fit function for the amplitudes of xenon can be defined

$$A_{\text{Xe,fit}}^{\text{g}}(t) = A_{0,\text{Xe}}^{\text{g}} \cdot e^{-t/T_{2,\text{Xe}}^*} \cdot (1 + g_{\text{F}}^{\text{Xe}}(t)). \quad (\text{B.24})$$

This fit function is used for a common fit, i.e. it is applied to the xenon amplitudes of all three gradiometers simultaneously, whereby  $T_{2,\text{Xe}}^*$  and the function  $g_{\text{F}}^{\text{Xe}}(t)$  are equal for all three gradiometers, but the initial amplitudes  $A_{0,\text{Xe}}^{\text{g}}$  are different. The fit parameters for measurement run C68 then result in  $A_{0,\text{Xe}}^1 = (5307.55 \pm 0.05)$  fT,  $A_{0,\text{Xe}}^2 = (3988.39 \pm 0.07)$  fT,  $A_{0,\text{Xe}}^3 = (2688.40 \pm 0.04)$  fT and  $T_{2,\text{Xe}}^* = (18792.3 \pm 0.3)$  s with  $\chi^2/\text{dof} = 1.93$ . Calculating the residuals of the xenon amplitude for the new fit function according to Eq. B.24, the main structure in the residuals disappear (Fig. B.11 left). Some small oscillations remain which can be attributed to the drift of the SQUIDs and/or the movement of the measurement cell relative to the SQUIDs. In addition, the comparison of the  $\chi^2/\text{dof}$  values of measurement run C68 resulting from the fits according to Eq. B.24 and Eq. B.2 demonstrate, that by using the method of the spline-interpolation a huge improvement of the  $\chi^2/\text{dof}$  values could be achieved. That shows that the new fit function describes the temporal dependence of the xenon amplitudes quite well.

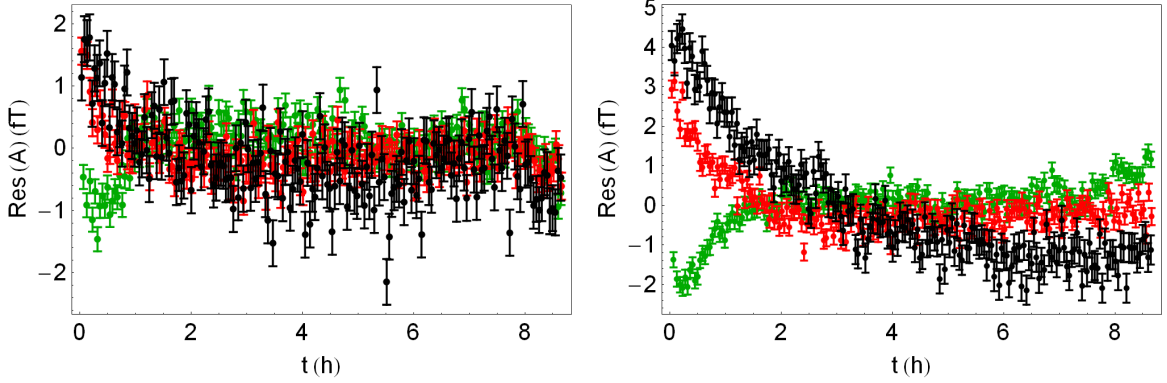


Figure B.11: Residuals of the xenon amplitudes  $A_{\text{Xe}}(t)$  (left) and helium signal amplitudes  $A_{\text{He}}(t)$  (right) for all three gradiometers of measurement run C68 (green: Z2E-Z5S, red: Z3D-Z2S, black: Z3I-Z1S) which were determined with a direct fit of the signal amplitudes using Eq. B.24. Each data point comprises 50 sub-data sets which corresponds to a time interval of 160 s. Thus the error bar of each data point is smaller by a factor of  $\approx \sqrt{50}$  compared to the error of the amplitude of a single sub-data set.

### Residuals of the Helium Amplitudes

For the signal amplitudes of helium the same procedure as for the xenon signal amplitudes can be used. The fit parameters according to Eq. B.24 results in  $A_{0,\text{He}}^1 = (11217.20 \pm 0.03)$  fT,  $A_{0,\text{He}}^2 = (8427.23 \pm 0.04)$  fT,  $A_{0,\text{He}}^3 = (5681.11 \pm 0.03)$  fT and  $T_{2,\text{He}}^* = (202706.0 \pm 6.7)$  s with  $\chi^2/dof = 1.49$ . The residuals of the helium signal amplitude resulting from the new fit model (Eq. B.24) are shown in Fig. B.11. Some small linear structures remain in the amplitude residuals, but similar to the xenon amplitudes this structures can be attributed to the drift of the SQUIDs and/or the movement of the measurement cell relative to the SQUIDs.

In Fig. B.12 the residuals of helium and xenon of measurement run C68, which result from the new fit model (Eq. B.24), are shown together. In Tab. B.2 the transverse relaxation times  $T_2^*$  of helium and xenon, which were determined by using a spline-interpolation, of all 10 measurement runs are summarized. The determination of the  $T_2^*$  time of helium for measurement run C60 was more complicated than for the other measurement runs. Here the structure in the amplitude residuals differed from the characteristic structure which occurred in the amplitude residuals of all the other measurement runs.

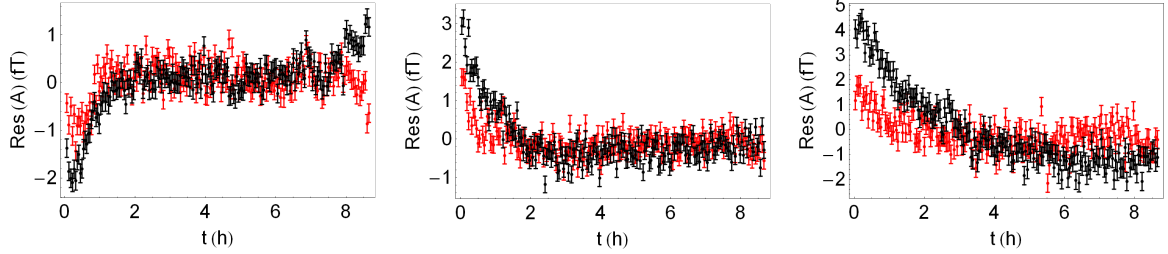


Figure B.12: Amplitude residuals of  $^3\text{He}$  (black) and  $^{129}\text{Xe}$  (red) of measurement run C68 for three different gradiometers (left: Z2E-Z5E, middle: Z3D-Z2S, right: Z3I-Z1S) which were determined with a direct fit (Eq. B.24) of the amplitudes of helium and xenon. Each data point comprises 50 sub-data sets which corresponds to a time interval of 160 s. Thus the error bar of each data point is smaller by a factor of  $\approx \sqrt{50}$  compared to the error of the amplitude of a single sub-data set.

	$T_{2,\text{He}}^*$ (s)	$\delta T_{2,\text{He}}^*$ (s)	$T_{2,\text{Xe}}^*$ (s)	$\delta T_{2,\text{Xe}}^*$ (s)
C54	111443	18	14742.6	0.4
C55	132567	3	14853.2	0.2
C60	176152	11	15395.9	0.3
C63	190472	7	18021.4	0.3
C65	217520	8	18773.9	0.4
C67	209171	9	18657.6	0.4
C68	212055	9	19049.7	0.3
C71	204661	7	18791.6	0.3
C80	229407	19	19165.1	0.4
C82	211347	32	18889.1	0.4

Table B.2: Transverse relaxation times of  $^3\text{He}$  and  $^{129}\text{Xe}$  of measurement runs C54-C82 which were determined by using a spline-interpolation (Eq. B.24).



## C. Derivation of the Amplitude in Case of a Time Dependent $T_2^*$ time

The time dependent transverse relaxation rate approximately is given by (Eq. B.12)

$$\frac{1}{T_2^*(t)} \approx \frac{m}{T_2^*} \left( 1 + \frac{2B_1}{B_{0,x}} \cdot e^{-t/\beta} + \frac{2B_2}{B_{0,x}} \cdot t \right), \quad (\text{C.1})$$

where  $m$  is a proportionality factor. With

$$r(t) = \frac{2B_1}{B_{0,x}} \cdot e^{-t/\beta} + \frac{2B_2}{B_{0,x}} \cdot t \quad (\text{C.2})$$

the time dependent transverse relaxation rate transforms to

$$\frac{1}{T_2^*(t)} = \frac{m}{T_2^*} (1 + r(t)), \quad (\text{C.3})$$

Since the signal amplitude decays with a characteristic time  $T_2^*(t)$ , the temporal dependence of the signal amplitude can be derived by

$$\begin{aligned} \frac{dA'}{dt'} &= -\frac{A'}{T_2^*(t')} \\ \Rightarrow \frac{dA'}{dt'} &= -m \frac{A'}{T_2^*} (1 + r(t')) \\ \Rightarrow \frac{dA'}{A'} &= -\frac{m}{T_2^*} (1 + r(t')) dt' \\ \Rightarrow \int_{A_0}^A \frac{dA'}{A'} &= -\frac{m}{T_2^*} \int_0^t dt' - \frac{m}{T_2^*} \int_0^t r(t') dt' \\ \Rightarrow A(t) &= A_0 \cdot e^{-t/T_2^*} \cdot e^{-\frac{m}{T_2^*} \int_0^t r(t') dt'} \end{aligned} \quad (\text{C.4})$$

Assuming that the expression in the exponent is small, an expansion of the exponential function leads to

$$A(t) \approx A_0 \cdot e^{-t/T_2^*} \left( 1 - \frac{m}{T_2^*} \int_0^t r(t') dt' \right). \quad (\text{C.5})$$

The integral can be calculated by using the expression of Eq. C.2

$$\begin{aligned} \int_0^t r(t') dt' &= \int_0^t \left( \frac{2B_1}{B_{x,0}} \cdot e^{-t'/\beta} + \frac{2B_2}{B_{x,0}} \cdot t' \right) dt' \\ &= \frac{2B_1\beta}{B_{x,0}} \left( 1 - e^{-t/\beta} \right) + \frac{B_2}{B_{x,0}} \cdot t^2. \end{aligned} \quad (\text{C.6})$$

### C. Derivation of the Amplitude in Case of a Time Dependent $T_2^*$ time

---

The temporal dependence of the amplitude in case that the magnetic field gradients change in time then is given by

$$A(t) \approx A_0 \cdot e^{-t/T_2^*} \left( 1 - \frac{m}{T_2^*} \left( \frac{2B_1\beta}{B_{x,0}} (1 - e^{-t/\beta}) + \frac{B_2}{B_{x,0}} \cdot t^2 \right) \right). \quad (\text{C.7})$$

## D. Derivation of Systematic Error $\Delta\nu_{\text{sys}}^{T_2^*}$

According to Eq. 3.50, the transverse relaxation time is changed if the BGO crystal produces field gradients. In this case the transverse relaxation time for the BGO in close and in distant position is not equal, i.e.  $T_{2,c}^* \neq T_{2,d}^*$ . The RBS frequency shifts (Eq. 6.52) of the weighted frequency difference for the BGO in close and distant position then are given by

$$\omega_{\text{RBS,d}}(t) = \xi_{\text{He}} \cdot A'_{0,\text{He}} \cdot e^{-\frac{t-t_0}{T_{2,\text{He}}^*}} - \frac{\gamma_{\text{He}}}{\gamma_{\text{Xe}}} \cdot \xi_{\text{Xe}} \cdot A'_{0,\text{Xe}} \cdot e^{-\frac{t-t_0}{T_{2,\text{Xe}}^*}}, \quad (\text{D.1})$$

$$\omega_{\text{RBS,c}}(t) = \xi_{\text{He}} \cdot A'_{0,\text{He}} \cdot e^{-\frac{t-t_0}{T_{2,\text{He}}^* + \Delta T_{2,\text{He}}^*}} - \frac{\gamma_{\text{He}}}{\gamma_{\text{Xe}}} \cdot \xi_{\text{Xe}} \cdot A'_{0,\text{Xe}} \cdot e^{-\frac{t-t_0}{T_{2,\text{Xe}}^* + \Delta T_{2,\text{Xe}}^*}}. \quad (\text{D.2})$$

The amplitudes are given by

$$A'_{0,\text{He}/\text{Xe}} \approx A_{0,\text{He}/\text{Xe}} \cdot e^{-\frac{t_0}{T_{2,\text{He(Xe)}}^*}} \quad (\text{D.3})$$

and the expression  $\Delta T_2^*$  is given by  $\Delta T_2^* = T_{2,c}^* - T_{2,d}^*$ , whereas  $T_2^*$  is defined as  $T_2^* = T_{2,d}^*$ . Using  $\epsilon_{\text{He}} = \xi_{\text{He}}$  and  $\epsilon_{\text{Xe}} = \frac{\gamma_{\text{He}}}{\gamma_{\text{Xe}}} \xi_{\text{Xe}}$  the RBS frequency shifts simplifies to

$$\omega_{\text{RBS,d}}(t) = \epsilon_{\text{He}} \cdot A'_{0,\text{He}} \cdot e^{-\frac{t-t_0}{T_{2,\text{He}}^*}} - \epsilon_{\text{Xe}} \cdot A'_{0,\text{Xe}} \cdot e^{-\frac{t-t_0}{T_{2,\text{Xe}}^*}}, \quad (\text{D.4})$$

$$\omega_{\text{RBS,c}}(t) = \epsilon_{\text{He}} \cdot A'_{0,\text{He}} \cdot e^{-\frac{t-t_0}{T_{2,\text{He}}^* + \Delta T_{2,\text{He}}^*}} - \epsilon_{\text{Xe}} \cdot A'_{0,\text{Xe}} \cdot e^{-\frac{t-t_0}{T_{2,\text{Xe}}^* + \Delta T_{2,\text{Xe}}^*}}. \quad (\text{D.5})$$

The total weighted frequency difference for the BGO crystal in close and distant position then is given by

$$\Delta\omega_{\text{d}}(t) = \epsilon_{\text{He}} \cdot A'_{0,\text{He}} \cdot e^{-\frac{t-t_0}{T_{2,\text{He}}^*}} - \epsilon_{\text{Xe}} \cdot A'_{0,\text{Xe}} \cdot e^{-\frac{t-t_0}{T_{2,\text{Xe}}^*}} + \Delta\omega_{\text{lin}}, \quad (\text{D.6})$$

$$\Delta\omega_{\text{c}}(t) = \epsilon_{\text{He}} \cdot A'_{0,\text{He}} \cdot e^{-\frac{t-t_0}{T_{2,\text{He}}^* + \Delta T_{2,\text{He}}^*}} - \epsilon_{\text{Xe}} \cdot A'_{0,\text{Xe}} \cdot e^{-\frac{t-t_0}{T_{2,\text{Xe}}^* + \Delta T_{2,\text{Xe}}^*}} + \Delta\omega_{\text{lin}} + \Delta\omega_{\text{sp}}. \quad (\text{D.7})$$

By integration over time one gets the weighted phase difference

$$\begin{aligned} \Delta\Phi_{\text{d}}(t) &= \Delta\omega_{\text{lin}} \cdot t \\ &+ \epsilon_{\text{He}} \cdot A'_{0,\text{He}} \cdot T_{2,\text{He}}^* \cdot e^{\frac{t_0}{T_{2,\text{He}}^*}} \cdot \left(1 - e^{-\frac{t}{T_{2,\text{He}}^*}}\right) \\ &- \epsilon_{\text{Xe}} \cdot A'_{0,\text{Xe}} \cdot T_{2,\text{Xe}}^* \cdot e^{\frac{t_0}{T_{2,\text{Xe}}^*}} \cdot \left(1 - e^{-\frac{t}{T_{2,\text{Xe}}^*}}\right), \end{aligned} \quad (\text{D.8})$$

$$\begin{aligned} \Delta\Phi_{\text{c}}(t) &= (\Delta\omega_{\text{sp}} + \Delta\omega_{\text{lin}}) \cdot t \\ &+ \epsilon_{\text{He}} \cdot A'_{0,\text{He}} \cdot (T_{2,\text{He}}^* + \Delta T_{2,\text{He}}^*) \cdot e^{\frac{-t+t_0}{T_{2,\text{He}}^* + \Delta T_{2,\text{He}}^*}} \cdot \left(e^{\frac{t}{T_{2,\text{He}}^* + \Delta T_{2,\text{He}}^*}} - 1\right) \\ &- \epsilon_{\text{Xe}} \cdot A'_{0,\text{Xe}} \cdot (T_{2,\text{Xe}}^* + \Delta T_{2,\text{Xe}}^*) \cdot e^{\frac{-t+t_0}{T_{2,\text{Xe}}^* + \Delta T_{2,\text{Xe}}^*}} \cdot \left(e^{\frac{t}{T_{2,\text{Xe}}^* + \Delta T_{2,\text{Xe}}^*}} - 1\right). \end{aligned} \quad (\text{D.9})$$

A Taylor expansion of the exponential functions around  $t = t_0$  up to second order then leads to

$$\begin{aligned}
 \Delta\Phi_{\text{d}}(t) &= (-\epsilon_{\text{He}} \cdot A'_{0,\text{He}} \cdot T_{2,\text{He}}^* + \epsilon_{\text{He}} \cdot A'_{0,\text{He}} \cdot T_{2,\text{He}}^* \cdot e^{\frac{t_0}{T_{2,\text{He}}^*}} \\
 &\quad + \epsilon_{\text{Xe}} \cdot A'_{0,\text{Xe}} \cdot T_{2,\text{Xe}}^* - \epsilon_{\text{Xe}} \cdot A'_{0,\text{Xe}} \cdot T_{2,\text{Xe}}^* \cdot e^{\frac{t_0}{T_{2,\text{Xe}}^*}} + \Delta\omega_{\text{lin}} \cdot t_0) \\
 &\quad + (\epsilon_{\text{He}} \cdot A'_{0,\text{He}} - \epsilon_{\text{Xe}} \cdot A'_{0,\text{Xe}} + \Delta\omega_{\text{lin}}) \cdot (t - t_0) \\
 &\quad \left( -\frac{\epsilon_{\text{He}} \cdot A'_{0,\text{He}}}{2 \cdot T_{2,\text{He}}^*} + \frac{\epsilon_{\text{Xe}} \cdot A'_{0,\text{Xe}}}{2 \cdot T_{2,\text{Xe}}^*} \right) \cdot (t - t_0)^2 + O[(t - t_0)]^3 \quad (\text{D.10})
 \end{aligned}$$

$$\begin{aligned}
 \Delta\Phi_{\text{c}}(t) &= (\Delta\omega_{\text{lin}} + \Delta\omega_{\text{sp}}) \cdot t_0 \\
 &\quad + \epsilon_{\text{He}} \cdot A'_{0,\text{He}} \cdot (T_{2,\text{He}}^* + \Delta T_{2,\text{He}}^*) \cdot \left( e^{\frac{t_0}{T_{2,\text{He}}^* + \Delta T_{2,\text{He}}^*}} - 1 \right) \\
 &\quad - \epsilon_{\text{Xe}} \cdot A'_{0,\text{Xe}} \cdot (T_{2,\text{Xe}}^* + \Delta T_{2,\text{Xe}}^*) \cdot \left( e^{\frac{t_0}{T_{2,\text{Xe}}^* + \Delta T_{2,\text{Xe}}^*}} - 1 \right) \\
 &\quad + (\epsilon_{\text{He}} \cdot A'_{0,\text{He}} - \epsilon_{\text{Xe}} \cdot A'_{0,\text{Xe}} + \Delta\omega_{\text{lin}} + \Delta\omega_{\text{sp}}) \cdot (t - t_0) \\
 &\quad + \left( -\frac{\epsilon_{\text{He}} \cdot A'_{0,\text{He}}}{2(T_{2,\text{He}}^* + \Delta T_{2,\text{He}}^*)} + \frac{\epsilon_{\text{Xe}} \cdot A'_{0,\text{Xe}}}{2(T_{2,\text{Xe}}^* + \Delta T_{2,\text{Xe}}^*)} \right) \cdot (t - t_0)^2 \\
 &\quad + O[(t - t_0)]^3. \quad (\text{D.11})
 \end{aligned}$$

The difference of  $\Delta\Phi_{\text{c}}(t)$  and  $\Delta\Phi_{\text{d}}(t)$  then is given by

$$\Delta\Phi_{\text{c}}(t) - \Delta\Phi_{\text{d}}(t) = \Delta\Phi_{\text{cd,const}} + \Delta\Phi_{\text{cd,lin}} + \Delta\Phi_{\text{cd,quad}} + O[(t - t_0)]^3, \quad (\text{D.12})$$

with

$$\begin{aligned}
 \Delta\Phi_{\text{cd,const}} &= \epsilon_{\text{He}} \cdot A'_{0,\text{He}} \cdot T_{2,\text{He}}^* - \epsilon_{\text{He}} \cdot A'_{0,\text{He}} \cdot T_{2,\text{He}}^* \cdot e^{\frac{t_0}{T_{2,\text{He}}^*}} \\
 &\quad + \epsilon_{\text{He}} \cdot A'_{0,\text{He}} \cdot (T_{2,\text{He}}^* + \Delta T_{2,\text{He}}^*) \cdot \left( e^{\frac{t_0}{T_{2,\text{He}}^* + \Delta T_{2,\text{He}}^*}} - 1 \right) \\
 &\quad - \epsilon_{\text{Xe}} \cdot A'_{0,\text{Xe}} \cdot T_{2,\text{Xe}}^* + \epsilon_{\text{Xe}} \cdot A'_{0,\text{Xe}} \cdot T_{2,\text{Xe}}^* \cdot e^{\frac{t_0}{T_{2,\text{Xe}}^*}} \\
 &\quad - \epsilon_{\text{Xe}} \cdot A'_{0,\text{Xe}} \cdot (T_{2,\text{Xe}}^* + \Delta T_{2,\text{Xe}}^*) \cdot \left( e^{\frac{t_0}{T_{2,\text{Xe}}^* + \Delta T_{2,\text{Xe}}^*}} - 1 \right) + \Delta\omega_{\text{sp}} \cdot t_0 \quad (\text{D.13})
 \end{aligned}$$

---


$$\Delta\Phi_{\text{cd,lin}} = \Delta\omega_{\text{sp}} \cdot (t - t_0) \quad (\text{D.14})$$

$$\Delta\Phi_{\text{cd,quad}} = \left( \frac{\epsilon_{\text{He}} \cdot A'_{0,\text{He}} \cdot \Delta T_{2,\text{He}}^*}{2T_{2,\text{He}}^* (T_{2,\text{He}}^* + \Delta T_{2,\text{He}}^*)} - \frac{\epsilon_{\text{Xe}} \cdot A'_{0,\text{Xe}} \cdot \Delta T_{2,\text{Xe}}^*}{2T_{2,\text{Xe}}^* (T_{2,\text{Xe}}^* + \Delta T_{2,\text{Xe}}^*)} \right) \cdot (t - t_0)^2 \quad (\text{D.15})$$

The constant term  $\Delta\Phi_{\text{cd,const}}$  depends on  $\Delta T_{2,\text{He}/\text{Xe}}^*$ . However, this term has no influence on the frequency shift  $\Delta\nu_{\text{sp}}$  due the spin-dependent short-range interaction, since by consideration of the frequency, i.e.  $\Delta\omega(t) = \frac{d\Delta\Phi(t)}{dt}$ , the constant term drops out. The linear term  $\Delta\Phi_{\text{cd,lin}}$  is independent of  $\Delta T_{2,\text{He}/\text{Xe}}^*$ . But the quadratic term  $\Delta\Phi_{\text{cd,quad}}$  depends on  $\Delta T_{2,\text{He}/\text{Xe}}^*$ , which leads to a systematic effect on the frequency shift  $\Delta\nu_{\text{sp}}$ . By considering Eq. 6.71, i.e.

$$\Delta\nu_{\text{sp}} = \frac{b_c - b_d}{2\pi \cdot \left(1 - \frac{\gamma_{\text{He}}}{\gamma_{\text{Xe}}}\right)}, \quad (\text{D.16})$$

the systematic effect can be calculated by replacing  $b_c - b_d$ <sup>1</sup> by the temporal mean of the derivative of the quadratic term, i.e.  $\left\langle \frac{d\Delta\Phi_{\text{cd,quad}}}{d(t-t_0)} \right\rangle_{t-t_0}$ . The systematic error then is given by

$$\begin{aligned} \left| \Delta\nu_{\text{sys}}^{T_2^*} \right| &= \left| \frac{\left\langle \frac{d\Delta\Phi_{\text{cd,quad}}}{d(t-t_0)} \right\rangle_{t-t_0}}{2\pi \cdot \left(1 - \frac{\gamma_{\text{He}}}{\gamma_{\text{Xe}}}\right)} \right| \\ &= \left| \frac{\frac{\epsilon_{\text{He}} \cdot A'_{0,\text{He}} \cdot \Delta T_{2,\text{He}}^*}{T_{2,\text{He}}^* (T_{2,\text{He}}^* + \Delta T_{2,\text{He}}^*)} - \frac{\epsilon_{\text{Xe}} \cdot A'_{0,\text{Xe}} \cdot \Delta T_{2,\text{Xe}}^*}{T_{2,\text{Xe}}^* (T_{2,\text{Xe}}^* + \Delta T_{2,\text{Xe}}^*)}}{2\pi \cdot \left(1 - \frac{\gamma_{\text{He}}}{\gamma_{\text{Xe}}}\right)} \cdot \langle t - t_0 \rangle_{t-t_0} \right|. \end{aligned} \quad (\text{D.17})$$

The temporal mean  $\langle t - t_0 \rangle_{t-t_0}$  for c→d as well as for d→c measurements is given by  $\langle t - t_0 \rangle_{t-t_0} \approx t_0/2$ . With  $E'_{\text{He}/\text{Xe}} = \epsilon_{\text{He}/\text{Xe}} \cdot A'_{0,\text{He}/\text{Xe}} \cdot T_{2,\text{He}/\text{Xe}}^*$  (Eq. 6.60 and Eq. D.3) the systematic error then results in

$$\left| \Delta\nu_{\text{sys}}^{T_2^*} \right| = \left| \frac{\frac{E'_{\text{He}} \cdot \Delta T_{2,\text{He}}^*}{(T_{2,\text{He}}^*)^2 (T_{2,\text{He}}^* + \Delta T_{2,\text{He}}^*)} - \frac{E'_{\text{Xe}} \cdot \Delta T_{2,\text{Xe}}^*}{(T_{2,\text{Xe}}^*)^2 (T_{2,\text{Xe}}^* + \Delta T_{2,\text{Xe}}^*)}}{2\pi \cdot \left(1 - \frac{\gamma_{\text{He}}}{\gamma_{\text{Xe}}}\right)} \cdot \frac{t_0}{2} \right| \quad (\text{D.18})$$

Using the relation given in Eq. 6.93, i.e.

$$\frac{\Delta T_{2,\text{He}}^*}{(T_{2,\text{He}}^*)^2} / \frac{\Delta T_{2,\text{Xe}}^*}{(T_{2,\text{Xe}}^*)^2} = \frac{\gamma_{\text{He}}^2}{D_{\text{He}}^{\text{GM}}} / \frac{\gamma_{\text{Xe}}^2}{D_{\text{Xe}}^{\text{GM}}} = \frac{\gamma_{\text{He}}^2}{D_{\text{He}}^{\text{GM}}} \cdot \frac{D_{\text{Xe}}^{\text{GM}}}{\gamma_{\text{Xe}}^2} \approx 2, \quad (\text{D.19})$$

the systematic error transforms to

$$\left| \Delta\nu_{\text{sys}}^{T_2^*} \right| \leq \left| \frac{\frac{\Delta T_{2,\text{He}}^*}{(T_{2,\text{He}}^*)^2}}{2\pi \cdot \left(1 - \frac{\gamma_{\text{He}}}{\gamma_{\text{Xe}}}\right)} \cdot \left( \frac{E'_{\text{He}(\text{Xe})}}{T_{2,\text{He}}^* + \Delta T_{2,\text{He}}^*} - \frac{1}{2} \cdot \frac{E'_{\text{He}(\text{Xe})}}{T_{2,\text{Xe}}^* + \Delta T_{2,\text{Xe}}^*} \right) \cdot \frac{t_0}{2} \right| \quad (\text{D.20})$$

---

<sup>1</sup> $b_c$  and  $b_d$  correspond to the fit paramters of the linear term of the weighted phase difference for the BGO crystal in close and in distant position.



## E. Derivation of the function $f_{\text{BGO}}^{\pm}(t)$

The temporal development of the ratio  $R(t)$  of the xenon and helium amplitudes can be described by (Eq. B.15)

$$R(t) = \frac{A_{\text{Xe}}(t)}{A_{\text{He}}(t)} = R_0 \cdot e^{-\frac{t}{T_{\text{eff}}}} (1 + g_{\text{F}}(t)) , \quad (\text{E.1})$$

where  $T_{\text{eff}}$  is an effective relaxation time given by  $\frac{1}{T_{\text{eff}}} = \frac{1}{T_{2,\text{Xe}}^*} - \frac{1}{T_{2,\text{He}}^*}$ .

If the  $T_2^*$  times of helium and xenon are changed due to the field gradients produced by the BGO crystal, the temporal development of the ratio  $R(t)$  then is given by

$$\begin{aligned} R(t) = & R_0 \cdot e^{-\frac{t}{T_{\text{eff}}}} (1 + g_{\text{F}}(t)) \cdot \Theta(\pm(t_0 - t)) \\ & + R_0 \cdot \underbrace{e^{-\frac{t}{T_{\text{eff}} + \Delta T_{\text{eff}}}}}_{F_{\text{exp}}(t)} (1 + g_{\text{F}}(t)) \cdot \Theta(\pm(t - t_0)) . \end{aligned} \quad (\text{E.2})$$

$\Delta T_{\text{eff}}$  describes the change of the effective relaxation time. The  $(\pm)$  in the argument of the Heaviside step function has to be set  $(-)$  for the measurement sequence  $c \rightarrow d$  of the BGO crystal and  $(+)$  for the reverse one, i.e.  $d \rightarrow c$ . The exponential function  $F_{\text{exp}}(t)$  of the second term can be converted as follows

$$\begin{aligned} F_{\text{exp}}(t) &= \exp\left(-\frac{t}{T_{\text{eff}} + \Delta T_{\text{eff}}}\right) \\ &= \exp\left(-\frac{t}{T_{\text{eff}} \left(1 + \frac{\Delta T_{\text{eff}}}{T_{\text{eff}}}\right)}\right) . \end{aligned} \quad (\text{E.3})$$

Assuming that  $\beta = \frac{\Delta T_{\text{eff}}}{T_{\text{eff}}} \ll 1$ , the relation  $\frac{1}{(1+\beta)} \approx 1 - \beta$  can be used, so that  $F_{\text{exp}}(t)$  transforms to

$$\begin{aligned} F_{\text{exp}}(t) &= \exp\left(-\frac{t}{T_{\text{eff}}} \cdot \left(1 - \frac{\Delta T_{\text{eff}}}{T_{\text{eff}}}\right)\right) \\ &= \exp\left(-\frac{t}{T_{\text{eff}}} + \frac{\Delta T_{\text{eff}}}{T_{\text{eff}}^2} \cdot t\right) \\ &= \exp\left(-\frac{t}{T_{\text{eff}}}\right) \cdot \exp\left(\frac{\Delta T_{\text{eff}}}{T_{\text{eff}}^2} \cdot t\right) . \end{aligned} \quad (\text{E.4})$$

### E. Derivation of the function $f_{\text{BGO}}^{\pm}(t)$

---

Inserting the expression of  $F_{\text{exp}}(t)$  in Eq. E.2 leads to

$$\begin{aligned}
R(t) &= R_0 \cdot e^{-\frac{t}{T_{\text{eff}}}} \cdot e^{\frac{\Delta T_{\text{eff}}}{T_{\text{eff}}^2} \cdot t} (1 + g_{\text{F}}(t)) \cdot \Theta(\pm(t - t_0)) \\
&\quad + R_0 \cdot e^{-\frac{t}{T_{\text{eff}}}} (1 + g_{\text{F}}(t)) \cdot \Theta(\pm(t_0 - t)) \\
&= R_0 \cdot e^{-\frac{t}{T_{\text{eff}}}} (1 + g_{\text{F}}(t)) \cdot \left( e^{\frac{\Delta T_{\text{eff}}}{T_{\text{eff}}^2} \cdot t} \Theta(\pm(t - t_0)) + \Theta(\pm(t_0 - t)) \right). \quad (\text{E.5})
\end{aligned}$$

Since we assumed that  $\frac{\Delta T_{\text{eff}}}{T_{\text{eff}}} \ll 1$ , the exponential function in brackets can be expanded in a polynomial around  $t_0$ :

$$e^{\frac{\Delta T_{\text{eff}}}{T_{\text{eff}}^2} \cdot t} \approx 1 + \frac{\Delta T_{\text{eff}}}{T_{\text{eff}}^2} (t - t_0). \quad (\text{E.6})$$

With this relation the amplitude ratio  $R(t)$  merges to

$$\begin{aligned}
R(t) &\approx R_0 \cdot e^{-\frac{t}{T_{\text{eff}}}} (1 + g_{\text{F}}(t)) \cdot \left( \left( 1 + \frac{\Delta T_{\text{eff}}}{T_{\text{eff}}^2} (t - t_0) \right) \Theta(\pm(t - t_0)) + \Theta(\pm(t_0 - t)) \right) \\
&= R_0 \cdot e^{-\frac{t}{T_{\text{eff}}}} (1 + g_{\text{F}}(t)) \cdot \left( \frac{\Delta T_{\text{eff}}}{T_{\text{eff}}^2} (t - t_0) \cdot \Theta(\pm(t - t_0)) + 1 \right) \\
&\approx R_0 \cdot e^{-\frac{t}{T_{\text{eff}}}} \left( 1 + g_{\text{F}}(t) + \frac{\Delta T_{\text{eff}}}{T_{\text{eff}}^2} (t - t_0) \cdot \Theta(\pm(t - t_0)) \right). \quad (\text{E.7})
\end{aligned}$$

With

$$f_{\text{BGO}}^{\pm}(t) = \frac{\Delta T_{\text{eff}}}{T_{\text{eff}}^2} (t - t_0) \cdot \Theta(\pm(t - t_0)), \quad (\text{E.8})$$

$$G(t) = g_{\text{F}}(t) + f_{\text{BGO}}^{\pm}(t) \quad (\text{E.9})$$

the amplitude ratio  $R(t)$  then results in

$$R(t) = R_0 \cdot e^{-\frac{t}{T_{\text{eff}}}} (1 + G(t)). \quad (\text{E.10})$$



## F. Calculation of $V_{\Sigma}^c$

The average potential of the spin-dependent short-range interaction  $V_{\Sigma}^c$  on each  ${}^3\text{He}$  and  ${}^{129}\text{Xe}$  atom can be obtained by integration of (Eq. 2.71)

$$V_{\text{sp}}(\vec{r}) = \frac{\hbar^2 g_s^N g_p^n}{8\pi \cdot m_{f_\sigma}} (\vec{\sigma} \cdot \hat{r}) \left( \frac{1}{\lambda r} + \frac{1}{r^2} \right) e^{-r/\lambda} \quad (\text{F.1})$$

over the volume of the BGO crystal (unpolarized sample) and over the volume of the polarized spin sample, i.e.

$$\langle V_{\text{sp}}(\vec{r}) \rangle = V_{\Sigma}^c = \frac{\hbar^2 g_s^N g_p^n}{8\pi \cdot m_{f_\sigma}} \cdot \left( \frac{1}{V_{\text{cell}}} \int_{V_{\text{cell}}} dV_{\text{cell}} \left( N \cdot \int_{V_{\text{BGO}}} dV_{\text{BGO}} \frac{x}{r} \left( \frac{1}{\lambda r} + \frac{1}{r^2} \right) e^{-r/\lambda} \right) \right). \quad (\text{F.2})$$

Here  $g_s^N$  and  $g_p^n$  are the coupling constants between the nucleons and the axions or axion like particles,  $\lambda$  is the range of the spin-dependent short-range force,  $N$  is the nucleon number density of the BGO crystal,  $V_{\text{cell}}$  is the volume of the polarized spin sample and  $\hbar$  is the reduced Planck constant. According to the Schmidt model [11], in  ${}^3\text{He}$  and  ${}^{129}\text{Xe}$  atoms the nuclear spin is carried by a neutron only. Thus  $m_{f_\sigma}$  corresponds to the mass of the bound neutron, i.e.  $m_{f_\sigma} = m_n$ .<sup>1</sup> Besides it was assumed that the unit distance vector  $\hat{r}$ , which points from the polarized to the unpolarized sample, and the spin vector  $\vec{\sigma}$  are aligned in x-direction, so that the scalar product of both vectors is given by:  $\vec{\sigma} \cdot \hat{r} = \vec{\sigma} \cdot \vec{r}/r = x/r$ . The two integrals in Eq. F.2 can be solved by numerical integration over the volume of our cylindrical spin sample cell ( $D = 6$  cm,  $r_D = 2.9$  cm) and the cylindrical BGO crystal ( $d = 7$  cm,  $r_d = 3$  cm)

$$\begin{aligned} \langle V^*(\lambda) \rangle &= \int_{V_{\text{cell}}} dV_{\text{cell}} \left( \int_{V_{\text{BGO}}} dV_{\text{BGO}} \frac{x}{r} \left( \frac{1}{\lambda r} + \frac{1}{r^2} \right) e^{-r/\lambda} \right) \\ \Rightarrow \langle V_{\text{sp}}(\vec{r}) \rangle &= V_{\Sigma}^c = \frac{\hbar^2 g_s^N g_p^n \cdot N \cdot \langle V^*(\lambda) \rangle}{8\pi \cdot m_n \cdot V_{\text{cell}}}. \end{aligned} \quad (\text{F.3})$$

In summary, for different values of the range  $\lambda$ , a numerical expression was calculated for  $\langle V^*(\lambda) \rangle$  respectively for  $V_{\Sigma}^c$ . However, for the purpose of illustration, an analytical expression for  $V_{\Sigma}^c$  can be calculated as well. This will be explained in the following: For a start a cylindrical cell with infinite geometry in transversal direction of the magnetic guiding field  $\vec{B}_0$  (x-direction) is considered. The effective spin-dependent short-range potential of such a

<sup>1</sup>In case that the refined nuclear shell model (see Chap 4.1) is used, the mass  $m_{f_\sigma}$  in Eq. 2.71 is slightly different for  ${}^3\text{He}$  and  ${}^{129}\text{Xe}$ :  $m_{f_\sigma}({}^3\text{He}) = 0.87 \cdot m_n$  and  $m_{f_\sigma}({}^{129}\text{Xe}) = 0.75 \cdot m_n$ .

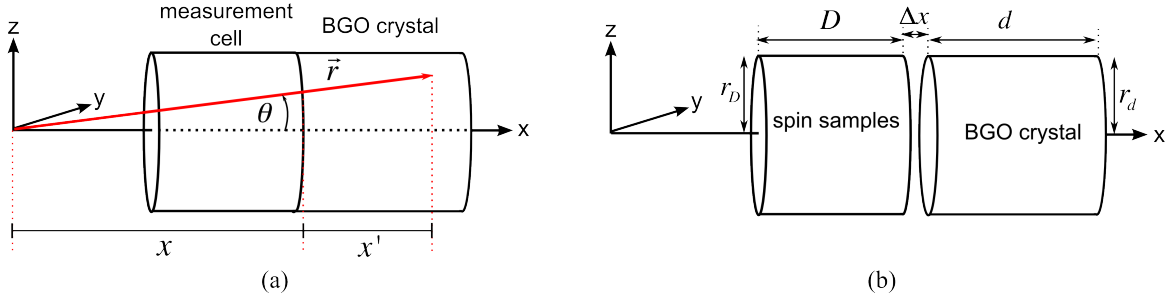


Figure F.1: (a) Illustration of the relation between Cartesian and cylinder coordinates. The  $x$ -component of the position vector  $\vec{r}$  within the measurement cell (external dimensions) is denoted by  $x$  and the one within the BGO crystal is denoted by  $x'$ . (b) Illustration of the arrangement of the BGO crystal and the spin samples (internal dimensions of the measurement cell). The length of the BGO crystal is given by  $d$  and its radius is given by  $r_d$ . On the contrary, the length of the spin sample is given by  $D$  and its radius is given by  $r_D$ . The finite thickness of the wall of the measurement cell is given by  $\Delta x$ . Since the calculations are independent of the transversal directions (i.e.  $y$ - and  $z$ -direction) the thickness of the wall of the measurement cell in transversal direction is neglected in the sketch.

cylindrical cell was calculated in [151] and will be devolved to our special case. The integration of  $V_{\text{sp}}(\vec{r})$  (Eq. F.2) over the volume of the unpolarized sample, i.e.

$$\bar{V}(x) = N \cdot \int_{V_{\text{BGO}}} dV_{\text{BGO}} V_{\text{sp}}(\vec{r}) , \quad (\text{F.4})$$

was solved analytically by using cylinder coordinates (see Fig. F.1a).  $\bar{V}(x)$  then is given by

$$\bar{V}(x) = \kappa \cdot N \cdot \int_0^{r_d} \int_0^{2\pi} \int_0^d \frac{x+x'}{r} \left( \frac{1}{\lambda r} + \frac{1}{r^2} \right) \cdot e^{-r/\lambda} \cdot \rho \, d\rho \, d\phi \, dx' \quad (\text{F.5})$$

with

$$\kappa = \frac{\hbar^2 g_s^N g_p^n}{8\pi \cdot m_n} . \quad (\text{F.6})$$

By introducing the angle  $\theta$  (see Fig. F.1a), which lies between the  $x$ -axis and the position vector  $\vec{r}$ , the relations

$$r = \frac{x+x'}{\cos \theta} , \quad \rho = (x+x') \cdot \tan \theta \quad \Rightarrow \quad \frac{d\rho}{d\theta} = \frac{x+x'}{\cos^2 \theta} \quad (\text{F.7})$$

can be used so that the potential  $\bar{V}(x)$  transforms to

$$\bar{V}(x) = \kappa \cdot N \cdot \int_0^{2\pi} d\phi \int_0^d \int_0^{\pi/2} \left( \frac{\tan \theta \cdot (x+x')}{\lambda} + \sin \theta \right) \cdot e^{-(x+x')/(\lambda \cdot \cos \theta)} \, d\theta \, dx' . \quad (\text{F.8})$$

With  $X = 1/\cos \theta$  and  $dX/d\theta = \sin \theta / \cos^2 \theta$  one gets

$$\bar{V}(x) = \kappa \cdot N \cdot 2\pi \cdot \int_0^d \int_1^\infty \left( \frac{x+x'}{\lambda \cdot X} + \frac{1}{X^2} \right) \cdot e^{-(x+x') \cdot X/\lambda} \, dX \, dx' . \quad (\text{F.9})$$

---

Partial integration over  $X$  gives

$$\bar{V}(x) = \kappa \cdot N \cdot 2\pi \int_0^d e^{-(x+x')/\lambda} dx' \quad (\text{F.10})$$

and partial integration over  $x'$  gives

$$\bar{V}(x) = \kappa \cdot N \cdot 2\pi \cdot \lambda \cdot e^{-x/\lambda} \cdot \left(1 - e^{-d/\lambda}\right). \quad (\text{F.11})$$

In our experimental setup we have a finite gap  $\Delta x$  between the spin samples and the unpolarized matter<sup>2</sup>. Hence,  $x$  has to be replaced by  $x + \Delta x$  (see Fig. F.1b), so that  $\bar{V}(x)$  results in

$$\bar{V}(x) = \kappa \cdot N \cdot 2\pi \cdot \lambda \cdot e^{-x/\lambda} \cdot e^{-\Delta x/\lambda} \cdot \left(1 - e^{-d/\lambda}\right). \quad (\text{F.12})$$

Finally, to get the average of the spin-dependent short-range potential of the cylindrical cell with infinite geometry in transversal direction, i.e.  $\langle V_{\text{sp}}(\vec{r}) \rangle = V_{\Sigma, \infty}^c$ , the expression  $\bar{V}(x)$  has to be averaged over the volume of the spin sample:

$$\begin{aligned} \langle V_{\text{sp}}(\vec{r}) \rangle = V_{\Sigma, \infty}^c &= \frac{1}{D} \int_0^D \bar{V}(x) dx \\ &= 2\pi \cdot \kappa \cdot N \cdot \frac{\lambda^2}{D} e^{-\Delta x/\lambda} \cdot \left(1 - e^{-D/\lambda}\right) \cdot \left(1 - e^{-d/\lambda}\right). \end{aligned} \quad (\text{F.13})$$

The analytical expression of the average of the spin-dependent short-range potential of the cylindrical spin sample with finite geometry in all directions, i.e.  $\langle V_{\text{sp}}(\vec{r}) \rangle = V_{\Sigma}^c$ , then can be expressed by

$$V_{\Sigma}^c = V_{\Sigma, \infty}^c \cdot \eta(\lambda, D, d, \Delta x). \quad (\text{F.14})$$

Comparing Eq. F.13 and Eq. F.3 leads to

$$\eta(\lambda, D, d, \Delta x) = \frac{D \cdot \langle V^*(\lambda) \rangle}{2\pi \cdot V_{\text{cell}} \cdot e^{-\Delta x/\lambda} \cdot \lambda^2 \cdot \left(1 - e^{-D/\lambda}\right) \cdot \left(1 - e^{-d/\lambda}\right)}. \quad (\text{F.15})$$

The function  $\eta(\lambda, D, d, \Delta x)$  takes account for the finite size in transverse direction (y- and z-direction) of the cylindrical samples. This function can be determined numerically for our cylindrically shaped spin sample ( $D = 6$  cm,  $r_D = 2.9$  cm) and matter sample ( $d = 7$  cm,  $r_d = 3$  cm) at close position ( $\Delta x = 2.2$  mm). The resulting function  $\eta(\lambda)$  for our cylindrical samples is shown in Fig. F.2 and can be parameterized by

$$\eta_{\text{fit}}(\lambda) = \frac{1 + 27.8 \cdot \lambda^{1.34}}{1 + 234 \cdot \lambda^{1.31}}. \quad (\text{F.16})$$

Here  $\lambda \ll (r_D, r_d, D, d)$  and  $\eta \rightarrow 1$  for  $r_D, r_d \rightarrow \infty$  applies. Hence the analytical expression for  $V_{\Sigma}^c$  for our cylindrical measurement cells is given by

$$V_{\Sigma}^c = V_{\Sigma, \infty}^c \cdot \eta_{\text{fit}}(\lambda) = V_{\Sigma, \infty}^c \cdot \frac{1 + 27.8 \cdot \lambda^{1.34}}{1 + 234 \cdot \lambda^{1.31}}. \quad (\text{F.17})$$

---

<sup>2</sup>In close position of the BGO crystal its end face had direct contact to the end face of the spin sample cell. Hence, the gap between the end face of the BGO crystal and the spin samples is given by the thickness of the glass of the spin sample cell. The maximal gap is given by  $\Delta x = 2.2$  mm.

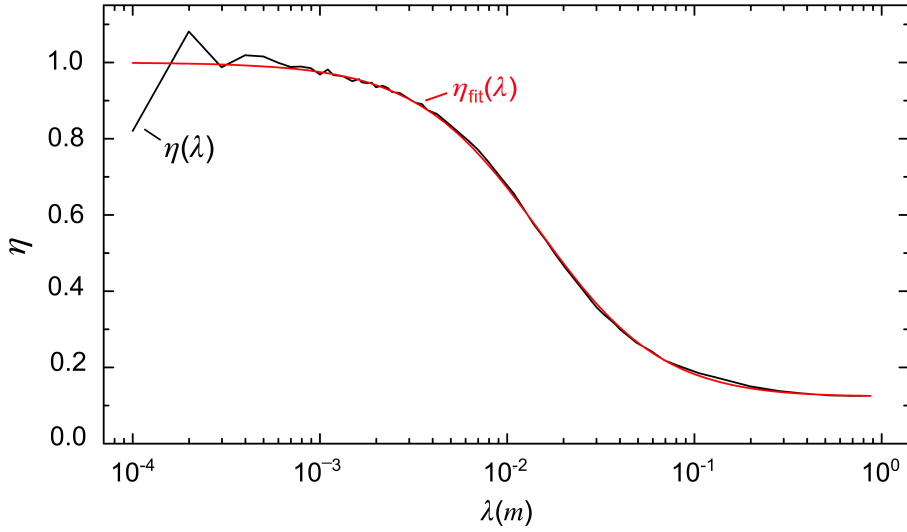


Figure F.2: Devolution of  $\eta(\lambda)$  for our cylindrical measurement cells. The black curve shows the function  $\eta(\lambda)$  which was determined numerically for our cylindrically shaped spin sample ( $D = 6$  cm,  $r_D = 2.9$  cm) and matter sample ( $d = 7$  cm,  $r_d = 3$  cm) with the matter sample, i.e. the BGO crystal, in close position. Hence the distance between the polarized gases and the end face of the BGO crystal is given by  $\Delta x = 2.2$  mm. The red curve shows the fit function  $\eta_{\text{fit}}(\lambda)$ . If  $\lambda \rightarrow 0$ , then  $\eta_{\text{fit}}(\lambda) \rightarrow 1$  and thus  $V_{\Sigma}^c = V_{\Sigma, \infty}^c$  (Eq. F.17). That means for  $\lambda \rightarrow 0$  the spin-dependent short-range interaction only appears in the volume elements of the spin sample which are closest to the BGO crystal. The transversal dimensions of the measurement cell then can be considered as infinitely large.

# Appendix: Paper





## Constraints on Spin-Dependent Short-Range Interaction between Nucleons

K. Tullney,<sup>1,\*</sup> F. Allmendinger,<sup>2</sup> M. Burghoff,<sup>3</sup> W. Heil,<sup>1</sup> S. Karpuk,<sup>1</sup> W. Kilian,<sup>3</sup> S. Knappe-Grüneberg,<sup>3</sup>  
W. Müller,<sup>3</sup> U. Schmidt,<sup>2</sup> A. Schnabel,<sup>3</sup> F. Seifert,<sup>3</sup> Yu. Sobolev,<sup>1,†</sup> and L. Trahms<sup>3</sup>

<sup>1</sup>*Institut für Physik, Johannes Gutenberg-Universität, 55099 Mainz, Germany*

<sup>2</sup>*Physikalisches Institut, Universität Heidelberg, 69120 Heidelberg, Germany*

<sup>3</sup>*Physikalisch-Technische Bundesanstalt Berlin, 10587 Berlin, Germany*

(Received 27 March 2013; published 3 September 2013)

We search for a spin-dependent  $P$ - and  $T$ -violating nucleon-nucleon interaction mediated by light pseudoscalar bosons such as axions or axionlike particles. We employ an ultrasensitive low-field magnetometer based on the detection of free precession of colocated  $^3\text{He}$  and  $^{129}\text{Xe}$  nuclear spins using SQUIDS as low-noise magnetic flux detectors. The precession frequency shift in the presence of an unpolarized mass was measured to determine the coupling of pseudoscalar particles to the spin of the bound neutron. For boson masses between 2 and 500  $\mu\text{eV}$  (force ranges between  $3 \times 10^{-4}$  m and  $10^{-1}$  m) we improved the laboratory upper bounds by up to 4 orders of magnitude.

DOI: [10.1103/PhysRevLett.111.100801](https://doi.org/10.1103/PhysRevLett.111.100801)

PACS numbers: 06.30.Ft, 07.55.Ge, 11.30.Er, 14.80.Va

Axions are light, pseudoscalar particles that arise in theories in which the Peccei-Quinn  $U(1)$  symmetry has been introduced to solve the strong  $CP$  problem [1]. They could have been created in early stages of the Universe being attractive candidates to the cold dark matter that could compose up to  $\sim 1/3$  of the ingredients of the Universe [2]. Several constraints from astrophysics, cosmology, and laboratory experiments have been applied in order to prove or rule out the existence of the axion, i.e., constrain the axion's mass  $m_a$  and/or its couplings. The mass range, in which axions are still likely to exist, could thus be narrowed down to a window reaching from  $\mu\text{eV}$  [3] up to some  $\text{meV}$  [4] (axion window).

Most axion searches look for the conversion of an axion of galactic [5], solar [6], or laboratory [7] origin into a photon in the presence of a static magnetic field. However, any axion or axionlike particle that couples with both scalar and pseudoscalar vertices to fundamental fermions would also mediate a parity and time-reversal symmetry-violating force between a fermion  $f$  and the spin of another fermion  $f_\sigma$ , which is parametrized by a Yukawa-type potential with range  $\lambda$  and a monopole-dipole coupling given by [8]

$$V_{\text{sp}}(\vec{r}) = \frac{\hbar^2 g_s^f g_p^{f_\sigma}}{8\pi m_{f_\sigma}} (\vec{\sigma} \cdot \hat{r}) \left( \frac{1}{\lambda r} + \frac{1}{r^2} \right) e^{-r/\lambda}, \quad (1)$$

where  $\vec{\sigma}$  is the spin vector and  $\lambda$  is the range of the Yukawa force with  $\lambda = \hbar/(m_a c)$ . Thus, the entire axion window can be probed by searching for spin-dependent short-range forces in the range between 20  $\mu\text{m}$  and 0.2 m.  $g_s^f$  and  $g_p^{f_\sigma}$  are dimensionless scalar and pseudoscalar coupling constants which in our case correspond to the scalar coupling of an axionlike particle to a nucleon ( $g_s^f = g_s^N$ ) and its pseudoscalar coupling to a polarized bound neutron ( $g_p^{f_\sigma} = g_p^n$ ). Accordingly, we have  $m_{f_\sigma} = m_n$ .  $\hat{r}$  is the

unit distance vector from the bound neutron to the nucleon. The potential given by Eq. (1) effectively acts near the surface of a massive unpolarized sample as a pseudomagnetic field and gives rise to a shift  $\Delta\nu_{\text{sp}} = 2V_\Sigma/h$ , e.g., in the precession frequency of nuclear spin-polarized gases ( $^3\text{He}$  and  $^{129}\text{Xe}$ ), which according to the Schmidt model [9] can be regarded as an effective probe of spin-polarized bound neutrons. The potential  $V_\Sigma$  is obtained by integration of  $V_{\text{sp}}(r)$  from Eq. (1) over the volume of the massive unpolarized sample averaged over the volume of the polarized spin sample, each having a cylindrical shape. Based on the analytical derivation of  $V_{\Sigma,\infty}$  for disk-shaped spin and matter samples with respective thicknesses  $D$  and  $d$  [10], we obtain

$$V_\Sigma = V_{\Sigma,\infty} \eta(\lambda) = 2\pi N \kappa \frac{\lambda^2}{D} e^{-\Delta x/\lambda} (1 - e^{-D/\lambda}) (1 - e^{-d/\lambda}) \eta(\lambda). \quad (2)$$

$\eta(\lambda)$  takes account for the finite size in transverse direction of our cylindrical samples and  $\Delta x$  represents the finite gap between them. Furthermore,  $\kappa = \hbar^2 g_s^N g_p^n / (8\pi m_n)$  and  $N$  is the nucleon number density of the unpolarized matter sample.  $\eta(\lambda)$  is determined numerically for our cylindrically shaped spin and matter samples at “close” position (see Fig. 1). [ $\eta(\lambda)$  can be expressed reasonably well by the fit function  $\eta_{\text{fit}}(\lambda) = (1 + 27.8\lambda^{1.34}) / (1 + 234\lambda^{1.31})$ .]

Our experimental approach to search for nonmagnetic, spin-dependent interactions is to use an ultrasensitive low-field comagnetometer based on detection of free spin precession of gaseous, nuclear polarized samples [11]. The Larmor frequencies of  $^3\text{He}$  and  $^{129}\text{Xe}$  in a guiding magnetic field  $B$  are given by  $\omega_{\text{L,He(Xe)}} = \gamma_{\text{He(Xe)}} B$ , with  $\gamma_{\text{He(Xe)}}$  being the gyromagnetic ratios of the respective gas species [12,13], with  $\gamma_{\text{He}}/\gamma_{\text{Xe}} = 2.754\,081\,59(20)$ . The influence of the ambient magnetic field and its temporal

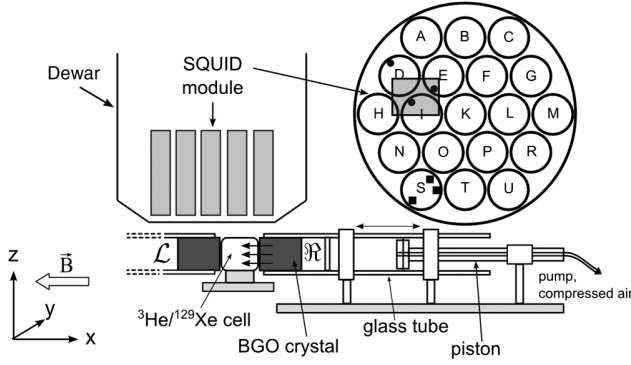


FIG. 1. Sketch of experimental setup. The lower plane SQUIDs in module *D*, *E*, and *I* marked as (●) are used to detect the  $^3\text{He}/^{129}\text{Xe}$  free spin precession. The center of the cylindrical spin sample cell ( $D = 60$  mm,  $\varnothing_D = 58$  mm) has an average distance of  $\bar{z} = 66$  mm to the sensors. The relative position of the cell in the projection onto the ( $x$ ,  $y$ ) plane is indicated by the gray square. SQUIDs in module *S* marked as (■) are used for the gradiometric sensor arrangements. The unpolarized mass (cylindrical BGO crystal:  $d = 70$  mm,  $\varnothing_d = 60$  mm) can be moved along the  $x$  axis ( $B$ -field axis) to “close” ( $\Delta x_c = 2.2$  mm) and “distant” ( $\Delta x_d = 170$  mm) positions and vice versa (see text). This is accomplished by a piston driven glass tube with the BGO fixed at its cell-facing side. The two measuring arrangements “left” (*L*) and “right” (*R*) are shown.

fluctuations cancels in the difference of measured Larmor frequencies of the colocated spin samples

$$\Delta\omega = \omega_{\text{He}} - \frac{\gamma_{\text{He}}}{\gamma_{\text{Xe}}} \omega_{\text{Xe}}. \quad (3)$$

On closer inspection, a resulting constant frequency shift  $\Delta\omega_{\text{lin}}$ , e.g., due to Earth’s rotation, is not compensated by comagnetometry. That is discussed in [14], together with frequency shifts due to the generalized Ramsey-Bloch-Siegert shift. The latter ones are directly proportional to the particular net magnetization  $A_{\text{He(Xe)}} e^{-t/T_{2,\text{He(Xe)}}^*}$  and also are included in the weighted frequency difference  $\Delta\omega(t)$ :

$$\Delta\omega(t) = \Delta\omega_{\text{lin}} + \epsilon_{\text{He}} A_{\text{He}} e^{-t/T_{2,\text{He}}^*} - \epsilon_{\text{Xe}} A_{\text{Xe}} \cdot e^{-t/T_{2,\text{Xe}}^*}. \quad (4)$$

Accordingly, its equivalent, the weighted phase difference  $\Delta\Phi(t) = \Phi_{\text{He}}(t) - (\gamma_{\text{He}}/\gamma_{\text{Xe}})\Phi_{\text{Xe}}(t)$ , is sensitive to a phase drift given by

$$\Delta\Phi(t) = \Phi_0 + \Delta\omega_{\text{lin}} t - \epsilon_{\text{He}} T_{2,\text{He}}^* A_{\text{He}} e^{-t/T_{2,\text{He}}^*} + \epsilon_{\text{Xe}} T_{2,\text{Xe}}^* A_{\text{Xe}} e^{-t/T_{2,\text{Xe}}^*}. \quad (5)$$

Because of the knowledge of these side effects, any anomalous frequency shifts generated by nonmagnetic spin interactions, such as the quested short-range interaction, can be analyzed by looking at  $\Delta\omega(t)$  and  $\Delta\Phi(t)$ , respectively. A sudden frequency change  $\Delta\omega_{\text{sp}}$  stemming from the pseudoscalar Yukawa potential  $V_{\text{sp}}(r)$  would occur at an

instant  $t = t_0$ , e.g., by moving a massive matter sample close to the precessing nuclei. This would lead to an additional linear phase drift  $\Delta\omega_{\text{sp}} t$  in Eq. (5) for  $t > t_0$ . For further analysis, it is useful to develop Eq. (5) in a Taylor expansion of 5th order around  $t_0$  (the criterion to use a Taylor expansion up to the 5th order was that the reduced  $\chi^2/\text{d.o.f.}$  of the fit equals 1). The weighted phase difference  $\Delta\Phi(t)$  can then be described by

$$\Delta\Phi(t') = a + b(t')t' + ct'^2 + dt'^3 + et'^4 + ft'^5, \quad (6)$$

with  $t' = t - t_0$ . The coefficient of the linear term now reads

$$b(t') = \Delta\omega_{\text{lin}} + \Delta\omega_{\text{sp}}^w(t') + \epsilon_{\text{He}} A'_{\text{He}} - \epsilon_{\text{Xe}} A'_{\text{Xe}}. \quad (7)$$

Note that  $\Delta\omega_{\text{sp}}^w(t') = 2\pi\Delta\nu_{\text{sp}}^w \Theta(\pm t')$  is the only time-dependent term in Eq. (7), so that a change  $\delta b = b_c - b_d = 2\pi\Delta\nu_{\text{sp}}^w$  of  $b(t')$  at  $t = t_0$  would directly indicate the existence of the short-range interaction. [ $(\pm)$  in the argument of the Heaviside step function has to be set  $(-)$  for the sequence  $c \rightarrow d$  and  $(+)$  for the reverse one,  $d \rightarrow c$ . Furthermore, for runs  $j = 1, 2, 3$  the BGO was moved at  $t_0 = 8700$  s, otherwise at  $t_0 = 10800$  s.] With our special choice of  $t' = t - t_0$ , the linear coefficient of the Taylor expansion does not depend on  $T_2^*$  and thus is insensitive to possible changes in  $T_2^*$ . The impact of the  $T_2^*$  dependence of higher order terms on the determination of  $b(t')$  is discussed in detail in the section on systematic uncertainties.

The experiments were performed inside the magnetically shielded room BMSR-2 at the Physikalisch-Technische Bundesanstalt Berlin (PTB) [15]. A homogeneous guiding magnetic field of about 350 nT was provided inside the shielded room by means of a square coil pair ( $B_x$  coils) of edge length 1800 mm. A second square coil pair ( $B_y$  coils) arranged perpendicular to the  $B_x$  coils was used to manipulate the sample spins, e.g.,  $\pi/2$  spin flip by nonadiabatic switching [11]. The major components of the experimental setup within BMSR-2 are shown in Fig. 1. For the detection of spin precession we used a multichannel low- $T_c$  dc-SQUID device [16,17]. The  $^3\text{He}/^{129}\text{Xe}$  nuclear spins were polarized outside the shielding by means of optical pumping. Low-relaxation cylindrical glass cells (GE180) were filled with the polarized gases and placed directly beneath the Dewar as close as possible to the SQUID sensors. The SQUID sensors detect a sinusoidal change in magnetic flux due to the nuclear spin precession of the gas atoms. In order to obtain a high common mode rejection ratio, three first order gradiometric sensor combinations were used in order to suppress environmental disturbance fields such as vibrational modes. Figure 1 shows their positions with respect to each other and with respect to the  $^3\text{He}/^{129}\text{Xe}$  sample cell. The system noise of the SQUID gradiometer configurations was between 3 and 10 fT/ $\sqrt{\text{Hz}}$  in the range of the  $^3\text{He}/^{129}\text{Xe}$  spin-precession frequencies, i.e.,  $4 < \nu_L < 12$  Hz, while typical signal amplitudes reached



10 pT for helium and 3 pT for xenon at the beginning of the spin-precession cycle.

Typically, the optimum conditions in terms of long transverse relaxation times ( $T_2^*$ ) and high SNR were met at a gas mixture with pressures of  ${}^3\text{He}:\text{Xe}(91\%{}^{129}\text{Xe}):N_2 \approx (2:8:35)$  mbar. Nitrogen was added to suppress spin-rotation coupling in bound Xe-Xe van der Waals molecules [18,19]. As unpolarized matter sample we used a cylindrical BGO crystal ( $\text{Bi}_4\text{Ge}_3\text{O}_{12}$ ,  $\rho = 7.13$  g/cm $^3$ ). BGO has a high nucleon number density, is a nonconductive material that shows low Johnson-Nyquist noise, and is said to have an unusual magnetism-related behavior in weak constant magnetic fields ( $\chi_{\text{mag}} \approx 0$  ppm) [20–22]. For systematic checks, the BGO crystal could be placed left ( $\mathcal{L}$ ) and right ( $\mathfrak{R}$ ) with respect to the  ${}^3\text{He}/{}^{129}\text{Xe}$  sample cell (see Fig. 1). Since  $V_{\text{sp}}(\vec{r}) \propto \vec{\sigma} \cdot \hat{r}$ ,  $\Delta\nu_{\text{sp}}$  changes its sign in going from  $\mathcal{L}$  to  $\mathfrak{R}$ . This has to be considered by averaging the  $\mathcal{L}$  and  $\mathfrak{R}$  results. On the other hand,  $\Delta\nu_{\text{sp}}$  drops out averaging  $\mathcal{L}$  and  $\mathfrak{R}$  without sign change. In case of a nonzero spin-dependent axion fermion interaction, a shift  $\Delta\nu_{\text{sp}}^w$  in the weighted frequency difference [Eq. (3)] can be extracted from respective frequency measurements in “close” and “distant” positions given by

$$\Delta\nu_{\text{sp}}^w = \frac{2V_{\Sigma}^c}{h} \left( 1 - \frac{\gamma_{\text{He}}}{\gamma_{\text{Xe}}} \right), \quad (8)$$

assuming  $V_{\Sigma,\text{He}} = V_{\Sigma,\text{Xe}} = V_{\Sigma,n} \equiv V_{\Sigma}$  (Schmidt model) and  $V_{\Sigma}^d \ll V_{\Sigma}^c$ .

We performed 10 measurement runs lasting approximately 9 h each. For each measurement run, the BGO crystal was moved after  $t_0 \approx 3$  h from close to distant position ( $c \rightarrow d$ ) or vice versa ( $d \rightarrow c$ ). The asymmetric timing takes account for the smaller SNR in the second measurement block due to the exponential damping ( $T_2^*$ ) of the signal amplitude which was  $T_{2,\text{He}}^* \approx 53$  h and  $T_{2,\text{Xe}}^* \approx 5$  h, typically. By this measure, comparable statistics were obtained for both BGO positions.

As discussed in detail in [14], the data from each run were divided into sequential time intervals of  $\tau = 3.2$  s. For each obtained subdata set, a  $\chi^2$  minimization was performed using an appropriate fit function to extract the phases  $\phi_{\text{He}}$ ,  $\phi_{\text{Xe}}$  and the frequencies  $\omega_{\text{He}}$ ,  $\omega_{\text{Xe}}$  with the corresponding errors. In a further step, the accumulated phase  $\Phi_{\text{He(Xe)}}(t')$  was determined for each run in order to derive the weighted phase difference  $\Delta\Phi(t')$ . Then, Eq. (6) was fitted simultaneously to the data set  $\Delta\Phi(t')$  that was determined for the three gradiometers of each measurement run. From the resulting fit parameters  $\bar{a}$ ,  $\bar{b}_c$ ,  $\bar{b}_d$ ,  $\bar{c}$ ,  $\bar{d}$ ,  $\bar{e}$ ,  $\bar{f}$  and by use of Eqs. (7) and (8), the frequency shift  $\Delta\nu_{\text{sp}}$  is then extracted from

$$\overline{\Delta\nu}_{\text{sp}} = \frac{\bar{b}_c - \bar{b}_d}{2\pi \left( 1 - \frac{\gamma_{\text{He}}}{\gamma_{\text{Xe}}} \right)}. \quad (9)$$

For six runs (2, 3, 4, 5, 9, 10), the BGO crystal was positioned at  $\mathcal{L}$ , otherwise at  $\mathfrak{R}$ . For all  $\mathcal{L}$  runs, the results were multiplied by  $(-1)$ :  $\overline{\Delta\nu}_{\text{sp}} = -\overline{\Delta\nu}_{\text{sp},\mathcal{L}}$ . In Fig. 2(a), values  $\overline{\Delta\nu}_{\text{sp}}$  for the individual runs are shown together with their correlated  $1\sigma$  errors. [The correlated errors are calculated as the square root of the diagonal elements of the covariance matrix of the least  $\chi^2$  fit model of Eq. (6) with the proper statistical weights. The uncorrelated errors are about a factor of 30 smaller and not included in the error bars shown in Fig. 2.] From the calculation of the weighted mean, one gets  $\overline{\Delta\nu}_{\text{sp}} = (-2.9 \pm 2.3)$  nHz. As a consistency check, we reanalyzed our 2009 data, where we looked for a possible Lorentz-violating (LV) sidereal frequency modulation [14]. Since no mass was moved,  $\bar{b}_c = \bar{b}_d$  should hold, using the fit function of Eq. (6) and a hypothetical time  $t_0 = 10800$  s. Figure 2(b) shows the results  $\overline{\Delta\nu}_{\text{check}}$  for all 7 measurement runs together with their correlated  $1\sigma$  errors. The weighted mean of the LV data gives  $\overline{\Delta\nu}_{\text{check}} = (-1.4 \pm 3.4)$  nHz. The  $\chi^2/\text{d.o.f.}$  of the data to their respective weighted means ( $\overline{\Delta\nu}_{\text{sp}}$ ,  $\overline{\Delta\nu}_{\text{check}}$ ) gives 2.29 and 2.38, indicating that the errors on the measured frequency shifts (Fig. 2) are somewhat underestimated. In order to take this into account, the errors are scaled to obtain a  $\chi^2/\text{d.o.f.}$  of one, as recommended, e.g., by [23,24].

At the 95% C.L., our results for the measured frequency shifts are

$$\overline{\Delta\nu}_{\text{sp}} = (-2.9 \pm 6.9) \text{ nHz}, \quad (10)$$

$$\overline{\Delta\nu}_{\text{check}} = (-1.4 \pm 10.5) \text{ nHz}, \quad (11)$$

indicating that (i) we find no evidence for a pseudoscalar short-range interaction mediated by axionlike particles and

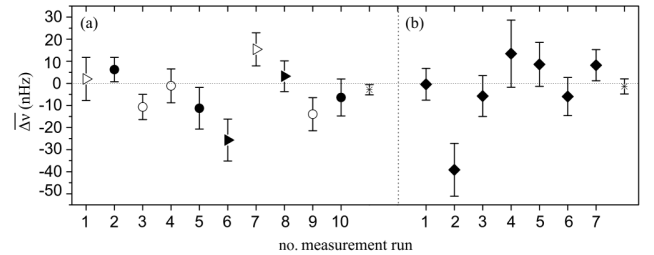


FIG. 2. (a) Extracted frequency shifts  $\overline{\Delta\nu}_{\text{sp}}$  (with correlated  $1\sigma$  error) of the 10 measurement runs. The triangles specify the  $\mathfrak{R}$ , the circles the  $\mathcal{L}$  arrangement of the BGO crystal. Full symbols indicate the  $c \rightarrow d$  sequence, hollow symbols the opposite case ( $d \rightarrow c$ ). (b) Results  $\overline{\Delta\nu}_{\text{check}}$  obtained from the LV data using the same fit model [Eq. (6)]. Since no mass was moved, we expect no shift in the spin precession frequency. The rightmost symbols (stars) indicate the respective weighted means ( $1\sigma$  error).

(ii) the cross-check analysis of our LV data is compatible with zero within the error bars, as expected.

*Discussion of systematic uncertainties.*—The movement of the BGO crystal can produce correlated effects that may mimic a pseudoscalar frequency shift or even compensate the effect we are looking for. Two effects caused by a nonzero magnetic susceptibility of the BGO have to be considered, by taking  $\chi_{\text{mag}} = -19$  ppm, which is the high-field limit ( $B > 0.1$  T) [21]. (a) The BGO at the close position slightly changes the magnetic field across the volume of the  $^3\text{He}/^{129}\text{Xe}$  sample cell. This effect drops out to first order due to comagnetometry. To second order, however, the difference in their molar masses leads to a difference ( $\Delta z$ ) in their center of masses (barometric formula), which is  $\Delta z = 1.2 \times 10^{-7}$  m for our cylindrical sample cell. This results in a frequency shift of  $\Delta\nu_{\text{sys}} = \Delta z \langle \partial B / \partial z \rangle_{\text{ind}} \gamma_{\text{He}} / 2\pi \leq 0.03$  nHz for induced field gradients in the vertical direction of  $\langle \partial B / \partial z \rangle_{\text{ind}} \leq 0.08$  pT/cm. The field gradients were calculated using COMSOL MULTIPHYSICS, a finite element analysis software. Compared to the measured frequency shift [Eq. (10)], this systematic effect is negligible. (b) More serious is the fact that a change of the magnetic field gradient by the BGO also influences the  $T_2^*$  times of  $^3\text{He}$  and  $^{129}\text{Xe}$ . The direct approach is to extract  $T_2^*$  and thus  $\Delta T_2^*$  via the exponential decay of the signal amplitudes with the BGO in close and distant positions. The most accurate distinction between  $(T_2^*)_c$  and  $(T_2^*)_d$  was obtained through a fit to the amplitude ratio  $A_{\text{Xe}}(t')/A_{\text{He}}(t')$  given by  $f_{\text{fit}}(t') = W e^{-t'/T_{\text{eff}}^*}$  with  $T_{\text{eff}}^* = T_{2,\text{He}}^* T_{2,\text{Xe}}^* / (T_{2,\text{He}}^* - T_{2,\text{Xe}}^*)$ . According to [11,25,26], a relation between  $\Delta T_{2,\text{He}}^*$ ,  $\Delta T_{2,\text{Xe}}^*$ , and  $\Delta T_{\text{eff}}^*$  can be derived

$$\frac{\Delta T_{\text{eff}}^*}{(T_{\text{eff}}^*)^2} = -\frac{\Delta T_{2,\text{He}}^*}{(T_{2,\text{He}}^*)^2} + \frac{\Delta T_{2,\text{Xe}}^*}{(T_{2,\text{Xe}}^*)^2} \approx -0.5 \frac{\Delta T_{2,\text{He}}^*}{(T_{2,\text{He}}^*)^2} \quad (12)$$

by taking the respective diffusion coefficients of  $^3\text{He}$  and  $^{129}\text{Xe}$  in the gas mixture and using the approximation  $\phi_D/2 = D/2 \approx R = 30$  mm for our cylindrically shaped cell. We obtain an upper limit of  $|\Delta T_{2,\text{He}}^*| < 160$  s for a possible  $T_2^*$  change. From that the systematic frequency shift  $\Delta\nu_{\text{sys}}^{T_2^*}$  on  $b(t')$  due to the higher order terms of Eq. (6) can be estimated to be

$$\left| \Delta\nu_{\text{sys}}^{T_2^*} \right| \leq \left| \frac{\frac{\Delta T_{2,\text{He}}^*}{(T_{2,\text{He}}^*)^2} \left( \frac{E'_{\text{He}}}{T_{2,\text{He}}^*} - \frac{1}{2} \frac{E'_{\text{Xe}}}{T_{2,\text{Xe}}^*} \right) \frac{t_0}{2}}{2\pi(1 - \gamma_{\text{He}}/\gamma_{\text{Xe}})} \right| \approx 0.1 \text{ nHz}. \quad (13)$$

Here we used Eq. (9), replacing  $\bar{b}_c$  and  $\bar{b}_d$  by the temporal means  $2\bar{c}_c \langle t' \rangle_{t'}$  and  $2\bar{c}_d \langle t' \rangle_{t'}$  of the quadratic term in Eq. (6) with  $\bar{c}_{c(d)} = \{ -(E'_{\text{He}}/2)/(T_{2,\text{He}}^*)^2 + (E'_{\text{Xe}}/2)/(T_{2,\text{Xe}}^*)^2 \}_{c(d)}$  and  $E'_{\text{He(Xe)}} = \epsilon_{\text{He(Xe)}} A'_{\text{He(Xe)}} T_{2,\text{He(Xe)}}^*$ . Values for the respective  $E'_{\text{He(Xe)}}$  phase amplitudes were extracted from the fit function [Eq. (6)] applied to the data

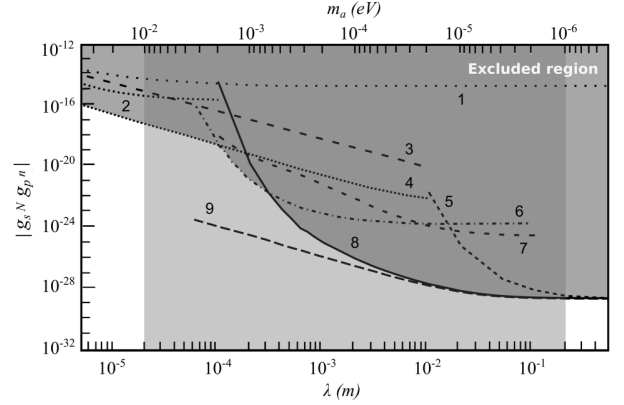


FIG. 3. The experimental 95% confidence upper limit on  $|g_s^N g_p^N|$  plotted versus  $\lambda$ , the range of the Yukawa force with  $\lambda = \hbar/(m_a c)$ . The axion window is indicated by the light gray area. (1) result of [28], (2) result of [29], (3) result of [30], (4) result of [31], (5) result of [32], (6) result of [33], (7) result of [34], (8) this experiment ( $\Delta x = 2.2$  mm) [35], (9) expected results for  $\Delta x \approx 0$  mm using the same data set demonstrates the gain in measurement sensitivity for  $\lambda < 10^{-3}$  m. See [36] for bounds on the pseudoscalar short-range force between polarized electrons and unpolarized nucleons. Raffelt [37] points out that much tighter constraints on  $|g_s^N g_p^N|$  can be inferred by combining constraints on  $g_s$  from stellar energy-loss arguments and  $g_p$  from searches for anomalous monopole-monopole forces.

and result to be  $\langle E'_{\text{He}} \rangle = 11.5$  rad and  $\langle E'_{\text{Xe}} \rangle = 0.1$  rad. Finally,  $\langle t' \rangle_{t'}$  was taken to be  $\langle t' \rangle_{t'} \approx t_0/2$ .

From Eq. (13) a conservative estimate of the systematic error can be made with  $|\Delta\nu_{\text{sys}}^{T_2^*}| = \pm 0.2$  nHz (95% C.L.), which brings us to the final result

$$\overline{\Delta\nu}_{\text{sp}} = (-2.9 \pm 6.9 \pm 0.2) \text{ nHz} \quad (95\% \text{ C.L.}) \quad (14)$$

for the measured pseudoscalar frequency shift.

From the total error  $\delta(\overline{\Delta\nu}_{\text{sp}}) = \pm 7.1$  nHz, we can then derive exclusion bounds for  $|g_s^N g_p^N|$  using Eq. (2) and  $|\delta(\overline{\Delta\nu}_{\text{sp}})| \geq 2V_{\Sigma}^c/h$ , which are shown in Fig. 3.

We have substantially improved the bounds on a spin-dependent short-range interaction between polarized (bound) neutrons and unpolarized nucleons over most of the axion window, tightening existing constraints on axion-like particles heavier than  $20 \mu\text{eV}$  by up to 4 orders of magnitudes.

And there are clear strategies on how to improve our experimental sensitivity. (i) Close contact of the spin system with the matter sample. For  $\Delta x \approx 0$  mm, our present measurement sensitivity will significantly increase for  $\lambda < 10^{-3}$  m (see Fig. 3). (ii) Moving the spin-matter sample more frequently between its set positions ( $c \leftrightarrow d$  and/or  $\mathcal{L} \leftrightarrow \mathfrak{R}$ ). This results in a different time structure for the linear term in the fit model of Eq. (6) such that the correlated error approaches the uncorrelated one. This was already demonstrated in [14]. (iii) Magnetic susceptibility related

artifacts have to be eliminated by taking zero-susceptibility matched matter samples ( $\chi_{\text{mag}} \approx 0$  ppm) as it is common practice in high resolution NMR spectroscopy [27].

This work was supported by the Deutsche Forschungsgemeinschaft (DFG) under Contract No. BA 3605/1-1 and the research center “Elementary Forces and Mathematical Foundations” (EMG) of the University in Mainz, and by PRISMA cluster of excellence at Mainz. We are grateful to our glass blower R. Jera for preparing the low relaxation glass cells from GE180.

---

\*Corresponding author.  
tullnek@uni-mainz.de

†On leave from PNPI, St. Petersburg, Russia.

- [1] R. D. Peccei and H. R. Quinn, *Phys. Rev. Lett.* **38**, 1440 (1977).
- [2] J. Jaeckel and A. Ringwald, *Annu. Rev. Nucl. Part. Sci.* **60**, 405 (2010).
- [3] S. Asztalos *et al.*, *Phys. Rev. D* **69**, 011101(R) (2004).
- [4] G. G. Raffelt, *Annu. Rev. Nucl. Part. Sci.* **49**, 163 (1999).
- [5] S. Asztalos *et al.*, *Phys. Rev. Lett.* **104**, 041301 (2010).
- [6] E. Arik *et al.*, *J. Cosmol. Astropart. Phys.* **02** (2009) 008.
- [7] K. Ehret *et al.*, *Phys. Lett. B* **689**, 149 (2010).
- [8] J. E. Moody and F. Wilczek, *Phys. Rev. D* **30**, 130 (1984).
- [9] Th. Schmidt, *Z. Phys.* **106**, 358 (1937).
- [10] O. Zimmer, *Phys. Lett. B* **685**, 38 (2010).
- [11] C. Gemmel *et al.*, *Eur. Phys. J. D* **57**, 303 (2010).
- [12] M. Pfeffer and O. Lutz, *J. Magn. Reson., Ser. A* **108**, 106 (1994).
- [13] <http://www.codata.org>.
- [14] C. Gemmel *et al.*, *Phys. Rev. D* **82**, 111901 (2010).
- [15] J. Bork *et al.*, in *Proceedings of Biomag. 2000: The 12th International Conference on Biomagnetism, Espoo, Finland, 2000* (Helsinki University of Technology, Espoo, Finland, 2000), p. 970.
- [16] D. Drung, *Physica (Amsterdam)* **368C**, 134 (2002).
- [17] M. Burghoff, S. Hartwig, W. Kilian, A. Vorwerk, and L. Trahms, *IEEE Trans. Appl. Supercond.* **17**, 846 (2007).
- [18] B. Chann, I. A. Nelson, L. W. Anderson, B. Driehuys, and T. G. Walker, *Phys. Rev. Lett.* **88**, 113201 (2002).
- [19] B. C. Anger, G. Schrank, A. Schoeck, K. A. Butler, M. S. Solum, R. J. Pugmire, and B. Saam, *Phys. Rev. A* **78**, 043406 (2008).
- [20] E. A. Kravchenko, V. G. Orlov, and M. P. Shlykov, *Russ. Chem. Rev.* **75**, 77 (2006).
- [21] S. Yamamoto, K. Kuroda, and M. Senda, *IEEE Trans. Nucl. Sci.* **50**, 1683 (2003).
- [22] B. C. Grabmaier and R. Oberschmid, *Phys. Status Solidi (a)* **96**, 199 (1986).
- [23] Particle Data Group, *Phys. Lett. B* **592**, 11 (2004).
- [24] W. H. Press, S. A. Teukolsky, W. T. Vetterling, and B. P. Flannery, *Numerical Recipes: The Art of Scientific Computing* (Cambridge University Press, New York, 2007), 3rd ed.
- [25] G. D. Cates, S. R. Schaefer, and W. Happer, *Phys. Rev. A* **37**, 2877 (1988).
- [26] W. Kilian, A. Haller, F. Seifert, D. Grosenick, and H. Rinneberg, *Eur. Phys. J. D* **42**, 197 (2007).
- [27] R. Kc, Y. N. Gowda, D. Djukovic, I. D. Henry, G. H. J. Park, and D. Rafferty, *J. Magn. Reson.* **205**, 63 (2010).
- [28] S. Baeßler, V. V. Nesvizhevsky, K. V. Protasov, and A. Yu. Voronin, *Phys. Rev. D* **75**, 075006 (2007).
- [29] T. Jenke *et al.*, [arXiv:1208.3875v1](https://arxiv.org/abs/1208.3875).
- [30] A. P. Serebrov *et al.*, *JETP Lett.* **91**, 6 (2010).
- [31] A. K. Petukhov, G. Pignol, D. Jullien, and K. H. Andersen, *Phys. Rev. Lett.* **105**, 170401 (2010).
- [32] A. N. Youdin, D. Krause, Jr., K. Jagannathan, L. R. Hunter, and S. K. Lamoreaux, *Phys. Rev. Lett.* **77**, 2170 (1996).
- [33] M. Bulatowicz, R. Griffith, M. Larsen, J. Mirijanian, C. B. Fu, E. Smith, W. M. Snow, H. Yan, and T. G. Walker, preceding Letter, *Phys. Rev. Lett.* **111**, 102001 (2013).
- [34] P.-H. Chu *et al.*, *Phys. Rev. D* **87**, 011105(R) (2013).
- [35] See A. G. Glenday, C. E. Cramer, D. F. Phillips, and R. L. Walsworth, *Phys. Rev. Lett.* **101**, 261801 (2008) for a discussion on theoretical calculations of the neutron spin contribution to the nuclear angular momentum in  $^3\text{He}$  ( $I = 1/2$ ) and  $^{129}\text{Xe}$  ( $I = 1/2$ ) (approximately 87% and 75%). This refinement of nuclear model that goes beyond the Schmidt model used in [31,32,34] of Fig. 3 increases our upper bounds by a factor of 1.4.
- [36] S. A. Hoedel, F. Fleischer, E. G. Adelberger, and B. R. Heckel, *Phys. Rev. Lett.* **106**, 041801 (2011).
- [37] G. G. Raffelt, *Phys. Rev. D* **86**, 015001 (2012).



# Bibliography

- [1] J.H. Christenson et al. *Phys. Rev. Lett.*, **13**, 138 (1964).
- [2] J. H. Christenson et al. *Phys. Rev.*, **140**, (B74–B84) 1965.
- [3] K. Abe. *Phys. Rev. Lett.*, **87**, 091802 (2001).
- [4] B. Aubert et al. *Phys. Rev. Lett.*, **87**, 091801 (2001).
- [5] A. Riotto and M. Trodden. *Ann. Rev. Nucl. Part. Sc.*, **49**, 35 (1999).
- [6] A.D. Sakharov. *JETP Lett.*, 5, (24) 1967.
- [7] D.N. Spergel et al. *Astrophys. J. Supp.*, **170**, 377 (2007).
- [8] J.E. Moody and F. Wilczek. *Phys. Rev. D*, **30**, 130 (1984).
- [9] V.A. Kostelecký and C.D. Lane. *Phys. Rev. D*, 60, (116010) 1999.
- [10] M.A. Rosenberry and T.E. Chupp. *Phys. Rev. Lett.*, 86, (22) 2001.
- [11] Th. Schmidt. *Zeitschrift für Physik A, Hadronen und Kerne*, **106**, 358 (1937).
- [12] T.P. Cheng and L.F. Li. *Gauge Theory of Elementary Particle Physics*. Oxford: Clarendon Press, 2005.
- [13] C. Quigg. *Gauge Theories of the Strong, Weak, and Electromagnetic Interactions*. Addison-Wesley Publishing Company, 1983.
- [14] S. Weinberg. *Phys. Rev. D*, 11, (3583) 1975.
- [15] C. Amsler et al. (Particle Data Group). *Phys. Lett. B*, **667**(1-5), 2008.
- [16] G. t'Hooft. *Phys. Rev. Lett.*, **37**, (1976) 8.
- [17] G. t'Hooft. *Phys. Rev. D*, **14**, (1976) 3432.
- [18] H.V. Klapdor-Kleingrothaus and K. Zuber. *Particle Astrophysics*. Institute of Physics Publishing, Bristol and Philadelphia 1997.
- [19] J.E. Kim. *Phys. Rep.*, **150**, (1987) 1.
- [20] R.D. Peccei. *CP-Violation Advanced Series in High Energy Physics*, volume 3. World Scientific, Singapore 1989.

- [21] V. Baluni. *Phys. Rev. D*, **19**, (1979) 2227.
- [22] M. Morgan and G. Miller. *Phys. Rev. B*, **179**, (1986) 379.
- [23] E.P. Shabalin. *Sov. J. Nucl. Phys.*, **36**, (1982) 575.
- [24] R.D. Peccei and H.R. Quinn. *Phys. Rev. Lett.*, **38**, (1977) 1440.
- [25] R.D. Peccei and H.R. Quinn. *Phys. Rev. D*, **16**, (1977) 1791.
- [26] S. Weinberg. *Phys. Rev. Lett.*, **40**, (1978) 223.
- [27] F. Wilczek. *Phys. Rev. Lett.*, **40**, (1978) 279.
- [28] M.S. Turner. *Phys. Rep.*, **197**, (1990) 67.
- [29] G.G. Raffelt. *Stars as Laboratories for Fundamental Physics*. University of Chicago Press, Chicago/London 1996.
- [30] W.A. Bardeen and S.H. Tye. *Phys. Lett. B*, **74**, (1978) 229.
- [31] J. Gasser and H. Leutwyler. *Phys. Rep.*, **87**, (1982) 77.
- [32] H. Leutwyler. *Phys. Lett. B*, **378**, (1996) 313.
- [33] W.M. Yao et al. *J. Phys. G: Nucl. Part. Phys.*, **33**, (2006) 1.
- [34] R.D. Peccei. *The Strong CP Problem and Axions*. In: *Axions – Theory, Cosmology, an Experimental Searches*, Springer, 2008.
- [35] D.B. Kaplan. *Nucl. Phys. B*, **260**, (1985) 215.
- [36] M. Srednicki. *nucl. Phys. B*, **260**, (1985) 689.
- [37] V.Y. Alexakhin. *Phys. Lett. B*, **647**(1), (2007) 8.
- [38] Airapetian *et al.* *Phys. Rev. D*, **75**, (2007) 012007.
- [39] Y. Asano *et al.* *Phys. Lett. B*, **107**, (1981) 159.
- [40] J.E. Kim. *Phys. Rev. Lett.*, **43**, (1979) 103.
- [41] M.A. Shifman, A.I. Vainshtein, and V.I. Zakharov. *Nucl. Phys. B*, **166**, (1980) 493.
- [42] M. Dine, W. Fischler, and M. Srednicki. *Phys. Lett. B*, **260**, (1985) 689.
- [43] A.R. Zhitnitsky. *Sov. J. Nucl. Phys.*, **31**, (1980) 260.
- [44] R.D. Peccei. *The strong CP-Problem*. World Scientific, Deutsches Elektronen Synchrotron DESY, Hamburg 1987.
- [45] P. Sikivie. *Axion Cosmology*. In: *Axions – Theory, Cosmology, an Experimental Searches*, Springer, 2008.

- [46] B. Lakić, R. Horvat, and M. Krcmar. *Axions and Large Extra Dimensions*. In: *Axions – Theory, Cosmology, an Experimental Searches*, Springer, 2008.
- [47] A. Mirizzi, G. Raffelt, and P. Serpico. *Photon-axion Conversion in Intergalactic Magnetic Fields and Cosmological Consequences*. In: *Axions – Theory, Cosmology, an Experimental Searches*, Springer, 1987.
- [48] E.J. Kim. *Light Pseudoscalars, Particle Physics and Cosmology*. Department of Physics, Seoul National University, Korea, 1987.
- [49] J. Preskill, M.B. Wise, and F. Wilczek. *Phys. Lett. B*, **120**, (1983) 127.
- [50] L.F. Abbott and P. Sikivie. *Phys. Lett. B*, **120**, (1983) 133.
- [51] M. Dine and W. Fischler. *Phys. Lett. B*, **120**, (1983) 137.
- [52] P. Fox, A. Pierce, and S.D. Thomas. *arXiv:hep-th/0409059*, (2004).
- [53] D.N. Spergel et al. *Astrophys. J. Suppl.*, **170**, (2007) 377.
- [54] G.G. Raffelt. *Astrophysical Axion Bounds*. In: *Axions – Theory, Cosmology, an Experimental Searches*, Springer, 1987.
- [55] G.G. Raffelt. *Stars as Laboratories for Fundamental Physics*. University of Chicago Press, 1996.
- [56] G.G. Raffelt. *Phys. Rep.*, **198**, (1990).
- [57] E.W. Kolb and M.S. Turner. *The Early Universe*. Westview Press, 1990.
- [58] J. Engel, D. Seckel, and A.C. Hayes. *Phys. Rev. Lett.*, **65**, (1990) 960.
- [59] H.T. Janka et al. *Phys. Rev. Lett.*, **76**, (1996) 2621.
- [60] R. Bradley et al. *Rev. Mod. Phys.*, **75**, (2003) 777.
- [61] S. De Panfilis et al. *Phys. Rev. Lett.*, **59**, (1987) 839.
- [62] W.U. Wuensch et al. *Phys. Rev. Lett. D*, **40**, (1989) 3153.
- [63] C. Hagmann et al. *Phys. Rev. D*, **42**, (1990) 1297.
- [64] C. Hagmann et al. *Phys. Rev. Lett.*, **80**, (1998) 2043.
- [65] S.J. Asztalos. *Phys. Rev. D*, **69**, (2004) 011101.
- [66] M. Mück, J.B. Kycia, and J. Clarke. *Appl. Phys. Lett.*, **78**, (2001) 967.
- [67] M. Tada et al. *Nucl. Phys. Proc. Suppl.*, **72**, (1999) 164.
- [68] M. Tada et al. *arXiv:physics/0101028*, (2001).

- [69] M.T. Ressell. *Phys. Rev. D*, **44**, (1991) 3001.
- [70] M.A. Bershad, M.T. Ressell, and M.S. Turner. *Phys. Rev. Lett.*, **66**, (1991) 1398.
- [71] B.D. Blout et al. *Astrophys. J.*, **546**, (2001) 825.
- [72] K. Van Bibber et al. *Phys. Rev. Lett.*, **59**, (1987) 759.
- [73] G. Ruoso et al. *Z. Phys. C*, **56**, (1992) 505.
- [74] R. Cameron et al. *Phys. Rev. D*, **47**, (1993) 3707.
- [75] L. Mainani, R. Petronzio, and E. Zavattini. *Phys. Lett. B*, **175**, (1986) 359.
- [76] Y. Semertzidis et al. *Phys. Rev. Lett.*, **64**, (1990) 2988.
- [77] E.A. Paschos and K. Ziqutas. *Phys. Lett. B*, **323**, (1994) 367.
- [78] A. Morales. *Astropart. Phys.*, **16**, (2002) 325.
- [79] F.T. Avignone. *Phys. Rev. Lett.*, **81**, (1998) 5068.
- [80] R. Bernabei et al. *Phys. Lett. B*, **515**, (2001) 6.
- [81] D.M. Lazarus et al. *Phys. Rev. Lett.*, **69**, 2333 (1992).
- [82] W.A. Bardeen, R.D. Peccei, and T. Yanagida. *Nucl. Phys. B*, **279**, (1987) 401.
- [83] S. Moriyama. *Phys. Lett. B*, **434**, (1998) 147.
- [84] T. Dafni. *A Search for Solar Axions with the MICROMEGAS Detector in CAST*. Dissertation, Technische Universität Darmstadt, 2005.
- [85] G.D. Hammond et al. *Phys. Rev. Lett.*, **98**, 081101 (2007).
- [86] R. Hammond et al. *Phys. Rev. Lett.*, **70**, 701 (1993).
- [87] A.N. Youdin et al. *Phys. Rev. Lett.*, **77**, 2170 (1996).
- [88] G. Vasolakis et al. *Phys. Rev. Lett.*, **103**, 261801 (2009).
- [89] A.G. Glenday et al. *Phys. Rev. Lett.*, **101**, 261801 (2008).
- [90] W. Zheng et al. *Phys. Rev. D*, **85**, 031505(R) (2012).
- [91] S. Baessler et al. *Phys. Rev. D*, **75**, 075006 (2007).
- [92] <http://physics.nist.gov/cuu/Constants/> , Latest (2010) values of the constants.
- [93] M. Wolf. *Erzeugung höchster  $^3\text{He}$ -Kernspinpolarisation durch metastabiles optisches Pumpen*. PhD thesis, Universität Mainz, 2004.



- [94] S. Appelt, A.B.A. Baranga, C.J. Erickson, M.V. Romalis, A.R. Young, and W. Happer. Theory of spin-exchange optical pumping of  $^3\text{He}$  and  $^{129}\text{Xe}$ . *Physical Review A*, 58(2):1412–1439, 1998.
- [95] Wolfgang Kilian. *Erzeugung von hyperpolarisiertem  $^{129}\text{Xe}$ -Gas und Nachweis mittels in vivo NMR-Bildgebung, NMR-Spektroskopie sowie SQUID-Messtechnik*. Dissertation, Freie Universität Berlin, 2001.
- [96] C. Gemmel. *Test of Lorentz Symmetry with a  $^3\text{He}/^{129}\text{Xe}$  Clock-Comparison Experiment*. Dissertation, Universität Mainz, 2010.
- [97] P.J. Nacher and M. Leduc. Optical pumping in  $^3\text{He}$  with a laser. *J. Physique*, 46:2057–2073, 1985.
- [98] E. Coutarde. *Pompage optique de l'hélium dans des conditions non-standard*. PhD thesis, École Normale Supérieure Paris (France), 2001.
- [99] S. D. Rosner and F. M. Pipkin. Hyperfine structure of the  $2^3s_1$  state of  $^3\text{He}$ . *Phys. Rev. A*, 1:571–586, 1970.
- [100] C. P. Slichter. *Principles of Magnetic Resonance*. Springer, 1978.
- [101] J.D. Jackson. *Classical Electrodynamics*. John Wiley and Sons, 1998.
- [102] J. Schmiedeskamp, W. Heil, E. W. Otten, R. K. Kremer, A. Simon, and J. Zimmer. Paramagnetic relaxation of spin polarized  $^3\text{He}$  at bare glass surfaces. *European Physical Journal D*, 38:427 – 438, 2006.
- [103] J. Schmiedeskamp, H.-J. Elmers, W. Heil, E. W. Otten, Yu. Sobolev, W. Kilian, H. Rinneberg, T. Sander-Thömmes, F. Seifert, and J. Zimmer. Paramagnetic relaxation of spin polarized  $^3\text{He}$  by magnetized ferromagnetic contaminants. *European Physical Journal D*, 38:445 – 454, 2006.
- [104] A. Deninger, W. Heil, E. W. Otten, M. Wolf, R. K. Kremer, and A. Simon. Paramagnetic relaxation of spin polarized  $^3\text{He}$  at coated glass walls. *European Physical Journal D*, 38:439 – 443, 2006.
- [105] G.D. Cates, S.R. Schaefer, and W. Happer. Relaxation of spins due to field inhomogeneities in gaseous samples at low magnetic fields and low pressure. *Phys. Rev. A*, 37, 1988.
- [106] A.E. Morbach. *Diffusionsgewichtete Helium-3 Magnetresonanztomographie zur Untersuchung der Lunge*. PhD thesis, Universität Mainz, 2006.
- [107] L.A. Pedrós. *Diffusion of laser polarized gases in MRI*. PhD thesis, Universität Mainz, 2007.

- [108] K.C. et al. Hasson. Spin relaxation due to magnetic-field inhomogeneities: Quartic dependence and diffusion-constant measurements. *Phys. Rev. A*, 41(7):3672–3688, 1990.
- [109] N.R. Newbury, A.S. Barton, G.D. Cates, W. Happer, and H. Middleton. Gaseous  $^3\text{He}$ - $^3\text{He}$  magnetic dipolar spin relaxation. *Phys. Rev. A*, 48(6), 1993.
- [110] E.R. Hunt and H.Y. Carr. Nuclear magnetic resonance of  $^{129}\text{Xe}$  in natural xenon. *Phys. Rev.*, 130(6), 1963.
- [111] B. Chann, I.A. Nelson, L.W. Anderson, B. Driehuys, and T.G. Walker.  $^{129}\text{Xe}$ -Xe molecular spin relaxation. *Phys. Rev. Lett.*, 88(11), 2002.
- [112] B. Saam, W. Happer, and H. Middleton. Nuclear relaxation of  $^3\text{He}$  in the presence of  $\text{O}_2$ . *Phys. Rev. A*, 52(1):862–865, 1995.
- [113] C.J. Jameson, A.K. Jameson, and J.K. Hwang. Nuclear spin relaxation by intermolecular magnetic dipole coupling in the gas phase.  $^{129}\text{Xe}$  in oxygen. *Journal of Chemical Physics*, 89(7):4074–4081, 1988.
- [114] M. Pfeffer and O. Lutz. *J. Magn. Reson.*, Ser. A **108**, 106 (1994).
- [115] <http://www.codata.org>.
- [116] D.M. Hopstock. A reexamination of the performance of demagnetizing coils on finely ground natural magnetite. *Int. J. Miner. Process.*, 59:45–68, 1999.
- [117] C. Ludwig. *Voruntersuchungen zu Lorentzinvarianz-Tests mit Hilfe eines  $^3\text{He}$ - $^{129}\text{Xe}$ -Komagnetometers*. Dipl. thesis, Universität Mainz, 2008.
- [118] J. Bork, H.-D. Hahlbohm, R. Klein, and A. Schnabel. The 8-layered magnetically shielded room of the ptb: design and construction. *Biomag2000; Proceedings, 12th International Conference on Biomagnetism, Helsinki*, pages 970–973, 2000.
- [119] D. Drung. *Physica C*, **368**, 134 (2002).
- [120] S. Hiebel, T. Großmann, D. Kiselev, J. Schmiedeskamp, Y. Gusev, W. Heil, S. Karpuk, J. Krimmer, E.W. Otten, and Z. Salhi. Magnetized boxes for housing polarized spins in homogeneous fields. *J. of Magn. Res.*, 204(1), 2010.
- [121] K. Tullney. *Test der Lorentzinvarianz mit Hilfe eines  $^3\text{He}$ - $^{129}\text{Xe}$ -Komagnetometers*. Dipl. thesis, Universität Mainz, 2009.
- [122] C. Gemmel et al. *Phys. Rev. D*, **82**, 111901 (2010).
- [123] E.A. Kravchenko, V.G. Orlov, and M.P. Shlykov. *Russian Chemical Reviews*, **75(1)**, 77-93 (2006).
- [124] S. Yamamoto, K. Kuroda, and M. Senda. *IEEE Transactions On Nuclear Science*, **50**, 1683 (2003).

- [125] B.C. Grabmaier and R. Oberschmid. *Phys. Stat. Sol.*, (a) **96**, 199 (1986).
- [126] C. Cohen-Tannoudji, J. DuPont-Roc, S. Haroche, and F. Lalo  
"e. Detection of the Static Magnetic Field Produced by the Oriented Nuclei of Optically Pumped  $^3\text{He}$  Gas. *Physical Review Letters*, 22(15):758–760, 1969.
- [127] G. Tastevin et al. *Appl. Phys. B*, **78**, 145 (2004).
- [128] F.W. Hersman H. Zhu, I.C. Ruset. *Opt. Lett.*, **30**, 1342 (2005).
- [129] Ya.S. Greenberg. *Rev. Mod. Phys.*, **70**, 175 (1998).
- [130] W. Kilian et al. *Eur. Phys. J. D*, **42**, 197 (2007).
- [131] M. Burghoff et al. *IEEE Trans. App. Supercon.*, **17**, 846 (2007).
- [132] S. M. Kay. *Fundamentals of Statistical Signal Processing*. Prentice Hall PTR, 1993.
- [133] C. Gemmel et al. *Eur. Phys. Journal D*, **57**, 303 (2010).
- [134] J. Allred. *Phys. Rev. Lett.*, **89**, 130801 (2002).
- [135] W.C. Griffith. *Limiting CP Violation Through a Search for a Permanent Electric Dipole Moment of Mercury 199 Atoms*. Dissertation, University of Washington, 2005.
- [136] J.A. Barnes. *IEEE Trans. Instrum. Meas.*, **20**, 105 (1971).
- [137] P. Lesage and A. Siegert. *Phys. Rev.*, **57**, 522 (1940).
- [138] H.H. Albrecht. *Proc. ICASSP2001, May 7-11, Salt Lake City, UT*, (2001).
- [139] P.D. Welch. *Audio and Electroacoustics, IEEE Transactions*, **15**, 70-73 (1967).
- [140] W.H. Press. *Numerical Recipes in C++, The Art of Scientific Computing*. Cambridge, University Press, 2003.
- [141] Iers earth orientation centre. <http://hpiers.obspm.fr/eop-pc/models/constants.html>.
- [142] Google maps, <http://pagesperso-orange.fr/universimedia/geo/loc.htm>.
- [143] D. Raftery et al. *J. Phys. Chem.*, 97(1649), 1993.
- [144] N. Segebarth et al. Novel method for the measurement of xenon gas solubility using  $^{129}\text{Xe}$  nmr spectroscopy. *J. Phys. Chem. A*, 110:10770–10776, 2006.
- [145] C.J. Jameson, A.K. Jameson, and H. Parker. *J. Chem. Phys.*, 8(68), 1978.
- [146] G.D. Cates, D.J. White, T. Chien, S.R. Schaefer, and W. Happer. Spin relaxation due to inhomogeneous static and oscillating magnetic fields. *Phys. Rev. A*, 38, 1988.
- [147] N.F. Ramsey. *Phys. Rev.*, **100**, 1191 (1955).

- [148] F. Bloch and A. Siegert. *Phys. Rev.*, **57**, 522 (1940).
- [149] The Particle Data Group. *Phys. Lett. B*, **592**, 14 (2004).
- [150] W. H. Press, S.A. Tenkolsky, W.T. Vetterling, and B.P. Flannery. *Numerical Recipes 3rd Edition: The Art of Scientific Computing*. Cambridge University Press, New York, 2007.
- [151] O. Zimmer. *Phys. Lett. B*, **38**, 685 (2010).
- [152] T. Jenke et al. *arXiv: 1208.3875v1*, (2012).
- [153] M. Bulatowicz et al. *arXiv: 1301.5224v1*, (2013).
- [154] S.A. Hoedel et al. *Phys. Rev. Lett.*, **106**, 041801 (2011).
- [155] W.-T. Ni et al. *Phys. Rev. Lett.*, **82**, 2439 (1998).
- [156] R. Ravi et al. *J. Magn. Res.*, **205**, 63 (2010).

# Erklärung

Hiermit versichere ich, dass ich die vorliegende Arbeit selbstständig verfasst und keine anderen, als die angegebenen Quellen und Hilfsmittel verwendet habe. Alle Stellen, die dem Wortlaut oder Sinn nach anderen Werken entnommen sind, habe ich durch die Angabe der Quelle kenntlich gemacht. Die Arbeit ist in dieser oder ähnlicher Form noch nicht als Prüfungsarbeit eingereicht worden.

Beselich, November 2013

(Kathlyne Tullney)



# Danksagung

Hiermit möchte ich mich bei allen Menschen ganz herzlich bedanken, die mich in den vergangenen Jahren unterstützt haben und somit zum Gelingen dieser Arbeit beigetragen haben. Mein besonderer Dank gilt:

- Meinem Doktorvater Prof. Dr. W.H. für die interessante Themenstellung und seiner Betreuung. Dank der regelmäßigen Besprechungen und vieler kritischer Diskussionen konnten schwierige physikalische Fragen beantwortet werden und somit die Arbeit zum gewünschten Abschluss gebracht werden.
- Den Mitgliedern der Kollaboration: L.T., M.B., A.S., S.K.-G., W.K., F.S., W.M., F.P. und D.G. von der PTB Berlin für die freundliche Zusammenarbeit, die vielen Denkanstöße und die großartige Unterstützung während den Messperioden. Desweiteren danke ich auch Prof. U.S. und F.A. von der Universität Heidelberg für ihre freundliche Zusammenarbeit und die große Unterstützung bei der Datenanalyse. Außerdem möchte ich auch S.K., I.S. und C.G. von der Universität Mainz für ihre tatkräftige Unterstützung vor, während und nach den Messzeiten danken.
- Allen derzeitigen und ehemaligen Mitgliedern der  $^3\text{He}$ -Arbeitsgruppe. Ein ganz besonderer Dank geht an W.S., der mir mit seinem fachmännischen Wissen immer mit Rat und Tat zur Seite stand und in brenzligen Situationen auch immer eine Lösung parat hatte. Desweiteren danke ich auch G.K., Z.S., J.K., P.B., M.B., M.G., M.B., F.A.G., J.-P.K., M.B., A.W., C.S., A.S., A.K., T.L. und allen Diplomanden und Staatsexamenskandidaten, die während meiner Doktorandenzeit der Gruppe beiwohnten, für u. a. das Polarisieren von  $^3\text{He}$ , ihre Hilfsbereitschaft und das angenehme und unterhaltsame Arbeitsklima. Special thanks goes to M.R., A.N. and C.M. for the nice hours we spent together in the office. You made this office “legen – wait for it – dary”.
- Den Sekretärinnen unserer Arbeitsgruppe, C.B. und E.S.-K., für ihre freundliche, unkomplizierte und herzliche Art.
- Den Mitarbeitern aus der mechanischen Werkstatt, Herrn S.F., E.W., L.F., H.L., S.V. und R.S. für das Anfertigen der Haltefeldspulen und anderen Bauteilen.
- Den Mitarbeitern der Glasbläserei, R.J. und B.S., für die freundliche Zusammenarbeit, das Anfertigen der Messzellen, Reparaturen von Glasteilen und den Arbeitseinsatz kurz vor den Messzeiten.
- Meinem Physik Lehrer Dr. H.-P.B., der mir die Welt der Physik näher brachte. Seine Freude und Begeisterung an der Physik, sowie sein Glaube an mich, ermöglichten mir erst das Physikstudium und somit auch das Fertigstellen dieser Arbeit. Vielen Dank.

- Allen meinen Freunden, die mir beigestanden haben und immer ein offenes Ohr für mich hatten. Ein ganz besonderer Dank geht an A.S., J.S., J.M., T.E., J.J., T.J. und D.L.. Danke für eure liebe Unterstützung, eure Aufmunterungen sowie jede Art der Ablenkung.
- Meiner Familie für ihre Liebe und Unterstützung in allen Lebenslagen. Danke dafür, dass ihr immer an mich geglaubt habt. Ein besonderer Dank gilt meinen Eltern, K. und E.T.. Danke, dass ihr immer für mich da seid. Danke, dass ihr euch mein Gejammer immer angehört habt und auch meine schlechten Launen immer ertragen habt. Danke für alles, denn ohne euch wäre das hier alles nicht möglich gewesen. Ebenso möchte ich auch meiner Schwester C. für ihre Unterstützung und ihre ruhige, aufmerksame Art danken. Danke, dass du immer ein offenes Ohr für mich hast. Last but not least, möchte ich meinem Freund H. danken, dafür, dass er mich in schwierigen Zeiten, wo es mal nicht so lief wie es sollte, immer wieder aufmuntert oder abgelenkt hat.



# Lebenslauf